Universität Stuttgart

Institut für Wasser- und Umweltsystemmodellierung

Mitteilungen

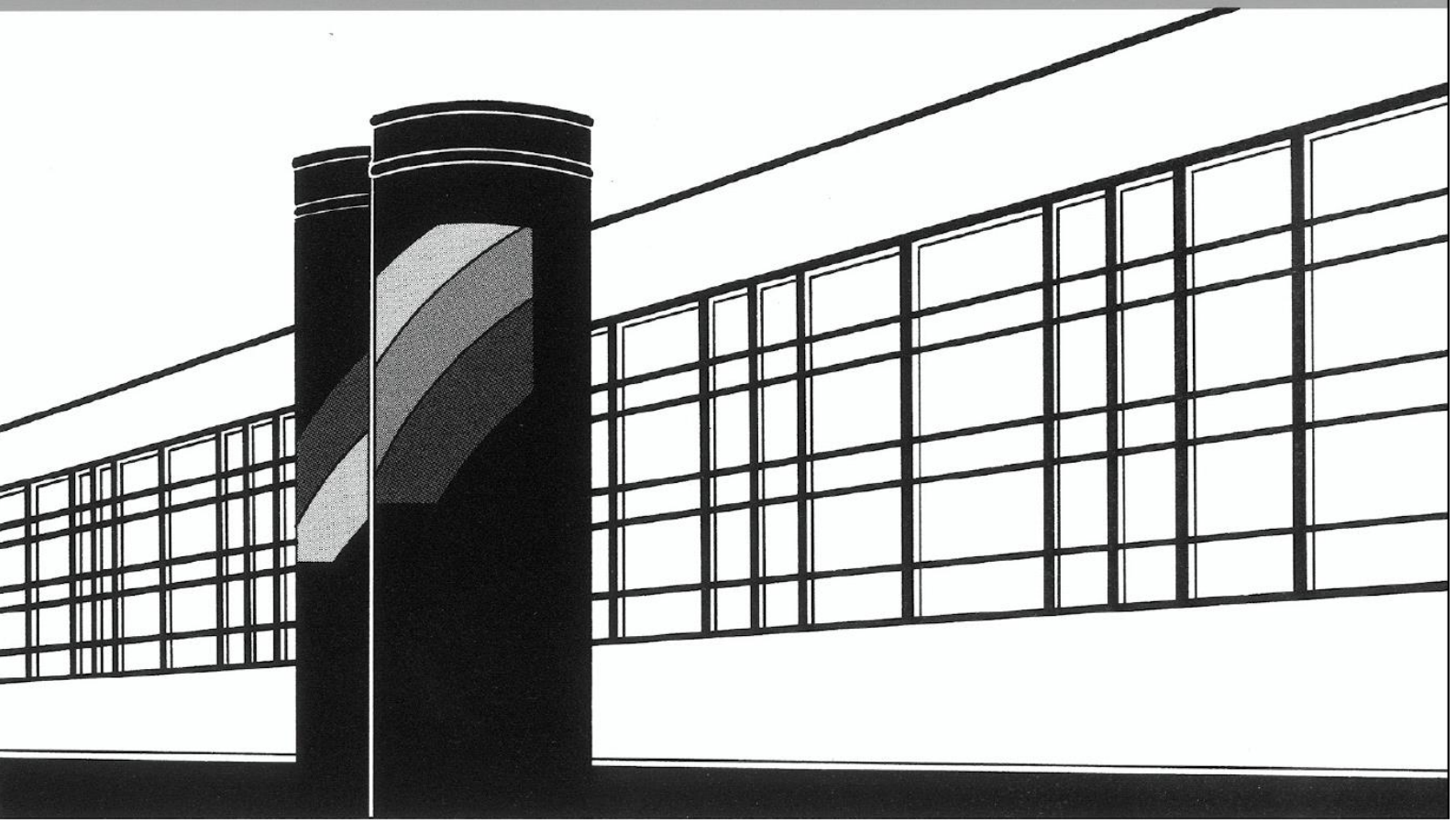

Heft 307 Kilian Mouris

A holistic approach to assess the impact of global change on reservoir sedimentation

A holistic approach to assess the impact of global change on reservoir sedimentation

Von der Fakultät Bau- und Umweltingenieurwissenschaften
der Universität Stuttgart zur Erlangung der Würde eines
Doktor-Ingenieurs (Dr.-Ing.) genehmigte Abhandlung

vorgelegt von
Kilian Mouris
aus Lörrach

Hauptberichterin:	Prof. Dr.-Ing. Silke Wieprecht
Mitberichter:	Prof. Dr. phil. Nils Rüther
	PD Dr. Stefan Haun

Tag der mündlichen Prüfung: 21. Februar 2024

Institut für Wasser- und Umweltsystemmodellierung
der Universität Stuttgart
2024

Heft 307

A holistic approach to assess the impact of global change on reservoir sedimentation

von
Dr.-Ing.
Kilian Mouris

Eigenverlag des Instituts für Wasser- und Umweltsystemmodellierung
der Universität Stuttgart

D93 A holistic approach to assess the impact of global change on reservoir sedimentation

Bibliografische Information der Deutschen Nationalbibliothek
Die Deutsche Nationalbibliothek verzeichnet diese Publikation in der Deutschen Nationalbibliografie; detaillierte bibliografische Daten sind im Internet über http://www.d-nb.de abrufbar

Mouris, Kilian:
A holistic approach to assess the impact of global change on reservoir sedimentation, Universität Stuttgart. - Stuttgart: Institut für Wasser- und Umweltsystemmodellierung, 2024

(Mitteilungen Institut für Wasser- und Umweltsystemmodellierung, Universität Stuttgart: H. 307)
Zugl.: Stuttgart, Univ., Diss., 2024
ISBN 978-3-910293-11-3

NE: Institut für Wasser- und Umweltsystemmodellierung <Stuttgart>: Mitteilungen

Herausgegeben 2024 vom Eigenverlag des Instituts für Wasser- und Umweltsystem-modellierung

Druck: P+K Solutions GmbH & Co. KG, Stuttgart

Acknowledgements

I would like to express my sincere gratitude to Prof. Dr.-Ing. Silke Wieprecht. Her unwavering guidance and support have been invaluable throughout my academic journey. I was greatly inspired by Prof. Wieprecht's lectures on hydraulic engineering, and her mentorship as my Ph.D. supervisor was essential for my academic and professional development.

I would like to thank PD Dr. Stefan Haun for his constant support since my master studies. His collaboration on numerous projects and his guidance during my dissertation were of great importance. Dr. Haun's confidence in my abilities enabled me to develop my own ideas, and our joint endeavors were enriched by memorable excursions, business trips, and countless refreshing lunch breaks.

I am also grateful to Prof. Dr. phil. Nils Rüther, who has also acted as examiner for this thesis. His insights into catchment processes and data, coupled with his expertise in numerical modeling and hydro-morphological processes, have enriched my research.

I extend special gratitude to my co-authors Dr. sc. Sebastian Schwindt, María Herminia Pesci, Eduardo Acuna Espinoza, María Fernanda Morales Oreamuno, Dr.-Ing. Farid Mohammadi, Prof. Dr. Kristian Förster and apl. Prof. Dr.-Ing. Sergey Oladyshkin for their valuable contributions to the publications included in this cumulative thesis.

It was a pleasure to work with the international partners in the DIRT-X project from Norrköping, Innsbruck, Utrecht, Hannover, and Trondheim, who taught me how exciting and interesting it is to be part of an international, transdisciplinary research project. Thank you for the great experiences, scientific exchange, and good times we had in Sweden, Norway, Austria, and Albania. I'm also grateful to the international doctoral program ENWAT for the financial support to attend the IAHR World Congress 2024 in Vienna.

Many others have accompanied and supported me over the years and a big thank you goes out to all my colleagues, student assistants, and graduates with whom I have had the great pleasure of working. I have been blessed to work with outstanding colleagues who have made my working experience enjoyable. I have appreciated the professional dialogue as well as the fun coffee breaks and exciting field trips.

I would like to thank my parents, family, and friends for their constant encouragement and moral support throughout my studies and doctoral research. My parents made many things

possible for me without interfering or putting pressure on me. This allowed me to go my own way and follow my inner compass. I will always be grateful for this.

Words cannot express my gratitude to Jasmin. Thank you for your unwavering support, patience and love over the past years.

Kilian Mouris

April 14, 2024

Stuttgart, Germany

Contents

List of Figures

List of Tables

List of Symbols

The following symbols are used in this thesis:

A	Soil loss
C	Cover and management factor
K	Soil erodibility factor
LS	Slope length and steepness factor
P	Support practice factor
$p(z_{\text{meas}})$	Bayesian model evidence
$p(z_{\text{meas}}\|\omega)$	Likelihood function that quantifies how well the model, characterized by ω, predicts z_{meas}
$p(\omega)$	Prior probability distribution of the calibration parameter values ω
$p(\omega\|z_{\text{meas}})$	Posterior probability of the calibration parameter values ω given the observed bed levels z_{meas}
R	Annual rainfall-runoff erosivity factor
R_m	Monthly rainfall-runoff erosivity factor
z_{meas}	Observed bed levels
ω	Vector of calibration parameters values

List of Abbreviations

The following abbreviations are used in this thesis:

ADCP	Acoustic Doppler current profiler
BAL	Bayesian active learning
BME	Bayesian model evidence
DEM	Digital elevation model
ESDB	European Soil Database
FOSM method	First-Order Second-Moment method
GCM	Global Climate Model
GHG	Greenhouse gas
GPE	Gaussian process emulator
HWSD	Harmonized World Soil Database
LOO-CV	Leave-one-out cross-validation
NDSI	Normalized Difference Snow Index
NDVI	Normalized Difference Vegetation Index
RCM	Regional Climate Model
RCP	Representative Concentration Pathways
RUSLE	Revised Universal Soil Loss Equation
SDR	Sediment delivery ratio
SEDD	SEdiment Delivery Distributed Model
SSIIM2	Sediment Simulation In Intakes with Multiblock Option 2
SSP	Shared Socioeconomic Pathways
SY	Sediment yield
TE	Trapping efficiency
WaSiM	Water Flow and Balance Simulation Model

Abstract

Global change is altering land use and hydro-climatic conditions, leading to more frequent and more severe droughts and floods in the future. Acknowledging the need for adaptive measures, large artificial reservoirs emerge as powerful tools to mitigate the effects of hydrological extremes. However, reservoirs interrupt the longitudinal continuity of river systems, causing sediment deposition due to an abrupt decrease in flow velocity. Consequently, reservoir sedimentation reduces storage volume and compromises buffering capacity, increasing local water scarcity and flood risk. Hence, reservoir sedimentation poses a substantial global challenge, reducing net reservoir storage despite the construction of many new reservoirs. Compounding this challenge, projected hydro-climatic and land use changes will likely increase soil erosion and suspended sediment loads, further accelerating reservoir sedimentation. However, the variation in sediment production and projected trends among regions highlights the complexity of predicting reservoir sedimentation and subsequent storage loss for individual reservoirs, requiring objective and holistic assessments of sediment production, delivery, and reservoir processes.

Existing modeling tools for assessing the global impacts of climate change face limitations in simulating the complex processes that drive reservoir sedimentation. While some models can estimate the effects of climate change on sediment production, they neglect the influence of land use changes. Moreover, only some models integrate hydro-climatic and land use changes, often relying on oversimplified representations of reservoirs. Therefore, the overarching goal of this thesis is to develop objective methods for predicting long-term sediment dynamics, reservoir sedimentation, and deposition patterns under various global change scenarios, including future hydro-climatic and land use changes. By quantifying the impact of global change on reservoir sedimentation, the developed holistic approach aims to facilitate sustainable reservoir operations.

Four research articles form the core of this cumulative thesis. The first three publications are fundamental building blocks that contribute to the ultimate objective addressed in the fourth publication. Publication I introduces a practical and objective approach for calculating sediment loads, utilizing satellite imagery and climate reanalysis data. The approach is designed to be applicable in data-sparse regions where precise field measurements and high-resolution precipitation data may be lacking. A novel feature of this developed method is the consideration of non-erosive snowfall, which gradually accumulates over months, followed by erosive

snowmelt. The integration of seasonal snow memory into the Revised Universal Soil Loss Equation (RUSLE) significantly improves the accuracy of soil erosion and sediment transport predictions in the studied mountainous Mediterranean catchment.

Publication II focuses on calibrating multidimensional reservoir models to simulate reservoir sedimentation processes. A surrogate-based Bayesian calibration approach is used to circumvent the drawbacks of time-consuming trial-and-error calibration procedures. Modeling reservoir sedimentation is challenging due to the concurrent simulation of deep waters, shallow shores, and tributary deltas prone to deltaic avulsion and erosion. Publication II examines the calibration of a complex numerical model, considering competing model simplifications, and additionally analyzes the importance of the four calibration parameters to prioritize them accordingly in field surveys. Bayesian calibration only yields meaningful parameter combinations within the valid geospatial range of the numerical model, with dry bulk density identified as the most important and influential parameter. Consequently, collecting dry bulk density data before setting up a numerical model for predicting reservoir sedimentation is recommended.

Publication III introduces an interdisciplinary model chain to predict reservoir sedimentation and preceding catchment processes for various climate change scenarios. Emphasizing the essential consideration of uncertainties and their propagation within the modeling chain, the main objective of the article is to assess whether simulation results are more influenced by model parameter uncertainties or climate model uncertainties. The First-Order Second-Moment (FOSM) method is identified as a suitable approach for approximating model parameter uncertainties in this complex modeling chain. The results show that the uncertainties arising from different climate projections significantly exceed the approximate model parameter uncertainties for the investigated low emissions scenario. Therefore, using an ensemble of climate models is recommended to reduce the bias of individual climate models. Ultimately, this method enables modelers to communicate various sources of uncertainty in complex modeling chains efficiently.

Publication IV builds on the previous publications by addressing the central issue of reservoir sedimentation in the context of global change. The interdisciplinary model chain integrates catchment characteristics, hydro-climatic conditions, and land use data to assess the impact of different global change scenarios on river discharge, sediment production and delivery, and reservoir sedimentation processes. The model chain predicts reduced river discharges and increased sediment loads for high and medium emissions scenarios when applied to the mountainous Mediterranean catchment of the Devoll River. Low emissions scenarios project elevated river discharges. Shifts in precipitation patterns, such as the increase in winter rainfall, the decrease in snowfall, and the reduction in summer precipitation, contribute significantly to water scarcity during Mediterranean summers. This finding highlights the importance of water storage in artificial reservoirs. Furthermore, increased winter precipitation amplifies sediment pro-

duction and reservoir sedimentation. Although hydro-climatic changes contribute to increased reservoir sedimentation, the results show that the effects of land use change can outweigh these effects, emphasizing the importance of localized interventions, such as afforestation, to mitigate sediment production. Finally, a 3D hydro-morphodynamic model illustrates the interplay between global change and reservoir sedimentation, providing spatially explicit information on future deposition patterns to facilitate the implementation of sustainable reservoir management strategies.

This dissertation presents a comprehensive and interdisciplinary approach to predicting and understanding reservoir sedimentation under the influence of global change. By addressing key modeling and calibration challenges, the thesis provides valuable insights into sedimentation processes and contributes to the sustainable management of reservoirs under changing hydro-climatic and land use conditions.

Kurzfassung

Der globale Wandel umfasst eine Vielzahl von weltweiten Veränderungsprozessen, wie z. B. die globale Erwärmung, die Umwandlung von Wäldern in landwirtschaftliche Nutzflächen, aber auch die Zunahme der Weltbevölkerung und der damit einhergehende steigende Wasser- und Energiebedarf. Diese zukünftigen Entwicklungen beeinflussen die hydroklimatischen Bedingungen und die Landnutzung, was zu häufigeren und intensiveren Dürreperioden und Hochwasserereignissen führen wird. Eine bewährte Maßnahme zur Abschwächung dieser hydrologischen Extreme ist die Schaffung künstlicher Stauseen. Stauseen unterbrechen jedoch die longitudinale Sedimentdurchgängigkeit von Flusssystemen und die im Fluss transportierten Sedimente lagern sich aufgrund der verringerten Fließgeschwindigkeit im Stauraum ab. Dadurch reduziert sich das Speichervolumen, und die Pufferkapazität der Stauseen wird eingeschränkt, was wiederum die Wahrscheinlichkeit von Hochwasserereignissen und Dürren erhöht. Die Verlandung von Stauseen stellt weltweit eine große Herausforderung dar und führt trotz des Baus zahlreicher neuer Stauseen zu einer Verringerung des Nettospeichervolumens. Erschwerend kommt hinzu, dass die zu erwartenden hydroklimatischen und landschaftlichen Veränderungen voraussichtlich die Bodenerosion und die Schwebstofffracht erhöhen und damit die Stauraumverlandung weiter beschleunigen werden. Die Sedimentproduktion und die zu erwartenden Trends sind jedoch regional sehr unterschiedlich, so dass eine Prognose der Stauraumverlandung für einzelne Stauseen eine genaue und umfassende Bewertung der Sedimentproduktion, des Sedimenteintrags und der Verlandungsprozesse in den Stauseen erfordert.

Bestehende Modellierungsansätze können die komplexen Prozesse, welche die Sedimentation von Stauseen beeinflussen, nur bedingt simulieren. Einige Modelle können zwar die Auswirkungen des Klimawandels auf die Sedimentproduktion und -fracht für bestimmte Einzugsgebiete abschätzen, vernachlässigen aber den Einfluss von Landnutzungsänderungen. Umgekehrt können Modelle, die historische Veränderungen in der Landnutzung berücksichtigen, die Auswirkungen zukünftiger und langfristiger Klima- und Landnutzungsänderungen nicht einbeziehen. Die wenigen Modelle, welche sowohl hydroklimatische als auch Landnutzungsänderungen berücksichtigen, verwenden jedoch stark vereinfachte Stauraummodelle. Das übergeordnete Ziel dieser Arbeit ist daher die Entwicklung objektiver Methoden zur Vorhersage der langfristigen Sedimentdynamik, Stauraumverlandung und deren Ablagerungsmuster unter Berücksichtigung von zukünftigen hydro-klimatischen und Landnut-

zungsänderungen. Durch die Quantifizierung der Auswirkungen des globalen Wandels auf die Verlandung von Stauseen soll der entwickelte umfassende Ansatz den nachhaltigen Betrieb von Stauseen zukünftig ermöglichen.

Die vorliegende Dissertation wurde in kumulativer Form erstellt und basiert auf vier wissenschaftlichen Veröffentlichungen. In Publikation I wird ein objektiver und praxisorientierter Ansatz zur Berechnung der Sedimentfracht vorgestellt. Dieser Ansatz verwendet Satellitenbilder und Reanalysedaten, wodurch er auch in Regionen mit geringer Datengrundlage und ohne hochauflösende Niederschlagsdaten anwendbar ist. Eine wichtige Neuerung der entwickelten Methode ist die Berücksichtigung von nicht-erosivem Schneefall und der erosiven Wirkung der nachfolgenden Schneeschmelze. Die Ergebnisse zeigen, dass die Einbindung des saisonalen Schneespeichers in die Revised Universal Soil Loss Equation (RUSLE) die Vorhersage von Bodenerosion und Sedimentfracht, im untersuchten gebirgigen mediterranen Einzugsgebiet, erheblich verbessert.

Der Fokus der zweiten Publikation liegt auf der Kalibrierung von mehrdimensionalen numerischen Modellen zur Simulation von Verlandungsprozessen in Stauseen. Zur Umgehung der Nachteile zeitaufwendiger Trial-and-Error Kalibrierungsverfahren wird ein surrogatgestützter Bayes'scher Kalibrierungsansatz verwendet. Die Modellierung von Stauraumverlandung ist besonders herausfordernd, da gleichzeitig die Sedimenttransportprozesse in den flachen Bereichen des Flussdeltas und entlang der Ufer sowie in den tiefen Bereichen des Stauraums simuliert werden. Die Vorhersage der Wechselwirkung von Depositions- und Erosionsprozessen im Stauwurzelbereich sowie die Bestimmung des zukünftigen, oft verzweigten Flussverlaufs im Delta sind herausfordernd und nur schwer mit numerischen Modellen zu erfassen. Publikation II untersucht die Kalibrierung eines komplexen numerischen Modells unter Berücksichtigung konkurrierender Modellvereinfachungen und analysiert zusätzlich den Einfluss von vier Kalibrierungsparametern auf die simulierten Verlandungsprozesse. Die Ergebnisse zeigen, dass die Bayes'sche Kalibrierung nur dann zu physikalisch sinnvollen Parameterkombinationen führt, wenn die zur Kalibrierung verwendeten Messpunkte innerhalb des gültigen Bereichs des numerischen Modells liegen und der Bereich der Stauwurzel nicht berücksichtigt wird. Zusätzlich wird die Schüttdichte der angelandeten Sedimente als wichtigster Parameter identifiziert und sollte daher vor der Erstellung des numerischen Modells messtechnisch bestimmt werden.

In Publikation III wird die entwickelte Modellkette zur Vorhersage von Stauraumverlandung und der vorangehenden Prozesse im Einzugsgebiet für verschiedene Klimawandelszenarien vorgestellt. Dabei ist es wichtig, die Fortpflanzung von Unsicherheiten innerhalb der Modellierungskette zu berücksichtigen. Das Hauptziel der Veröffentlichung besteht darin, zu bewerten, ob die Simulationsergebnisse mehr durch die Unsicherheiten der Modellparameter oder durch die Unsicherheiten der Klimamodelle beeinflusst werden. Zur Abschätzung von Modellparameterunsicherheiten wird im Rahmen der Studie die First-Order-Second-Moment-Methode

(FOSM) verwendet. Die Ergebnisse zeigen, dass die Unsicherheiten, die sich aus den verschiedenen Klimaprojektionen ergeben, die approximierten Modellparameterunsicherheiten für das untersuchte Niedrigemissionsszenario deutlich übersteigen. Daher wird die Verwendung von mehreren Klimamodellen empfohlen, um Verzerrungen durch einzelne Klimamodelle zu reduzieren. Schlussendlich ermöglicht die vorgestellte Methode eine effektive Kommunikation der verschiedenen Unsicherheitsquellen in komplexen Modellierungsketten.

Publikation IV knüpft an die vorangegangenen Publikationen an und befasst sich mit den Auswirkungen des globalen Wandels auf die Verlandung von Stauseen. Die entwickelte interdisziplinäre Modellkette untersucht die Auswirkungen verschiedener Zukunftsszenarien auf den Abfluss, die Sedimentproduktion, den Sedimenteintrag und die Verlandungsprozesse von Stauseen. Dazu werden die Charakteristika des Einzugsgebietes, hydroklimatische Bedingungen und Landnutzungsdaten berücksichtigt. Für das untersuchte bergige mediterrane Einzugsgebiet prognostiziert die Modellkette eine Abnahme des Abflusses und eine Zunahme der Sedimentfracht bei hohen und mittleren Emissionsszenarien. Niedrige Emissionen hingegen führen zu erhöhten Abflüssen. Veränderte Niederschlagsmuster, wie die Zunahme der Niederschläge im Winter, der Rückgang der Schneefälle und die Verringerung der Niederschläge im Sommer, führen zunehmend zu Wasserknappheit in den Sommermonaten. Dies verdeutlicht, dass die Wasserspeicherung in künstlichen Stauseen auch in Zukunft von Bedeutung sein wird. Insbesondere die Zunahme von Regenfällen in den Wintermonaten führt zu einer erhöhten Sedimentproduktion und damit zu einer Zunahme der Stauraumverlandung. Jedoch zeigen die Ergebnisse der Studie, dass eine Zunahme der Stauraumverlandung aufgrund hydroklimatischer Veränderungen durch die Auswirkungen von Landnutzungsänderungen kompensiert werden kann. Die Bedeutung von lokalen Maßnahmen zur Begrenzung der Sedimentproduktion, wie beispielsweise Aufforstungen, wird dadurch unterstrichen. Abschließend veranschaulicht ein 3D hydro-morphodynamisches Modell die Wechselwirkung zwischen globalem Wandel und Stauraumverlandung und liefert räumlich explizite Informationen über zukünftige Verlandungsmuster, welche die Umsetzung nachhaltiger Strategien für das Stauraummanagement erleichtern.

Die vorliegende Arbeit präsentiert einen umfassenden und interdisziplinären Ansatz zur Vorhersage der Stauraumverlandung unter dem Einfluss des globalen Wandels. Durch die Berücksichtigung der wichtigsten Herausforderungen bei der Modellierung und Kalibrierung, liefert die Arbeit wertvolle Einblicke in Sedimentationsprozesse und trägt zu einem nachhaltigen Management von Stauseen unter sich ändernden hydroklimatischen Bedingungen und Landnutzungsänderungen bei.

The thesis may contain similar and/or identical material from my publications:

”Introducing seasonal snow memory into the RUSLE”,
”Stability criteria for Bayesian calibration of reservoir sedimentation models”,
”Assessment of uncertainties in a complex modeling chain for predicting reservoir sedimentation under changing climate”, and
”An interdisciplinary model chain quantifies the footprint of global change on reservoir sedimentation”.

I omit a clear identification for readability and use these parts from the articles with kind permission from the publisher.

1. Introduction

Global change encompasses a broad range of changes caused by the significant increase in human activity since the mid-twentieth century (Steffen et al., 2005). Over the past 70 years, the global population has grown from 2.5 billion to 8 billion, while economic activity has increased nearly 12-fold (World Bank and Maddison Project, 2017). These remarkable changes have reshaped socioeconomic dynamics and left an indelible mark on Earth system trends (Steffen et al., 2005). Significant socioeconomic changes, such as urban population growth, increased energy consumption, and increased water use, concur with Earth system trends reflecting rising greenhouse gas concentrations and surface temperatures, expanded cultivated land, and tropical forest loss (Steffen et al., 2005). These global changes substantially impact hydro-climatic patterns and land use, which in turn affect the availability and distribution of water resources (Alcamo and Henrichs, 2002; García-Ruiz et al., 2011; Nilawar and Waikar, 2019; Dallison et al., 2021). Additionally, global warming intensifies the impact on water resources by increasing evapotranspiration and exacerbating extreme weather patterns, leading to more frequent and intense droughts (Dai, 2013; Trenberth et al., 2014) and floods (Alfieri et al., 2017). Recognizing the need for adaptive strategies, large artificial reservoirs emerge as one of the most effective tools for buffering the effects of such hydrological extremes. However, reservoirs interrupt the longitudinal continuity of fluvial systems, and the abrupt decrease in flow velocities leads to sediment deposition in reservoirs (Morris and Fan, 1998; Hinderer et al., 2013; Sun et al., 2021). Therefore, reservoir sedimentation threatens buffer capacity by reducing the storage volume, exacerbating local water availability problems and flood risks (Kondolf et al., 2014; Yasarer and Sturm, 2016; Schleiss et al., 2016).

Reservoir sedimentation is a substantial global problem, resulting in annual losses of 0.5-1% of existing storage (Mahmood, 1987; Yoon, 1992; Bruk, 1996; Basson, 2009). This trend has led to a decline in net reservoir volume despite the construction of more than 3,500 large dams worldwide since 2000 for hydropower generation alone (Annandale, 2013; Zarfl et al., 2015). Furthermore, the global per-capita storage capacity is declining even faster due to a lack of construction to keep up with population growth (UNESCO, 2021). To make matters worse, anticipated hydro-climatic and land use changes are expected to increase soil erosion and suspended sediment loads, thereby accelerating reservoir sedimentation (Shrestha et al., 2013; Panagos et al., 2021; Shi et al., 2022; Patro et al., 2022). However, sediment production and expected trends vary significantly across regions, depending on climate, lithology, topography, precipitation,

temperature, and anthropogenic influences (Walling and Webb, 1996; Annandale, 2013; Panagos et al., 2021). Consequently, predicting reservoir sedimentation and subsequent storage loss for individual reservoirs requires accurate, holistic assessments of sediment production, delivery, and reservoir sedimentation processes. Because every system is unique, simulating relevant processes and considering global change impacts is challenging but necessary for designing reservoirs and ensuring sustainable reservoir sediment management.

One of the key challenges in assessing the global impacts of climate change is the limited detail and capacity of existing modeling tools to simulate the essential processes that govern sediment production, delivery, and reservoir sedimentation. For example, the accurate prediction of reservoir sedimentation through hydro-morphodynamic numerical models (Rüther and Olsen, 2005; Haun et al., 2013; Olsen and Hillebrand, 2018; Mouris, Acuna Espinoza, Schwindt, Mohammadi, Haun, Wieprecht and Oladyshkin, 2023) demands an objective approach to calculate sediment supply based on catchment characteristics and hydro-climatic parameters. While some models can assess the impact of climate change on sediment production and loads for specific catchments (Shrestha et al., 2013; Nerantzaki et al., 2015; Azari et al., 2016; Hirschberg et al., 2021; Ahmad et al., 2021) or continents (Moragoda and Cohen, 2020; de Oliveira Fagundes et al., 2023), they often disregard the influence of land use changes, despite recognizing their importance. Conversely, models that account for historical changes in land use may not incorporate the effects of future long-term changes in climate and land use (Khoi and Suetsugi, 2014; Zhao et al., 2018; Shi et al., 2022). Only a few models can effectively consider the impact of hydro-climatic change and land use on sediment dynamics (Mullan et al., 2012; Nunes et al., 2013; Routschek et al., 2014; Sinha et al., 2020). However, these models usually oversimplify reservoirs by representing them as lines in one-dimensional hydro-morphodynamic models (Ehrbar et al., 2018; Khan et al., 2020) or relying on basic empirical estimates such as the Brune (1953) or Churchill (1948) curve to assess the effect of climate change on reservoir sedimentation (Bussi et al., 2021).

Such simplistic models approximate reservoir storage loss but cannot account for spatially explicit deposition patterns. However, information on the location of sediment depositions is crucial for reservoir operation management decisions. For example, sedimentation at the head of the reservoir can lead to increased upstream flood levels. At the same time, sediment accumulation near the dam outlets poses a substantial risk to the safe operation of the reservoir (Morris and Fan, 1998). Local measures to remobilize sediment deposition, such as dredging or flushing, provide strategies to reduce these risks. However, dredging and spatiotemporally efficient flushing necessitate multidimensional comprehension of hydro-morphodynamic processes. Currently, no modeling system or model chain offers such extensive information. Consequently, state-of-the-art modeling tools fall short of the multidisciplinary simulations needed to predict reservoir sedimentation processes and patterns, especially in global change scenarios.

To overcome these challenges, the overarching goal of this thesis is to develop objective methods for predicting long-term sediment dynamics and multidimensional reservoir sedimentation under different global change scenarios, including hydro-climatic and land use changes. The proposed model chain considers changes in temperature, precipitation, river discharge, sediment production and delivery, and reservoir sedimentation. This comprehensive approach aims to facilitate sustainable reservoir operations by quantifying the impact of global change on reservoir sedimentation.

1.1. Motivation and objectives

Reliable long-term predictions of reservoir sedimentation for climate or global change scenarios require an objective method for calculating sediment loads. However, existing approaches often lack objectivity in their calculation, and the uncertainties in their final results remain unknown (Song et al., 2011). Therefore, the primary goal of Publication I is to establish a practical and objective workflow for generating monthly sediment loads, considering catchment characteristics and hydro-climatic parameters (see Figure 1.1). This method uses freely available datasets, such as satellite imagery and reanalysis data, ensuring applicability even in data-sparse regions where high-resolution precipitation data and detailed field surveys are unavailable.

In addition, the widely employed Revised Universal Soil Loss Equation (RUSLE, Renard et al., 1991) lacks differentiation between precipitation in the form of rain or snow (Alewell et al., 2019), leading to a recognized research gap (Yin et al., 2017). To bridge this gap, a core element of the developed method is an algorithm that considers both the non-erosivity of snowfall and the erosivity of snowmelt by introducing a seasonal memory into the RUSLE. Thus, Publication I further evaluates whether incorporating snowfall and snowmelt into the RUSLE improves the accuracy compared to existing approaches that neglect the influence of snow on soil erosion.

Publication II focuses on calibrating hydro-morphodynamic numerical models to simulate reservoir sedimentation (see Figure 1.1). During this process, the calibration parameters are adjusted within a physically reasonable range to achieve satisfactory agreement between modeled and measured data within appropriate tolerances (Simons et al., 2000; Oberkampf et al., 2004; Paul and Negahban-Azar, 2018). The conventional trial-and-error approach is not only time-consuming and labor-intensive but also subjectively biased, lacking consideration for uncertainty in measured data, modeling errors, and equifinality. While Bayesian calibration can overcome some of these limitations, its iterative nature makes it impractical for computationally intensive models (Schmelter and Stevens, 2013; Muehleisen and Bergerson, 2016; Beckers

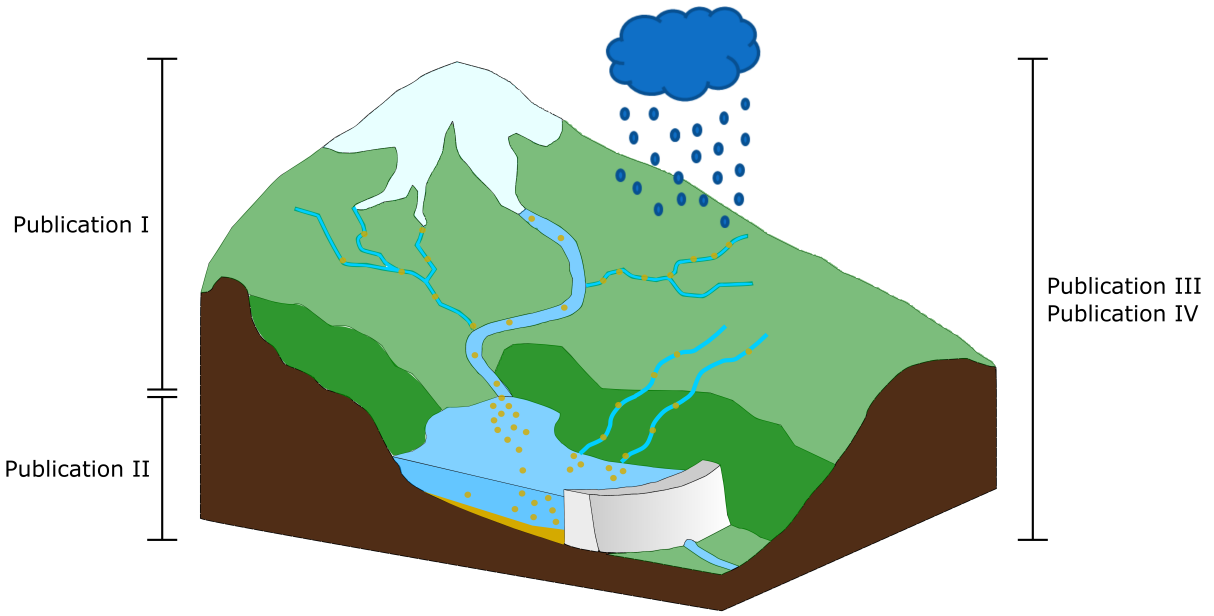

Figure 1.1. Simplified schematic representation of a catchment and reservoir illustrating the processes governing reservoir sedimentation. The figure delineates the focus and chronological sequence of the publications.

et al., 2020). Therefore, meta- or surrogate models emerge as a viable solution to mitigate long computing times and accurately replicate the input-output behavior of complex models.

Modeling reservoir sedimentation is particularly challenging due to the simultaneous simulation of shallow shores, tributary deltas, and deep waters. Predicting the exact location of channel erosion and deltaic avulsion at the head of the reservoir is inherently difficult (Hajek and Wolinsky, 2012; Chadwick et al., 2019), leading to inaccuracies in representing some regions of a reservoir model due to global model assumptions. Therefore, Publication II examines the calibration of a complex numerical model for predicting reservoir sedimentation in the presence of competing model simplifications. It also explores whether Bayesian calibration converges towards physically meaningful parameters only when the model is well-conditioned. Moreover, important calibration parameters, such as grain size distribution, critical bed shear stress for erosion of cohesive sediments, and dry-bulk density, often require labor-intensive and costly field sampling. Hence, Publication II investigates whether at least one of the calibration parameters significantly dominates the deposition of suspended sediment in reservoirs, addressing the importance of identifying and prioritizing influential parameters to reduce the workload and costs associated with extensive field sampling.

Publication III delves into the developed model chain, which includes several state-of-the-art models designed to predict sedimentation processes for different hydro-climatic and land use conditions (see Figure 1.1). However, when multiple models contribute to predicting a vari-

able, superposition effects of uncertainties from different sources may arise, leading to an increase in the uncertainty of the final target variable. Determining model parameters and their corresponding values can be challenging, especially when limited measurements are available. Therefore, it is crucial to understand the impact of the model parameters on the final simulation results and the confidence in these results (Moges et al., 2021). Moreover, considerable uncertainties are associated with the results of climate models (Prudhomme and Davies, 2009). In Publication III, we quantify the approximate uncertainties in the model parameters and compare them to the spread of climate projections. Ultimately, Publication III examines whether simulation results are impacted more by perturbations in the model parameters (approximate parameter uncertainties) than by the spread of climate projections (climate model uncertainties).

The results from the initial three publications pave the way for the fourth and concluding Publication IV, which explores the influence of various global change scenarios on future river discharge, sediment production, and reservoir sedimentation, thereby addressing the overarching research question of this thesis (see Figure 1.1). An additional objective is to compare the predicted impacts of hydro-climatic changes on reservoir sedimentation with the predicted impacts of land use changes.

1.2. Structure of this thesis

This doctoral thesis is a cumulative dissertation based on four peer-reviewed journal articles. Following the introduction in Chapter 1, Chapter 2 covers the fundamentals of reservoir sedimentation, starting from sediment production in the catchment to delivery and deposition in the reservoir. Furthermore, the consequences of reservoir sedimentation downstream and upstream of the dam are discussed. Chapter 3 details the materials and methods used and developed in this thesis. In Chapter 4, concise summaries of the published journal articles are presented, while the full articles are included in individual chapters: Publication I, II, III, and IV. Finally, Chapter 5 presents the conclusions and recommendations.

2. Fundamentals on reservoir sedimentation

Artificial reservoirs constitute indispensable elements of modern infrastructure, providing drinking water, irrigation water, flood protection, recreation, and hydropower (e.g., Kim et al., 2020; Schleiss et al., 2016). However, reservoirs interrupt the longitudinal continuity of fluvial systems (Kondolf, 1997; Hinderer et al., 2013; Sun et al., 2021). The diminished flow forces and turbulence levels result in sediment accumulation within the reservoir, creating a sediment deficit downstream of the dam (Morris and Fan, 1998; Morris et al., 2008). This chapter focuses on the origin of sediments, sediment delivery, sedimentation processes, and the consequences of reservoir sedimentation.

2.1. Origin of sediments

The primary source of sediment deposition in reservoirs is soil erosion triggered by rainfall and subsequent transport by streams (Morris and Fan, 1998). Water is the predominant natural erosive agent responsible for the majority of global soil erosion (Bridges and Oldeman, 1999; Quinton et al., 2010), as reflected by a literature review that found that 95% of modeling applications between 1994 and 2017 considered only water as erosive agent (Borrelli et al., 2021). Therefore, this chapter focuses on water-induced erosion processes and does not consider wind and glacial erosion.

The contribution of individual erosion processes to total sediment production is complex and depends on catchment characteristics, including vegetation, soil type, topography, and hydroclimatic conditions. Rill and inter-rill erosion are emerging as crucial processes worldwide, particularly on agricultural land. Soil erosion from agricultural land can account for 40 to 70% of the total sediment load in streams and is a primary contributor to reservoir sedimentation (Fox et al., 2016). However, in some catchments, gully erosion is the dominant source of sediment (e.g., Caitcheon et al., 2012; Zhang et al., 2018). Figure 2.1 shows the main erosion processes and sediment sources that will be introduced in the following chapter.

Splash erosion Splash erosion or raindrop impact constitutes the first stage of the rainfall-induced erosion process (see Figure 2.1). It breaks up the granular structure of the soil due to

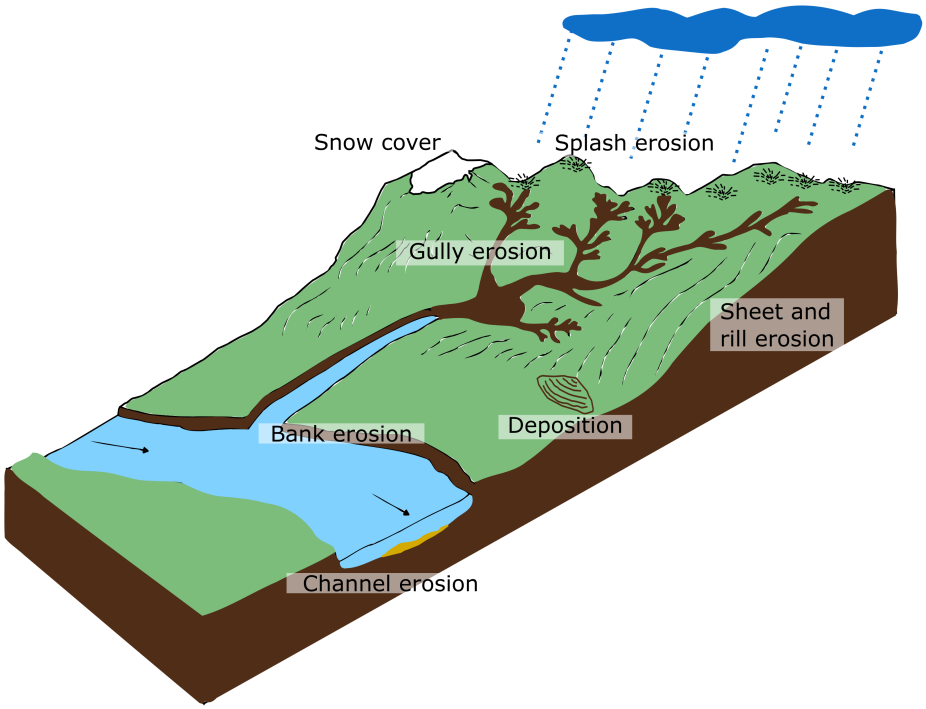

Figure 2.1. Schematic representation of typical erosion processes and sediment sources (modified after Vanoni, 1975; Klaghofer et al., 1992).

the kinetic energy of the raindrops (Fernández-Raga et al., 2010). This fragmentation produces particles small enough to be carried by shallow flows, while raindrop impact also transports particles up to 1.5 m horizontally through rain splash (Ryżak et al., 2015). Additionally, splash erosion creates surface crusts, which reduce infiltration and increase surface runoff (Poesen, 1984; Fernández-Raga et al., 2010). Unlike rainfall, snowfall does not cause splash erosion due to the low kinetic energy of the snowflakes.

Rill and inter-rill or sheet erosion Sheet and inter-rill erosion are often used interchangeably to describe the uniform topsoil erosion caused by water flowing in a sheet rather than in specific rills or channels (Morgan, 2009). Inter-rill transport distances are typically limited to a few meters before flow concentrates in rills (Morris and Fan, 1998). The microtopography of the terrain governs the formation and location of these rills on hillslopes (Carollo et al., 2015). As water flow concentrates in rills, the bed shear stress increases, facilitating the detachment of soil particles. Consequently, sediment transport efficiency is enhanced because concentrated flow is characterized by greater depth and velocity compared to uniform overland flow (Bruno et al., 2008). Rill and inter-rill erosion are mainly caused by rainfall but may also occur due to snowmelt.

Gully erosion Gully erosion occurs when water runoff accumulates in narrow channels, causing rapid soil erosion of significant depths (Poesen et al., 2003). In contrast to rill erosion, gully erosion entails larger and deeper channels ranging from 0.5 m to as much as 30 m (see Figure 2.1). Conventional cultivation techniques can no longer remove or mitigate these channels. Gully erosion often initiates through the enlargement of a rill or intensified flow caused by structures like roads, trails, ditches, or drains (Morris and Fan, 1998; Poesen et al., 2003). The upper limit of gullies remains indistinct, as there is no precise boundary between large gullies and (ephemeral) river channels. Although gullies share similarities with river channels in shape, they exhibit distinct features such as retreating headcuts and knickpoints along their course (Vanmaercke et al., 2016; Sun et al., 2016).

Bank and channel erosion Depending on the catchment, channel and bank erosion may also be significant sources of sediment (Wilson et al., 2008; Fox et al., 2016). Bank erosion is the gradual erosion of the soil on the banks of a river (see Figure 2.1). Eroding banks often have almost vertical profiles with newly exposed roots. The vegetation on these banks usually does not adequately protect them when undercutting occurs beneath the root zone (Morris and Fan, 1998). In addition to the banks, the bed can also erode if the bed shear stress exerted on the bed by the flow exceeds the critical shear stress of the bed material. Therefore, bed erosion is governed by particle diameters, the density of the bed material, and the shear velocity that can be approximated by the slope of the river and its water depth (e.g., Zanke, 1982).

Mass wasting Mass wasting involves various processes in which material is moved downslope by gravity, ranging from rapid events such as landslides and rockfalls, to debris and mudflows, to slow deformational creep (Coleman and Prior, 1988). Recently, the term mass wasting has been frequently used interchangeably with landslide (Pradhan and Siddique, 2019), which encompasses the downward movement of all slope-forming material without the involvement of surface runoff as a transport medium (Crozier, 1986). Mass wasting occurs episodically, usually in response to extreme events when the driving forces exceed the resisting forces to pull the slope-forming material down the slope. These events can produce large volumes of sediment but are challenging to predict in space and time. Important factors that can trigger mass wasting include heavy rainfall, thawing and snowmelt, removal of vegetation, seismic or volcanic activity, changes in water levels, and anthropogenic influences such as excavation at the toe or loading at the crest of a slope (Pradhan and Siddique, 2019). Besides the initial sediment load contributed during mass wasting, additional sediment is contributed by rainfall on landslide scars and the mass of destabilized material (Morris and Fan, 1998). Another potential sediment source is subaqueous landslides from reservoir banks and subaqueous slopes (Mulder and Alexander, 2001).

Drivers of sediment production García-Ruiz et al. (2015) conducted a comprehensive meta-analysis of data encompassing over 4,000 global sites, highlighting the substantial variability in erosion rates. This spatial variation in erosion rates also results in significant variability in rivers' global suspended sediment load (Walling and Webb, 1996). Precipitation is a crucial driver of sediment production, affecting all the erosion types described. High erosion rates are primarily related to precipitation totals and the duration and intensity of individual events (Renard, 1997; García-Ruiz et al., 2015; Battista et al., 2020). Another important erosion driver is the catchment's topography and the steepness and length of the slopes. Steeper slopes result in greater overland flow velocities, heightened shear stresses, and increased erosion rates (Liu et al., 1994; Nearing, 1997). In addition, land use and land cover significantly impact erosion and sediment production processes. Vegetated soil is less prone to erosion due to the canopy's ability to absorb the kinetic energy of raindrops, and vegetation increases bottom roughness, diminishing the energy of overland flow (Morgan, 2009). It is also crucial to consider artificial soil stabilization practices such as contouring, strip cropping, or terracing that reduce the erosion potential of surface runoff (Wischmeier and Smith, 1965; Panagos, Borrelli, Meusburger, van der Zanden, Poesen and Alewell, 2015). Another factor that significantly impacts local erosion rates is the soil type. The susceptibility to erosion depends on the soil structure, permeability, texture, and organic matter content (Wischmeier and Smith, 1978).

2.2. Sediment delivery, transport, and yield quantification

Sediment yield and sediment delivery ratio Only a part of the eroded sediments reaches the river network, reservoir, or catchment outlet. Most eroded sediments deposit in areas with limited transport capacity, like the base of slopes or floodplains (see Figure 2.1), either temporarily or permanently (Walling, 1983; de Vente et al., 2007). The sediment that ultimately reaches a specific boundary, such as a catchment outlet, is called sediment yield (SY) and is relevant for predicting reservoir sedimentation (ASCE, 1982; White, 2006).

The sediment delivery ratio (SDR) is the ratio of the SY to the gross erosion and indicates the sediment transport efficiency of hillslopes and river networks within a catchment (de Vente et al., 2007; Zhang et al., 2015). SDR values can range from a few percent to nearly 100%, with higher delivery ratios typically observed in smaller catchments with steep slopes (Boyce, 1975). While basic methods for quantifying the SDR rely mainly on the catchment area and specific empirical parameters (e.g., Boyce, 1975; Milliman and Meade, 1983; Renwick et al., 2005), recent research underscores the importance of considering geomorphological characteristics such as topography, soil type and land use, and the hydrological regime of the catchment (Lu et al., 2005; de Vente et al., 2013; Battista et al., 2020). The presence of gullies and channels not only affects sediment production and erosion but also increases SDR because effective connectiv-

ity between hillslopes and the channel network results in more efficient sediment transport processes (Walling, 1983; Cavalli et al., 2013; Zhang et al., 2015).

Furthermore, the SDR is impacted by spatial variations in erosion and transportation processes and temporal scales. SDR values offer a snapshot of erosion and deposition processes within the catchment and apply only to the period from which they were obtained, ensuring consistent temporal averaging (e.g., monthly or yearly). For example, the long-term SDR should approach 100% when a basin is in approximate equilibrium between erosion and SY over long time scales, differing significantly from the SDR of shorter periods at the event or annual scale (Lu et al., 2005).

Sediment transport processes in the catchment and rivers Sediment transport typically initiates when the bed shear stress exerted by water on the sediment particles surpasses the critical shear stress for erosion (Shields, 1936). Sediment particles are transported primarily by two distinct processes: bedload and suspended sediment transport (see Figure 2.2). Bedload transport involves particles rolling, sliding, and saltating while maintaining continuous contact with the river bed (Einstein, 1950; Van Rijn, 1984a). When hydraulic turbulence's upward force surpasses the settling velocity of particles, sediments are suspended and carried as suspended sediment loads (Rouse, 1937; Van Rijn, 1984b). Although bedload and suspended sediment transport are commonly associated with rivers, they can also occur in gullies, erosion channels, or overland flow, particularly during and after heavy rainfall or snowmelt.

The proportion of bedload to suspended sediment transport is highly site-dependent and governed by sediment particle characteristics and flow conditions. Existing literature indicates that river bedload typically comprises 5 to 20% of the total load (Turowski et al., 2010). Lower bedload fractions may occur in gravel-bed or bedrock rivers with high suspended sediment concentrations. In contrast, sand-bed rivers with low suspended load concentrations may exhibit bedload fractions exceeding 20% (Lane and Borland, 1951). A particular aspect of suspended sediment transport is hyperconcentrated flow, characterized by sediment concentrations high enough to affect flow behavior (Wan and Wang, 1994; Pierson, 2005). In this case, suspended particles in the sediment-water mixture form a weak structural lattice, resulting in a pseudo-one-phase flow that behaves more like a pseudoplastic or Bingham fluid than a Newtonian fluid (Morris and Fan, 1998). Typical examples are turbidity currents (see Chapter 2.3) and mudflows.

Sediment yield quantification Several techniques can be applied to estimate and quantify the SY of a catchment. Monitoring soil erosion processes at a small scale, such as a plot or slope, by using erosion pins, fabric dams, or silt fences provides insight into the temporal dynamics of soil erosion (Morris and Fan, 1998; Bugg et al., 2017; Kearney et al., 2018). Furthermore, fallout

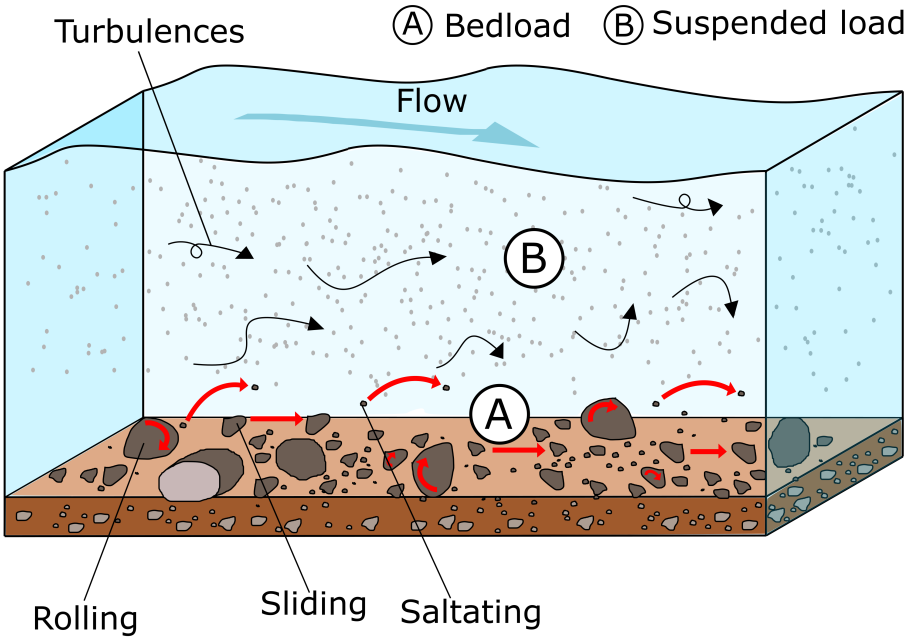

Figure 2.2. Schematic representation of a) bedload and b) suspended sediment transport processes (modified after Marshak, 2018).

radionuclides can offer quantitative information on soil erosion (Mabit et al., 2008). While these methods capture the temporal dynamics of erosion processes, their local results must be extrapolated to a catchment scale for SY quantification. Since obtaining representative coverage of large catchments with erosion plots is not feasible, the methods are deemed unsuitable for large catchments.

Long-term monitoring of river sediment transport is frequently used to determine the SY at the catchment scale and to capture the temporal dynamics. However, monitoring periods are often constrained, emphasizing the importance of measuring floods or extreme events to prevent underestimation of SY. Most existing studies rely on suspended sediment measurements because of the higher proportion of the total load and because it is easier to obtain representative measurements. Typical techniques used to quantify suspended sediment loads include direct physical sampling followed by laboratory analysis or indirect methods using optical or acoustic methods, typically used to develop sediment rating curves (Annandale et al., 2016; Aberle et al., 2017). Bedload is typically estimated as a percentage of the suspended load (Galy and France-Lanord, 2001; Grams et al., 2013). However, state-of-the-art techniques for quantifying bedload include passive (e.g., geophones) and active acoustic measurements (e.g., ADCPs), monitoring of bed form movement, tracer methods (e.g., tracking individual pebbles), and direct sampling methods (e.g., physical traps and samplers). More details on the introduced measurement techniques for bedload and suspended load, their calibration, and error sources are provided by Aberle et al. (2017).

Bed level measurements in reservoirs are also used for quantifying SY (e.g., Verstraeten and Poesen, 2002; de Vente et al., 2004; Millares and Moñino, 2018; Banasik et al., 2021). Since reservoir deposition encompasses all sediment erosion and transportation processes, including extreme events, it is considered the most reliable approximation (Morris and Fan, 1998). The final SY can be calculated by dividing the deposited sediment mass by the trapping efficiency of the reservoir (< 1). However, this method applies only to reservoirs without active sediment management, such as dredging and flushing, and has lower temporal resolution than sediment transport measurements. Additionally, measuring the dry bulk density of the deposited sediment is crucial since it greatly influences the calculation of the final SY based on volume changes (Mouris, Acuna Espinoza, Schwindt, Mohammadi, Haun, Wieprecht and Oladyshkin, 2023). Typical bathymetric survey methods are single and multibeam echosounders or side-scan sonars (Morris and Fan, 1998; Sotiri et al., 2021). Additional sediment coring or grab sampling provides valuable information regarding sediment properties, including grain size distributions or bulk densities (Beckers et al., 2018; Mouris, Schwindt, Pesci, Wieprecht and Haun, 2023).

A cost-effective and common technique for estimating catchment SY is soil erosion modeling. Modeling approaches include physically deterministic, stochastic, empirical, and conceptual models (Benavidez et al., 2018). The choice of an appropriate modeling approach hinges upon the spatio-temporal scales of input data and data quality (Nearing, 2013; Alewell et al., 2019). Therefore, areas with limited data availability often favor using empirical soil erosion models (Efthimiou et al., 2017; Benavidez et al., 2018). However, the results are often unreliable due to a lack of calibration and validation data.

2.3. Sediment transport and deposition in reservoirs

Sediment transport and consolidation processes in reservoirs Sediments are transported within a reservoir in different ways. Coarse material is transported as bedload and deposits at the head of the reservoir due to a sudden reduction in the river's transport capacity (see Figure 2.3). Furthermore, the coarse fractions of suspended particles deposit immediately and contribute to the delta growth, while the finer fractions are transported further into the reservoir as non-stratified flow or turbidity current (Morris and Fan, 1998; Annandale et al., 2016). Turbidity currents develop when the sediment-water mixture, entering a reservoir, significantly exceeds the density of the stored water. This dense sediment-laden water flows downward at the plunging point to the bottom of the reservoir, where it moves as a discernible current, often along the thalweg (see Figure 2.3). Turbidity currents can extend for considerable distances and eventually reach the dam, forming a muddy lake deposit (Fan and Morris, 1992; Alavian et al., 1992; Morris and Fan, 1998; Schleiss et al., 2016). Non-stratified flow transports

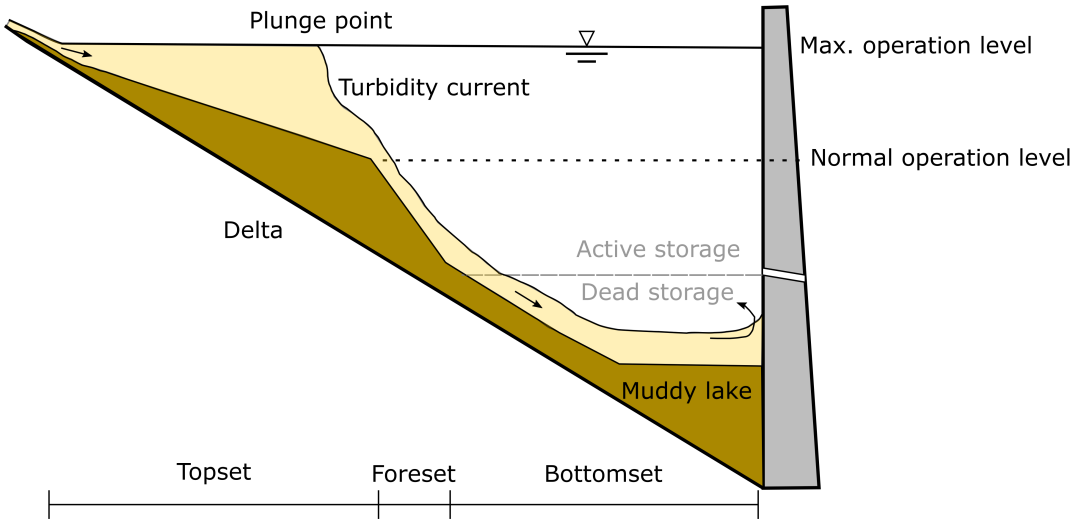

Figure 2.3. Schematic representation of delta deposition and turbidity current along with generalized deposition zones in a reservoir (modified after Fan and Morris, 1992; Morris and Fan, 1998; Annandale et al., 2016).

sediment particles throughout the entire water column and not only along the bed as with turbidity currents. Hence, the bathymetry of the reservoir does not primarily determine particle transport, and the particles may settle throughout the reservoir. Assuming either a characteristic logarithmic vertical sediment concentration profile (Rouse, 1937) or a uniform distribution within the water column, the deepest part of each cross section will have the highest deposition.

After deposition, sediments undergo compaction through consolidation and dewatering processes. These processes predominantly affect cohesive sediment depositions, characterized by a flocculent mass with low bulk density and high water content. During compaction, the water is squeezed out of the structural lattice by its weight and the overburden of the sediment deposits, increasing its bulk density (Mehta et al., 1989; Winterwerp and Kesteren, 2004; Lo et al., 2014). The consolidation process can extend over decades, resulting in temporal and spatial heterogeneity in bulk density within a reservoir (Morris and Fan, 1998). This variability is critical because the ultimate volume loss of a reservoir is highly dependent on the dry bulk density of the deposited sediment mass.

Deposition patterns In addition to the storage volume loss, the distribution of sediment deposition in the reservoir is crucial for planning long-term reservoir operations or sustainable sediment management strategies. The longitudinal deposition patterns in reservoirs vary greatly depending on reservoir geometry, operation, inflowing discharge, and sediment characteristics (Morris and Fan, 1998). Most reservoirs can be characterized by one or more of the four basic deposition patterns shown in Figure 2.4. Nevertheless, these representations are simplified as the characteristic deposition patterns often occur concurrently.

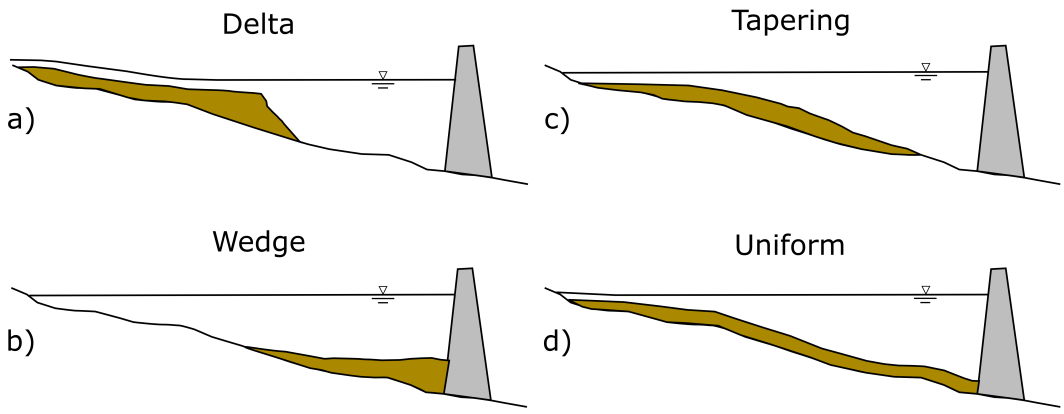

Figure 2.4. Characteristic longitudinal deposition patterns in reservoirs (modified after Morris and Fan, 1998).

Delta depositions primarily consist of the coarsest sediment fraction, settling rapidly near the inflow zone (see Figure 2.4a). While these depositions often comprise coarse particles, a significant amount of silt and fine sediment may also be present (Fan and Morris, 1992). These delta depositions start at the highest operating water level, and the topset slope ranges from equal to about 20% of the original riverbed slope (see Figure 2.3 and Figure 2.4a) (Strand and Pemberton, 1987; Annandale et al., 2016). The wedge-shaped sediment accumulations are thickest near the dam and gradually decrease upstream (see Figure 2.4b). This pattern typically occurs when turbidity currents transport fine sediment towards the dam. Alternatively, this pattern may occur in small reservoirs with significant fine sediment inflows and in large reservoirs when water levels are lowered during flood events (Morris and Fan, 1998). Consequently, engineers typically assume a wedge-shaped deposition pattern when designing dead storage. Nevertheless, the wedge shape is uncommon and rarely occurs in isolation, which explains why most sediment is deposited in the active rather than the dead storage (Annandale et al., 2016). The dead storage is the volume beneath the lowest outlet and cannot be drained (see Figure 2.3). In contrast, active storage can be used for flood management and holds water that can be released for power generation and water supply (Morris and Fan, 1998). Tapering sediment deposits exhibit a gradual decrease in thickness towards the dam (see Figure 2.4c). This trend is commonly observed in long reservoirs maintained at high water levels, indicating the gradual settlement of fine particles. Uniform sediment depositions are rare but can occur in narrow reservoirs with frequent water level fluctuations and limited fine sediment supply (see Figure 2.4d) (Morris and Fan, 1998).

Three distinct phases of reservoir sedimentation can be distinguished, from the dam's construction to its eventual abandonment due to the complete filling of the reservoir's storage volume (Rulot et al., 2012). After impoundment, the reservoir continuously traps sediments due to reduced flow velocities and turbulences (Figure 2.5a). The second stage is a partial

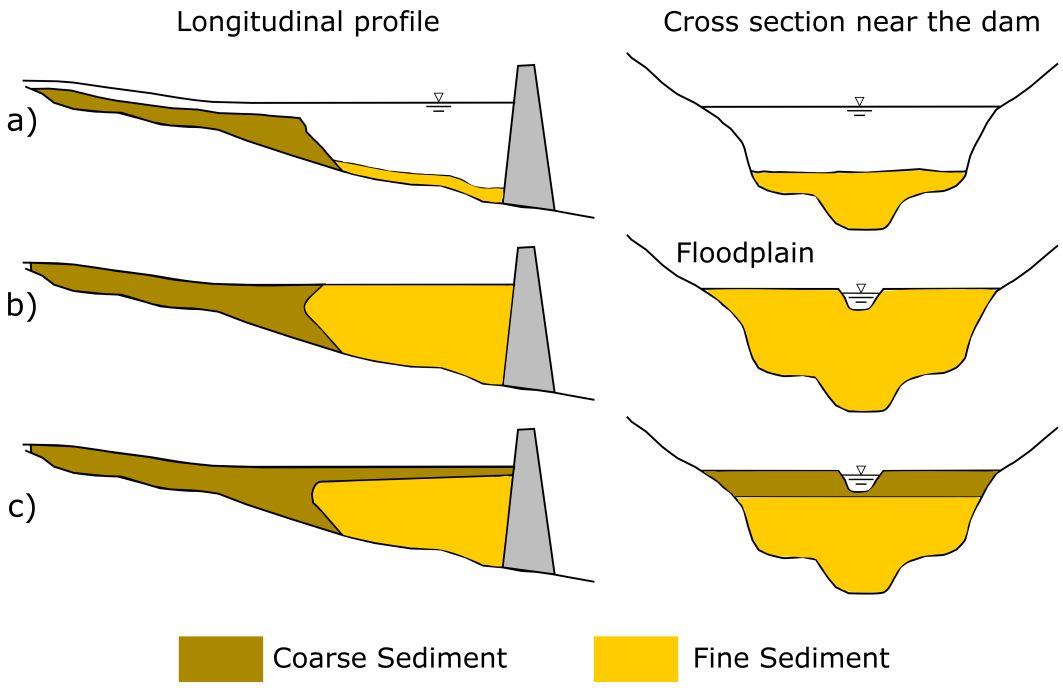

Figure 2.5. Schematic representation of the characteristic stages of long-term reservoir sedimentation showing a) continuous sediment trapping, b) partial sediment balance, and c) full sediment balance between long-term sediment in- and outflow (modified after Morris and Fan, 1998; Rulot et al., 2012).

sediment balance, whereas the former reservoir resembles a channel-floodplain configuration (Figure 2.5b). Here, a primary channel typically forms following the thalweg of the impounded river, with fine sediment deposition on both sides. While the inflow and outflow of fine sediments may approximate equilibrium, coarser sediments continue accumulating. In the final stage, the reservoir theoretically reaches a full sediment balance, and long-term sediment inflow equals long-term sediment outflow (Figure 2.5c) (Rulot et al., 2012).

Trapping efficiency The sedimentation rate and the subsequent reduction in reservoir storage volume are influenced by sediment inflow and reservoir characteristics and, hence, the reservoir-specific trapping efficiency (TE). TE is the ratio of deposited sediment mass to time-integrated sediment inflow over a specified period. In practice, the empirical approaches developed by Brune (1953) and Churchill (1948) are commonly used to estimate TE. Both approaches consider the ratio of reservoir volume to inflow, while the Churchill approach also accounts for reservoir length. It is worth noting that TE typically diminishes with increasing water inflow and decreasing reservoir volume. Many large reservoirs have a TE of approximately 100%, meaning they capture all incoming sediments, making them valuable for assessing catchment SY (e.g., Kokpinar et al., 2015; Millares and Moñino, 2018). However, these straightforward

methods overlook sediment grain size distributions, outlet configuration, location, and flow patterns, including recirculation zones induced by lateral inflows. Reservoir operation is minimally considered when selecting the representative reservoir volume when utilizing simplified approaches. Therefore, multidimensional hydro-morphodynamic numerical models are essential to calculate more reliable TE, considering single extreme events, complex flow patterns, reservoir operation, and sediment characteristics (Mouris, Schwindt, Pesci, Wieprecht and Haun, 2023).

2.4. Consequences of reservoir sedimentation

Impacts upstream of the dam Direct consequences of reservoir sedimentation generally impact the functions of the dam, which are often no longer or only partially maintained due to sedimentation (Schleiss et al., 2016; George et al., 2017). Sedimentation processes affecting the storage volume of the reservoir govern typical upstream dam impacts. A common misconception is that most sediment particles deposit in the dead storage (see Chapter 2.3). However, sediment deposition occurs in active and inactive storage, particularly in large reservoirs (Annandale et al., 2016). Reservoir sedimentation often affects active storage in the early stages of the reservoir's lifetime as sediments gradually move downstream in the form of a delta. The decreased active storage reduces water availability for designated uses, such as hydropower generation, flood protection, or irrigation. Even small sediment accumulations can be harmful, depending on their location. For instance, deposits in front of bottom outlets cause operational restrictions and safety problems (Morris and Fan, 1998).

Furthermore, reservoir sedimentation can affect hydraulic structures as sediment particles are more likely to reach the dam, resulting in abrasive wear on concrete (Horszczaruk, 2004) or turbine parts (Sangal et al., 2018). For example, turbine abrasion occurs when water flowing through turbines carries sediment particles, such as Quartz minerals, and results in significantly higher maintenance costs (Sangal et al., 2018). The degree of abrasion is primarily influenced by factors such as particle shape, particle size distribution, sediment concentration, and particle hardness and density (Duan and Karelin, 2003).

Another significant impact of reservoir sedimentation is the rise in flood levels upstream of the reservoir, for example, due to delta deposition and resulting higher water levels, as shown in Figure 2.4a (Fan and Morris, 1992; Annandale et al., 2016). Not only sediment accumulates in reservoirs, but also nutrients (Kunz et al., 2011; Wang, 2020), pollutants (Zhao et al., 2017), and microplastic particles (Di and Wang, 2018; Lin et al., 2021). Reservoirs also emit greenhouse gases (GHGs) because they retain large stocks of organic matter that fuel microbial decomposition, which converts organic matter into GHGs such as carbon dioxide, methane, and nitrous oxide (Deemer et al., 2016).

Impacts downstream of the dam Reservoir sedimentation impacts the fluvial morphology downstream of the dam. By trapping sediment, reservoirs reduce the amount of sediment released into downstream waters, which are often referred to as sediment-hungry or hungry water (Kondolf, 1997). Due to the substantially reduced sediment supply, rivers experience increased erosion and degradation of the aquatic ecosystem downstream of the dam. Since fluvial sediments are essential building blocks of deltas and coastal zones, reduced sediment loads contribute to increased susceptibility of coastlines to erosion and degradation (Kondolf, 1997; Syvitski et al., 2005; Warrick et al., 2019). Furthermore, the fine sediments that carry nutrients are also trapped in the reservoir, resulting in a decrease in nutrients downstream of the dam, affecting the fishery and aquatic ecosystem (Kunz et al., 2011; Shi and Qin, 2023).

Economic consequences The impacts of reservoir sedimentation outlined above extend to economic consequences. For example, diminished reservoir storage leads to increased costs related to reduced hydropower generation, higher maintenance costs due to abrasion, and diminished (irrigation) water supply (Gunatilake and Gopalakrishnan, 1999; Schleiss et al., 2016). Additional economic impacts may arise from reduced fishery yields due to nutrient trapping and artificial migration barriers such as dams. Recovering annual storage losses is expensive, estimated at $10 to $20 billion annually in 2006 (Annandale, 2006). Historically, cost-benefit analyses of dam projects overlooked factors such as dam decommissioning, retrofitting with sediment management facilities, or environmental impacts. Incorporating these costs into the analysis is essential, as they can exceed construction costs when all infrastructure and environmental damage is considered (George et al., 2017). Furthermore, cost-benefit analyses should consider the increasing scarcity of suitable sites for constructing new reservoirs. This inclusion would improve the economic feasibility of extending reservoir life through sediment management strategies (Schleiss et al., 2016).

From an economic perspective, maintaining sediment continuity has advantages over extracting and disposing of reservoir sediments (Detering et al., 2019). The sediment deficit downstream of the dam often requires costly government intervention, such as bed and bank stabilization or sediment replenishment. Without implementing these measures, there could be negative consequences for water availability and ecology that are difficult or impossible to quantify in monetary terms.

3. Materials and Methods

As stated in the introduction, the primary objective of this thesis is to develop objective methods for predicting long-term sediment production, delivery, and multidimensional reservoir sedimentation, accounting for changes in land use and hydro-climatic conditions. This chapter describes the research methods used to achieve the research objectives (see Chapter 1.1), focusing on scientific contributions and advancements in particular.

Since all the developed methods are applied to the Banja reservoir and its catchment area, an overview of the study area and the available data is given first. Subsequently, the focus is on the developed approach for modeling erosion and sediment delivery processes in the Devoll catchment and the multidimensional modeling of sedimentation processes in the Banja reservoir. Emphasis is also given to the fundamentals of surrogate-assisted Bayesian calibration of the hydro-morphodynamic numerical model. The final subchapter presents the model chain used to investigate the effects of land use and hydro-climatic changes on reservoir sedimentation. Further details on the developed and applied methods used to address the research questions are provided in the respective research articles I to IV.

3.1. Study area

The methods developed in this doctoral thesis are applied to the Banja reservoir and its associated catchment located in Southeast Albania on the Balkan Peninsula (see Figure 3.1). The mountainous catchment covers approximately 2,900 km^2, encompasses elevations ranging from 118 to 2,388 ma.s.l., and is geographically divided into two climatic zones, as classified by the Köppen climate classification (Kottek et al., 2006; Beck et al., 2018). The eastern part of the catchment, which includes the sub-catchment of the gauging station near the village of Kokel, is characterized by a warm-summer Mediterranean climate. In contrast, the western portion of the catchment exhibits a hot-summer Mediterranean climate.

The land use in the catchment comprises 30% forest, 25% scrub and herbaceous vegetation, and 25% agriculture. Other minor but not negligible land cover types include pasture, natural grassland, and sparse vegetation (Copernicus Land Monitoring Service, 2018). Historically, deforestation has had a substantial impact on land use. However, in recent decades, particularly

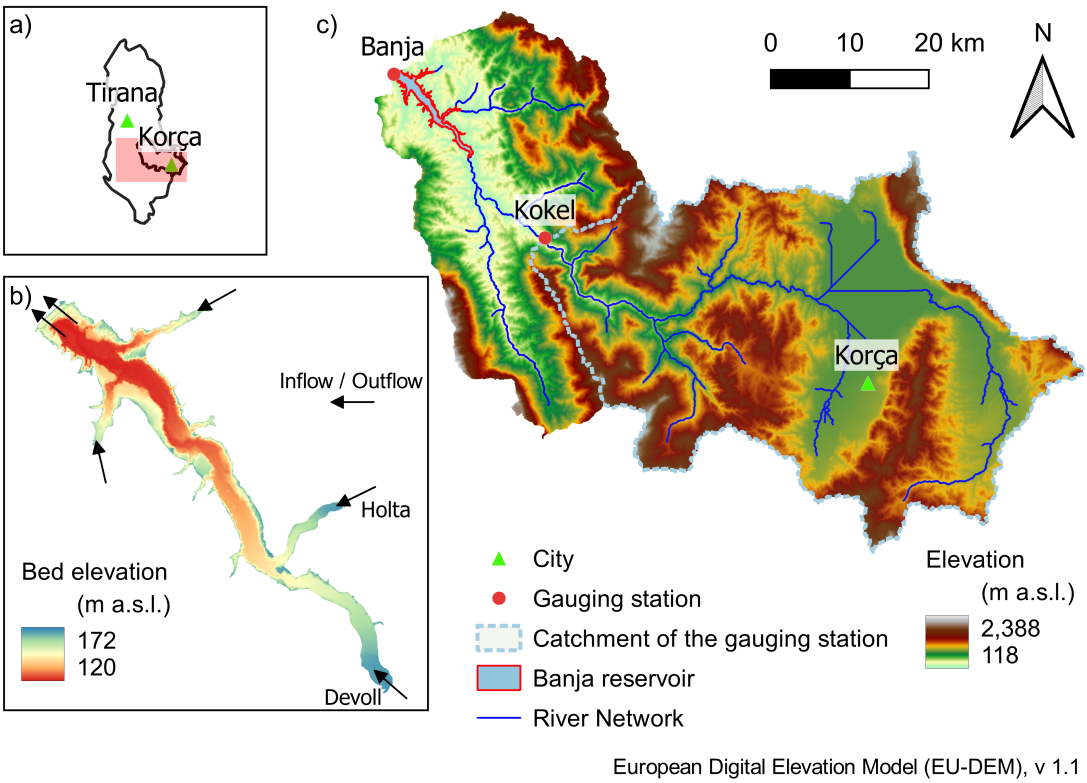

Figure 3.1. a) Location of the study area in Albania, b) bed elevations of the Banja reservoir, including tributaries and outflows, and c) catchment topography with gauging stations and the location of the Banja reservoir.

after the fall of communism in Albania, significant transformations have occurred, increasingly influenced by global market principles (Müller and Sikor, 2006). The soils prevalent in the catchment area are primarily comprised of Eutric Regosol (37%), Calcic Cambisol (30%), Calcaric Lithosol (12%), and Orthic Luvisol (11%) (Fischer et al., 2008; Hiederer, 2013). Additionally, the presence of weak sedimentary rocks, such as flysch, combined with high rainfall erosivity, contributes to notably high erosion rates and SYs, characteristic of mountainous Mediterranean catchments (Walling and Webb, 1996; Borrelli et al., 2020). Consequently, this region exhibits considerable potential for soil erosion and subsequent reservoir sedimentation in existing and planned reservoirs.

The Devoll River stretches 196 kilometers and has its source in the Gramos Mountains near the Greek border. In winter, the high elevations of the catchment are frequently covered by snow. Hence, the flow regime of the Devoll River and its tributaries are driven not only by precipitation but also by snowfall and subsequent snowmelt. The river flows northwest and is dammed after 160 km, forming the Banja reservoir (see Figure 3.1). Commissioned in 2016, the reservoir has a length of 14 km, a maximum water depth of 60 m near the dam, and a surface area of 14 km^2 at the highest storage level, leading to a maximum storage capacity of approximately

400 million m^3. The Devoll River is the most significant contributor to the annual inflow at approximately 89%, with the Holta River representing a significant tributary at 9%. Close to the dam, two minor tributaries collectively account for a small share of approximately 2% of the annual inflow. The upstream part of the reservoir is very shallow, whereas the central part of the reservoir is up to 55 m deep (see Figure 3.1). The Moglica reservoir, situated further upstream and commissioned in 2020, is not included in this thesis due to the unavailability of ground truth data during the calibration period.

The study area was selected due to its high erosion rates (Walling and Webb, 1996; Borrelli et al., 2020), the high vulnerability of the Mediterranean region to climate change (Bangash et al., 2013), and the substantial investments in hydropower in this region (Carolli et al., 2023).

3.2. Available data

Data obtained by the gauging station The gauging station located near the village of Kokel (see Figure 3.1) continuously recorded discharge and suspended sediment concentrations between May 2016 and April 2018, when the water depth exceeded 1 m (387 of 730 days). The determination of suspended sediment concentrations and discharge is derived from analyzing acoustic backscatter signals acquired by two stationary-mounted horizontal acoustic Doppler current profilers (H-ADCPs). The method for calculating suspended sediment concentrations from acoustic backscatter data is detailed in Aleixo et al. (2020). Subsequently, the suspended sediment load is computed by multiplying the measured suspended sediment concentration with corresponding discharge values.

The gauging station measures suspended sediment load exclusively at high and medium discharges. Additionally, intermittent data gaps exist due to a low signal-to-noise ratio (Aleixo et al., 2020). A continuous sediment load dataset is essential to calibrate the soil erosion and sediment transport model. Consequently, interpolation techniques are employed to fill temporal measurement gaps, and missing individual values are linearly interpolated. However, concentrations for water levels below 1 m cannot be reliably estimated and used for calibration. This restriction results from the possible occurrence of high sediment concentrations even during low-flow periods following isolated rain events.

Reservoir-specific data A digital elevation model (DEM) of the bathymetry was generated from a drone survey before filling the Banja reservoir in 2016. In 2019, the bathymetry of the reservoir was re-surveyed using moving ADCP measurements. These topographic surveys from 2016 and 2019 are projected onto a numerical mesh, enabling the calculation of sediment deposition heights within the reservoir. In 2021, a field survey was conducted to collect sediment samples from the reservoir bed using an Ekman grab sampler. The particle size distribu-

tion of the samples is assessed using a portable analyzer that uses laser diffraction. The results show that the sediment deposits primarily consist of cohesive particles (<63 μm). Furthermore, laboratory analysis of these deposited sediments reveals dry bulk densities ranging from 726 to 950 kg m^{-3}. The median diameters of the deposited sediment vary from 5.7 to 37.4 μm, with a mean of 10.5 μm.

Climate reanalysis datasets Climate reanalysis datasets provide a feasible substitute for in-situ precipitation and temperature measurements, among other parameters. These datasets merge observations with predictive weather models to create a comprehensive and consistent historical global weather and climate record. This integration combines information from different sources such as satellites, ground-based radar systems, and in-situ measurements from weather stations, aircraft, ships, and buoys (Hersbach et al., 2020). In this thesis, the ERA5 reanalysis dataset is used to obtain temperature and precipitation data for the historical period and as reference data for the bias adjustment of the climate models. It has a spatial resolution of 30-31 km and an hourly temporal resolution since 1950 (Hersbach et al., 2020).

Satellite imagery Various land use features exhibit different ways of reflecting and emitting light in different spectral bands. Multispectral satellite imagery, which captures data across multiple spectral bands, facilitates the differentiation of land cover types based on their spectral signatures. Consequently, satellite imagery serves as a widely adopted remote sensing technique for land use classification (e.g., Teng et al., 2016), monitoring vegetation changes (e.g., Borrelli et al., 2017; Gianinetto et al., 2019), and detecting snow-covered areas (e.g., Hall et al., 2002). This thesis employs Sentinel-2 satellite imagery to observe changes in vegetation and snow cover dynamics across seasons through a comprehensive analysis of spectral signatures. Table 3.1 summarizes the input data used in this thesis, including its source and purpose.

3.3. Modeling of soil erosion and sediment delivery

Revised Universal Soil Loss Equation The Revised Universal Soil Loss Equation (RUSLE) predicts the gross soil erosion at the catchment scale (Renard et al., 1991; Renard, 1997). The RUSLE directly accounts for splash, rill, and sheet erosion (see Chapter 2.1) and calculates soil loss A (t ha^{-1} yr^{-1}) by considering six major erosion risk factors:

$$A = R \cdot K \cdot C \cdot LS \cdot P \tag{3.1}$$

where R is a rainfall-runoff erosivity factor (MJ mm ha^{-1} h^{-1} yr^{-1}), K is a soil erodibility factor (t h MJ^{-1} mm^{-1}), LS is a combined dimensionless topographic factor of slope length $L(-)$ and

Table 3.1. Input data used in this thesis.

Input data	Source	Purpose of the data in this thesis
Topography (DEM)	EU-DEM v1.1	Erosion and sediment delivery – required for calculation Hydrological processes – required for calculation
Precipitation and temperature (past)	Post-processed ERA5 Reanalysis dataset	Erosion and sediment delivery – required for calculation Hydrological processes – required for calculation
Precipitation and temperature (future)	Climate model results for different scenarios	Erosion and sediment delivery – required for calculation Hydrological processes – required for calculation
Soil data	ESDB v2.0 and HWSD v1.21	Erosion and sediment delivery – required for calculation Hydrological processes – required for calculation
Land cover (past)	CORINE Land Cover 2018	Erosion and sediment delivery – required for calculation Hydrological processes – required for calculation
Land cover (future)	Future land use projections for different scenarios (Chen et al. 2020)	Erosion and sediment delivery – required for calculation Hydrological processes – required for calculation
Satellite imagery	Sentinel 2 – Copernicus Open Access Hub	Erosion and sediment delivery – detection of snow cover and seasonal vegetation change
Suspended sediment concentrations and sediment load	ADCP measurements (Aleixo et al., 2020)	Erosion and sediment delivery – model calibration
Data on agricultural practice	Albanian Institute of Statistics	Erosion and sediment delivery – required for calculation
Bathymetry/bed levels in the reservoir	Drone-based photogrammetric survey (2016) and acoustic survey using ADCP measurements (2019)	Reservoir processes – model generation and calibration
Bulk density and grain size distribution of deposited sediments	Sediment samples from the reservoir bed using a grab sampler and laboratory analysis	Reservoir processes – sediment characteristics
Reservoir water levels and outflow discharges	Direct measurement from the operator	Reservoir processes – implementation of reservoir operation

slope steepness $S(-)$, C is a cover and management factor $(-)$, and P is a support practice factor $(-)$.

The soil erodibility factor K is calculated from soil structure, organic matter content, soil texture, and soil permeability according to Wischmeier and Smith (1978), while the LS factors, which account for the influence of topography on soil erosion, are determined according to the approach of Zhang et al. (2017). The effect of contouring on soil erosion is considered in calculating the P factor as a function of slope and land cover class. The C factor, which assesses the influence of land cover and management practices on soil erosion, is determined based on land cover characteristics. This thesis uses 20 distinct land cover categories obtained from the satellite-based CORINE Land Cover database for the Devoll catchment (Copernicus Land Monitoring Service, 2018). The range for the C factor values is derived from a synthesis of notable European studies (Panagos, Borrelli, Meusburger, Alewell, Lugato and Montanarella, 2015). In addition, satellite imagery is used to calculate seasonal C factors that account for the seasonality of vegetated land cover classes (e.g., forests, grasslands, or croplands) using the Normalized Difference Vegetation Index (NDVI), as proposed by Gianinetto et al. (2019). C factors for land cover classes unaffected by seasonality (e.g., urban fabric) remain constant.

The R factor quantifies the erosive potential of precipitation and resultant surface runoff, considering effects like duration, intensity, and strength of each precipitation event (Brown and Foster, 1987; Renard, 1997). Traditionally, annual R factors were computed by summing up the erosivities over a specified period and dividing them by the number of years. However, the scarcity of high-resolution (< 0.5 hours) precipitation data in many regions, including the Devoll catchment, led to the development of empirical regression equations. These equations relate the R factor to available precipitation data in daily, monthly, or annual resolution with satisfactory accuracy (Arnoldus, 1980; de Santos Loureiro and de Azevedo Coutinho, 2001; Diodato et al., 2013). In this thesis, the Rainfall Erosivity Model for Complex Terrains is chosen due to the compatibility with available data (temporal and spatial resolution) and its development for estimating the monthly erosivity factor (R_m) in Italy, which shares geographical and hydro-climatic characteristics with Albania (Beck et al., 2018). R_m is calculated as a function of monthly precipitation, elevation, latitude, and seasonal characteristics (Diodato and Bellocchi, 2007).

Conventionally, the R factor does not consider the erosive forces of snowmelt runoff (Renard, 1997), although previous attempts have been made to estimate snowmelt erosivity from winter precipitation totals. Therefore, this thesis presents a novel method to account for snowfall and subsequent snowmelt in the R factor. It distinguishes between non-erosive snowfall and delayed erosion associated with snowmelt weeks to months after the snowfall event. The total monthly R_m factor is obtained by adding the monthly $R_{m,rain}$ factor (resulting from rainfall), and the monthly $R_{m,snowmelt}$ factor (resulting from snowmelt). The quantity of melted snow is

determined through satellite-based snow cover detection as well as temperature and precipitation data analysis.

SEdiment Delivery Distributed Model While the RUSLE evaluates the spatial pattern of gross soil loss, the Sediment Delivery Distributed (SEDD) Model (Ferro and Porto, 2000) is a sediment routing method to estimate SY at the catchment scale. The pixel-specific SDRi is calculated based on the travel time along the flow path to the nearest river channel (Ferro and Minacapilli, 1995). Therefore, the SDRi depends on the overland flow velocity calculated as a function of the pixel-specific slope and surface roughness, which is a function of land use (Jain and Kothyari, 2000).

Algorithmic methods to calculate sediment loads The modified RUSLE-SEDD combination has been implemented as a semi-automated algorithmic model chain to calculate monthly suspended sediment loads considering snowfall and snowmelt. The developed Python algorithms require precipitation and temperature data, satellite imagery, soil data, topographic data, and land cover information as input. Additionally, observations of suspended sediment loads are required for model calibration and validation.

The model chain is executed with three different R factors to assess the significance of snow-related processes for predicting soil erosion and suspended sediment loads in mountainous Mediterranean regions. The conventional approach considers all precipitation as erosive rain, the snow-only approach considers snowfall as non-erosive, and the combined snowfall-snowmelt approach categorizes snowfall as non-erosive while treating snowmelt as erosive. The algorithm computes the spatial distribution of monthly rainfall intensity and snow water equivalent using precipitation and temperature rasters. For this purpose, a temperature threshold of 0 °C is applied to distinguish whether precipitation falls as snow or rain. To identify the extent of snow coverage at the end of each month, the snow detection algorithm utilizes three spectral bands present in Sentinel-2 imagery. The green and the short-wave infrared bands are used to calculate the Normalized Difference Snow Index (NDSI) for every raster pixel to detect snow, and a threshold value for the blue band is implemented to avoid false snow detection of pixels in turbid lakes and rivers. Snow-covered pixels exposed at the end of the considered month create erosive snowmelt, showcasing the algorithm's seasonal memory. Finally, the algorithms generate soil loss and SY rasters with monthly resolution and a table of monthly averages for soil loss, SY, and suspended sediment load at the outlet of the previously defined catchments.

Expert judgment of true-color satellite imagery and overlays of snow cover delineation from code and elevation contours is required to calibrate the satellite image band (NDSI and blue)

thresholds for snow detection. Furthermore, the developed model chain is coupled with the Parameter ESTimation software PEST (Doherty, 2001) to calibrate a catchment-specific parameter using measured suspended sediment loads obtained from the Kokel gauging station, considering a calibration period of 10 months. For comparison, the 10 months are divided into two separate 5-month periods for calibration and validation. Furthermore, leave-one-out cross-validation (LOO-CV, Sammut and Webb 2010) is used to evaluate the model performance of the three different approaches and to assess the effect of limited data from just two wet seasons.

3.4. Hydro-morphodynamic modeling of reservoir sedimentation

In this thesis, two hydro-morphodynamic numerical models are used to simulate the processes in the reservoir: SSIIM2 (Sediment Simulation In Intakes with Multiblock Option; Olsen, 2018) and Telemac-2D (Hervouet, 2007) with its sediment transport and bed evolution module GAIA (Audouin et al., 2020). The 3d numerical model SSIIM2 is used in Publications III and IV to carry out long-term simulations, while the 2d numerical model Telemac-2D is used in Publication II for a Bayesian calibration of the reservoir model.

SSIIM2 To accurately represent changes in the vertical distribution of suspended sediment concentrations, flow velocities, and complex three-dimensional flow patterns, including helical flows, three-dimensional modeling is essential. The three-dimensional numerical model SSIIM2 solves the Reynolds-averaged Navier-Stokes equations in three dimensions using a finite volume method for spatial discretization. The Reynolds stress term is calculated through the concept of eddy viscosity utilizing the standard k-ϵ turbulence model. SSIIM2 uses the transient convection-diffusion equation to calculate suspended sediment transport, along with van Rijn's empirical formula for bedload transport calculations (Van Rijn, 1984a). To address the significant computational requirements of a 3d hydro-morphodynamic model, which can often span several weeks to months, various simplifications are incorporated to ensure acceptable runtimes for projecting global change impacts by 2100 while maintaining high-quality results. For example, the adaptive mesh features mainly coarse cells with a spatial resolution of 50 m x 50 m in x- and y-direction and up to 10 vertical cells in the deepest areas of the reservoir (z-direction). SSIIM2 uses an implicit time discretization to solve the Navier-Stokes equations, enabling the use of large time steps (5,400 seconds) and reasonable computing times (3.5 weeks per run until 2100, using 8 cores, 3.7 - 4.8 GHz). Further algorithms, such as flow limiters, are implemented for computational stability in flat and triangular cells close to the reservoir banks that result from the wetting and drying algorithm. A notable advantage of SSIIM2 is that it only considers wetted cells, thereby decreasing the computational demands of the cal-

culations, particularly as water levels fluctuate and reservoir sedimentation causes bed level changes.

The model incorporates four inflow and two outflow boundaries, encompassing the spillway and turbine inlet (see Figure 3.1), and is used for long-term simulations until the year 2100. The inflow discharges and corresponding sediment concentrations are determined using data from the hydrological model and the soil erosion and sediment transport model. The reservoir outflow is calculated based on the water level in the reservoir, inflow rates, storage curve, and site-specific operating regulations designed to maintain a seasonal water level target. Model calibration is performed by comparing the observed bed level changes between the bathymetric surveys conducted in 2016 and 2019.

Telemac-2D Telemac-2D uses a combined explicit-implicit solver to approximate the shallow water equations and compute the flow field. The hydrodynamic module transmits the computed hydrodynamic variables, including water depth, depth-averaged flow velocities, and bed shear stresses, to the sediment transport and bed evolution module GAIA.

The unstructured mesh used in this thesis comprises triangles with edge lengths of approximately 40 m. Two roughness coefficients are specified to distinguish between the original river course (before impoundment) and the newly flooded areas. The parameters of the numerical model are configured with a focus on numerical and computational stability while ensuring efficient computations. Therefore, a finite element numerical scheme is employed, following the recommended practice for tidal flats (or dry-wet elements) to consider only positive water depths (Hervouet et al., 2011). Furthermore, the method of characteristics is applied to address the advective component of the hydrodynamic equations, significantly enhancing model stability. In addition, the mixing length turbulence model is used to calculate the turbulent viscosity coefficient.

The depth-averaged sediment concentrations are calculated by solving the advection-diffusion-equation. The erosion fluxes of mainly cohesive sediment deposits are calculated from the Krone-Partheniades erosion constant, the bed shear stress, and the critical shear stress for erosion. The settling velocity, bed shear stress, and critical shear stress for deposition govern the deposition fluxes. After calculating the erosion and deposition fluxes and the net transport flux per element, GAIA applies the Exner equation (Paola and Voller, 2005) to update the bed levels. The sediment concentrations are obtained from the soil erosion and sediment transport model (Mouris et al., 2022). Telemac-2D is only used to simulate the period between the two surveys in August 2016 and August 2019. Therefore, the water inflows are calculated as a function of the measured water levels and outflows, considering the storage curves of 2016 and 2019.

The Telemac-2D model aims to efficiently simulate suspended sediment transport in a large reservoir for repetitive calibration runs (13.5 hours per run, using 12 cores, 3.4 GHz). However,

it omits bedload and uses a coarse mesh, limiting its ability to predict deltaic avulsion, channel, or bank erosion at the head of the reservoir. Consequently, the bed level changes in this domain cannot be predicted in a physically correct and stable manner, and the model setup is only valid in deep areas outside the shallow delta at the head of the reservoir. Therefore, two distinct data scenarios are used in this thesis for calibration (see Chapter 4.2). One scenario includes measurements from the entire upstream section of the reservoir. The other scenario considers only measurements within the geospatial domain of the numerical model, excluding measurements affected by deltaic avulsion and channel erosion.

3.5. Bayesian calibration

Bayesian inference In the context of calibrating a numerical model, Bayesian inference is a powerful approach that helps to estimate and refine the calibration parameters of the model. This procedure entails analyzing measured data (here observed bed levels z_{meas}) to update the initial parameter beliefs $p(\omega)$, resulting in the posterior distribution $p(\omega|z_{\text{meas}})$ through the application of Bayes' theorem:

$$p(\omega|z_{\text{meas}}) = \frac{p(z_{\text{meas}}|\omega) \cdot p(\omega)}{p(z_{\text{meas}})} \tag{3.2}$$

The first step is to create a prior probability distribution $p(\omega)$, reflecting the prior beliefs about parameter values before new or additional evidence z_{meas} is incorporated. The likelihood function $p(z_{\text{meas}}|\omega)$ quantifies the model's ability to replicate the observed data for various parameter combinations ω. This Bayesian inference process aids in narrowing down the range of likely parameter values, resulting in a posterior probability $p(\omega|z_{\text{meas}})$, that is typically narrower than $p(\omega)$ (Box and Tiao, 1992; Oladyshkin and Nowak, 2019). Additionally, the process involves a normalization factor $p(z_{\text{meas}})$, known as Bayesian model evidence (BME), which becomes crucial when comparing different posterior distributions or evaluating multiple competing models (Mohammadi et al., 2018).

Assuming that the differences between observed and modeled bed levels follow a normal distribution and are independent, the likelihood function $p(z_{\text{meas}}|\omega)$ is calculated proportionally to the sum of the squared errors between measured and simulated bed levels, weighted by the total error. In this novel error calculation method, the total error of each calibration node is determined from its measurement error and metamodel error. Finally, the influence of the difference between the measured and modeled bed levels on the likelihood score decreases when the total errors are large.

The measurement errors originate from interpolating bed level measurements at numerical mesh calibration nodes and uncertainties from field measurements. A 3 m interpolation radius

around calibration nodes was applied, resulting in a variable number of measurements per node (ranging from 1 to 35). The number of measurements affects the confidence level. Therefore, 15 available measurements close to the node are assumed to be more reliable than two. As the number of measurements increases, the node-specific measurement error decreases. The average measurement error across all calibration nodes is 0.4 m, which equals the measurement precision according to the operator, accounting for the high concentration of suspended sediment near the bottom, uncertainties in the reservoir's water level, and the movement of the ADCP boat due to waves. Since the metamodel (see following paragraph) is just an approximation of the full complexity numerical model, metamodel errors are also considered. These errors are determined via LOO-CV, where the model is repeatedly fitted on n-1 calibration nodes. LOO-CV errors are then calculated for each calibration node and training point, with the resulting per-node error variance implemented as metamodel error.

Metamodel Bayes' theorem can be approximated using Monte Carlo sampling, which typically requires thousands of numerical model runs. However, simulating hydromorphodynamic processes with time-consuming models makes conducting thousands of model runs computationally unfeasible. A surrogate-assisted Bayesian inversion method (Oladyshkin et al., 2020) addresses this challenge, wherein a metamodel replaces the computationally intensive full-complexity model. The metamodel mimics the output of the complex hydromorphodynamic model while significantly reducing computing time (Beckers et al., 2020; An et al., 2022). This thesis utilizes a Gaussian process emulator (GPE) as a metamodel. The GPE metamodel is trained using numerical model responses generated by exploring different potential calibration parameter value combinations. However, a metamodel cannot replace the numerical model and is only used to speed up model calibration.

Bayesian active learning The accuracy of surrogate-assisted Bayesian calibration depends on the ability of the metamodel to emulate the behavior of the complex numerical model accurately. Increasing the number of training points enhances predictive accuracy by reducing gaps in the parameter space. However, exhaustive parameter space coverage with a computationally expensive full-complexity model is impractical, taking hours to compute each training point. Therefore, Bayesian active learning (BAL) avoids long computing times and identifies the most optimal regions in the parameter space based on metamodel responses. For this purpose, the so-called relative entropy or Kullback-Leibler divergence (Kullback and Leibler, 1951; Oladyshkin et al., 2020) between the prior and posterior distributions is calculated. Here, relative entropy describes the information gained from the prior to the posterior distribution. The set of calibration parameters with the highest relative entropy is employed to rerun the full-complexity model, initiating the next BAL iteration. The results of the new full-complexity model serve as new training points for the GPE in the subsequent BAL step. Iterations are

carried out until meeting a specified stop criterion, which usually involves the convergence of relative entropy and BME (Beckers et al., 2020). However, this thesis also considers the evolution of the root-mean-square error. Consequently, the metamodel is refined in those regions of parameter space that are most important (highest information gain) for Bayesian inference. The complete BAL process is implemented in a Python-based workflow. More detailed information on the workflow can be found in Mouris, Acuna Espinoza, Schwindt, Mohammadi, Haun, Wieprecht and Oladyshkin (2023) and Oladyshkin et al. (2020).

3.6. Model chain to predict long-term reservoir sedimentation

Model chain The model chain (see Figure 3.2) investigates how climate, land use, and the resulting hydrological changes affect soil production and subsequent reservoir sedimentation. This thesis uses three different climate models to assess the primary impacts of climate change, such as precipitation and temperature, for three Representative Concentration Pathways (RCPs). To comprehensively predict secondary climate change impacts driven by changes in temperature, precipitation, and land use change, an advanced hydrological model, a soil erosion and sediment transport model (see Chapter 3.3), and a 3d hydro-morphodynamic model of the reservoir (see Chapter 3.4) are employed. The combination of these models takes advantage of their specific capabilities and accurately represents the physical processes at different scales.

The Water Flow and Balance Simulation Model (WaSiM) utilizes the process-oriented Richards approach to integrate the hydrological processes of the catchment into the model chain (Schulla, 1997, 2021). WaSiM generates inflow hydrographs for the reservoir model as upstream boundary conditions. The projected snow cover serves as input to the soil erosion and sediment transport model, enabling long-term predictions when satellite imagery is unavailable. To achieve higher spatial resolution, climate model precipitation and temperature data are post-processed using a combination of elevation-dependent regression and inverse distance weighting.

In the soil erosion and sediment transport model, the R and C factors are considered to be affected by global change, while the K, LS, and P factors do not change over time in future scenarios. As there are no discernible trends in the erosivity and intensity (e.g., annual maximum five-day precipitation or extreme precipitation totals) of precipitation events for the study area, the equations used to determine the R factor remain unchanged for predicting global change scenarios. In addition to the C factor's seasonal variation, projected land use changes under different global change scenarios are considered. Hence, the C factor is calculated for each pixel according to the pixel-specific land use percentages. For instance, a greater share of natural grassland and forest leads to lower C factors, while increasing arable land leads to higher

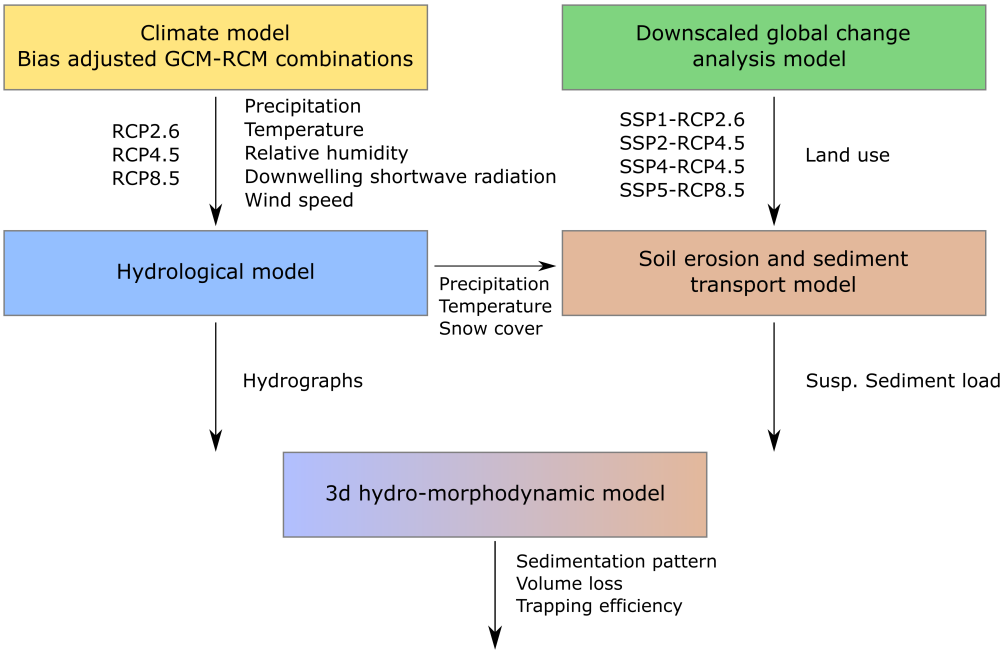

Figure 3.2. Model chain analyzing the impact of global change on reservoir sedimentation considering land use change and using Shared Socioeconomic Pathways (SSPs) and climate change based on Representative Concentration Pathways (RCPs) (modified after Mouris, Schwindt, Pesci, Wieprecht and Haun, 2023).

C factors. A downscaled global change analysis model (Chen et al., 2020) produces these future land use changes for four Shared Socioeconomic Pathways (SSP-RCPs). The results of the preceding models are used as inputs to the subsequent models, and the soil erosion and sediment transport model predicts the monthly suspended sediment loads of the reservoir inflows (see Figure 3.2). In total, three scenarios that include only hydro-climatic changes and four scenarios that include both climate and land use changes are considered in this thesis.

Climate and global change scenarios Three Global Climate Models (GCMs), dynamically downscaled by two different Regional Climate Models (RCMs), are used to generate meteorological information on total precipitation, near-surface temperature, near-surface relative humidity, surface downwelling, shortwave radiation, and near-surface wind speed to assess the impact of climate change on reservoir sedimentation and its preceding processes (see Figure 3.2). To reduce potential bias caused by the selection of climate models, model combinations with similar climate trends for precipitation and temperature are grouped. Consequently, one model from each group is selected to represent the wide variety of GCMs, with only 3 GCM-RCM combinations. In addition, a bias adjustment is carried out to reduce the systematic deviation between the climate model results and the ERA5 reference data using the Multi-scale bias AdjuStment (MidAS) tool (Berg et al., 2022), with a reference period spanning

from 01/1981 to 12/2010. The climate projections ultimately possess a spatial resolution of 0.11 degrees and a temporal resolution of 3 hours, ranging from 01/1981 to 12/2100. Representative Concentration Pathways (RCPs) are a set of standardized greenhouse gas concentration trajectories, denoted by their radiative forcing targets for the year 2100 (van Vuuren et al., 2011). The thesis examines three RCPs, including a low greenhouse gas emissions pathway (RCP2.6), a medium greenhouse gas emissions pathway (RCP4.5), and a high greenhouse gas emissions pathway (RCP8.5).

Besides these hydro-climatic change-only scenarios, land use projections (Chen et al., 2020) through four SSPs are incorporated into the model chain. The SSPs offer comprehensive global change scenarios considering climate change resulting from greenhouse gas emissions, population growth, economic development, and technological progress (Riahi et al., 2017). Catchment responses and reservoir sedimentation are analyzed for sustainable development (SSP1-RCP2.6), middle-of-the-road development (SSP2-RCP4.5), unequal development (SSP4-RCP4.5), and fossil-fueled development (SSP5-RCP8.5) using the different GCM-RCM combinations. The model chain is executed for 21 scenarios, comprising 3 RCP scenarios (only climate change) and 4 SSP-RCP scenarios (land use and climate change), each utilizing 3 GCM-RCM combinations.

Uncertainty quantification Although the capabilities of the individual models facilitate the achievement of satisfactory results, it is essential to consider the propagation of uncertainties in such a model chain. If multiple models are used to predict a target variable, uncertainties from various sources may superimpose and propagate, increasing the uncertainty in the final target variable. The difficulty of selecting model parameters, often compounded by limited measurements, underscores the need to assess their influence on simulation results and the confidence associated with those results (Moges et al., 2021).

The First-Order Second-Moment (FOSM) method (Gelleszun et al., 2017) approximates parameter uncertainties based on variance-covariance propagation. FOSM demonstrates how variations or uncertainties in model parameters lead to uncertainty in the model results. This method is more economical regarding computing time than other stochastic methods (e.g., Monte Carlo simulations), while the results are comparable (Kunstmann et al., 2002). Each model has a specific target variable or result, such as discharge for the hydrological model or SY for the soil erosion and sediment transport model. The most influential parameters with the greatest impact on the target variable are selected for each model and changed by 1% of the calibrated optimal value. Ultimately, the standard deviation of the target variable quantifies the approximate parameter uncertainties.

Additional significant sources of uncertainty encompass the spread in climate projections, the downscaling techniques employed to bridge large-scale Global Climate Models (GCMs) to Re-

gional Climate Models (RCMs), and the process of scaling down to the appropriate scale for process models (Prudhomme and Davies, 2009). The analysis considers mean values derived from the climate model ensemble and their corresponding standard deviations to address climate model uncertainty.

4. Summary of Scientific Papers

The findings of this dissertation have been published in four articles in peer-reviewed scientific journals. This chapter serves as a concise yet comprehensive overview of the conducted research. It provides each research article's objectives, key findings, and specific contributions. For more detailed insights, please refer to the appended published research articles.

The publications encompassed within this thesis address the modeling of soil erosion, sediment delivery, and reservoir sedimentation. The focal point lies in scrutinizing the impacts of land use and hydro-climatic changes on these phenomena. The sequence of these publications follows a chronological order and shows a clear progression from catchment processes to reservoir sedimentation modeling and finally to the comprehensive model chain. It mirrors the sequential steps to achieve the objectives outlined in Chapter 1.1 and Figure 1.1.

4.1. Publication I: Introducing seasonal snow memory into the RUSLE

This paper addresses two main objectives related to estimating sediment load in general and the influence of snow on soil erosion and suspended sediment loads in particular (Mouris et al., 2022). The first objective is to develop an objective calculation method for predicting suspended sediment loads incorporating catchment characteristics and hydro-climatic parameters. This approach should remain applicable even in data-sparse regions and climate impact studies where high-resolution precipitation and detailed measurement data are unavailable. Additionally, the paper investigates the effects of snow on suspended sediment load by comparing existing approaches that neglect snow with newly developed techniques that account for the effects of snowfall and snowmelt on soil erosion.

The strong agreement between predicted and observed suspended sediment loads provides compelling evidence for the efficacy of the developed algorithmic method for predicting sediment loads in data-sparse regions. This approach strikes a reasonable balance between applicability and reliability by leveraging monthly sediment load predictions based on Sentinel-2 satellite imagery and climate reanalysis precipitation data. A core element of this innovative method is the integration of non-erosive snowfall, which accumulates over months, followed

by erosive snowmelt. The incorporation of a seasonal snow memory into the RUSLE significantly enhances the accuracy of soil erosion and sediment transport predictions in mountainous Mediterranean catchments, particularly when measured data are limited. Consequently, the approach provides valuable insights into suspended sediment loads with a spatio-temporal resolution that facilitates the subsequent prediction of hydro-morphological processes in rivers, lakes, and reservoirs. Furthermore, this methodology holds promise for future climate change scenario studies. To this end, the historical climate reanalysis data is replaced by projected data from climate projections.

The primary scientific contribution of this research lies in the development of innovative Python algorithms, the adept utilization of freely available datasets, and the novel integration of seasonal snow memory into the RUSLE.

4.2. Publication II: Stability criteria for Bayesian calibration of reservoir sedimentation models

This paper focuses on the challenges of modeling reservoir sedimentation by employing a surrogate-assisted Bayesian calibration approach (Mouris, Acuna Espinoza, Schwindt, Mohammadi, Haun, Wieprecht and Oladyshkin, 2023). The main objective is to achieve accurate predictions of reservoir sedimentation by effectively calibrating complex numerical models, even in the presence of competing model simplifications. These simplifications are often not valid throughout the entire model domain due to the varying dominance of distinct physical processes in different areas of the reservoir. Furthermore, key calibration parameters, namely the grain size distribution, the critical bed shear stresses for the erosion and deposition of cohesive sediments, and the dry bulk density, require extensive field sampling for determination. Hence, this paper examines whether our modified approach can identify the importance of calibration parameters, facilitating their prioritization in field surveys.

Four calibration parameters are adjusted to achieve the most accurate simulation of bed level changes between 2016 and 2019. The calibration process involves two distinct data scenarios. One scenario integrates measurements from the entire upstream half of the reservoir, where small channels with low water depths lead to high topographic gradients and substantial model uncertainty. The other scenario utilizes measurements within the geospatially valid range of the numerical model (see Chapter 3.4). The results indicate that Bayesian calibration only produces physically meaningful parameter combinations when the calibration nodes are within the valid range of the numerical model. Notably, Bayesian calibration identifies the dry bulk density as the dominant and most influential parameter for accurately simulating reservoir sedimentation. As a result, it is recommended to prioritize collecting dry bulk density data before setting up a reservoir sedimentation model. Moreover, the innovative and adapted BAL

approach addresses measurement and metamodel errors. This framework facilitates a comprehensive parameter comparison and helps to determine the critical calibration parameters, even within the intricate four-dimensional parameter space.

The primary scientific contributions of this paper encompass the development of a Python-based BAL workflow, the adaptive integration of measurement and metamodel errors, its application to four calibration parameters, and its extension to the simulation of reservoir sedimentation processes.

4.3. Publication III: Assessment of uncertainties in a complex modeling chain for predicting reservoir sedimentation under changing climate

This paper presents a complex model chain to forecast reservoir sedimentation and its preceding processes for various climate change scenarios (Pesci et al., 2023). An ensemble of climate models is employed to analyze future climate change scenarios. However, it is essential to consider the propagation of uncertainties within the modeling chain. The main objective is to investigate whether model parameter uncertainties affect the simulation results more than climate model uncertainties. A simplified method is used to answer this question by calculating approximate model parameter uncertainties and comparing them to the spread of climate projections.

The FOSM method proves to be a suitable approach for approximating model parameter uncertainties in a complex modeling chain. The study reveals that the uncertainties from different climate projections significantly surpass the model parameter uncertainties for the investigated low emissions scenario RCP2.6. The selection of RCP2.6 stems from a methodological perspective, aiming to discern whether the range of outcomes from a climate projection ensemble, even in scenarios like RCP2.6 with minimal change signals, exceeds typical variations attributed to model parameter uncertainty. Hence, the spread of climate projection is expected to be more prominent in higher emissions scenarios. To mitigate biases originating from individual climate models, the use of multiple climate model ensembles is recommended. The proposed method facilitates the communication of diverse sources of uncertainty within complex modeling chains, including climate models. Furthermore, it highlights how model parameters and climate model uncertainties compare to climate change signals.

The main scientific contribution of this paper lies in the developed method that enables the modeler to communicate different sources of uncertainty. This approach enhances the assessment of predicted outcomes and facilitates the estimation of their associated uncertainty.

4.4. Publication IV: An interdisciplinary model chain quantifies the footprint of global change on reservoir sedimentation

This paper builds upon the previous publications and addresses the urgent issue of reservoir sedimentation in the context of global change (Mouris, Schwindt, Pesci, Wieprecht and Haun, 2023). The primary aim is to assess the impacts of hydro-climatic and land use changes for various global change scenarios on river discharge, sediment production and delivery, and reservoir sedimentation. Recognizing the limitations of existing modeling approaches, the paper introduces a novel, interdisciplinary model chain that integrates catchment characteristics, hydro-climatic conditions, and land use data to predict long-term soil erosion, sediment delivery, and multidimensional reservoir sedimentation processes. This holistic approach aims to facilitate sustainable reservoir operations by quantifying the impact of global change on reservoir sedimentation.

Applied to a typical mountainous Mediterranean catchment, the model chain predicts reduced river discharge and increased SYs for high and medium emissions scenarios. Low emissions scenarios project higher discharges by 2100, while high emissions scenarios exacerbate water scarcity. In particular, increased winter precipitation and a shift from snowfall to rain are projected to aggravate reduced summer precipitation, underscoring the need for artificial water storage in reservoirs during hot and dry Mediterranean summers. Additionally, higher winter rainfall amplifies sediment production and reservoir sedimentation.

Land use composition plays a crucial role, with higher proportions of forest and grassland reducing sediment concentrations, while higher proportions of agricultural land intensify sediment concentrations and yields. Scenarios with increased SYs experience a significant loss of storage volume and the delta moves further downstream into the reservoir, resulting in a lower TE. The hydro-morphodynamic numerical model provides crucial insights into sedimentation patterns. For instance, the spatially explicit 3d model identifies sedimentation hotspots and provides information on the suitability of possible sediment management measures. Another key finding emphasizes that land use change can outweigh increased reservoir sedimentation due to hydro-climatic change, underscoring the importance of localized actions (e.g., afforestation) to reduce sediment production.

The main scientific contribution is the development of an interdisciplinary model chain to assess the substantial impacts of hydro-climatic and land use changes on river discharge, sediment production and delivery, and reservoir sedimentation. The spatial and temporal explicit insights provided by the model chain provide valuable information on future sediment deposition patterns to facilitate sustainable management strategies.

5. Conclusions and Recommendations

Reservoirs are crucial structures that serve multiple purposes and are essential for sustainable development in the face of global change. However, their functions are threatened by reservoir sedimentation, which reduces their storage volume. Therefore, the main goal of this thesis is to establish objective methods for predicting long-term sediment dynamics and multidimensional reservoir sedimentation under different global change scenarios, including hydro-climatic and land use changes.

Innovative sediment load predictions with seasonal snow memory An objective method for calculating sediment loads entering the reservoir is essential to predict reservoir sedimentation in the face of climate and global change. The developed algorithmic approach, using freely available datasets like satellite imagery and climate reanalysis data, proves effective even in regions lacking detailed precipitation data and field surveys (e.g., regarding soil characteristics and land use), such as for the Devoll catchment in Albania. The agreement between predicted and observed suspended sediment loads underscores the method's viability. A key innovation is the integration of non-erosive snowfall that accumulates over months as a function of temperature, followed by erosive snowmelt. By integrating a seasonal snow memory into the RUSLE, the accuracy of the prediction of soil erosion and sediment delivery in the studied mountainous Mediterranean catchment substantially improves. This improvement, resulting from a more realistic representation of physical processes, enables monthly predictions of hydro-morphological changes in reservoirs. Therefore, the developed approach bridges gaps in existing methodologies and advances long-term predictions on sediment production and subsequent reservoir sedimentation under changing environmental conditions.

Bayesian calibration of reservoir sedimentation models and parameter prioritization The calibration of multidimensional hydro-morphodynamic models is crucial for predicting reservoir sedimentation. The findings emphasize that Bayesian calibration generates meaningful parameter combinations only when calibration nodes are within the valid model range of the numerical model. In particular, locating calibration nodes in the shallow areas at the head of the reservoir increases model uncertainty. The modified BAL method, which handles measurement and metamodel errors, proves robust in the complex four-dimensional parameter space

resulting from the four calibration parameters considered. Hence, the Bayesian calibration approach facilitates comprehensive parameter comparison and identifies key calibration parameters, providing practical guidance for researchers and practitioners. Bayesian calibration determines dry bulk density as the most important and influential parameter for simulating reservoir sedimentation. Therefore, it is recommended to prioritize collecting dry bulk density data as input data for setting up a reservoir sedimentation model.

Uncertainty of an interdisciplinary model chain in predicting reservoir sedimentation The developed model chain integrates three state-of-the-art models to predict sedimentation processes in the Banja reservoir under diverse future hydro-climatic and land use conditions. Despite the inherent challenges of using multiple models in a chain, the approach leverages the strengths of each to predict bed level changes in the reservoir accurately. The assessment of model parameter uncertainties in predicting final bed changes using the FOSM method shows that they are relatively small compared to the measured bed elevations, confirming the robustness of the modeling chain. However, the uncertainties arising from different climate projections significantly surpass the model parameter uncertainties. Thus, there may be significant uncertainty in absolute sediment quantities, primarily due to variations in climate projections that propagate through the model chain. Nevertheless, this research provides modelers and practitioners valuable insights for effectively communicating uncertainty in complex modeling chains. Furthermore, it is recommended to use multiple climate projections to obtain robust trends and derive a range of possible outcomes.

Impacts of global change on reservoir sedimentation The interdisciplinary model chain predicts that mean annual river discharge will decrease, and SYs will increase in high and medium emissions scenarios for the investigated Mediterranean catchment. Higher winter rainfall and peak flows in winter enhance sediment production and reservoir sedimentation. However, lower summer rainfall and decreased winter snow storage result in less available water in spring and summer, even though winter precipitation increases. Low emissions scenarios exhibit increased discharges, leading to higher SYs but lower sediment concentrations compared to higher emissions scenarios. Forest and grassland dominance reduces sediment concentrations, while higher agricultural proportions significantly amplify sediment concentrations and SYs. Therefore, land use change outweighs the impact of hydro-climatic changes on reservoir sedimentation in the investigated Devoll catchment. As a direct consequence, targeted interventions such as policy-driven crop adaptations and afforestation can mitigate soil loss and reservoir sedimentation in the future. The reservoir model demonstrates that scenarios with elevated SYs experience more significant storage volume loss and a decreasing TE. Furthermore, the delta migrates further downstream into the reservoir. However, the 3d numerical model goes beyond bulk parameters such as total storage loss or TE, revealing sedimentation

hotspots crucial for future sustainable sediment management practices like informed dredging or flushing operations.

Recommendations for future work The methods developed in this thesis offer an objective prediction of reservoir sedimentation processes, yet there are opportunities for methodological improvements and future research. Specifically, the current SY prediction using RUSLE and SEDD does not consider mass wasting and fluvial erosion, even though these factors can be significant sediment sources dependent on the catchment characteristics (see Chapter 2.1 and Publication I). Especially when sub-monthly temporal resolution is required, it is necessary to simulate erosion and deposition processes within the river network. Furthermore, the model's seasonal snow memory is tailored to Mediterranean mountainous regions with local snow cover of 2-4 months. For regions with prolonged snow cover, it is recommended to use temperature-dependent snowmelt models that account for partial snowmelt (e.g., Hock, 2003).

The two numerical reservoir sedimentation models have certain limitations that warrant attention in future studies. For example, the assumption of a constant dry bulk density over space and time neglects the variability caused by grain size distribution, consolidation, and dewatering processes (see Chapter 2.3). Therefore, future research should incorporate semi-empirical formulas and a multi-layer discretization to account for consolidation processes at the reservoir bed (e.g., Audouin et al., 2020). Another limitation is neglecting temperature-related density differences and stratification in the reservoir, which can affect suspended sediment transport. Since sediment management has not been conducted in the study area, the numerical models did not incorporate any strategies for sediment management. If sediment management actions like flushing or dredging are foreseen, they should also be implemented in the numerical model for reliable prediction of deposition patterns and storage loss estimates.

Additionally, it is essential to note that the models may underestimate sediment production during extreme events due to the highly non-linear nature of sediment dynamics (e.g., Roering et al., 1999). These high-magnitude, low-frequency extreme events are often unmonitored and can result in sediment inputs equivalent to the ones from several years during a single event (Coppus and Imeson, 2002; Baynes et al., 2023). Regardless of the modeling approach used, the model's response to extreme precipitation events is uncertain, especially if such events have not occurred during the calibration period. Additionally, dominant processes in a specific catchment may change due to climate change, with previously negligible processes like landslides or mudflows potentially becoming significant sediment sources (see Chapter 2.1). Thus, models may perform well for decades but fail during extreme events. Using long time series for calibration is recommended, acknowledging the inherent uncertainty in long-term sediment production.

References

Aberle, J., Rennie, C., Admiraal, D., Muste, M., Nikora, V. and Garcia, M. H. (2017). *Experimental Hydraulics: Methods, Instrumentation, Data Processing and Management: Volume II: Instrumentation and Measurement Techniques: Methods, ... Techniques*, Taylor & Francis Ltd, Boca Raton London New York Leiden.

Ahmad, M.-u.-D., Peña-Arancibia, J. L., Yu, Y., Stewart, J. P., Podger, G. M. and Kirby, J. M. (2021). Climate change and reservoir sedimentation implications for irrigated agriculture in the Indus Basin Irrigation System in Pakistan, *Journal of Hydrology* **603**: 126967.

Alavian, V., Jirka, G. H., Denton, R. A., Johnson, M. C. and Stefan, H. G. (1992). Density currents entering lakes and reservoirs, *Journal of Hydraulic Engineering* **118**(11): 1464–1489.

Alcamo, J. and Henrichs, T. (2002). Critical regions: A model-based estimation of world water resources sensitive to global changes, *Aquatic Sciences* **64**(4): 352–362.

Aleixo, R., Guerrero, M., Nones, M. and Ruther, N. (2020). Applying ADCPs for Long-Term Monitoring of SSC in Rivers, *Water Resources Research* **56**(1).

Alewell, C., Borrelli, P., Meusburger, K. and Panagos, P. (2019). Using the USLE: Chances, challenges and limitations of soil erosion modelling, *International Soil and Water Conservation Research* **7**(3): 203–225.

Alfieri, L., Bisselink, B., Dottori, F., Naumann, G., de Roo, A., Salamon, P., Wyser, K. and Feyen, L. (2017). Global projections of river flood risk in a warmer world, *Earth's Future* **5**(2): 171–182.

An, Y., Yan, X., Lu, W., Qian, H. and Zhang, Z. (2022). An improved Bayesian approach linked to a surrogate model for identifying groundwater pollution sources, *Hydrogeology Journal* **30**(2): 601–616.

Annandale, G. (2013). *Quenching the thirst: sustainable water supply and climate change*, CreateSpace Independent Publishing Platform, North Charleston, South Carolina, USA.

Annandale, G. W. (2006). Reservoir Sedimentation, *Encyclopedia of Hydrological Sciences*, John Wiley & Sons, Ltd, Hoboken, NJ, USA.

Annandale, G. W., Morris, G. L. and Karki, P. (2016). *Extending the Life of Reservoirs: Sustainable Sediment Management for Dams and Run-of-River Hydropower*, The World Bank, Washington, D.C., USA.

Arnoldus, H. M. J. (1980). An approximation of the rainfall factor in the Universal Soil Loss Equation., *Assessment of Erosion* **6**: 127–132.

ASCE, N. (1982). Relationships Between Morphology of Small Streams and Sediment Yield, *Journal of the Hydraulics Division* **108**(11): 1328–1365.

Audouin, Y., Benson, T., Delinares, M., Fontaine, J., Glander, B., Huybrechts, N., Kopmann, R., Leroy, A., Pavan, S., Pham, C.-T., Taccone, F., Tassi, P. and Walther, R. (2020). Introducing gaia, the brand new sediment transport module of the telemac-mascaret system, *Telemac User Conference 2019*, Toulouse, France.

Azari, M., Moradi, H. R., Saghafian, B. and Faramarzi, M. (2016). Climate change impacts on streamflow and sediment yield in the North of Iran, *Hydrological Sciences Journal* **61**(1): 123–133.

Banasik, K., Hejduk, L., Krajewski, A. and Wasilewicz, M. (2021). The intensity of siltation of a small reservoir in Poland and its relationship to environmental changes, *Catena* **204**: 105436.

Bangash, R. F., Passuello, A., Sanchez-Canales, M., Terrado, M., López, A., Elorza, F. J., Ziv, G., Acuña, V. and Schuhmacher, M. (2013). Ecosystem services in Mediterranean river basin: Climate change impact on water provisioning and erosion control, *Science of The Total Environment* **458-460**: 246–255.

Basson, G. (2009). Management of siltation in existing and new reservoirs, *Proc. of the 23rd Congress of the Int. Commission on Large Dams CIGB-ICOLD*, Vol. 2.

Battista, G., Molnar, P. and Burlando, P. (2020). Modelling impacts of spatially variable erosion drivers on suspended sediment dynamics, *Earth Surface Dynamics* **8**(3): 619–635.

Baynes, E. R. C., Kincey, M. E. and Warburton, J. (2023). Extreme Flood Sediment Production and Export Controlled by Reach-Scale Morphology, *Geophysical Research Letters* **50**(10).

Beck, H. E., Zimmermann, N. E., McVicar, T. R., Vergopolan, N., Berg, A. and Wood, E. F. (2018). Present and future Köppen-Geiger climate classification maps at 1-km resolution, *Scientific Data* **5**(1).

Beckers, F., Haun, S. and Noack, M. (2018). Experimental investigation of reservoir sediments, *in* A. Paquier and N. Rivière (eds), *River Flow 2018 - Ninth International Conference on Fluvial Hydraulics*, Vol. 40, p. 03030.

Beckers, F., Heredia, A., Noack, M., Nowak, W., Wieprecht, S. and Oladyshkin, S. (2020). Bayesian Calibration and Validation of a Large-Scale and Time-Demanding Sediment Transport Model, *Water Resources Research* **56**(7).

Benavidez, R., Jackson, B., Maxwell, D. and Norton, K. (2018). A review of the (Revised) Universal Soil Loss Equation ((R)USLE): with a view to increasing its global applicability and improving soil loss estimates, *Hydrology and Earth System Sciences* **22**(11): 6059–6086.

Berg, P., Bosshard, T., Yang, W. and Zimmermann, K. (2022). MIdASv0.2.1 – MultI-scale bias AdjuStment, *Geoscientific Model Development* **15**(15): 6165–6180.

Borrelli, P., Alewell, C., Alvarez, P., Anache, J., Baartman, J., Ballabio, C., Bezak, N., Biddoccu, M., Cerdà, A., Chalise, D., Chen, S., Chen, W., De Girolamo, A., Gessesse, G., Deumlich, D., Diodato, N., Efthimiou, N., Erpul, G., Fiener, P. and Panagos, P. (2021). Soil erosion modelling: A global review and statistical analysis, *Science of The Total Environment* p. 146494.

Borrelli, P., Panagos, P., Märker, M., Modugno, S. and Schütt, B. (2017). Assessment of the impacts of clear-cutting on soil loss by water erosion in Italian forests: First comprehensive monitoring and modelling approach, *Catena* **149**: 770–781.

Borrelli, P., Robinson, D. A., Panagos, P., Lugato, E., Yang, J. E., Alewell, C., Wuepper, D., Montanarella, L. and Ballabio, C. (2020). Land use and climate change impacts on global soil erosion by water (2015-2070), *Proceedings of the National Academy of Sciences* **117**(36): 21994–22001.

Box, G. E. P. and Tiao, G. C. (1992). *Bayesian Inference in Statistical Analysis*, 1st edition edn, Wiley-Interscience, New York.

Boyce, R. (1975). Sediment routing with sediment delivery ratios, *Present and Prospective Technology for Predicting Sediment Yields and Sources* (Present and Prospective Technology for Predicting Sediment Yields and Sources, U.S.): 61–65.

Bridges, E. M. and Oldeman, L. R. (1999). Global Assessment of Human-Induced Soil Degradation, *Arid Soil Research and Rehabilitation* **13**(4): 319–325.

Brown, L. and Foster, G. (1987). Storm Erosivity Using Idealized Intensity Distributions, *Transactions of the ASAE* pp. 379–386.

Bruk, S. (1996). Reservoir sedimentation and sustainable management of water resources–The international perspective, *Proceedings of the International Conference on Reservoir Sedimentation, Fort Collins, CL, USA*, pp. 9–13.

Brune, G. M. (1953). Trap efficiency of reservoirs, *Eos, Transactions American Geophysical Union* **34**(3): 407–418.

Bruno, C., Stefano, C. D. and Ferro, V. (2008). Field investigation on rilling in the experimental Sparacia area, South Italy, *Earth Surface Processes and Landforms* **33**(2): 263–279.

Bugg, R. A., Donald, W., Zech, W. and Perez, M. (2017). Performance Evaluations of Three Silt Fence Practices Using a Full-Scale Testing Apparatus, *Water* **9**(7): 502.

Bussi, G., Darby, S. E., Whitehead, P. G., Jin, L., Dadson, S. J., Voepel, H. E., Vasilopoulos, G., Hackney, C. R., Hutton, C., Berchoux, T., Parsons, D. R. and Nicholas, A. (2021). Impact of dams and climate change on suspended sediment flux to the Mekong delta, *Science of The Total Environment* **755**: 142468.

Caitcheon, G. G., Olley, J. M., Pantus, F., Hancock, G. and Leslie, C. (2012). The dominant erosion processes supplying fine sediment to three major rivers in tropical Australia, the Daly (NT), Mitchell (Qld) and Flinders (Qld) Rivers, *Geomorphology* **151-152**: 188–195.

Carolli, M., Garcia de Leaniz, C., Jones, J., Belletti, B., Huđek, H., Pusch, M., Pandakov, P., Börger, L. and van de Bund, W. (2023). Impacts of existing and planned hydropower dams on river fragmentation in the Balkan Region, *Science of The Total Environment* **871**: 161940.

Carollo, F. G., Di Stefano, C., Ferro, V. and Pampalone, V. (2015). Measuring rill erosion at plot scale by a drone-based technology, *Hydrological Processes* **29**(17): 3802–3811.

Cavalli, M., Trevisani, S., Comiti, F. and Marchi, L. (2013). Geomorphometric assessment of spatial sediment connectivity in small Alpine catchments, *Geomorphology* **188**: 31–41.

Chadwick, A. J., Lamb, M. P., Moodie, A. J., Parker, G. and Nittrouer, J. A. (2019). Origin of a Preferential Avulsion Node on Lowland River Deltas, *Geophysical Research Letters* **46**(8): 4267–4277.

Chen, M., Vernon, C. R., Graham, N. T., Hejazi, M., Huang, M., Cheng, Y. and Calvin, K. (2020). Global land use for 2015–2100 at 0.05 resolution under diverse socioeconomic and climate scenarios, *Scientific Data* **7**(1): 320.

Churchill, M. A. (1948). Discussion of "Analysis and Use of Reservoir Sedimentation Data", *Proceedings of the Federal Inter-Agency Sedimentation Conference*, Denver, USA, pp. 139–140.

Coleman, J. M. and Prior, D. B. (1988). Mass Wasting on Continental Margins, *Annual Review of Earth and Planetary Sciences* **16**(1): 101–119.

Copernicus Land Monitoring Service (2018). Corine land cover 2018. European Environment Agency (EEA). https://land.copernicus.eu/pan-european/corine-land-cover/clc2018.

Coppus, R. and Imeson, A. C. (2002). Extreme events controlling erosion and sediment transport in a semi-arid sub-andean valley, *Earth Surface Processes and Landforms* **27**(13): 1365–1375.

Crozier, M. J. (1986). *Landslides : causes, consequences, and environment*, Croom Helm Ltd, London, United Kingdom.

Dai, A. (2013). Increasing drought under global warming in observations and models, *Nature Climate Change* **3**(1): 52–58.

Dallison, R. J. H., Patil, S. D. and Williams, A. P. (2021). Impacts of climate change on future water availability for hydropower and public water supply in Wales, UK, *Journal of Hydrology: Regional Studies* **36**: 100866.

de Oliveira Fagundes, H., de Paiva, R. C. D., Brêda, J. P. L. F., Fassoni-Andrade, A. C., Borrelli, P. and Fan, F. M. (2023). An assessment of South American sediment fluxes under climate changes, *Science of The Total Environment* **879**: 163056.

de Santos Loureiro, N. and de Azevedo Coutinho, M. (2001). A new procedure to estimate the RUSLE EI30 index, based on monthly rainfall data and applied to the Algarve region, Portugal, *Journal of Hydrology* **250**(1): 12–18.

de Vente, J., Poesen, J., Arabkhedri, M. and Verstraeten, G. (2007). The sediment delivery problem revisited, *Progress in Physical Geography: Earth and Environment* **31**(2): 155–178.

de Vente, J., Poesen, J. and Verstraeten, G. (2004). Evaluation of reservoir sedimentation as a methodology for sediment yield assessment in the Mediterranean: challenges and limitations, *Soil Conservation And Protection for Europe* .

de Vente, J., Poesen, J., Verstraeten, G., Govers, G., Vanmaercke, M., Van Rompaey, A., Arabkhedri, M. and Boix-Fayos, C. (2013). Predicting soil erosion and sediment yield at regional scales: Where do we stand?, *Earth-Science Reviews* **127**: 16–29.

Deemer, B. R., Harrison, J. A., Li, S., Beaulieu, J. J., DelSontro, T., Barros, N., Bezerra-Neto, J. F., Powers, S. M., dos Santos, M. A. and Vonk, J. A. (2016). Greenhouse Gas Emissions from Reservoir Water Surfaces: A New Global Synthesis, *BioScience* **66**(11): 949–964.

Detering, M., Bolsenkötter, L. and Küppers, J. (2019). Kosteneffizienter Umgang mit Sediment unter neuen Regelwerken, *Wasserwirtschaft* **109**: 158–161.

Di, M. and Wang, J. (2018). Microplastics in surface waters and sediments of the Three Gorges Reservoir, China, *Science of The Total Environment* **616-617**: 1620–1627.

Diodato, N. and Bellocchi, G. (2007). Estimating monthly (R)USLE climate input in a Mediterranean region using limited data, *Journal of Hydrology* **345**(3-4): 224–236.

Diodato, N., Knight, J. and Bellocchi, G. (2013). Reduced complexity model for assessing patterns of rainfall erosivity in Africa, *Global and Planetary Change* **100**: 183–193.

Doherty, J. (2001). PEST-ASP user's manual, *Watermark Numerical Computing, Brisbane, Australia* .

Duan, C. G. and Karelin, V. I. (2003). *Abrasive Erosion And Corrosion Of Hydraulic Machinery*, illustrated edition edn, Imperial College Press, London.

Efthimiou, N., Lykoudi, E. and Karavitis, C. (2017). Comparative analysis of sediment yield estimations using different empirical soil erosion models, *Hydrological Sciences Journal* **62**(16): 2674–2694.

Ehrbar, D., Schmocker, L., Doering, M., Cortesi, M., Bourban, G., Boes, R. M. and Vetsch, D. F. (2018). Continuous Seasonal and Large-Scale Periglacial Reservoir Sedimentation, *Sustainability* **10**(9): 3265.

Einstein, H. A. (1950). The Bed-Load Function for Sediment Transport in Open Channel Flows, *Technical Bulletin of the USDA Soil Conservation Service* **1026**: 71.

Fan, J. and Morris, G. L. (1992). Reservoir sedimentation. i: Delta and density current deposits, *Journal of Hydraulic Engineering* **118**(3): 354–369.

Fernández-Raga, M., Fraile, R., Keizer, J. J., Varela Teijeiro, M. E., Castro, A., Palencia, C., Calvo, A. I., Koenders, J. and Da Costa Marques, R. L. (2010). The kinetic energy of rain measured with an optical disdrometer: An application to splash erosion, *Atmospheric Research* **96**(2): 225–240.

Ferro, V. and Minacapilli, M. (1995). Sediment delivery processes at basin scale, *Hydrological Sciences Journal* **40**(6): 703–717.

Ferro, V. and Porto, P. (2000). Sediment delivery distributed (sedd) model, *Journal of Hydrologic Engineering* **5**(4): 411–422.

Fischer, G., Nachtergaele, F., Prieler, S., van Velthuizen, H. T., van, V., Verelst, L. and Wiberg, D. (2008). The harmonized world soil database v 1.2, *IIASA, Laxenburg, Austria and FAO, Rome, Italy* .

Fox, G. A., Sheshukov, A., Cruse, R., Kolar, R. L., Guertault, L., Gesch, K. R. and Dutnell, R. C. (2016). Reservoir Sedimentation and Upstream Sediment Sources: Perspectives and Future Research Needs on Streambank and Gully Erosion, *Environmental Management* **57**(5): 945–955.

Galy, A. and France-Lanord, C. (2001). Higher erosion rates in the Himalaya: Geochemical constraints on riverine fluxes, *Geology* **29**(1): 23–26.

García-Ruiz, J. M., Beguería, S., Nadal-Romero, E., González-Hidalgo, J. C., Lana-Renault, N. and Sanjuán, Y. (2015). A meta-analysis of soil erosion rates across the world, *Geomorphology* **239**: 160–173.

García-Ruiz, J. M., López-Moreno, J. I., Vicente-Serrano, S. M., Lasanta–Martínez, T. and Beguería, S. (2011). Mediterranean water resources in a global change scenario, *Earth-Science Reviews* **105**(3): 121–139.

Gelleszun, M., Kreye, P. and Meon, G. (2017). Representative parameter estimation for hydrological models using a lexicographic calibration strategy, *Journal of Hydrology* **553**: 722–734.

George, M. W., Hotchkiss, R. H. and Huffaker, R. (2017). Reservoir sustainability and sediment management, *Journal of Water Resources Planning and Management* **143**(3): 04016077.

Gianinetto, M., Aiello, M., Polinelli, F., Frassy, F., Rulli, M. C., Ravazzani, G., Bocchiola, D., Chiarelli, D. D., Soncini, A. and Vezzoli, R. (2019). D-RUSLE: a dynamic model to estimate potential soil erosion with satellite time series in the Italian Alps, *European Journal of Remote Sensing* **52**(sup4): 34–53.

Grams, P. E., Topping, D. J., Schmidt, J. C., Hazel, J. E. and Kaplinski, M. (2013). Linking morphodynamic response with sediment mass balance on the Colorado River in Marble Canyon: Issues of scale, geomorphic setting, and sampling design, *Journal of Geophysical Research: Earth Surface* **118**(2): 361–381.

Gunatilake, H. M. and Gopalakrishnan, C. (1999). The Economics of Reservoir Sedimentation: A Case Study of Mahaweli Reservoirs in Sri Lanka, *International Journal of Water Resources Development* **15**(4): 511–526.

Hajek, E. A. and Wolinsky, M. A. (2012). Simplified process modeling of river avulsion and alluvial architecture: Connecting models and field data, *Sedimentary Geology* **257-260**: 1–30.

Hall, D. K., Riggs, G. A., Salomonson, V. V., DiGirolamo, N. E. and Bayr, K. J. (2002). MODIS snow-cover products, *Remote Sensing of Environment* **83**(1): 181–194.

Haun, S., Kjærås, H., Løvfall, S. and Olsen, N. R. B. (2013). Three-dimensional measurements and numerical modelling of suspended sediments in a hydropower reservoir, *Journal of Hydrology* **479**: 180–188.

Hersbach, H., Bell, B., Berrisford, P., Hirahara, S., Horányi, A., Muñoz-Sabater, J., Nicolas, J., Peubey, C., Radu, R., Schepers, D., Simmons, A., Soci, C., Abdalla, S., Abellan, X., Balsamo, G., Bechtold, P., Biavati, G., Bidlot, J., Bonavita, M., Chiara, G. D., Dahlgren, P., Dee, D., Diamantakis, M., Dragani, R., Flemming, J., Forbes, R., Fuentes, M., Geer, A., Haimberger, L., Healy, S., Hogan, R. J., Hólm, E., Janisková, M., Keeley, S., Laloyaux, P., Lopez, P., Lupu, C., Radnoti, G., Rosnay, P. d., Rozum, I., Vamborg, F., Villaume, S. and Thépaut, J.-N. (2020). The ERA5 global reanalysis, *Quarterly Journal of the Royal Meteorological Society* **146**(730): 1999–2049.

Hervouet, J.-M. (2007). *Hydrodynamics of Free Surface Flows: Modelling with the Finite Element Method*, 1. edition edn, Wiley, Chichester ; Hoboken, N.J.

Hervouet, J.-M., Razafindrakoto, E. and Villaret, C. (2011). Dealing with dry zones in free surface flows: A new class of advection schemes, *Proceedings of the 34th World Congress of the International Association for Hydro-Environment Research and Engineering: 33rd Hydrology and Water Resources Symposium and 10th Conference on Hydraulics in Water Engineering*, Engineers Australia, Barton, A.C.T.

Hiederer, R. (2013). *Mapping soil properties for Europe: spatial representation of soil database attributes.*, Scientific and Technical Research series, European Commission. Joint Research Centre. Institute for Environment and Sustainability., Ispra, Italy.

Hinderer, M., Kastowski, M., Kamelger, A., Bartolini, C. and Schlunegger, F. (2013). River loads and modern denudation of the Alps — A review, *Earth-Science Reviews* **118**: 11–44.

Hirschberg, J., Fatichi, S., Bennett, G. L., McArdell, B. W., Peleg, N., Lane, S. N., Schlunegger, F. and Molnar, P. (2021). Climate Change Impacts on Sediment Yield and Debris-Flow Activity in an Alpine Catchment, *Journal of Geophysical Research: Earth Surface* **126**(1): e2020JF005739.

Hock, R. (2003). Temperature index melt modelling in mountain areas, *Journal of Hydrology* **282**(1): 104–115.

Horszczaruk, E. (2004). The model of abrasive wear of concrete in hydraulic structures, *Wear* **256**(7): 787–796.

Jain, M. K. and Kothyari, U. C. (2000). Estimation of soil erosion and sediment yield using GIS, *Hydrological Sciences Journal* **45**(5): 771–786.

Kearney, S. P., Fonte, S. J., García, E. and Smukler, S. M. (2018). Improving the utility of erosion pins: absolute value of pin height change as an indicator of relative erosion, *Catena* **163**: 427–432.

Khan, M. A., Stamm, J. and Haider, S. (2020). Simulating the Impact of Climate Change with Different Reservoir Operating Strategies on Sedimentation of the Mangla Reservoir, Northern Pakistan, *Water* **12**(10): 2736.

Khoi, D. N. and Suetsugi, T. (2014). Impact of climate and land-use changes on hydrological processes and sediment yield—a case study of the Be River catchment, Vietnam, *Hydrological Sciences Journal* **59**(5): 1095–1108.

Kim, G.-E., Kim, J.-H. and Yoo, S.-H. (2020). Assessing the environmental benefits of multipurpose water uses of hydropower reservoirs on the Han River in South Korea, *Energy & Environment* **31**(7): 1167–1180.

Klaghofer, E., Summer, W. and Villeneuve, J. (1992). Some remarks on the determination of the sediment delivery ratio, *Erosion, Debris Flows and Environment in Mountain regions (Proceedings of the Chengdu Symposium)*, 209, IAHS.

Kokpinar, M. A., Altan-Sakarya, A. B., Kumcu, S. Y. and Gogus, M. (2015). Assessment of sediment yield estimations for large watershed areas: a case study for the Seyhan, Demirköprü and Hirfanlı reservoirs in Turkey, *Hydrological Sciences Journal* **60**(12): 2189–2203.

Kondolf, G. M. (1997). Hungry Water: Effects of Dams and Gravel Mining on River Channels, *Environmental Management* **21**(4): 533–551.

Kondolf, G. M., Gao, Y., Annandale, G. W., Morris, G. L., Jiang, E., Zhang, J., Cao, Y., Carling, P., Fu, K., Guo, Q., Hotchkiss, R., Peteuil, C., Sumi, T., Wang, H.-W., Wang, Z., Wei, Z., Wu, B., Wu, C. and Yang, C. T. (2014). Sustainable sediment management in reservoirs and regulated rivers: Experiences from five continents, *Earth's Future* **2**(5): 256–280.

Kottek, M., Grieser, J., Beck, C., Rudolf, B. and Rubel, F. (2006). World Map of the Köppen-Geiger climate classification updated, *Meteorologische Zeitschrift* **15**(3): 259–263.

Kullback, S. and Leibler, R. A. (1951). On Information and Sufficiency, *The Annals of Mathematical Statistics* **22**(1): 79–86.

Kunstmann, H., Kinzelbach, W. and Siegfried, T. (2002). Conditional first-order second-moment method and its application to the quantification of uncertainty in groundwater modeling, *Water Resources Research* **38**(4): 6–1–6–14.

Kunz, M. J., Wüest, A., Wehrli, B., Landert, J. and Senn, D. B. (2011). Impact of a large tropical reservoir on riverine transport of sediment, carbon, and nutrients to downstream wetlands, *Water Resources Research* **47**(12).

Lane, E. W. and Borland, W. M. (1951). Estimating bed load, *Eos, Transactions American Geophysical Union* **32**(1): 121–123.

Lin, L., Pan, X., Zhang, S., Li, D., Zhai, W., Wang, Z., Tao, J., Mi, C., Li, Q. and Crittenden, J. C. (2021). Distribution and source of microplastics in China's second largest reservoir - Danjiangkou Reservoir, *Journal of Environmental Sciences* **102**: 74–84.

Liu, B. Y., Nearing, M. A. and Risse, L. M. (1994). Slope Gradient Effects on Soil Loss for Steep Slopes, *Transactions of the ASAE* **37**(6): 1835–1840.

Lo, E. L., Bentley, S. J. and Xu, K. (2014). Experimental study of cohesive sediment consolidation and resuspension identifies approaches for coastal restoration: Lake Lery, Louisiana, *Geo-Marine Letters* **34**(6): 499–509.

Lu, H., Moran, C. J. and Sivapalan, M. (2005). A theoretical exploration of catchment-scale sediment delivery, *Water Resources Research* **41**(9).

Mabit, L., Benmansour, M. and Walling, D. E. (2008). Comparative advantages and limitations of the fallout radionuclides 137Cs, 210Pbex and 7Be for assessing soil erosion and sedimentation, *Journal of Environmental Radioactivity* **99**(12): 1799–1807.

Mahmood, K. (1987). Reservoir sedimentation-impact, extent and mitigation, *World Bank technical paper* **71**.

Marshak, S. (2018). *Earth: Portrait of a Planet*, 6 edn, W W Norton & Co Inc, New York.

Mehta, A. J., Hayter, E. J., Parker, W. R., Krone, R. B. and Teeter, A. M. (1989). Cohesive sediment transport. i: Process description, *Journal of Hydraulic Engineering* **115**(8): 1076–1093.

Millares, A. and Moñino, A. (2018). Sediment yield and transport process assessment from reservoir monitoring in a semi-arid mountainous river, *Hydrological Processes* **32**(19): 2990–3005.

Milliman, J. D. and Meade, R. H. (1983). World-Wide Delivery of River Sediment to the Oceans, *The Journal of Geology* **91**(1): 1–21.

Müller, D. and Sikor, T. (2006). Effects of postsocialist reforms on land cover and land use in South-Eastern Albania, *Applied Geography* **26**(3): 175–191.

Moges, E., Demissie, Y., Larsen, L. and Yassin, F. (2021). Review: Sources of Hydrological Model Uncertainties and Advances in Their Analysis, *Water* **13**(1): 28.

Mohammadi, F., Kopmann, R., Guthke, A., Oladyshkin, S. and Nowak, W. (2018). Bayesian selection of hydro-morphodynamic models under computational time constraints, *Advances in Water Resources* **117**: 53–64.

Moragoda, N. and Cohen, S. (2020). Climate-induced trends in global riverine water discharge and suspended sediment dynamics in the 21st century, *Global and Planetary Change* **191**: 103199.

Morgan, R. P. C. (2009). *Soil Erosion and Conservation*, John Wiley & Sons, Hoboken, NJ, USA.

Morris, G. L., Annandale, G. and Hotchkiss, R. (2008). Reservoir Sedimentation, *in* M. H. García (ed.), *Sedimentation Engineering*, number 110 in *ASCE Manuals and Reports on Engineering Practice*, American Society of Civil Engineers, Reston, VA, USA, pp. 579–612.

Morris, G. L. and Fan, J. (1998). *Reservoir sedimentation handbook: design and management of dams, reservoirs, and watersheds for sustainable use*, McGraw-Hill, New York, NY, USA.

Mouris, K., Acuna Espinoza, E., Schwindt, S., Mohammadi, F., Haun, S., Wieprecht, S. and Oladyshkin, S. (2023). Stability criteria for Bayesian calibration of reservoir sedimentation models, *Modeling Earth Systems and Environment* .

Mouris, K., Schwindt, S., Haun, S., Morales Oreamuno, M. F. and Wieprecht, S. (2022). Introducing seasonal snow memory into the RUSLE, *Journal of Soils and Sediments* .

Mouris, K., Schwindt, S., Pesci, M. H., Wieprecht, S. and Haun, S. (2023). An interdisciplinary model chain quantifies the footprint of global change on reservoir sedimentation, *Scientific Reports* **13**: 20160.

Muehleisen, R. T. and Bergerson, J. (2016). Bayesian Calibration - What, Why And How, *International High Performance Buildings Conference*, Vol. Paper 167, Purdue University, West Lafayette, IN, USA.

Mulder, T. and Alexander, J. (2001). The physical character of subaqueous sedimentary density flows and their deposits, *Sedimentology* **48**(2): 269–299.

Mullan, D., Favis-Mortlock, D. and Fealy, R. (2012). Addressing key limitations associated with modelling soil erosion under the impacts of future climate change, *Agricultural and Forest Meteorology* **156**: 18–30.

Nearing, M. A. (1997). A Single, Continuous Function for Slope Steepness Influence on Soil Loss, *Soil Science Society of America Journal* **61**(3): 917.

Nearing, M. A. (2013). Soil Erosion and Conservation, *Environmental Modelling: Finding Simplicity in Complexity*, Wiley-Blackwell, Chichester, West Sussex ; Hoboken, NJ, pp. 365–378.

Nerantzaki, S. D., Giannakis, G. V., Efstathiou, D., Nikolaidis, N. P., Sibetheros, I. ., Karatzas, G. P. and Zacharias, I. (2015). Modeling suspended sediment transport and assessing the impacts of climate change in a karstic Mediterranean watershed, *Science of The Total Environment* **538**: 288–297.

Nilawar, A. P. and Waikar, M. L. (2019). Impacts of climate change on streamflow and sediment concentration under RCP 4.5 and 8.5: A case study in Purna river basin, India, *Science of The Total Environment* **650**: 2685–2696.

Nunes, J. P., Seixas, J. and Keizer, J. J. (2013). Modeling the response of within-storm runoff and erosion dynamics to climate change in two Mediterranean watersheds: A multi-model, multi-scale approach to scenario design and analysis, *Catena* **102**: 27–39.

Oberkampf, W. L., Trucano, T. G. and Hirsch, C. (2004). Verification, validation, and predictive capability in computational engineering and physics, *Applied Mechanics Reviews* **57**(5): 345–384.

Oladyshkin, S., Mohammadi, F., Kroeker, I. and Nowak, W. (2020). Bayesian3 Active Learning for the Gaussian Process Emulator Using Information Theory, *Entropy* **22**(8): 890.

Oladyshkin, S. and Nowak, W. (2019). The Connection between Bayesian Inference and Information Theory for Model Selection, Information Gain and Experimental Design, *Entropy* **21**(11): 1081.

Olsen, N. R. B. (2018). *A Three-Dimensional Numerical Model For Simulation Of Sediment Movements In Water Intakes With Multiblock Option. User's Manual*, Trondheim, Norway.

Olsen, N. R. B. and Hillebrand, G. (2018). Long-time 3D CFD modeling of sedimentation with dredging in a hydropower reservoir, *Journal of Soils and Sediments* **18**(9): 3031–3040.

Panagos, P., Ballabio, C., Himics, M., Scarpa, S., Matthews, F., Bogonos, M., Poesen, J. and Borrelli, P. (2021). Projections of soil loss by water erosion in Europe by 2050, *Environmental Science & Policy* **124**: 380–392.

Panagos, P., Borrelli, P., Meusburger, K., Alewell, C., Lugato, E. and Montanarella, L. (2015). Estimating the soil erosion cover-management factor at the European scale, *Land Use Policy* **48**: 38–50.

Panagos, P., Borrelli, P., Meusburger, K., van der Zanden, E. H., Poesen, J. and Alewell, C. (2015). Modelling the effect of support practices (P-factor) on the reduction of soil erosion by water at European scale, *Environmental Science & Policy* **51**: 23–34.

Paola, C. and Voller, V. R. (2005). A generalized Exner equation for sediment mass balance, *Journal of Geophysical Research: Earth Surface* **110**(F4).

Patro, E. R., De Michele, C., Granata, G. and Biagini, C. (2022). Assessment of current reservoir sedimentation rate and storage capacity loss: An Italian overview, *Journal of Environmental Management* **320**: 115826.

Paul, M. and Negahban-Azar, M. (2018). Sensitivity and uncertainty analysis for streamflow prediction using multiple optimization algorithms and objective functions: San Joaquin Watershed, California, *Modeling Earth Systems and Environment* **4**(4): 1509–1525.

Pesci, M. H., Mouris, K., Haun, S. and Förster, K. (2023). Assessment of uncertainties in a complex modeling chain for predicting reservoir sedimentation under changing climate, *Modeling Earth Systems and Environment* .

Pierson, T. C. (2005). Hyperconcentrated flow - transitional process between water flow and debris flow, *in* M. Jakob and O. Hungr (eds), *Debris-flow Hazards and Related phenomena*, Springer-Verlag, Berlin, Heidelberg, Germany, pp. 159–202.

Poesen, J. (1984). The influence of slope angle on infiltration rate and Hortonian overland flow, *Zeitschrift für Geomorpholgie* (49): 117 – 131.

Poesen, J., Nachtergaele, J., Verstraeten, G. and Valentin, C. (2003). Gully erosion and environmental change: importance and research needs, *Catena* **50**(2): 91–133.

Pradhan, S. P. and Siddique, T. (2019). Mass Wasting: An Overview, *in* S. Pradhan, V. Vishal and T. Singh (eds), *Landslides: Theory, Practice and Modelling*, Advances in Natural and Technological Hazards Research, Springer International Publishing, Cham, pp. 3–20.

Prudhomme, C. and Davies, H. (2009). Assessing uncertainties in climate change impact analyses on the river flow regimes in the UK. Part 1: baseline climate, *Climatic Change* **93**(1): 177–195.

Quinton, J. N., Govers, G., Van Oost, K. and Bardgett, R. D. (2010). The impact of agricultural soil erosion on biogeochemical cycling, *Nature Geoscience* **3**(5): 311–314.

Renard, K. G. (ed.) (1997). *Predicting soil erosion by water: a guide to conservation planning with the revised universal soil loss equation (RUSLE)*, number 703 in *Agriculture handbook*, Washington, D. C. OCLC: 36721564.

Renard, K. G., Foster, G. R., Weesies, G. A. and Porter, J. P. (1991). RUSLE: Revised universal soil loss equation, *Journal of Soil and Water Conservation* **46 (1)**: 30–33.

Renwick, W. H., Carlson, K. J. and Hayes-Bohanan, J. K. (2005). Trends in recent reservoir sedimentation rates in southwestern Ohio, *Journal of Soil and Water Conservation* **60**(2): 72–79.

Riahi, K., van Vuuren, D. P., Kriegler, E., Edmonds, J., O'Neill, B. C., Fujimori, S., Bauer, N., Calvin, K., Dellink, R., Fricko, O., Lutz, W., Popp, A., Cuaresma, J. C., Kc, S., Leimbach, M., Jiang, L., Kram, T., Rao, S., Emmerling, J., Ebi, K., Hasegawa, T., Havlik, P., Humpenöder, F., Da Silva, L. A., Smith, S., Stehfest, E., Bosetti, V., Eom, J., Gernaat, D., Masui, T., Rogelj, J., Strefler, J., Drouet, L., Krey, V., Luderer, G., Harmsen, M., Takahashi, K., Baumstark, L., Doelman, J. C., Kainuma, M., Klimont, Z., Marangoni, G., Lotze-Campen, H., Obersteiner, M., Tabeau, A. and Tavoni, M. (2017). The Shared Socioeconomic Pathways and their energy, land use, and greenhouse gas emissions implications: An overview, *Global Environmental Change* **42**: 153–168.

Roering, J. J., Kirchner, J. W. and Dietrich, W. E. (1999). Evidence for nonlinear, diffusive sediment transport on hillslopes and implications for landscape morphology, *Water Resources Research* **35**(3): 853–870.

Rouse, H. (1937). Modern Conceptions of the Mechanics of Fluid Turbulence, *Transactions of the American Society of Civil Engineers* **102**(1): 463–505.

Routschek, A., Schmidt, J. and Kreienkamp, F. (2014). Impact of climate change on soil erosion — A high-resolution projection on catchment scale until 2100 in Saxony/Germany, *Catena* **121**: 99–109.

Rüther, N. and Olsen, N. R. (2005). Three-dimensional modeling of sediment transport in a narrow 90 channel bend, *Journal of Hydraulic Engineering* **131**(10): 917–920.

Rulot, F., Dewals, B. J., Erpicum, S., Archambeau, P. and Pirotton, M. (2012). Long-Term Sediment Management for Sustainable Hydropower, *in* A. Sayigh (ed.), *Comprehensive Renewable Energy*, Elsevier, Oxford, pp. 355–376.

Ryżak, M., Bieganowski, A. and Polakowski, C. (2015). Effect of Soil Moisture Content on the Splash Phenomenon Reproducibility, *PLOS ONE* **10**(3): e0119269.

Sammut, C. and Webb, G. I. (2010). Leave-One-Out Cross-Validation, *in* C. Sammut and G. I. Webb (eds), *Encyclopedia of Machine Learning*, Springer US, Boston, MA, pp. 600–601.

Sangal, S., Singhal, M. K. and Saini, R. P. (2018). Hydro-abrasive erosion in hydro turbines: a review, *International Journal of Green Energy* **15**(4): 232–253.

Schleiss, A. J., Franca, M. J., Juez, C. and De Cesare, G. (2016). Reservoir sedimentation, *Journal of Hydraulic Research* **54**(6): 595–614.

Schmelter, M. L. and Stevens, D. K. (2013). Traditional and bayesian statistical models in fluvial sediment transport, *Journal of Hydraulic Engineering* **139**(3): 336–340.

Schulla, J. (1997). *Hydrologische Modellierung von Flussgebieten zur Abschätzung der Folgen von Klimaänderungen*, Doctoral Thesis, ETH Zurich.

Schulla, J. (2021). Model Description WaSiM, *Technical report*, Hydrology Software Consulting J. Schulla, Zürich, Switzerland.

Shi, W. and Qin, B. (2023). Sediment and Nutrient Trapping by River Dams: A Critical Review Based on 15-Year Big Data, *Current Pollution Reports* **9**(2): 165–173.

Shi, X., Zhang, F., Lu, X., Zhang, Y., Zheng, Y., Wang, G., Wang, L., Jagirani, M. D., Wang, T. and Piao, S. (2022). The response of the suspended sediment load of the headwaters of the Brahmaputra River to climate change: Quantitative attribution to the effects of hydrological, cryospheric and vegetation controls, *Global and Planetary Change* **210**: 103753.

Shields, A. (1936). *Anwendung der Ähnlichkeitsmechanik und der Turbulenzforschung auf die Geschiebebewegung*, Vol. 26, Preußische Versuchsanstalt für Wasserbau und Schiffbau, Berlin, Germany.

Shrestha, B., Babel, M. S., Maskey, S., van Griensven, A., Uhlenbrook, S., Green, A. and Akkharath, I. (2013). Impact of climate change on sediment yield in the Mekong River basin: a case study of the Nam Ou basin, Lao PDR, *Hydrology and Earth System Sciences* **17**(1): 1–20.

Simons, R. K., Canali, G. E., Anderson-Newton, G. and Cotton, G. K. (2000). Sediment Transport Modeling: Calibration, Verification, and Evaluation, *Journal of Soil Contamination* **9**(3): 261–289.

Sinha, R. K., Eldho, T. I. and Subimal, G. (2020). Assessing the impacts of land cover and climate on runoff and sediment yield of a river basin, *Hydrological Sciences Journal* **65**(12): 2097–2115.

Song, X., Zhan, C., Kong, F. and Xia, J. (2011). Advances in the study of uncertainty quantification of large-scale hydrological modeling system, *Journal of Geographical Sciences* **21**(5): 801.

Sotiri, K., Hilgert, S., Mannich, M., Bleninger, T. and Fuchs, S. (2021). Implementation of comparative detection approaches for the accurate assessment of sediment thickness and sediment volume in the Passaúna Reservoir, *Journal of Environmental Management* **287**: 112298.

Steffen, W., Sanderson, A., Tyson, P., Jäger, J., Matson, P., Moore, B., Oldfield, F., Richardson, K., Schellnhuber, H. J., Turner, B. L. and Wasson, R. J. (2005). *Global Change and the Earth System: A Planet Under Pressure*, Global Change — The IGBP Series, Springer, Berlin, Heidelberg, Germany.

Strand, R. I. and Pemberton, E. L. (1987). Reservoir Sedimentation, *Design of small dams*, U.S. Department of the Interior, Washington, D. C, USA.

Sun, C., Wan, T., Xie, X., Shen, X. and Liang, K. (2016). Knickpoint series of gullies along the Luoyunshan Piedmont and its relation with fault activity since late Pleistocene, *Geomorphology* **268**: 266–274.

Sun, J., Zhang, F., Zhang, X., Lin, B., Yang, Z., Yuan, B. and Falconer, R. A. (2021). Severely Declining Suspended Sediment Concentration in the Heavily Dammed Changjiang Fluvial System, *Water Resources Research* **57**(11): e2021WR030370.

Syvitski, J. P. M., Vörösmarty, C. J., Kettner, A. J. and Green, P. (2005). Impact of Humans on the Flux of Terrestrial Sediment to the Global Coastal Ocean, *Science* **308**(5720): 376–380.

Teng, H., Viscarra Rossel, R. A., Shi, Z., Behrens, T., Chappell, A. and Bui, E. (2016). Assimilating satellite imagery and visible–near infrared spectroscopy to model and map soil loss by water erosion in Australia, *Environmental Modelling & Software* **77**: 156–167.

Trenberth, K. E., Dai, A., van der Schrier, G., Jones, P. D., Barichivich, J., Briffa, K. R. and Sheffield, J. (2014). Global warming and changes in drought, *Nature Climate Change* **4**(1): 17–22.

Turowski, J. M., Rickenmann, D. and Dadson, S. J. (2010). The partitioning of the total sediment load of a river into suspended load and bedload: a review of empirical data: The partitioning of sediment load, *Sedimentology* **57**(4): 1126–1146.

UNESCO (2021). *The United Nations World Water Development Report 2021: Valuing Water*, United Nations, Paris, France.

Van Rijn, L. C. (1984a). Sediment Transport, Part I: Bed Load Transport, *Journal of Hydraulic Engineering* **110**(10): 1431–1456.

Van Rijn, L. C. (1984b). Sediment Transport, Part II: Suspended Load Transport, *Journal of Hydraulic Engineering* **110**(11): 1613–1641.

van Vuuren, D. P., Edmonds, J., Kainuma, M., Riahi, K., Thomson, A., Hibbard, K., Hurtt, G. C., Kram, T., Krey, V., Lamarque, J.-F., Masui, T., Meinshausen, M., Nakicenovic, N., Smith, S. J. and Rose, S. K. (2011). The representative concentration pathways: an overview, *Climatic Change* **109**(1): 5.

Vanmaercke, M., Poesen, J., Van Mele, B., Demuzere, M., Bruynseels, A., Golosov, V., Bezerra, J. F. R., Bolysov, S., Dvinskih, A., Frankl, A., Fuseina, Y., Guerra, A. J. T., Haregeweyn, N., Ionita, I., Makanzu Imwangana, F., Moeyersons, J., Moshe, I., Nazari Samani, A., Niacsu, L., Nyssen, J., Otsuki, Y., Radoane, M., Rysin, I., Ryzhov, Y. V. and Yermolaev, O. (2016). How fast do gully headcuts retreat?, *Earth-Science Reviews* **154**: 336–355.

Vanoni, V. A. (ed.) (1975). *Sediment engineering*, number 54 in *ASCE manuals and reports on engineering practice*, American Society of Civil Engineers, New York, NY, USA.

Verstraeten, G. and Poesen, J. (2002). Using sediment deposits in small ponds to quantify sediment yield from small catchments: possibilities and limitations, *Earth Surface Processes and Landforms* **27**(13): 1425–1439.

Walling, D. E. (1983). The sediment delivery problem, *Journal of Hydrology* **65**(1): 209–237.

Walling, D. E. and Webb, B. W. (1996). Erosion and sediment yield: a global overview, *Proceedings of the Exeter Symposium*, Vol. 236, IAHS, Exeter, UK, pp. 3 – 19.

Wan, Z. and Wang, Z. (1994). *Hyperconcentrated flow*, IAHR-AIRH monograph series, A. A. Balkema, Rotterdam Brookfield.

Wang, F. (2020). Impact of a large sub-tropical reservoir on the cycling of nutrients in a river, *Water Research* **186**: 116363.

Warrick, J. A., Stevens, A. W., Miller, I. M., Harrison, S. R., Ritchie, A. C. and Gelfenbaum, G. (2019). World's largest dam removal reverses coastal erosion, *Scientific Reports* **9**(1): 13968.

White, S. (2006). Sediment Yield Prediction and Modeling, *Encyclopedia of Hydrological Sciences*, John Wiley & Sons, Ltd, Hoboken, NJ, USA.

Wilson, C. G., Kuhnle, R. A., Bosch, D. D., Steiner, J. L., Starks, P. J., Tomer, M. D. and Wilson, G. V. (2008). Quantifying relative contributions from sediment sources in Conservation Effects Assessment Project watersheds, *Journal of Soil and Water Conservation* **63**(6): 523–532.

Winterwerp, J. C. and Kesteren, W. G. M. v. (2004). *Introduction to the physics of cohesive sediment in the marine environment*, number 56 in *Developments in sedimentology*, Elsevier, Amsterdam ; Boston.

Wischmeier, W. H. and Smith, D. D. (1965). Predicting rainfall-erosion losses from cropland east of the Rocky Mountains, *Agriculture Handbook* (282): 74.

Wischmeier, W. H. and Smith, D. D. (1978). *Predicting Rainfall Erosion Losses: A Guide to Conservation Planning*, Department of Agriculture, Science and Education Administration, Washington, D.C., USA.

World Bank and Maddison Project (2017). Our World In Data based on World Bank & Maddison. https://ourworldindata.org/grapher/world-gdp-over-the-last-two-millennia. Accessed 9 Nov 2023.

Yasarer, L. M. and Sturm, B. S. (2016). Potential impacts of climate change on reservoir services and management approaches, *Lake and Reservoir Management* **32**(1): 13–26.

Yin, S., Nearing, M. A., Borrelli, P. and Xue, X. (2017). Rainfall Erosivity: An Overview of Methodologies and Applications, *Vadose Zone Journal* **16**(12): vzj2017.06.0131.

Yoon, Y. (1992). The state and the perspective of the direct sediment removal methods from reservoirs, *International Journal of Sediment Research* **7**: 99–115.

Zanke, U. (1982). *Grundlagen der Sedimentbewegung*, Springer, Berlin, Heidelberg, Germany.

Zarfl, C., Lumsdon, A. E., Berlekamp, J., Tydecks, L. and Tockner, K. (2015). A global boom in hydropower dam construction, *Aquatic Sciences* **77**(1): 161–170.

Zhang, H., Wei, J., Yang, Q., Baartman, J. E., Gai, L., Yang, X., Li, S., Yu, J., Ritsema, C. J. and Geissen, V. (2017). An improved method for calculating slope length () and the LS parameters of the Revised Universal Soil Loss Equation for large watersheds, *Geoderma* **308**: 36–45.

Zhang, X., Fan, J., Liu, Q. and Xiong, D. (2018). The contribution of gully erosion to total sediment production in a small watershed in Southwest China, *Physical Geography* **39**(3): 246–263.

Zhang, X., Wu, S., Cao, W., Guan, J. and Wang, Z. (2015). Dependence of the sediment delivery ratio on scale and its fractal characteristics, *International Journal of Sediment Research* **30**(4): 338–343.

Zhao, G., Mu, X., Jiao, J., Gao, P., Sun, W., Li, E., Wei, Y. and Huang, J. (2018). Assessing response of sediment load variation to climate change and human activities with six different approaches, *Science of The Total Environment* **639**: 773–784.

Zhao, X., Gao, B., Xu, D., Gao, L. and Yin, S. (2017). Heavy metal pollution in sediments of the largest reservoir (Three Gorges Reservoir) in China: a review, *Environmental Science and Pollution Research* **24**(26): 20844–20858.

Publication I.

Introducing seasonal snow memory into the RUSLE

Table 5.1. Metadata of publication I

Title	Introducing seasonal snow memory into the RUSLE
Authors	**Kilian Mouris**, Sebastian Schwindt, Stefan Haun, Maria Fernanda Morales Oreamuno, Silke Wieprecht
Journal	Journal of Soils and Sediments
submitted	November 23, 2021
accepted	March 13, 2022
published	March 23, 2022 (online)
DOI	https://doi.org/10.1007/s11368-022-03192-1

Journal of Soils and Sediments (2022) 22:1609–1628
https://doi.org/10.1007/s11368-022-03192-1

SEDIMENTS, SEC 3 • HILLSLOPE AND RIVER BASIN SEDIMENT DYNAMICS • RESEARCH ARTICLE

Introducing seasonal snow memory into the RUSLE

Kilian Mouris[1] · Sebastian Schwindt[1] · Stefan Haun[1] · Maria Fernanda Morales Oreamuno[1] · Silke Wieprecht[1]

Received: 23 November 2021 / Accepted: 13 March 2022 / Published online: 23 March 2022

Abstract

Purpose The sediment supply to rivers, lakes, and reservoirs has a great influence on hydro-morphological processes. For instance, long-term predictions of bathymetric change for modeling climate change scenarios require an objective calculation procedure of sediment load as a function of catchment characteristics and hydro-climatic parameters. Thus, the overarching objective of this study is to develop viable and objective sediment load assessment methods in data-sparse regions.

Methods This study uses the Revised Universal Soil Loss Equation (RUSLE) and the SEdiment Delivery Distributed (SEDD) model to predict soil erosion and sediment transport in data-sparse catchments. The novel algorithmic methods build on free datasets, such as satellite and reanalysis data. Novelty stems from the usage of freely available datasets and the introduction of a seasonal snow memory into the RUSLE. In particular, the methods account for non-erosive snowfall, its accumulation over months as a function of temperature, and erosive snowmelt months after the snow fell.

Results Model accuracy parameters in the form of Pearson's *r* and Nash–Sutcliffe efficiency indicate that data interpolation with climate reanalysis and satellite imagery enables viable sediment load predictions in data-sparse regions. The accuracy of the model chain further improves when snow memory is added to the RUSLE. Non-erosivity of snowfall makes the most significant increase in model accuracy.

Conclusion The novel snow memory methods represent a major improvement for estimating suspended sediment loads with the empirical RUSLE. Thus, the influence of snow processes on soil erosion and sediment load should be considered in any analysis of mountainous catchments.

Keywords Soil erosion · RUSLE · Snow · Sediment load · Satellite imagery · Climate reanalysis

1 Introduction

Hydro-morphological processes in rivers, lakes, and reservoirs strongly depend on the sediment supply from the catchment area. Hence, information on sediment load is required as an upstream boundary condition for long-term predictions of bathymetric changes with deterministic hydro-morphodynamic numerical models (Haun et al. 2013; Mouris et al. 2018; Hanmaiahgari et al. 2018; Olsen and Hillebrand 2018). In addition, engineering interventions, such as implementing sustainable reservoir operations, require accurate predictions of sediment load, at sufficiently high temporal resolution. To this end, a model chain for assessing sediment dynamics typically starts with a parametric characterization of the catchment to estimate the sediment yield, defined as the amount of sediment load passing the outlet of the catchment. Yet, modeling soil erosion and sediment transport processes in the catchment area relies

Responsible editor: Paolo Porto

✉ Kilian Mouris
kilian.mouris@iws.uni-stuttgart.de

Sebastian Schwindt
sebastian.schwindt@iws.uni-stuttgart.de

Stefan Haun
stefan.haun@iws.uni-stuttgart.de

Maria Fernanda Morales Oreamuno
maria.morales@iws.uni-stuttgart.de

Silke Wieprecht
wieprecht@iws.uni-stuttgart.de

[1] Institute for Modeling Hydraulic and Environmental Systems, University of Stuttgart, Pfaffenwaldring 61, Stuttgart 70569, Germany

on subjective decision-making, which results in partially non-measurable uncertainty (Melsen et al. 2019). Thus, objectively calculated sediment loads are rarely available and the uncertainties of final outputs are often unknown (Song et al. 2011).

Soil erosion and sediment transport processes can be described by a variety of models that involve, for instance, conceptual, empirical, or physical-deterministic approaches (Benavidez et al. 2018). The choice of a suitable modeling approach depends on the spatio-temporal scales of input data, the quality of available data, and the target model output (Nearing 2013; Alewell et al. 2019). However, more complex process-based physical models do not necessarily reduce uncertainty compared to simple empirical models (Brazier 2013; de Vente et al. 2013; Alewell et al. 2019) because the quality or gaps of available measurement data play a superordinate role for large-scale applications (> 1 km^2) (Tan et al. 2018; Haun and Dietrich 2021; Borrelli et al. 2021). Thus, simple empirical soil erosion models are often preferred to complex models in areas with limited data availability (Efthimiou et al. 2017; Benavidez et al. 2018). A performance evaluation of different empirical soil erosion models in mountainous Mediterranean catchments showed that the Revised Universal Soil Loss Equation (RUSLE) (Renard et al. 1991; Renard 1997) yields the best results, in particular for investigating long-term trends (Efthimiou et al. 2017). This is why we adapted the RUSLE in this study along with the SEdiment Delivery Distributed (SEDD) model (Ferro and Porto 2000) to estimate the suspended sediment load in a region where data are only sparsely available. Still, the RUSLE involves sketchy empirical parameters and subjective decision-making. For instance, the RUSLE uses a rainfall-runoff factor that does not distinguish between precipitation in the form of rain or snow (Renard 1997; Alewell et al. 2019), which may lead to an overestimation of erosion during the event, as snowfall is not erosive. For this reason, recent studies ignore precipitation (i.e., consider it a non-erosive) that occurs at temperatures below 0 °C (Meusburger et al. 2012; Schmidt et al. 2016). The subsequent snowmelt, which can be highly erosive (Lana-Renault et al. 2011; Wu et al. 2018), however, is neglected in these approaches (Alewell et al. 2019), resulting in an underestimation of eroded sediments. Thus, Yin et al. (2017) propose that future research should focus on the effect of snowmelt on erosion. This study aims to close this gap by vetting approaches that neglect snow against novel techniques that consider the effects of snowfall and snowmelt on suspended sediment loads in a Mediterranean catchment. In addition, to overcome challenges related to subjective decision-making and snow-driven erosion processes in mountainous Mediterranean catchments, this study has the goal to establish an objective workflow for generating monthly suspended sediment loads. Another challenge in many regions of the world is a lack of measurement data on catchment characteristics and hydro-climatic processes, including precipitation. Thus, the superordinate research question in this study is as follows: How can viable and objective sediment loads from mountainous Mediterranean catchments and sparse data be generated? To answer this question, this study develops a series of algorithms, which constitute an objective workflow. The algorithms combine the RUSLE and the SEDD model to predict monthly suspended sediment loads coming from the Devoll catchment (Southeast Albania, Fig. 1) with mostly free data. The SEDD model estimates sediment transport and delivery, while the RUSLE calculates the spatial distribution of the gross soil erosion in the catchment. In particular, to leverage re-using the workflow in other data-sparse regions, the approach involves testing the relevance of free global datasets (e.g., satellite imagery and hydro-climatic parameters from reanalysis datasets). A core element of the methods is an algorithm that takes into account both the non-erosivity of snowfall and the erosivity of snowmelt by introducing a seasonal memory into the RUSLE. The results feature the output of the novel algorithmic workflow.

2 Materials and methods

The methods feature study site characteristics, challenges associated with data-sparse regions, and a comprehensive literature review on the RUSLE and the SEDD model. Thus, this section describes step by step the implementation of modular research products, related hypotheses, and the pathway to validate the hypotheses in a novel algorithmic workflow.

2.1 Study area

This study focuses on the upper catchment of the Banja Reservoir at the Devoll River in the Southeast of Albania (Fig. 1). The 1875 km^2 large catchment is surrounded by up to 2390 m a.s.l-high mountains, a highland plain in the Southeast where the Devoll River has its source, and the, in 2016, commissioned Banja Reservoir in the Northwest. Downstream of its source, in the Gramos Mountains near the Greek border, the Devoll River flows toward the Northwest, passing the Korçë plain, and falls into a narrow v-shaped canyon section. A monitoring station (close to the village of Kokel, red dot in Fig. 1) at the downstream end of the canyon section has been measuring sediment concentration and discharge instantaneously, but not consistently since March 2016. Downstream of the Kokel monitoring station, the Devoll River passes into a braided river section that leads into the Banja Reservoir.

Approximately 30% of the catchment area is forested, 25% is covered by scrubs and herbaceous vegetation, and

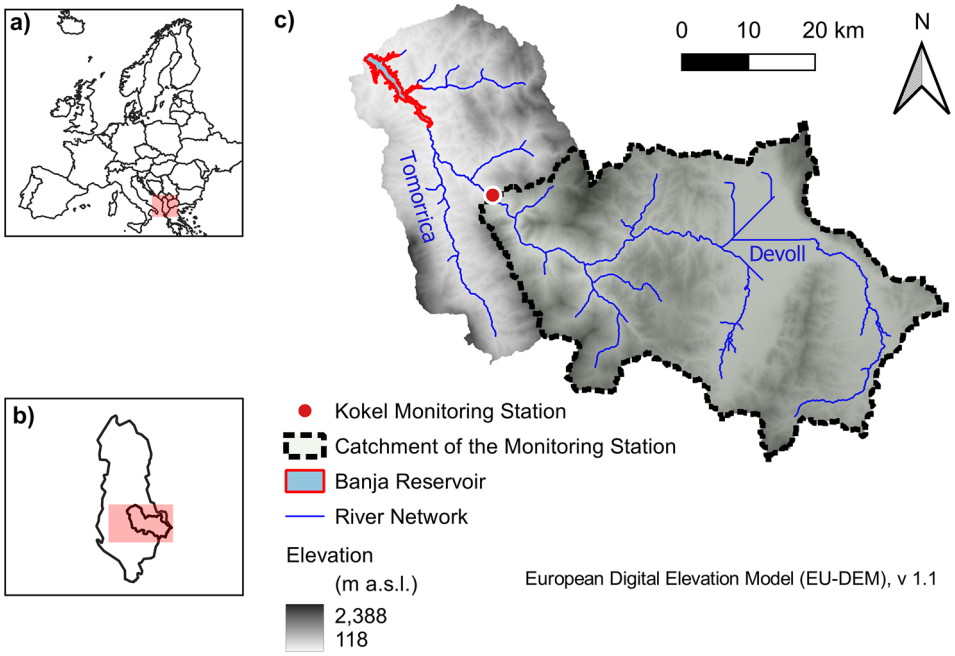

Fig. 1 Location of the study area. **a**) European context, **b**) national context, and **c**) the catchment of the Banja reservoir with indication of the Kokel monitoring station, the Devoll river network, the subcatchment of the monitoring station, and the Banja Reservoir in the Northwest (datasource: EU-DEM v1.1)

25% is used for agriculture (Copernicus Land Monitoring Service 2018). Other minor but non-negligible land cover types are pasture, natural grasslands, and sparse vegetation. The soils are mainly composed of Eutric Regosol (37%), Calcic Cambisol (30%), Calcaric Lithosol (12%), and Orthic Luvisol (11%) (Fischer et al. 2008; Hiederer 2013).

The catchment of the Banja reservoir is divided into two climatic zones (Kottek et al. 2006; Beck et al. 2018). The Eastern (upstream) part of the catchment, including the sub-catchment of the Kokel monitoring station, is characterized by a warm-summer Mediterranean climate (Csb according to the Köppen climate classification). The Western (downstream) part of the catchment is characterized by a hot-summer Mediterranean climate (Csa according to the Köppen climate classification). Both parts of the catchment typically experience dry and hot summers and humid winters, but the precipitation amounts decrease with increasing distance from the coast (i.e., moving in the Eastern direction). Thus, the Eastern part receives an average of 660 mm year^{-1}, while the Western part receives up to 1600 mm year^{-1} (Almestad 2015). In winter, snowfall is frequent in elevations higher than 1000 m a.s.l. Hence, the flow regime of the Devoll River and its tributaries are driven by precipitation, and also by snowfall and snowmelt.

As a part of geographical Mediterranean Europe, the Devoll catchment is an erosion hotspot (Walling and Webb 1996; Borrelli et al. 2017b, 2020), where high soil loss occurs because of a combination of high precipitation erosivity and steep topography.

2.2 Revised Universal Soil Loss Equation (RUSLE)

The RUSLE has been developed based on worldwide datasets and has already been applied on various spatial scales ranging from local case studies (e.g., Yang 2015; Koirala et al. 2019; Schmidt et al. 2019; Chuenchum et al. 2019) to continental (Panagos et al. 2015c; Teng et al. 2016) and global assessments (Yang et al. 2003; Borrelli et al. 2020). The RUSLE computes soil loss A (t ha^{-1} year^{-1}) as the product of six erosion risk factors:

$$A = R \cdot K \cdot C \cdot LS \cdot P \quad (1)$$

where R is a rainfall-runoff erosivity factor (MJ mm ha^{-1} h^{-1} year^{-1}), K is a soil erodibility factor (t h MJ^{-1} mm^{-1}), LS is a combined dimensionless topographic factor of slope length L (-) and steepness S (-), C is a cover and management factor (-), and P is a support practice factor (-).

The following sections briefly describe the factors and hypotheses made in this study to yield a possibly objective sediment load calculation.

2.2.1 Rainfall-runoff erosivity factor R

The rainfall-runoff erosivity factor (R factor) estimates the erosive forces of precipitation and the resulting surface runoff. The R factor accounts for the combined effect of duration, strength, and intensity of every precipitation event. The rainfall erosivity of an event is the product of its kinetic energy and its maximum 30-min intensity (Brown and Foster

1987; Renard 1997). The original approach introduces the annual R factor as the sum of the rainfall erosivities during a defined period divided by the number of years. However, high temporal resolution (< 0.5 h) precipitation data are not available in many regions of the world, including the Devoll catchment. To overcome high-resolution data shortage, empirical regression equations have been developed to correlate the R factor with any available precipitation data resolution, such as daily, monthly, or annual totals. Such region-specific regression equations calculate the R factor with sufficient accuracy and have been successfully applied in various case studies (Arnoldus 1980; de Santos and de Azevedo 2001; Torri et al. 2006; Diodato and Bellocchi 2010; Diodato et al. 2013). The so-called rainfall erosivity model for complex terrains REM_{DB} (Diodato and Bellocchi 2007) is one of the most recent developments for calculating the R factor and is used in this study for the Devoll catchment. The choice was made because the REM_{DB} is the most suitable regarding the available data (temporal and spatial resolution) and it was developed to estimate the monthly erosivity factor (R_m) in the geographically closely located Italy, which shares similar topographic (range of elevations) and hydro-climatic conditions with Albania (Beck et al. 2018). In addition to the monthly precipitation p_m (mm month^{-1}), the approach considers the elevation, latitude, and seasonal characteristics of precipitation (Diodato and Bellocchi 2007):

$$R_m = 0.207 \cdot \left[p_m \cdot (f(m) + f(E,L))\right]^{1.561} \quad (2)$$

where $f(m)$ is a monthly sinusoidal function and $f(E,L)$ is a parabolic function expressing the influence of site elevation E and the latitude L.

The erosive forces of runoff from snowmelt are typically not included in the R factor (Renard 1997), though their importance was recognized in the RUSLE's predecessor's R factor by estimating the snowmelt erosivity based on precipitation totals in winter months (Wischmeier and Smith 1978; McCool et al. 1982; Schwertmann et al. 1987; Banasik et al. 2021). Expanding on the insights from the past, this study tests a novel method to account for snowfall and snowmelt in the R factor. This method accounts for non-erosive snowfall and snowmelt that becomes erosive weeks to months after the precipitation event. The method calculates a monthly total R factor $R_{m,\text{total}}$ (MJ mm ha^{-1} h^{-1} month^{-1}) as the sum of the monthly $R_{m,\text{rain}}$ factor resulting from the erosive forces of rainfall and monthly $R_{m,\text{snowmelt}}$ factor resulting from the erosive forces of snowmelt.

$$R_{m,\text{total}} = R_{m,\text{rain}} + R_{m,\text{snowmelt}} \quad (3)$$

where $R_{m,\text{snowmelt}} = 2\frac{MJ}{ha \cdot h} \cdot SWE_{\text{snowmelt}}$ and SWE_{snowmelt} denote the snow water equivalent of the melted snow (mm month^{-1}). The amount of melted snow is derived from satellite-based snow cover detection and the analysis of temperature and precipitation data.

This study tests a novel method for calculating the snow-cover-dependent monthly R factor to improve the accuracy of predicted monthly sediment yield in mountainous Mediterranean regions.

2.2.2 Soil erodibility factor K

The soil erodibility factor (K factor) describes the susceptibility of soils to be mobilized by the impact of precipitation and surface runoff. In this study, the most used and cited equation to calculate soil erodibility from Wischmeier and Smith (1978) was applied. The equation calculates the soil erodibility as a function of organic matter content, soil structure, soil permeability, and soil texture (Wischmeier and Smith 1978). In addition, the erodibility of soils reduces in the presence of cobbles, which can be accounted for by a correction factor (Panagos et al. 2014). This study uses the correction for the K factor and derives soil parameters from the free soil information of the European Soil Database (Hiederer 2013) and the Harmonized World Soil Database (Fischer et al. 2008). The here-presented approach is suitable for data-sparse regions but does not account for seasonal changes and therefore, it should only be used when local data is not available. Further details are provided in the supplementary information SI 1.

2.2.3 Land cover and management factor C

The land cover and management factor (C factor) describes the ratio of long-term soil loss from vegetated areas and the soil loss from bare grounds (fallow land) with a defined gradient and length (Renard 1997). The C factor is a function of land cover and takes values between 0 and 1, where 1 corresponds to a reference condition of an area of clean-tilled fallow land. C factor values can be derived from land cover classes (Jain and Kothyari 2000; Märker et al. 2008; Vente et al. 2009; Borrelli et al. 2014) or satellite imagery (de Asis and Omasa 2007; Schönbrodt et al. 2010; Teng et al. 2016). This study combines both approaches by first defining a plausible range for the C factor for every land cover class and second, by calculating seasonal C factors for winter and summer months based on satellite imagery and using the normalized difference vegetation index (NDVI), as proposed by Gianinetto et al. (2019).

For non-arable land, this study calculates the C factor as a function of 20 different land cover classes (Copernicus Land Monitoring Service 2018), which stem from a summary of the most cited European studies (Panagos et al. 2015a). The land cover classes are derived from the satellite imagery-based CORINE Land Cover database (Copernicus Land Monitoring Service 2018). For arable land, we calculate the

C factor range as a function of cultivated crop types and tillage practices. Thus, the arable-land *C* factor is the weighted average of crop types and their share of a region unit, multiplied by a tillage factor (Panagos et al. 2015a). Satellite imagery serves to calculate seasonal *C* factors that account for seasonal dynamics of vegetated land cover classes (e.g., forests, grasslands, or croplands). The *C* factors of the land cover classes that are not influenced by seasonality (e.g., urban fabric) remain constant. Since satellite imagery and satellite-based land cover products are globally available, this approach is applicable worldwide. The implemented *C* factors and calculation details can be found in the supplementary information SI 2.

2.2.4 Slope length and steepness LS

The dimensionless factors slope length (*L* factor) and slope steepness (*S* factor) are typically combined into the *LS* factor that accounts for topographic landscape characteristics. The slope length *L* is defined as "the distance from the point of origin of the overland flow to the point where each slope gradient decreases enough for the beginning of deposition or when the flow comes to concentrate in a defined channel" (Wischmeier and Smith 1978). To account for flow accumulation from complex topographies, the slope length is substituted by the upslope drainage area per unit of contour length (Desmet and Govers 1996). The slope steepness *S* can be calculated with empirical equations as a function of the slope angle θ (Wischmeier and Smith 1978; McCool et al. 1987; Liu et al. 1994; Nearing 1997).

This study builds upon the latest development for calculating *LS* with a multi-flow direction algorithm as a function of slope, aspect, and downhill flow direction using the LS-Tool (Zhang et al. 2017). The herein-used approach considers both flow convergence based on the contributing surface and slope cutoff conditions according to Griffin et al. (1988).

2.2.5 Support practice factor P

The support practice factor (*P* factor) accounts for artificial soil stabilization measures (e.g., contouring, strip-cropping, or terrace farming) that reduce the erosion potential by altering surface runoff paths, patterns, and hydraulic forces (Wischmeier and Smith 1965; Renard et al. 1991; Panagos et al. 2015b).

In many studies, the *P* factor predominantly expresses the influence of contouring on soil erosion also for larger areas. Contouring (i.e., contour farming) is the practice of planting and tilling along contours that are perpendicular to the flow direction of the runoff. This practice decreases the runoff velocity and leaves more time for infiltration (Stevens et al. 2009). The effectiveness of this method depends on the slope and is applied exclusively to agricultural land (Haan et al. 1994; Morgan and Nearing 2010). Also, in this study, satellite imagery indicates that in the region of interest, farmers are contouring the landscape to reduce soil erosion. Thus, the *P* factor values are calculated as a function of the slope and the land cover class (SI Table 3).

2.3 SEdiment Delivery Distributed (SEDD) model

The RUSLE only assesses the spatial distribution of the gross soil loss A_i, and this is why an additional sediment routing is needed to estimate the sediment yield Y_b of a catchment. The sediment yield Y_b is defined as the sediment mass per unit time or sediment load that passes a defined boundary, such as the outlet of a (sub-)catchment (here, the Kokel monitoring station) or a hillslope (ASCE 1982; White 2006). In addition, the ratio between the sediment yield Y_b (t) and the gross soil erosion of the catchment A_b (t) represents the catchment's sediment delivery ratio SDR_b (-). Without this additional equation, the soil loss A_i calculated with the RUSLE cannot be applied to compute suspended sediment loads (e.g., for comparison with measured data). Hence, this study uses the Sediment Delivery Distributed (SEDD) model for calculating the net sediment delivery on a catchment scale, where the catchment's sediment yield Y_b is the sum of the sediment yield $Y_i(t)$ of morphological units (i.e., grid pixels) (Ferro and Porto 2000):

$$Y_b = SDR_b \cdot A_b = \sum_{i=1}^{n_u} Y_i = \sum_{i=1}^{n_u} SDR_i \cdot A_i \cdot SU_i \tag{4}$$

where SDR_i (-) is the pixel-wise sediment delivery ratio, A_i (t ha^{-1}) is the soil loss resulting from the RUSLE, SU_i (ha) denotes the area of a pixel i, and n_u is the total number of pixels where every pixel is considered a morphological unit that has length, steepness, and aspect attributes. The pixel-specific parameter SDR_i can be calculated as follows (Ferro and Minacapilli 1995):

$$SDR_i = \exp\left(-\beta \cdot t_i\right) \tag{5}$$

where t_i is the travel time along the flow path to the closest river channel and β is a catchment-specific parameter that depends on the time scale. Thus, the SDR_i represents "a measurement of the probability that the eroded particles from the entire upland area arrive into the nearest stream reach" (Ferro and Minacapilli 1995). Moreover, the travel time t_i is the sum of pixel-specific travel times along hydraulic pathways crossing n_p pixels (Jain and Kothyari 2000):

$$t_i = \sum_{i=1}^{N_p} \frac{l_i}{v_i} = \sum_{i=1}^{N_p} \frac{l_i}{\sqrt{s_i} \cdot d_i} \tag{6}$$

where l_i (m) is the length of a pixel i along the flow path and v_i is the pixel-specific flow velocity (m s^{-1}) that can be calculated by multiplying the square root of the slope s_i of a pixel and the surface roughness coefficient d_i, which is a function of land cover classes (Haan et al. 1994). A minimum pixel slope of $s_{i,min} = 0.3\%$ is required to ensure sediment routing.

This study implements the SEDD model to calculate monthly suspended sediment loads in the Devoll catchment with an algorithmic model chain. A model calibration is performed that involves the modification of the catchment-specific β parameter to fit the output of the SEDD model to measure suspended sediment data monitored at the Kokel monitoring station (Ferro and Porto 2000; Porto and Walling 2015).

2.4 Data

2.4.1 Available ground truth

To evaluate the soil loss and the resulting sediment yield from the catchment, the Kokel monitoring station (Fig. 1) continuously recorded discharge and suspended sediment concentrations between May 2016 and April 2018, when the water depth exceeded 1 m (387 of 730 days). Measurements were performed with two side-mounted H-ADCPs (horizontal-acoustic Doppler current profilers) and the mean and maximum concentrations (averaged over 1 h) in the observation period were 1 g L^{-1} and 11.6 g L^{-1}, respectively (Aleixo et al. 2020). Figure 2 plots the measured sediment concentrations against the discharge where no strong correlation is visible. For small discharge values, a large scattering can be seen, whereas for higher discharges, almost uniform suspended sediment concentrations were recorded. One reason for the large scatter in Fig. 2 can be the hysteresis effects of single events that cannot be reproduced in the absence of a time dimension (Aleixo et al. 2020). The highest discharges (above 150 $m^3 \cdot s^{-1}$) occurred during one single event in March 2018. In addition, the low concentration of suspended load might be attributed to snowmelt runoff subjected to pronounced dilution effects (Lana-Renault et al. 2011). Thus, commonly used sediment rating curves, such as a power-law function (e.g., Asselman 2000; Vercruysse et al. 2017), are not suitable for sediment load prediction.

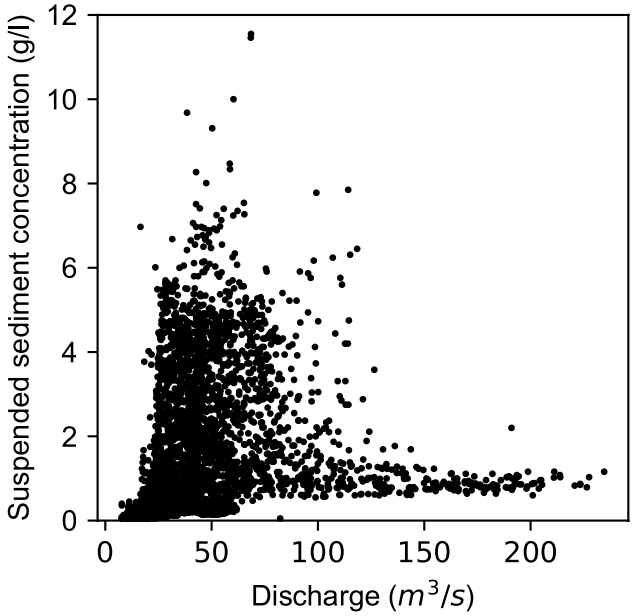

Fig. 2 Discharge versus suspended sediment concentration at the Kokel monitoring station, recorded for the time period from March 2016 to May 2018

2.4.2 Data sparsity and interpolation methods

Soil erosion and sediment transport processes are functions of complex parameter sets that result from hydro-climatic conditions, topography, land cover types, soil types, and erosion control practices. Such complex datasets are rarely available without gaps, and therefore, this study tests to what extent incomplete datasets can be filled with interpolation methods using free climate reanalysis datasets and satellite imagery.

The Kokel monitoring station provides suspended sediment load measurements during high and average flows only. Furthermore, single values are missing within the observed period due to a low signal-to-noise ratio (Aleixo et al. 2020). However, the model chain in this study requires seamless sediment load data for calibration. Hence, interpolation methods are applied for filling in temporal measurement gaps, and missing single values are linearly interpolated. Concentrations at water levels less than 1 m (below the measuring threshold) cannot be objectively calculated and used for calibration because higher sediment concentrations may occur even during low-flow periods, after single rainfall events.

Climate reanalysis datasets are an alternative to in situ measurements (ground truth) of precipitation or temperature (among other parameters). A climate reanalysis uses observations and weather forecasting models to produce a globally complete and consistent dataset of the past weather and climate. In this process, observations from satellites and ground-based radars are used along with in situ measurements, for example, from weather stations, aircraft, ships, or buoys (Hersbach et al. 2020). To estimate precipitation patterns, this study employs the ERA5 reanalysis dataset that provides atmospheric, land, and hydro-climatic data with a spatial resolution of 30–31 km and an hourly time resolution since 1950 (Hersbach et al. 2020). In addition, temperature reanalysis datasets serve for the differentiation of rainfall and snowfall. However, the original calculation of the rainfall-runoff

erosivity (R) factor builds on 30-min data (Brown and Foster 1987) and cannot be derived from reanalysis datasets. Thus, we correlate reanalysis precipitation data through an empirical regression with the R factor by applying Eq. (2) (Mouris et al. 2021d).

Satellite imagery involves spectral bands and enables the classification of land cover or vegetation on a catchment scale (e.g., Teng et al. 2016; Borrelli et al. 2017a; Gianinetto et al. 2019). For instance, the CORINE Land Cover for Europe (Copernicus Land Monitoring Service 2018), the Dynamic Land Cover Dataset for Australia (Thackway et al. 2013), or the worldwide Global Land Cover Characterization (Earth Resources Observation and Science Center 2017) provide classification data. Such satellite imagery also enables tracking seasonal and other time-dependent changes in land use or vegetation and generates digital elevation models (Mulder et al. 2011). Furthermore, snow-covered areas can be detected on satellite imagery where the spectral band ratio called Normalized Difference Snow Index (NDSI) enables to differentiate between cloud and snow cover, even though snow cannot be detected below clouds (Gafurov and Bárdossy 2009). The NDSI assumes that snow absorbs light in the ShortWave InfraRed region ($SWIR$, e.g., band 11 of Sentinel 2 satellite imagery) and reflects light in the visible wavelength region (e.g., the green band 3 of Sentinel 2 satellite imagery) whereas most cloud types reflect both infrared and visible wavelengths. Pixels with an NDSI larger than a threshold value (typically 0.4, published values range from 0.18 to 0.7) are considered a snow and the NDSI is calculated as follows (Riggs et al. 1994; Härer et al. 2018):

$$NDSI = \frac{(\text{Green} - SWIR)}{(\text{Green} + SWIR)} \tag{7}$$

This study involves testing for an optimum NDSI threshold to detect snow cover. Snow cover thickness in the form of snow water equivalent is calculated by summing up the pixel-specific snowfall based on reanalysis temperature and precipitation data.

2.4.3 Summary of available data

The input data used in this study involve data from the Kokel monitoring station, data from public and free databases, and satellite imagery. Table 1 lists all data types, their sources, and their purpose in this study.

2.5 Model chain for calculating sediment loads

Figure 3 shows a flowchart of the model chain used in this study where satellite imagery, precipitation, soil data, topographic data, and land cover information are mandatory input data (white boxes), while temperature data is only needed when applying the modified R factor from this study (gray box), which enables the detection of snowfall and snowmelt. In the case that observed suspended load measurements are available, those can be used for calibration by defining them as an optional argument in the workflow. The model chain starts with input rasters to calculate the spatial distribution of soil loss, suspended sediment load, and, optionally, bedload at monthly resolution using the RUSLE, the SEDD model, and interpolation methods to fill in data gaps. The following sections explain the workflow modules in detail.

2.5.1 Pre-processing

The fully automated core of the model chain (dashed box in Fig. 3) requires the alignment of input data in the form of pre-processing, which, in contrast, cannot be meaningfully automated because of varying data formats.

Table 1 Input data used for the model chain to compute soil loss and suspended sediment load

Input data	Source	Data type	Purpose in this study
Topography (digital elevation model)	EU-DEM v1.1	Georeferenced raster	*LS* factor, *P* factor, *R* factor, *SDR*
Precipitation and temperature	Post-processed ERA5 Reanalysis dataset	Georeferenced raster files	*R* factor
Soil data	ESDB v2.0 and HWSD v1.21	Database/georeferenced shapefiles	K factor
Land cover	CORINE Land Cover 2018	Georeferenced raster	*C* factor, *P* factor, *SDR*
Satellite imagery	Sentinel 2 – Copernicus Open Access Hub	Georeferenced raster for each satellite band	Snow cover detection (R factor), seasonal variability of vegetation (*C* factor)
Suspended sediment load	ADCP measurements (Aleixo et al. 2020)	Text files	Calibration at the Kokel monitoring station
Data on agricultural practice	Albanian Institute of Statistics	Database	Share of a crop in the arable land (*C* factor)

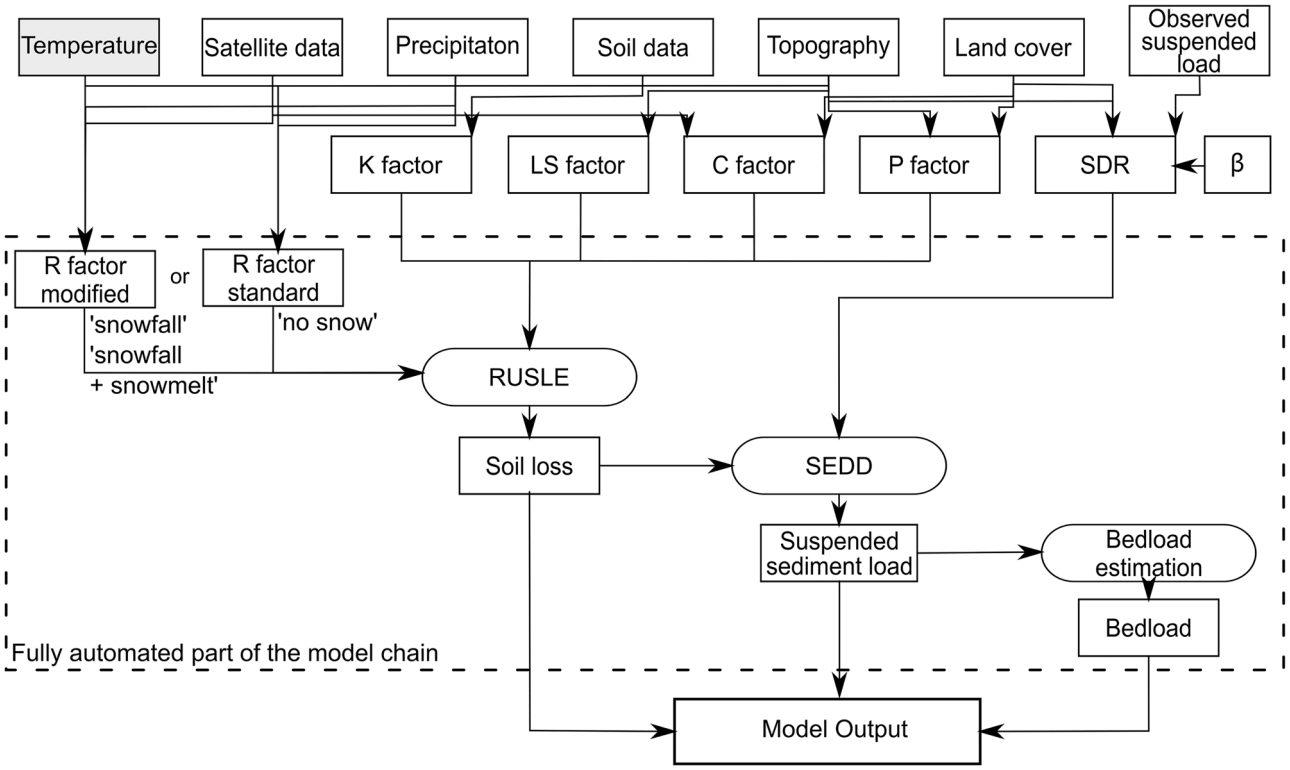

Fig. 3 Flowchart of the model chain for calculating soil loss and sediment loads. Input data in the upper part of the flowchart require user interaction while the tasks within the dashed box are fully automated in Python algorithms (Mouris et al. 2021b)

A digital elevation model (see Table 1) with sufficient spatial resolution (i.e., maximum pixel size of 50 m) describes the catchment topography and serves to identify the river network (SI 4). The Python algorithms (Mouris et al. 2021a) calculate the travel time from every raster pixel to the nearest channel reach by summing up pixel-specific travel times along the flow path (Eq. (6)). The pixel values for the C, LS, P, and K factors are assigned to the corresponding rasters as described in the section on the RUSLE. Every pixel represents a raster pixel and its size remains constant in the entire model chain, which is defined and achieved in the pre-processing along with coherent coordinate reference systems and no data values. The spatial interpolation of data pixels (e.g., to ensure equal raster resolutions) uses the nearest neighbor method for discrete (categorical) data, such as land cover classes or soil types. Inverse distance weighting with a combination of elevation-dependent regression and distance-based interpolation is applied for continuous data, such as precipitation or temperature.

2.5.2 Combination of RUSLE, SEDD, snowfall, and snowmelt recognition

The calculation of the sediment load at the outlet of a (sub-) catchment (here, the Kokel monitoring station) is fully implemented in a ready-to-use Python code (Mouris et al. 2021b) that performs the tasks in the dashed box in Fig. 3. The sediment delivery ratio and the RUSLE factors K, LS, C, and P represent constant input parameters in the form of rasters. The R factor is calculated at monthly resolution and represents a variable input parameter that makes the workflow using either the standard REM_{DB} (Eq. (2)) or the modified approach that additionally considers snowfall and snowmelt (Eq. (3)). The snowfall and snowmelt options require additional climate reanalysis and satellite imagery, respectively, and the R factor is calculated as illustrated in Fig. 4 (Mouris et al. 2021c). In particular, the algorithm uses precipitation and temperature rasters with an hourly or daily (here daily) resolution to calculate the spatial distributions of monthly rainfall intensity and snow water equivalent (SWEmonth) of snow cover. For this purpose, a temperature threshold of 0 °C is used in this study to define when precipitation falls as snow.

To detect the size of snow-covered areas at the end of every month, the snow detection algorithm uses three spectral bands of Sentinel-2 imagery, notably blue (band 2), green (band 3), and the Short-Wave InfraRed band 11 (*SWIR*). The green and the *SWIR* bands are used to calculate the NDSI (Eq. (7)) to detect snow for every raster pixel, which takes a value of 1 when snow is present and 0 without

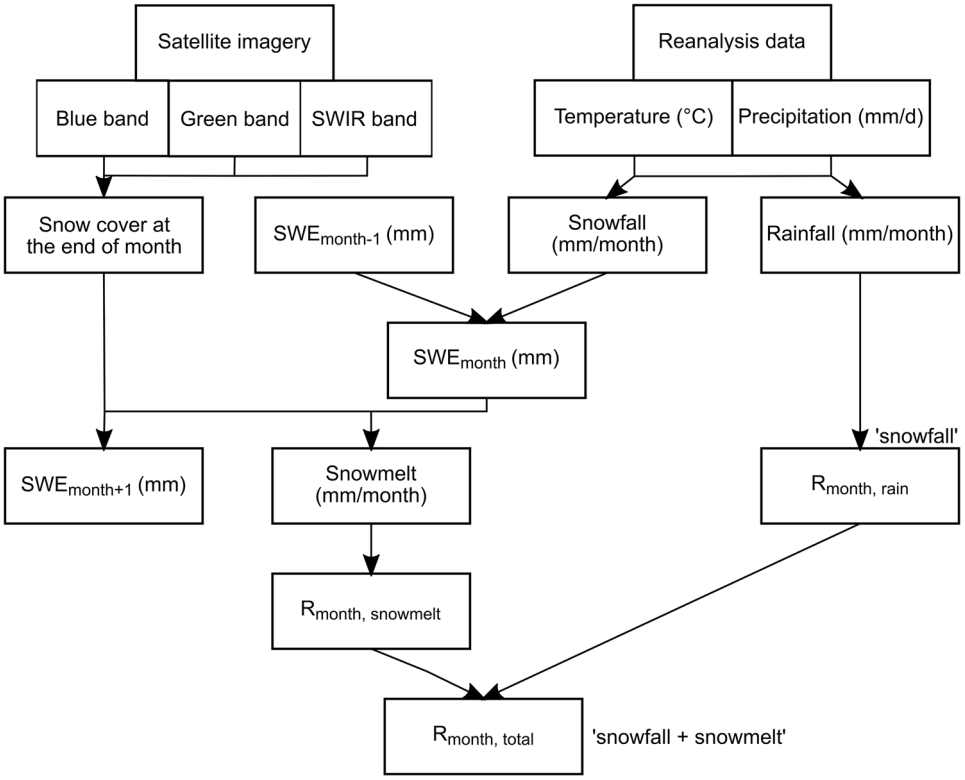

Fig. 4 Simplified flowchart of the modified R factor calculation, also accounting for snowfall and snowmelt

snow (binary value). In addition, a threshold value for the blue band is implemented to avoid false snow detection from water pixels (mainly turbid lakes and rivers). Subsequently, the snow cover rasters are multiplied by the SWE of the snow cover where unmelted snow did not have an erosive effect in the considered month. The SWE raster accumulates newly fallen snow. Snow-covered pixels that are no longer covered at the end of the considered month generate erosive snowmelt. Thus, the algorithm has a seasonal memory, which should not be applied for a single-month analysis only. Ultimately, the algorithm implemented in the Python code processes precipitation and optionally temperature raster files to calculate the resulting monthly R factor for every raster pixel. It outputs soil loss and sediment yield rasters with monthly resolution along with a table of monthly averages of soil loss, sediment yield, and suspended sediment load at the outlet of the catchment. In addition, the monthly bedload fraction can be optionally computed and written to the output table using an empirical equation that estimates bedload transport from suspended transport rates (Turowski et al. 2010). A comparison of the approaches without snow recognition ("no snow," where precipitation is considered erosive rain), with snow recognition only ("snowfall," where snowfall is considered non-erosive), and with combined snowfall-snowmelt ("snowfall + snowmelt," where snowfall is considered non-erosive, but snowmelt is considered erosive) consideration enables to quantify the importance and necessity of snow-related processes for sediment load prediction in this study. Thus, we test for the relevance of the consideration of snowfall and snowmelt in mountainous Mediterranean regions at a monthly resolution.

2.5.3 Calibration

The RUSLE parameters are calibrated in this study with respect to the effect of snowmelt in the R factor only, which is a core novelty in this study. All other parameters stem from the databases listed in Table 1. The calibration of satellite imagery band (NDSI and blue) thresholds for snow detection relies on expert assessment of true-color satellite imagery and overlays of snow cover delineation from the code and elevation contour lines. All pixels with values above the blue band threshold are considered snow-covered if also the NDSI is above the threshold value. In the calibration processes, the NDSI threshold is changed in 0.1-steps (i.e., increased and decreased by 0.1) starting from an initial threshold value of 0.4, which corresponds to the literature recommendation (Riggs et al. 1994). If the algorithm wrongly recognizes clouds or other pixels as snow, the NDSI threshold is increased by 0.1 and decreased if snow-covered pixels are not recognized. The additional blue band threshold is set to the highest blue band values of water pixels to avoid false snow detection, especially in turbid river stretches.

To obtain objective suspended sediment loads on a monthly resolution, the catchment-specific β parameter in the SEDD model is calibrated to measured suspended

sediment loads at the Kokel monitoring station for the observation period between May 2016 and April 2018. The calibration of the model chain varies the catchment-specific β parameter by coupling the soil erosion and sediment transport model with the parameter estimation software PEST (Doherty 2001). In this process, the weighted squares of the residuals between monthly computed and observed suspended sediment loads are minimized by using a Gauss-Levenberg–Marquardt algorithm in the model chain (Levenberg 1944; Marquardt 1963; Shoarinezhad et al. 2020). The β parameter requires recalibration for every model combination. Hence, the β parameter is calibrated in this study for the model chain without snow recognition, with snow recognition, and with combined snow recognition and additional snowmelt using the entire 10 months of observations embracing two wet seasons with inherently different hydro-climatic pattern. For comparison, we split the 10-month period additionally into two separate 5-month periods for calibration and validation, respectively. A complementary leave-one-out cross-validation is carried out to evaluate the model performance of the three different approaches to attempt an assessment of the consequences of limited data availability from two wet seasons only.

2.6 Synthesis of hypothesis testing

Testing the hypotheses starts with the calibration of the model chain (Fig. 3) to the catchment-specific β parameter for all scenarios ("no snow" without the recognition of snow, "snowfall" with snow recognition only, and "snowfall + snowmelt" with combined snowfall and snowmelt). When snowmelt recognition is activated in the model chain, an additional calibration of threshold values for snow cover detection on the satellite imagery is required with respect to the R factor (Fig. 4). After the calibration, the model chain runs the three snow scenarios to verify and refine hypotheses related to the superordinate research question of generating viable monthly suspended sediment loads from mountainous Mediterranean catchments with sparse data availability. In particular, the model chain results serve to verify the following hypotheses: (1) data interpolation with climate reanalysis and satellite imagery enables viable suspended sediment load predictions in data-sparse regions, (2) the accuracy of a model chain that relies on satellite and reanalysis data improves with the consideration of snowfall in the R factor, and (3) the accuracy of the model chain that relies on satellite and reanalysis data improves with the consideration of snowmelt in the R factor.

3 Results

Figure 5 shows the average monthly precipitation totals (post-processed reanalysis data) in the catchment, the observed monthly suspended sediment loads, and the computed monthly suspended sediment loads at the Kokel monitoring station for all three scenarios. The distribution of the observed monthly suspended sediment loads is heterogeneous and varies significantly with the monthly precipitation. Even though months without continuous data (water level < 1 m) were excluded and not used for calibration, the monthly observed loads cover a wide range from 25,800 t month^{-1} in June 2016 to 497,859 t month^{-1} in March 2018, whereas the average is 154,615 t month^{-1}. In addition, Fig. 6 compares the observed and computed

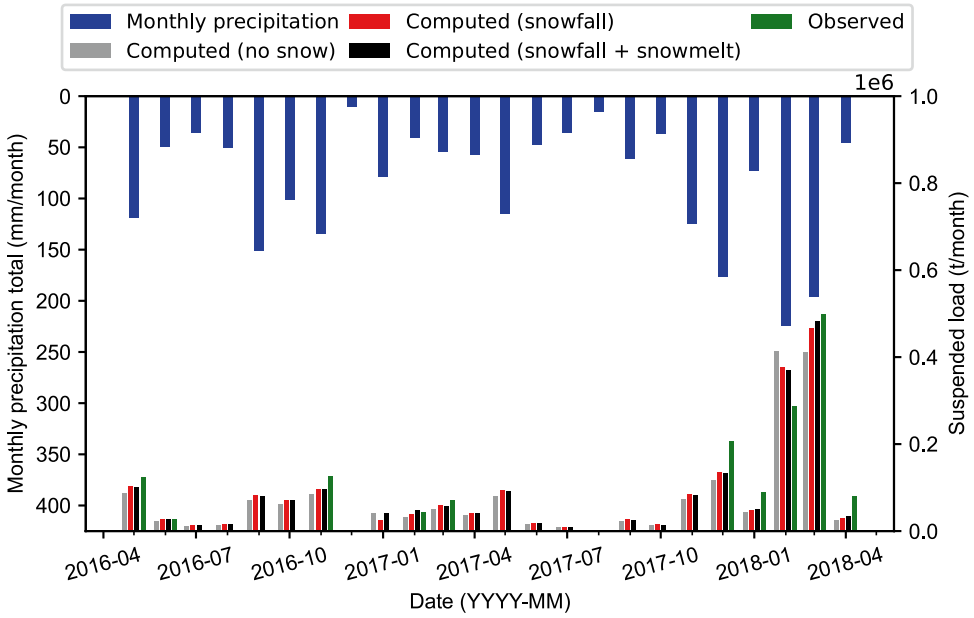

Fig. 5 Average monthly precipitation totals in the catchment, the observed monthly suspended sediment loads, and the computed monthly suspended sediment loads at the Kokel monitoring station for all three scenarios

monthly suspended sediment loads in the entire observation period (10 months) for all three scenarios, whereas the dashed line describes the hypothetic perfect model accuracy. A calibration with the split observation data (i.e., 5 months) yields similar predicted suspended loads that are 2% lower in average. The detailed results with the 5-months calibration are provided with the supplementary information (SI 5). The results of the leave-one-out cross-validation are presented in the SI 6. The following subsections describe the results and figures in detail and illustrate the differences between the scenarios. In the following, we will use the 10-month calibration procedure to avoid parameter overfitting regarding one particular season only.

3.1 Sediment load prediction without snowfall recognition

3.1.1 Calibration of the β parameter

Figure 7 plots the model accuracy in the form of Nash–Sutcliffe efficiency (NSE) as a function of the catchment-specific β parameter at monthly resolution. The figure shows that the most accurate result (NSE= 0.78) is yielded with a catchment-specific β parameter (Eq. (5)) of 0.85 where the monthly catchment's sediment delivery ratios SDR_b (Eq. (4)) range between 25 and 39%.

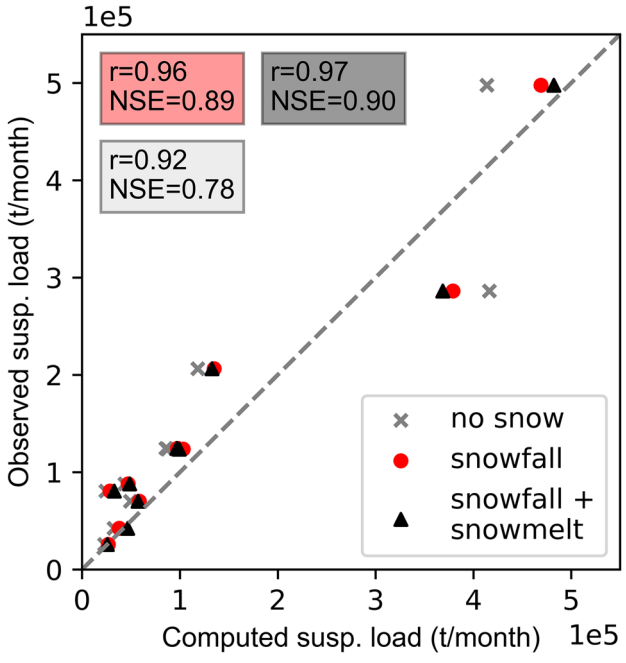

Fig. 6 Scatter plot of the observed and computed monthly sediment loads during the calibration period. The dashed line represents the hypothetic perfect model accuracy

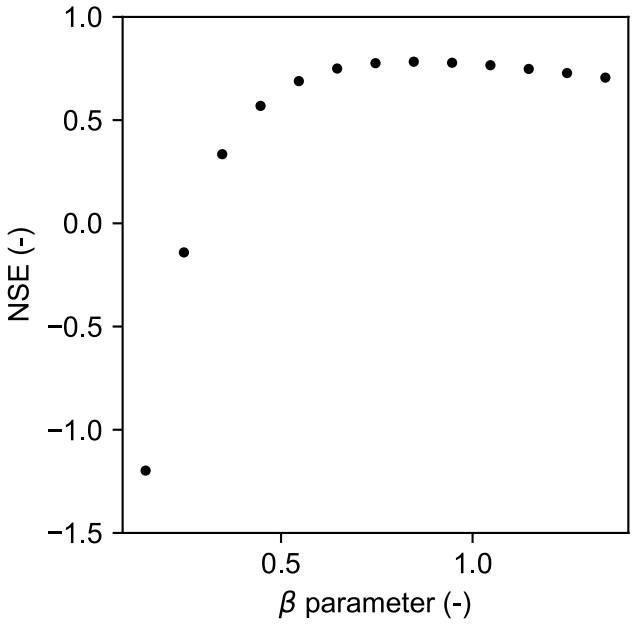

Fig. 7 Plot of Nash–Sutcliffe efficiency (NSE) against β parameter for the sediment load prediction without snow recognition

3.1.2 Sediment load prediction

Figure 5 shows the computed monthly suspended sediment loads without snow recognition ("no snow") in gray. The distribution of monthly computed suspended sediment loads is heterogeneous and varies to a large extent with monthly precipitation. The average computed monthly sediment load amounts to 71,900 t month^{-1}, and the sum of February and March 2018 represents 48% (823,000 t) of the total computed suspended sediment load in the 2-year observation period. Furthermore, because of the seasonal variability involved in the *C* factor and *R* factor for Mediterranean regions, the same amount of precipitation results in different suspended sediment loads depending on the month. For instance, precipitation in December is less erosive than precipitation in February and March and smaller sediment loads tend to be underestimated, whereas the absolute deviations are the largest in the 3 months with the highest loads (12/17, 02/18 and 03/18). The model predicts similar loads for February and March 2018, but the measurements indicate a difference of more than 200,000 t. Ultimately, Fig. 5 suggests that the model qualitatively reproduces observed sediment loads well, where the mean absolute error between computed and measured monthly loads is 51,190 t month^{-1}.

Figure 6 compares observed and computed monthly suspended sediment loads in the calibration period and indicates a larger deviation with increasing sediment loads. For instance, when the model predicts 4.1×10^5 t month^{-1}, the measurements vary between 2.9×10^5 t month^{-1} and 5.0×10^5 t month^{-1}, which stems from the aforementioned

seasonal effects. The overall model accuracy corresponds to a Pearson's correlation coefficient r of 0.92 and the Nash–Sutcliffe efficiency (NSE) is 0.78.

3.2 Sediment load prediction with snowfall recognition

3.2.1 Calibration of the β parameter

Since snowfall is not erosive, the β parameter requires a new calibration at a monthly resolution, which follows the approach underlying Fig. 7. The re-calibration results in an optimum catchment-specific β parameter of 0.58 for the model chain when snow recognition is implemented.

3.2.2 Sediment load prediction

Figure 5 shows the computed suspended load in the observation period using the modified R factor considering the non-erosivity of snowfall in red ("snowfall"). The most significant difference compared to the simulations without snow recognition ("no snow") is that the suspended sediment load is 36,300 t smaller in February 2018 and 55,000 t larger in March 2018. As a result, the significant errors in February 2018 (44%) and March 2018 (18%) reduce to 31% and 7%, respectively. The influence of snowfall recognition is less significant in the other months of the observation period, but the sediment load also decreases in other months with significant snowfall (January 2017 and February 2018). Moreover, the smaller β parameter causes the monthly catchments sediment delivery ratios SDR_b (Eq. (4)) to increase by an average of 9%, resulting in an increase in suspended sediment load during months without any snow influence. By considering snowfall, the overall mean absolute error reduces from 51,190 t month^{-1} to 35,090 t month^{-1}.

Figure 6 compares observed and computed monthly suspended sediment loads in the calibration period with the recognition of snowfall ("snowfall"), based on temperature reanalysis datasets. Compared to the simulations without snow recognition ("no snow"), the deviations are significantly lower. The improvements can mainly be attributed to the distinction between snow and rain in February 2018 and March 2018. The Pearson's correlation coefficient r increases to 0.96 and the Nash–Sutcliffe efficiency (NSE) increases to 0.89.

3.3 Sediment load prediction with snowfall and snowmelt recognition

3.3.1 Calibration of the R factor and NDSI threshold

Figure 8 shows an exemplary true-color satellite image (March 2018) that served for the expert assessment to identify the snow cover when calculating the R factor in the model chain (Fig. 4). The detected snow-covered areas are highlighted in green. The above-introduced expert verification (see chapter 2.5.3) of the snow cover algorithm with an overlay of elevation contour lines yields best results with an NDSI threshold of 0.4 in combination with a threshold of 1800 (top of atmosphere reflectance) for the blue band of Sentinel-2 satellite imagery.

3.3.2 Calibration of the β parameter

Since snowmelt is erosive (unlike snowfall), the β parameter again requires a new calibration at a monthly resolution, which follows the approach underlying Fig. 7. The re-calibration results in an optimum catchment-specific β parameter of 0.63 for the model chain when snow recognition and snowmelt are implemented.

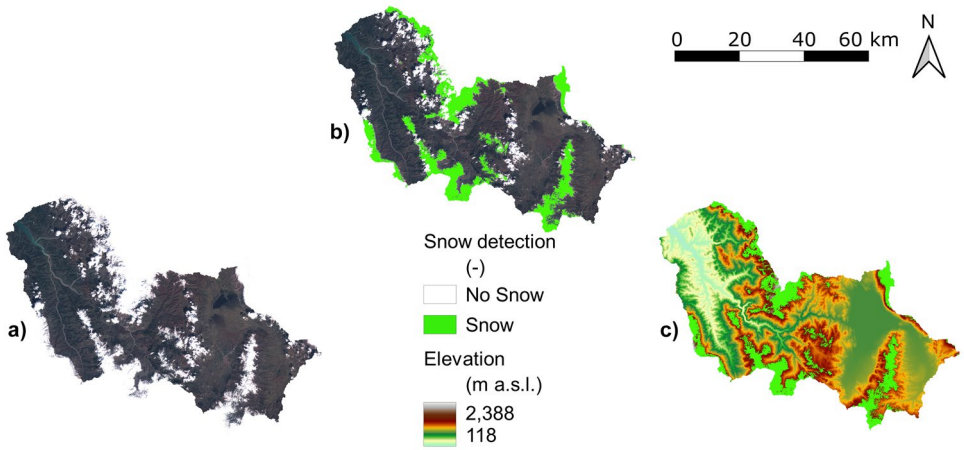

Fig. 8 True-color satellite image from March 2018 **a**) without and **b**) with detected snow cover in light green and **c**) topography with detected snow cover

3.3.3 Sediment load prediction

Figure 5 shows the computed suspended load in the observation period using the modified R factor for consideration of snowfall and snowmelt ("snowfall + snowmelt"). The most significant difference compared to the simulations without snow recognition ("no snow") is that the suspended sediment load is 44,100 t smaller in February 2018 and 72,000 t larger in March 2018 compared to the model without any snow recognition. As a result, the significant errors in February 2018 (44%) and March 2018 (18%) reduce to 29% and 3%, respectively, and compared with the model without any snow recognition. Compared to the case of snowfall consideration only ("snowfall"), the errors decrease by an additional 2% in February and 4% in March 2018. In April 2018, the error decreases by a further 6% because of significant snowmelt. The general trend indicates that the suspended sediment load decreases in the months with high snowfall (2017–01, 2018–02) and increases in the months with significant snowmelt (2017–02, 2018–03, and 2018–04). The β parameter causes the monthly catchment's sediment delivery ratios SDR_b (Eq. (4)) to increase by an average of 7% compared to the approach without snow recognition. This results in an increase in suspended sediment load during months without snow. By considering snow-related effects, the overall mean absolute error reduces from 51,190 t month^{-1} to 32,860 t month^{-1}.

Figure 6 compares observed and computed monthly suspended sediment loads in the calibration period with the combined consideration of snowfall and snowmelt. The accuracy further increases compared to the simulations without snow recognition ("no snow") and with snowfall recognition only ("snowfall"). The improvements can mainly be attributed to the time-shifted erosion in the spring seasons 2017 and 2018. Erosion attenuates in January 2017 and February 2018 because of the above-introduced snowfall and amplifies in the spring months February 2017, March 2018, and April 2018 because of additional runoff from snowmelt. The combined consideration of snowfall and snowmelt ultimately yields slightly higher accuracy compared to the snowfall-only case with a Pearson's correlation coefficient r of 0.97 and a Nash–Sutcliffe efficiency (NSE) of 0.90.

4 Discussion

4.1 Snow cover detection

The satellite imagery indicates that most of the precipitation in February 2018 fell in the form of snow, which was confirmed by an additional analysis of the temperature data. Figure 9 shows the percentage of snow coverage of the catchment area over the entire observation period with two peaks at the beginning of February 2017 and the beginning of March 2018. The significantly lower snow covers in the following months make that the model chain predicts higher erosion in February 2017 and the spring months of March 2018 and April 2018. In particular, the superpositioning of daily precipitation and temperature data results in 40% of the February 2018 precipitation as snowfall, leading to an average snow water equivalent of 60 mm across the catchment. In contrast, only 7% of the March 2018 precipitation was snowfall. Furthermore, the analysis of satellite imagery reveals that snow cover in the catchment reduced from over 80% to less than 20% from the beginning of March 2018 to the beginning of April 2018, indicating snowmelt processes. In February and March 2018, the largest deviation of the RUSLE approach without considering snow effects (e.g., 44% overestimation in February 2018, see Fig. 5) can be observed. The resulting erosion patterns are significantly different, in particular with regard to peak events. To ensure reliable results, any long-term analysis (e.g., of climate change scenarios) should not neglect snow-related effects. Although only a few months (December to March) of the hydrological year might be affected by snow and snowmelt in mountainous Mediterranean regions, this study shows that their consideration is essential.

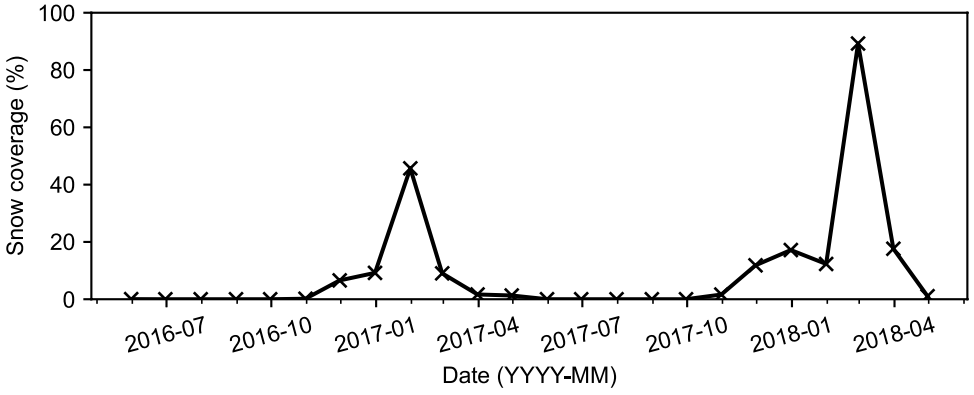

Fig. 9 Percentage of snow cover of the catchment area between 05/2016 and 04/2018 using the satellite-imagery-based snow detection algorithm

4.2 Improvement of the RUSLE

The original approach for calculating the *R* factor (Brown and Foster 1987; Renard 1997) in the RUSLE requires precipitation data with at least a 30-min resolution at every grid pixel. However, such data are not available in many regions of the world and the spatio-temporal resolution of reanalysis and climate forecast data underestimate the intensity of locally heavy rainfall events because of scale effects resulting from coarse spatial resolution (Chen and Knutson 2008). Without adjusting the *R* factor, every precipitation event (rain and snow) is considered to be erosive. Hence, the predicted suspended sediment transport is significantly overestimated in February 2018 since snowfall is not taken into account. The 74% higher suspended sediment load in March 2018 (compared to February 2018) cannot be modeled without considering snow in the *R* factor, because the precipitation (rain and snow) in March was 10% lower than in February 2018. This known limitation of the RUSLE has already been identified in previous studies (Alewell et al. 2019). This study indicates that the results improve significantly when a temperature threshold is set to consider snowfall in the *R* factor where the NSE increased by 14% to 0.89.

Thus, the results confirm the existing recommendations to set a temperature threshold for snow detection (Meusburger et al. 2012; Schmidt et al. 2016) by comparing modeled and observed suspended sediment loads. The RUSLE also does not consider snowmelt (Yin et al. 2017; Alewell et al. 2019) and this study shows that implementing snowmelt in the RUSLE's *R* factor results in a further accuracy improvement (NSE increases to 0.90). In regions where snow plays a more important role or where the time shift between snowfall and snowmelt is larger, an even greater influence of the novel approach can be expected.

4.3 Sediment delivery ratio

This study shows that the average sediment delivery ratio SDR_b of the catchment is higher than indicated in the literature (Boyce 1975; Walling 1983). However, the RUSLE does not reproduce all types of erosion. Thus, an underestimation of erosion because of gully erosion, fluvial erosion, or mass movement is a possible explanation. Since the model is calibrated to measured suspended sediment load and not to soil loss in the catchment area, the erosion may be underestimated. To compensate for the underestimated erosion, the SDR_b increases. For example, Borrelli et al. (2014) found that rill and interrill erosion, which are included in the RUSLE, are not the dominant processes contributing to the sediment yield of a Mediterranean mountainous catchment in Italy. As a result, the RUSLE significantly underestimates the observed sediment yield.

To verify the consistency of soil erosion and sediment transport, the soil loss and sediment yield can be mapped to identify sediment source areas where absolute soil erosion rates should be considered rather the best available hypotheses than exact predictions (Borrelli et al. 2021). Figure 10 shows the annual soil loss and the annual specific sediment yield per hectare for the catchment area of the Kokel monitoring station for the observation period from May 2016 to

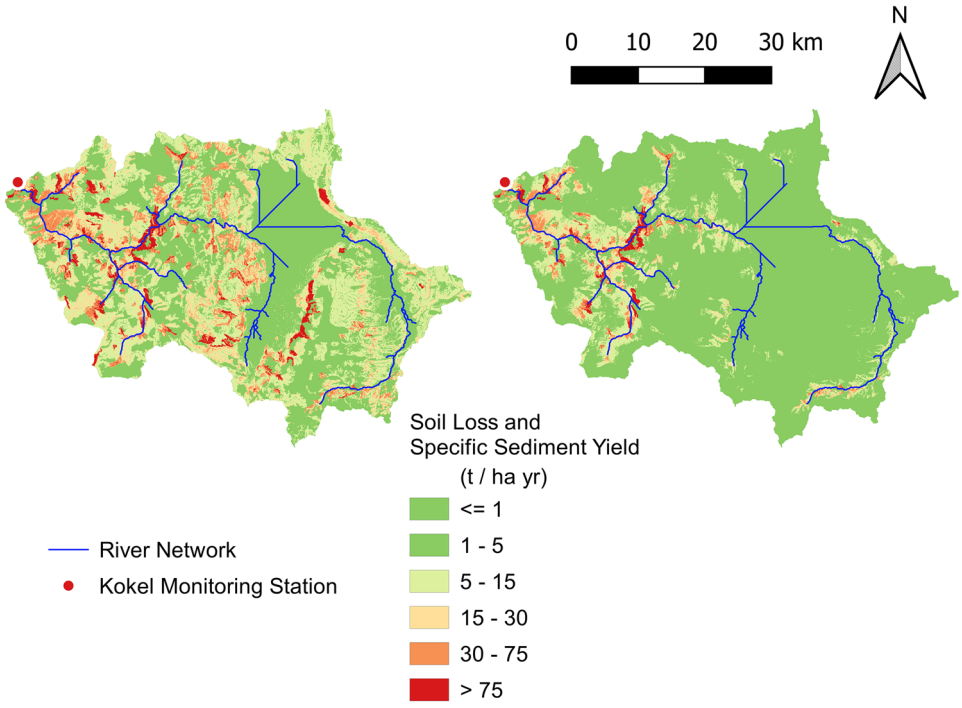

Fig. 10 Annual soil loss (left) and annual specific sediment yield (right) in the catchment area of the Kokel monitoring station for the observation period from May 2016 to April 2018

April 2018. In particular, the pixels with high slopes near the river network have both high soil erosion and high SDR_i s, which leads to a high sediment yield. Because these areas are close to the outlet of the catchment, a larger catchment area does not necessarily result in a reduction of the catchment's SDR_b. For instance, the mean annual soil loss in Italy is the highest in Europe (8.46 t ha^{-1}) and stems from a combination of high rainfall erosivity and steep topography (Panagos et al. 2015c). In comparison, the average annual soil loss in the Kokel catchment was 12.8 t ha^{-1} $year^{-1}$ in the observation period, whereas the highest values occurred at pixels with a steep slope and sparsely vegetated or agricultural areas. Remote areas with steep slopes close to the Korca plain (i.e., with a larger distance to the channel network) only have little effect on the catchment's sediment yield, even though the pixels show high local erosion rates (Fig. 10).

4.4 SEDD

The SEDD model does not account for erosion and deposition processes in the river network. The simplified assumption of an unlimited river transport capacity (i.e., all supplied suspended sediments in the river network are transported to the outlet of the catchment) is only valid for long-term observations. Thus, daily or event-based dynamics can solely be modeled in small catchments with an ephemeral channel network (Ferro and Porto 2000; Burguet et al. 2017). In addition, mass wasting and fluvial erosion are not considered in the presented approach, which opens the door for future research to better encompass the boundary conditions for numerical models of rivers and reservoirs with the required complexity.

The SEDD model may be replaced with alternative models when sub-monthly data and analysis are the focus of a study. These can be runoff-driven Modified Universal Soil Loss Equation (MUSLE) approaches, such as the Soil & Water Assessment Tool (SWAT) (Arnold et al. 2012; Prabhanjan et al. 2015), physics-based models, such as the Water Erosion Prediction Project (WEPP) model (Flanagan and Nearing 1995), or the improved Morgan approach (Tan et al. 2018). However, physics-based models require a larger amount of data than empirical models, which is rarely available at large temporal and spatial scales (Nearing 2013). For example, WEPP requires more than 100 parameters for the full application of a hillslope model (Brazier 2013). MUSLE-based approaches use storm-based runoff volumes and peak flows to simulate erosion and sediment yield. Whereas these approaches rely on calibrated hydrological models, the RUSLE only requires precipitation data to calculate erosive energy. Still, even with good data availability, SWAT does not always result in a reliable prediction of sediment load due to the high degree of complexity involved where, in particular, the high temporal resolution (daily data) is challenging (Prabhanjan et al. 2015).

4.5 Merits and challenges of free data

This study uses climate reanalysis and satellite data to calculate the R and C factors, which requires the availability of appropriate datasets for the region. This is the case almost everywhere in the world, by virtue of global reanalysis datasets and the availability of satellite imagery. Thus, climate reanalysis data enable the implementation of regression equations for determining the monthly and the annual rainfall-runoff erosivity factor R in the RUSLE for all climatic regions (Naipal et al. 2015; Benavidez et al. 2018). However, the quality or the suitability of available regression equations can significantly influence the quality of the results. For instance, the uncertainty of the R factor is considerable when the selected regression equation does not correctly reflect physics-driven trends in the data.

Even without snow recognition, the high NSE (0.78) demonstrates that the presented workflow is a viable method to calculate monthly suspended sediment loads by using free and accessible data when no precipitation data in high spatio-temporal resolution are available. The computed suspended sediment loads mainly depend on total precipitation, seasonal dynamics of vegetated land cover, and seasonal erosivity characteristics of rainfall, which is in line with theoretical expectations (Perks et al. 2015; Vercruysse et al. 2017). For instance, Ranzi et al. (2012) also simulated monthly sediment loads in the Lo watershed in Vietnam and obtained a lower NSE of 0.45 using directly measured precipitation.

4.6 Limitations of the model chain

The uneven distribution of the measurement data in this study additionally involves uncertainty concerning transport processes at low flow conditions. For instance, measurements in the dry summer months are scarce because the water depth rarely exceeded the measurement criterion of at least 1 m. Hence, the influence of intense but short rainfall events in the summer (e.g., thunderstorms) cannot be analyzed in this study. However, most erosion in Mediterranean catchments occurs during the wet season and the influence of low-flow periods is almost negligible (Rovira and Batalla 2006). More observations of snowfall may aid to confirm the validity of the modified approach of this study. For instance, Eq. (3) used to calculate $R_{m,\text{snowmelt}}$ requires additional data for accurate calibration and transferability to other studies.

The here-presented method accumulates snow over months and assumes that the snow cover thickness corresponds to the accumulated monthly snowfall since the last time that a pixel was not snow-covered. Snowmelt is only detected when a formerly snow-covered pixel is not

covered anymore in the month under consideration. Thus, snowmelt corresponds to the total accumulated amount of snow that has fallen before, but partial snowmelt (i.e., variation in snow cover thickness) cannot be detected. Although this approach yields good results in this study, it cannot be applied to regions permanently covered with snow where snow-driven runoff predominantly is a function of snow cover thickness variation. For permanently snow-covered regions, temperature-dependent snowmelt models (e.g., Hock 2003) are more suitable than the here shown approach.

4.7 Validity of hypotheses

The hypotheses made in this study can be partially verified and show that the presented model chain, based on free datasets, represents a viable approach.

The presented methods rely on empiric formulae that wrap complex processes into a simplified workflow. In a perfectly documented world, precise deterministic models would yield better results, but in the absence of omnipresent precise data, model uncertainty in simple empirical models is not larger than in deterministic models (Brazier 2013). Thus, the here-presented approach is a reasonable tradeoff between applicability and reliability of monthly sediment load predictions, where readily available climate reanalysis datasets serve as input data. Hence, the gridded climate reanalysis data can be considered suitable input data and may also be used to simulate historical scenarios and for long-term predictions of sediment load.

The expert-based refinement of threshold values for the NDSI and the blue band of Sentinel-2 satellite imagery contributes to a substantial increase in the overall accuracy of the model chain. In addition, the plot of monthly snow cover (Fig. 9) indicates that the used band thresholds provide reasonable estimates. Hence, it can be concluded that the proposed strategy for deriving snow cover by using thresholds for the NDSI and the blue band of Sentinel-2 satellite imagery represents a viable and reusable approach. Thus, the hypothesis that data interpolation with climate reanalysis and satellite imagery enables viable sediment load predictions in data-sparse regions is accepted.

Adding snowfall as a function of interpolated temperature yields an increase in Pearson's r between modeled and observed sediment loads at the Kokel monitoring station from 0.92 to 0.96 and the Nash–Sutcliffe efficiency (NSE) increases from 0.78 to 0.89. The increase in the accuracy of the model chain considering snowfall is most prominent comparing computed monthly suspended sediment loads with and without snowfall recognition (Fig. 5). The additional consideration of snowmelt results in a further increase in Pearson's r and NSE to 0.97 and 0.90, respectively. Figure 5 confirms that the trend of statistics corresponds to observations. Thus, the novel model chain represents a major improvement for mountainous Mediterranean catchments with sparse measurement data, which is also confirmed by the 5-month split model calibration and validation (SI 5) and leave-one-out cross-validation (SI 6). Ultimately, the improved overall model accuracy and the strong capacities of the model chain to account for snowfall and snowmelt make this novel approach that combines the RUSLE and the SEDD model, a viable method in mountainous Mediterranean regions. Thus, we accept the hypotheses that the accuracy of the model chain improves with the consideration of snowfall and snowmelt in the R factor.

4.8 Bedload

Beyond total sediment load, estimates of bedload are crucial for hydro-morphodynamic studies in fluvial systems. Yet, bedload is often ignored (Milliman and Syvitski 1991; Wright et al. 2010) or estimated as an overly simplified constant fraction of suspended load (Galy and France-Lanord 2001; Grams et al. 2013). This approach is not recommended because bedload can be a significant fraction of the total load and can vary relatively to suspended load because of changing suspension conditions (Ashley et al. 2020). Since none of the existing models for calculating the bedload fraction has been accepted yet as universally valid, an empirical equation is used to estimate bedload transport rates from suspended transport rates (Turowski et al. 2010). The algorithm in this study enables guesstimating bedload. However, this feature is not presented here because the validity of the bedload estimates cannot be evaluated in the absence of bedload measurement data. A more accurate estimate requires the consideration of hydro-morphodynamic processes in the river network and measurement data.

5 Conclusions

The good agreement between predicted and observed suspended sediment loads demonstrates that the combination of the RUSLE and the SEDD model is a viable approach to objectively estimate monthly sediment loads in data-scarce regions. The here-presented novel approach involves a model chain that requires one gauging station for calibration and most of the input data are interpolated from freely available satellite imagery and climate reanalysis data. To this end, Sentinel-2 satellite imagery and climate reanalysis precipitation data are relevant data sources.

Especially in mountainous Mediterranean regions, the implemented snowfall and snowmelt processes significantly increase the model accuracy, which can be clearly attributed to an improved reproduction of physical processes, enabling objective predictions with monthly resolution. The snow-related processes are incorporated in the rainfall-runoff

erosivity (R) factor of the RUSLE where temperature data informs about snowfall and satellite imagery enables the detection of snow cover and snowmelt.

Ultimately, the presented seasonal snow memory methods represent a major improvement in the prediction of soil erosion and sediment transport in mountainous Mediterranean catchments with limited measurement data availability. As a result, information on suspended sediment load is available at a resolution that enables the prediction of hydromorphological processes in rivers, lakes, and reservoirs. The approach may also be used in the future to investigate climate change scenarios. For this purpose, the historical climate reanalysis data are to be replaced by predicted data from climate projections.

Supplementary information The online version contains supplementary material available at https://doi.org/10.1007/s11368-022-03192-1.

Acknowledgements This study was carried out within the framework of the DIRT-X project, which is part of AXIS, an ERA-NET initiated by JPI Climate, and funded by FFG Austria, BMBF Germany, FORMAS Sweden, NWO NL, and RCN Norway with co-funding from the European Union (Grant No. 776608). The third author is indebted to the Baden-Württemberg Stiftung for the financial support by the Eliteprogramme for Postdocs. We thank two attentive Reviewers, the Editor, and the Associate Editor for their time and their critical and productive comments that helped us to significantly improve this study. We also thank Nils Rüther, Kristian Förster, and Maria Herminia Pesci for providing us with input data and fruitful discussions.

Author contribution KM: Methodology, conceptualization, writing-original draft, writing-review and editing, visualization, investigation, software, and formal analysis. SS: Writing-review and editing, software, conceptualization, and methodology. SH: Writing-review and editing, funding acquisition, and conceptualization. MFMO: Investigation and software. SW: Writing-review and editing, funding acquisition, project administration, and supervision.

Funding Open Access funding enabled and organized by Projekt DEAL.

Declarations

Conflict of interest The authors declare no competing interests.

References

Aleixo R, Guerrero M, Nones M, Ruther N (2020) Applying ADCPs for long-term monitoring of SSC in rivers. Water Resour Res 56: e2019WR026087. https://doi.org/10.1029/2019WR026087

Alewell C, Borrelli P, Meusburger K, Panagos P (2019) Using the USLE: chances, challenges and limitations of soil erosion modelling. Int Soil Water Conserv Res 7:203–225. https://doi.org/10.1016/j.iswcr.2019.05.004

Almestad C (2015) Modelling of water allocation and availability in Devoll River Basin, Albania. Master's Thesis, Norwegian University of Science and Technology

Arnold JG, Moriasi DN, Gassman PW et al (2012) SWAT: model use, calibration, and validation. Trans ASABE 55:1491–1508. https://doi.org/10.13031/2013.42256

Arnoldus HMJ (1980) An approximation of the rainfall factor in the Universal Soil Loss Equation. Assessment of Erosion 6:127–132

ASCE N (1982) Relationships between morphology of small streams and sediment yield. J Hydraulics Division 108:1328–1365. https://doi.org/10.1061/JYCEAJ.0005936

Ashley TC, McElroy B, Buscombe D et al (2020) Estimating bedload from suspended load and water discharge in sand bed rivers. Water Resour Res 56:e2019WR025883. https://doi.org/10.1029/2019WR025883

Asselman NEM (2000) Fitting and interpretation of sediment rating curves. J Hydrol 234:228–248. https://doi.org/10.1016/S0022-1694(00)00253-5

Banasik K, Hejduk L, Krajewski A, Wasilewicz M (2021) The intensity of siltation of a small reservoir in Poland and its relationship to environmental changes. CATENA 204 105436 https://doi.org/10.1016/j.catena.2021.105436

Beck HE, Zimmermann NE, McVicar TR et al (2018) Present and future Köppen-Geiger climate classification maps at 1-km resolution. Scientific Data 5, 180214 https://doi.org/10.1038/sdata.2018.214

Benavidez R, Jackson B, Maxwell D, Norton K (2018) A review of the (Revised) Universal Soil Loss Equation ((R)USLE): with a view to increasing its global applicability and improving soil loss estimates. Hydrol Earth Syst Sci 22:6059–6086. https://doi.org/10.5194/hess-22-6059-2018

Borrelli P, Alewell C, Alvarez P et al (2021) Soil erosion modelling: a global review and statistical analysis. Sci Total Environ 146494.https://doi.org/10.1016/j.scitotenv.2021.146494

Borrelli P, Märker M, Panagos P, Schütt B (2014) Modeling soil erosion and river sediment yield for an intermountain drainage basin of the Central Apennines, Italy. CATENA 114:45–58. https://doi.org/10.1016/j.catena.2013.10.007

Borrelli P, Panagos P, Märker M et al (2017a) Assessment of the impacts of clear-cutting on soil loss by water erosion in Italian forests: first comprehensive monitoring and modelling approach. CATENA 149:770–781. https://doi.org/10.1016/j.catena.2016.02.017

Borrelli P, Robinson DA, Fleischer LR et al (2017b) An assessment of the global impact of 21st century land use change on soil erosion. Nat Commun 8:2013. https://doi.org/10.1038/s41467-017-02142-7

Borrelli P, Robinson DA, Panagos P et al (2020) Land use and climate change impacts on global soil erosion by water (2015–2070). Proc Nat Acad Sci 117:21994–22001. https://doi.org/10.1073/pnas.2001403117

Boyce RC (1975) Sediment routing with sediment delivery ratios. Present and Prospective Technology for Predicting Sediment Yields and Sources US Dept Agric Publ 61–65

Brazier RE (2013) Erosion and sediment transport. Environmental Modelling: Finding Simplicity in Complexity, 2nd edn. Wiley-Blackwell, Chichester, pp 253–265

Brown LC, Foster GR (1987) Storm erosivity using idealized intensity d 180214istributions. Trans ASAE 379–386. https://doi.org/10.13031/2013.31957

Burguet M, Taguas EV, Gómez JA (2017) Exploring calibration strategies of the SEDD model in two olive orchard catchments. Geomorphology 290:17–28. https://doi.org/10.1016/j.geomorph.2017.03.034

Chen C-T, Knutson T (2008) On the verification and comparison of extreme rainfall indices from climate models. J Clim 21:1605–1621. https://doi.org/10.1175/2007JCLI1494.1

Chuenchum P, Xu M, Tang W (2019) Estimation of soil erosion and sediment yield in the Lancang-Mekong river using the Modified Revised Universal Soil Loss Equation and GIS techniques. Water 12:135. https://doi.org/10.3390/w12010135

Copernicus Land Monitoring Service (2018) Corine Land Cover 2018 Version 2020_20u1. European Environment Agency (EEA). https://land.copernicus.eu/pan-european/corine-land-cover/clc2018

de Asis AM, Omasa K (2007) Estimation of vegetation parameter for modeling soil erosion using linear Spectral Mixture Analysis of Landsat ETM data. ISPRS J Photogramm Remote Sens 62:309–324. https://doi.org/10.1016/j.isprsjprs.2007.05.013

de Santos LN, de Azevedo CM (2001) A new procedure to estimate the RUSLE EI30 index, based on monthly rainfall data and applied to the Algarve region, Portugal. J Hydrol 250:12–18. https://doi.org/10.1016/S0022-1694(01)00387-0

de Vente J, Poesen J, Verstraeten G et al (2013) Predicting soil erosion and sediment yield at regional scales: where do we stand? Earth-Sci Rev 127:16–29. https://doi.org/10.1016/j.earscirev.2013.08.014

de Vente J, Poesen J, Govers G, Boix-Fayos C (2009) The implications of data selection for regional erosion and sediment yield modelling. Earth Surf Process Landf 34:1994–2007. https://doi.org/10.1002/esp.1884

Desmet PJJ, Govers G (1996) A GIS procedure for automatically calculating the USLE LS factor on topographically complex landscape units. J Soil Water Conserv 51:427–433

Diodato N, Bellocchi G (2010) MedREM, a rainfall erosivity model for the Mediterranean region. J Hydrol 387:119–127. https://doi.org/10.1016/j.jhydrol.2010.04.003

Diodato N, Bellocchi G (2007) Estimating monthly (R)USLE climate input in a Mediterranean region using limited data. J Hydrol 345:224–236. https://doi.org/10.1016/j.jhydrol.2007.08.008

Diodato N, Knight J, Bellocchi G (2013) Reduced complexity model for assessing patterns of rainfall erosivity in Africa. Glob Planet Chang 100:183–193. https://doi.org/10.1016/j.gloplacha.2012.10.016

Doherty J (2001) PEST-ASP user's manual. Watermark Numerical Computing, Brisbane, Australia

Earth Resources Observation and Science Center (2017) Global Land Cover Characterization (GLCC). US Geological Survey. https://doi.org/10.5066/F7GB230D

Efthimiou N, Lykoudi E, Karavitis C (2017) Comparative analysis of sediment yield estimations using different empirical soil erosion models. Hydrol Sci J 62:2674–2694. https://doi.org/10.1080/02626667.2017.1404068

Ferro V, Minacapilli M (1995) Sediment delivery processes at basin scale. Hydrol Sci J 40:703–717. https://doi.org/10.1080/02626669509491460

Ferro V, Porto P (2000) Sediment Delivery Distributed (SEDD) model. J Hydrol Eng 5:411–422. https://doi.org/10.1061/(ASCE)1084-0699(2000)5:4(411)

Fischer G, Nachtergaele F, Prieler S et al (2008) The harmonized world soil database v 1.2. IIASA, Laxenburg, Austria and FAO, Rome, Italy. https://www.fao.org/soils-portal/data-hub/soil-maps-and-databases/harmonized-world-soil-database-v12/en/

Flanagan DC, Nearing MA (1995) USDA - water erosion prediction project: hillslope profile and watershed model documentation. Nserl Rep 10:1–123

Gafurov A, Bárdossy A (2009) Cloud removal methodology from MODIS snow cover product. Hydrol Earth Syst Sci 13:1361–1373. https://doi.org/10.5194/hess-13-1361-2009

Galy A, France-Lanord C (2001) Higher erosion rates in the Himalaya: geochemical constraints on riverine fluxes. Geology 29:23–26. https://doi.org/10.1130/0091-7613(2001)029<0023:HERITH>2.0.CO;2

Gianinetto M, Aiello M, Polinelli F et al (2019) D-RUSLE: a dynamic model to estimate potential soil erosion with satellite time series in the Italian Alps. Eur J Remote Sens 52:34–53. https://doi.org/10.1080/22797254.2019.1669491

Grams PE, Topping DJ, Schmidt JC et al (2013) Linking morphodynamic response with sediment mass balance on the Colorado River in Marble Canyon: issues of scale, geomorphic setting, and sampling design. J Geophys Res 118:361–381. https://doi.org/10.1002/jgrf.20050

Griffin ML, Beasley DB, Fletcher JJ, Foster GR (1988) Estimating soil loss on topographically non-uniform field and farm units. J Soil Water Conserv 43:326–331

Haan CT, Barfield BJ, Hayes JC (1994) Design hydrology and sedimentology for small catchments. Elsevier Science, San Diego, CA, USA

Hanmaiahgari PR, Gompa NR, Pal D, Pu JH (2018) Numerical modeling of the Sakuma Dam reservoir sedimentation. Nat Hazards 91:1075–1096. https://doi.org/10.1007/s11069-018-3168-4

Härer S, Bernhardt M, Siebers M, Schulz K (2018) On the need for a time- and location-dependent estimation of the NDSI threshold value for reducing existing uncertainties in snow cover maps at different scales. Cryosphere 12:1629–1642. https://doi.org/10.5194/tc-12-1629-2018

Haun S, Dietrich S (2021) Advanced methods to investigate hydromorphological processes in open-water environments. Earth Surf Process Landf 46:1655–1665. https://doi.org/10.1002/esp.5131

Haun S, Kjærås H, Løvfall S, Olsen NRB (2013) Three-dimensional measurements and numerical modelling of suspended sediments in a hydropower reservoir. J Hydrol 479:180–188. https://doi.org/10.1016/j.jhydrol.2012.11.060

Hersbach H, Bell B, Berrisford P et al (2020) The ERA5 global reanalysis. Q J R Meteorol Soc 146:1999–2049. https://doi.org/10.1002/qj.3803

Hiederer R (2013) Mapping soil properties for Europe: spatial representation of soil database attributes. European Commission. Joint Research Centre. Inst Environ Sustain LU

Hock R (2003) Temperature index melt modelling in mountain areas. J Hydrol 282:104–115. https://doi.org/10.1016/S0022-1694(03)00257-9

Jain MK, Kothyari UC (2000) Estimation of soil erosion and sediment yield using GIS. Hydrol Sci J 45:771–786. https://doi.org/10.1080/02626660009492376

Koirala P, Thakuri S, Joshi S, Chauhan R (2019) Estimation of soil erosion in Nepal using a RUSLE modeling and geospatial tool. Geosci 9:147. https://doi.org/10.3390/geosciences9040147

Kottek M, Grieser J, Beck C et al (2006) World Map of the Köppen-Geiger climate classification updated. Meteorol Zeitschrift 15:259–263. https://doi.org/10.1127/0941-2948/2006/0130

Lana-Renault N, Alvera B, García-Ruiz JM (2011) Runoff and sediment transport during the snowmelt period in a Mediterranean high-mountain catchment. Arct Antarct Alp Res 43:213–222. https://doi.org/10.1657/1938-4246-43.2.213

Levenberg K (1944) A method for the solution of certain non-linear problems in least squares. Q Appl Math 2:164–168. https://doi.org/10.1090/qam/10666

Liu BY, Nearing MA, Risse LM (1994) Slope gradient effects on soil loss for steep slopes. Trans ASAE 37:1835–1840. https://doi.org/10.13031/2013.28273

Märker M, Angeli L, Bottai L et al (2008) Assessment of land degradation susceptibility by scenario analysis: a case study in Southern Tuscany, Italy. Geomorphol 93:120–129. https://doi.org/10.1016/j.geomorph.2006.12.020

Marquardt DW (1963) An algorithm for least-squares estimation of nonlinear parameters. J Soc Indust Appl Math 11:431–441. https://doi.org/10.1137/0111030

McCool DK, Brown LC, Foster GR et al (1987) Revised slope steepness factor for the Universal Soil Loss Equation. Trans ASAE 30:1387–1396. https://doi.org/10.13031/2013.30576

McCool DK, Wischmeier WH, Johnson LC (1982) Adapting the Universal Soil Loss Equation to the Pacific Northwest. Trans ASAE 25:0928–0934. https://doi.org/10.13031/2013.33642

Melsen LA, Teuling AJ, Torfs PJJF et al (2019) Subjective modeling decisions can significantly impact the simulation of flood and drought events. J Hydrol 568:1093–1104. https://doi.org/10.1016/j.jhydrol.2018.11.046

Meusburger K, Steel A, Panagos P et al (2012) Spatial and temporal variability of rainfall erosivity factor for Switzerland. Hydrol Earth Syst Sci 16:167–177. https://doi.org/10.5194/hess-16-167-2012

Milliman J, Syvitski J (1991) Geomorphic tectonic control of sediment discharge to ocean – the importance of small mountainous rivers. J Geol 100:525–544. https://doi.org/10.1086/629606

Morgan RPC, Nearing MA (eds) (2010) Handbook of Erosion Modelling: Morgan/Handbook of Erosion Modelling. John Wiley & Sons, Ltd, Chichester, UK

Mouris K, Beckers F, Haun S (2018) Three-dimensional numerical modeling of hydraulics and morphodynamics of the Schwarzenbach reservoir. E3S Web of Conferences 40:03005. https://doi.org/10.1051/e3sconf/20184003005

Mouris K, Morales Oreamuno MF, Schwindt S (2021a) SEDD. Version 0.1.2. https://github.com/KMouris/SEDD

Mouris K, Morales Oreamuno MF, Schwindt S (2021b) Sediment_Load_Calculation. Version 0.1.3. https://github.com/KMouris/Sediment_Load_Calculation

Mouris K, Morales Oreamuno MF, Schwindt S (2021c) R_fac_snow. Version 0.1.3. https://github.com/KMouris/R_fac_snow

Mouris K, Schwindt S, Haun S et al (2021d) Climate reanalysis data with global coverage enable sediment load prediction in the absence of systematic field data. In: vEGU21: Gather Online. European Geosciences Union. https://doi.org/10.5194/egusphere-egu21-8432

Mulder VL, de Bruin S, Schaepman ME, Mayr TR (2011) The use of remote sensing in soil and terrain mapping — a review. Geoderma 162:1–19. https://doi.org/10.1016/j.geoderma.2010.12.018

Naipal V, Reick C, Pongratz J, Van Oost K (2015) Improving the global applicability of the RUSLE model - adjustment of the topographical and rainfall erosivity factors. Geosci Model Dev 8:2893–2913. https://doi.org/10.5194/gmd-8-2893-2015

Nearing MA (1997) A single, continuous function for slope steepness influence on soil loss. Soil Sci Soc Am J 61:917. https://doi.org/10.2136/sssaj1997.03615995006100030029x

Nearing MA (2013) Soil erosion and conservation. In: Environmental Modelling: Finding Simplicity in Complexity. Wiley-Blackwell, Chichester, West Sussex; Hoboken, NJ, pp 365–378

Olsen NRB, Hillebrand G (2018) Long-time 3D CFD modeling of sedimentation with dredging in a hydropower reservoir. J Soils Sediments 18:3031–3040. https://doi.org/10.1007/s11368-018-1989-0

Panagos P, Borrelli P, Meusburger K et al (2015a) Estimating the soil erosion cover-management factor at the European scale. Land Use Policy 48:38–50. https://doi.org/10.1016/j.landusepol.2015.05.021

Panagos P, Borrelli P, Meusburger K et al (2015b) Modelling the effect of support practices (P-factor) on the reduction of soil erosion by water at European scale. Environ Sci Policy 51:23–34. https://doi.org/10.1016/j.envsci.2015.03.012

Panagos P, Borrelli P, Poesen J et al (2015c) The new assessment of soil loss by water erosion in Europe. Environ Sci Policy 54:438–447. https://doi.org/10.1016/j.envsci.2015.08.012

Panagos P, Meusburger K, Ballabio C et al (2014) Soil erodibility in Europe: a high-resolution dataset based on LUCAS. Sci Total Environ 479–480:189–200. https://doi.org/10.1016/j.scitotenv.2014.02.010

Perks MT, OwenBenskin GJCMcWH et al (2015) Dominant mechanisms for the delivery of fine sediment and phosphorus to fluvial networks draining grassland dominated headwater catchments. Sci Total Environ 523:178–190. https://doi.org/10.1016/j.scitotenv.2015.03.008

Porto P, Walling DE (2015) Use of caesium-137 measurements and long-term records of sediment load to calibrate the sediment delivery component of the SEDD model and explore scale effect: examples from southern Italy. J Hydrol Eng 20:C4014005. https://doi.org/10.1061/(ASCE)HE.1943-5584.0001058

Prabhanjan A, Rao EP, Eldho TI (2015) Application of SWAT model and geospatial techniques for sediment-yield modeling in ungauged watersheds. J Hydrol Eng 20:C6014005. https://doi.org/10.1061/(ASCE)HE.1943-5584.0001123

Ranzi R, Le TH, Rulli MC (2012) A RUSLE approach to model suspended sediment load in the Lo river (Vietnam): effects of reservoirs and land use changes. J Hydrol 422–423:17–29. https://doi.org/10.1016/j.jhydrol.2011.12.009

Renard KG (ed) (1997) Predicting soil erosion by water: a guide to conservation planning with the Revised Universal Soil Loss Equation (RUSLE). D. C, Washington

Renard KG, Foster GR, Weesies GA, Porter JP (1991) RUSLE: Revised Universal Soil Loss Equation. J Soil Water Conserv 46(1):30–33

Riggs GA, Hall DK, Salomonson VV (1994) A snow index for the Landsat Thematic Mapper and Moderate Resolution Imaging Spectroradiometer. In: Proceedings of IGARSS '94 - 1994 IEEE Internatl Geosci Remote Sens Symp 4, 1942–1944

Rovira A, Batalla RJ (2006) Temporal distribution of suspended sediment transport in a Mediterranean basin: the lower Tordera (NE SPAIN). Geomorphology 79:58–71. https://doi.org/10.1016/j.geomorph.2005.09.016

Schmidt S, Alewell C, Meusburger K (2019) Monthly RUSLE soil erosion risk of Swiss grasslands. J Maps 15:247–256. https://doi.org/10.1080/17445647.2019.1585980

Schmidt S, Alewell C, Panagos P, Meusburger K (2016) Regionalization of monthly rainfall erosivity patterns in Switzerland. Hydrol Earth Syst Sci 20:4359–4373. https://doi.org/10.5194/hess-20-4359-2016

Schönbrodt S, Saumer P, Behrens T et al (2010) Assessing the USLE crop and management factor C for soil erosion modeling in a large mountainous watershed in Central China. J Earth Sci 21:835–845. https://doi.org/10.1007/s12583-010-0135-8

Schwertmann U, Vogl W, Kainz M (1987) Bodenerosion durch Wasser: Vorhersage des Abtrags und Bewertung von Gegenmaßnahmen. Ulmer, Stuttgart

Shoarinezhad V, Wieprecht S, Haun S (2020) Comparison of local and global optimization methods for calibration of a 3D

morphodynamic model of a curved channel. Water 12:1333. https://doi.org/10.3390/w12051333
Song X, Zhan C, Kong F, Xia J (2011) Advances in the study of uncertainty quantification of large-scale hydrological modeling system. J Geogr Sci 21:801. https://doi.org/10.1007/s11442-011-0881-2
Stevens CJ, Quinton JN, Bailey AP et al (2009) The effects of minimal tillage, contour cultivation and in-field vegetative barriers on soil erosion and phosphorus loss. Soil Tillage Res 106:145–151. https://doi.org/10.1016/j.still.2009.04.009
Tan Z, Leung LR, Li H-Y, Tesfa T (2018) Modeling sediment yield in land surface and earth system models: model comparison, development, and evaluation. J Adv Model Earth Syst 10:2192–2213. https://doi.org/10.1029/2017MS001270
Teng H, Viscarra Rossel RA, Shi Z et al (2016) Assimilating satellite imagery and visible–near infrared spectroscopy to model and map soil loss by water erosion in Australia. Environ Model Softw 77:156–167. https://doi.org/10.1016/j.envsoft.2015.11.024
Thackway R, Lymburner L, Guerschman J (2013) Dynamic land cover information: bridging the gap between remote sensing and natural resource management. Ecol Soc 18:2. https://doi.org/10.5751/ES-05229-180102
Torri D, Borselli L, Guzzetti F et al (2006) Italy. In: Soil Erosion in Europe. John Wiley & Sons, Ltd, Chichester, UK, pp 245–261
Turowski JM, Rickenmann D, Dadson SJ (2010) The partitioning of the total sediment load of a river into suspended load and bedload: a review of empirical data: the partitioning of sediment load. Sedimentology 57:1126–1146. https://doi.org/10.1111/j.1365-3091.2009.01140.x
Vercruysse K, Grabowski RC, Rickson RJ (2017) Suspended sediment transport dynamics in rivers: multi-scale drivers of temporal variation. Earth-Sci Rev 166:38–52. https://doi.org/10.1016/j.earscirev.2016.12.016
Walling DE (1983) The sediment delivery problem. J Hydrol 65:209–237. https://doi.org/10.1016/0022-1694(83)90217-2
Walling DE, Webb BW (1996) Erosion and sediment yield: a global overview. In: Erosion and Sediment Yield: Global and Regional Perspectives. IAHS Publ 236, pp 3–19
White S (2006) Sediment yield prediction and modeling. In: Encyclopedia of Hydrological Sciences. John Wiley & Sons, Ltd, Hoboken, NJ, USA
Wischmeier WH, Smith DD (1978) Predicting rainfall erosion losses: a guide to conservation planning. Department of Agriculture, Science and Education Administration
Wischmeier WH, Smith DD (1965) Predicting rainfall-erosion losses from cropland east of the Rocky Mountains. 74
Wright SA, Topping DJ, Rubin DM, Melis TS (2010) An approach for modeling sediment budgets in supply-limited rivers. Water Resour Res 46.https://doi.org/10.1029/2009WR008600
Wu Y, Ouyang W, Hao Z et al (2018) Snowmelt water drives higher soil erosion than rainfall water in a mid-high latitude upland watershed. J Hydrol 556:438–448. https://doi.org/10.1016/j.jhydrol.2017.11.037
Yang D, Kanae S, Oki T et al (2003) Global potential soil erosion with reference to land use and climate changes. Hydrol Process 17:2913–2928. https://doi.org/10.1002/hyp.1441
Yang X (2015) Digital mapping of RUSLE slope length and steepness factor across New South Wales. Australia Aust J Soil Res 53:216. https://doi.org/10.1071/SR14208
Yin S, Nearing MA, Borrelli P, Xue X (2017) Rainfall erosivity: an overview of methodologies and applications. Vadose Zone J 16:vzj2017.06.0131. https://doi.org/10.2136/vzj2017.06.0131
Zhang H, Wei J, Yang Q et al (2017) An improved method for calculating slope length (λ) and the LS parameters of the Revised Universal Soil Loss Equation for large watersheds. Geoderma 308:36–45. https://doi.org/10.1016/j.geoderma.2017.08.006

Publication II.

Stability criteria for Bayesian calibration of reservoir sedimentation models

Table 5.2. Metadata of publication II

Title	Stability criteria for Bayesian calibration of reservoir sedimentation models
Authors	**Kilian Mouris**, Eduardo Acuna Espinoza, Sebastian Schwindt, Farid Mohammadi, Stefan Haun, Sergey Oladyshkin, Silke Wieprecht
Journal	Modeling Earth Systems and Environment
submitted	November 16, 2022
accepted	January 18, 2023
published	February 3, 2023 (online)
DOI	https://doi.org/10.1007/s40808-023-01712-7

Modeling Earth Systems and Environment (2023) 9:3643–3661
https://doi.org/10.1007/s40808-023-01712-7

ORIGINAL ARTICLE

Stability criteria for Bayesian calibration of reservoir sedimentation models

Kilian Mouris[1] · Eduardo Acuna Espinoza[1,2] · Sebastian Schwindt[1] · Farid Mohammadi[1] · Stefan Haun[1] · Silke Wieprecht[1] · Sergey Oladyshkin[1]

Received: 16 November 2022 / Accepted: 18 January 2023 / Published online: 3 February 2023

Abstract
Modeling reservoir sedimentation is particularly challenging due to the simultaneous simulation of shallow shores, tributary deltas, and deep waters. The shallow upstream parts of reservoirs, where deltaic avulsion and erosion processes occur, compete with the validity of modeling assumptions used to simulate the deposition of fine sediments in deep waters. We investigate how complex numerical models can be calibrated to accurately predict reservoir sedimentation in the presence of competing model simplifications and identify the importance of calibration parameters for prioritization in measurement campaigns. This study applies Bayesian calibration, a supervised learning technique using surrogate-assisted Bayesian inversion with a Gaussian Process Emulator to calibrate a two-dimensional (2d) hydro-morphodynamic model for simulating sedimentation processes in a reservoir in Albania. Four calibration parameters were fitted to obtain the statistically best possible simulation of bed level changes between 2016 and 2019 through two differently constraining data scenarios. One scenario included measurements from the entire upstream half of the reservoir. Another scenario only included measurements in the geospatially valid range of the numerical model. Model accuracy parameters, Bayesian model evidence, and the variability of the four calibration parameters indicate that Bayesian calibration only converges toward physically meaningful parameter combinations when the calibration nodes are in the valid range of the numerical model. The Bayesian approach also allowed for a comparison of multiple parameters and found that the dry bulk density of the deposited sediments is the most important factor for calibration.

Keywords Bayesian calibration · Bayesian inference · Metamodel · Bayesian active learning · Calibration parameter importance · Reservoir sedimentation

Introduction

Artificial reservoirs are crucial infrastructure for providing drinking water, water for irrigation, flood protection, recreation, and hydroelectric power (Zarfl et al. 2015; Schleiss et al. 2016; Kim et al. 2020). However, reservoirs interrupt the longitudinal continuity of fluvial systems (Hinderer et al. 2013; Sun et al. 2021). For instance, low flow velocities lead to sediment deposition in reservoirs. The deposited sediment is missing in downstream reaches and reduces the active storage capacity of reservoirs (Kondolf 1997). To minimize sediment deposition and ensure sustainable reservoir operation, it is essential to quantify and accurately predict sedimentation processes. State-of-the-art tools for predicting reservoir sedimentation are two (2d) or three (3d) dimensional numerical models coupling hydrodynamics and sediment transport (Haun et al. 2013; Hanmaiahgari et al. 2018; Olsen and Hillebrand 2018; Khorrami and Banihashemi 2021).

Advances in numerical methods and computing power have led to remarkable improvements in the accuracy and speed of numerical models. Every numerical model requires calibration, which is a subjective and time-consuming process. Calibration is particularly important because the equations used in numerical models are based on simplified assumptions that are partly empirical. To calibrate a model, uncertain calibration parameters are adjusted within

✉ Kilian Mouris
kilian.mouris@iws.uni-stuttgart.de

[1] Institute for Modelling Hydraulic and Environmental Systems, University of Stuttgart, 70569 Stuttgart, Germany

[2] Institute of Water and River Basin Management – Hydrology, Karlsruhe Institute of Technology, 76131 Karlsruhe, Germany

a physically reasonable range to achieve a good agreement between modeled and measured data with appropriate tolerance (Simons et al. 2000; Oberkampf et al. 2004; Paul and Negahban-Azar 2018). A common approach to calibrating numerical models is the iterative trial-and-error adaption of calibration parameters. However, this method is time-consuming, labor-intensive, and subjectively biased because it does not account for uncertainty in measured data, modeling errors, nor equifinality (Schmelter and Stevens 2013; Muehleisen and Bergerson 2016; Beckers et al. 2020). While Bayesian inference, a type of stochastic calibration, can address some limitations, it requires many iterations and is therefore not practical for use with computationally intensive models (e.g., hydro-morphodynamic models to simulate reservoir sedimentation). Mohammadi et al. (2018), Beckers et al. (2020), and Scheurer et al. (2021) overcame this challenge using metamodels (also known as surrogate models, response surface, reduced model, etc.) to replicate the full complexity of a deterministic numerical model. These studies employed metamodel updating to reduce the total number of evaluations of the original model required to train the metamodel.

Modeling reservoir sedimentation requires specific simplifying assumptions regarding hydrodynamics and morphodynamics. In comparison to the simulation of rivers, fluctuating water levels and outflow conditions due to reservoir operation, and the simultaneous simulation of very shallow shores and tributary deltas along with deep waters are particularly challenging in reservoir modeling. For instance, wetting and drying of mesh nodes at the shoreline of a reservoir require model simplifications (e.g., the definition of a minimum water depth for a cell). In addition, channel erosion and deltaic avulsion might occur at the head of the reservoir. These erosion and avulsion processes and their exact location are hard to predict and result from stochastic environmental forcing (Hajek and Wolinsky 2012; Chadwick et al. 2019). Furthermore, these processes are still an open research topic (e.g., Langendoen et al. 2016) and difficult to simulate accurately, much less with the same model simplifications as the deposition of fine sediments in deeper waters. As a result of global model assumptions, some regions of a reservoir model may not be accurately represented by the numerical model. This is because the model is generally calibrated to accurately represent either fine sediment deposition in deep waters or delta progression and erosion processes at the head of the reservoir, but not both. *This is why we are investigating in this study how complex numerical models for reservoir sedimentation can be calibrated in light of competing model simplifications*. To this end, we test the hypothesis (i) that Bayesian calibration only converges toward physically meaningful calibration parameter combinations when the model is well-conditioned (i.e., measured data are in the validity domain of model assumptions). The verification of this hypothesis aims to enrich the scientific baseline for modeling complex hydro-morphodynamic processes in reservoirs, which inherently require modeling regions that may be physically invalid. To test this hypothesis, we adapt a Bayesian calibration technique that uses surrogate-assisted Bayesian inversion with a metamodel in the form of a Gaussian Process Emulator (GPE) according to Oladyshkin et al. (2020). The metamodel and its updating build on Bayesian active learning (BAL), which we further improve through the cumulative consideration of measurement and metamodel errors. To test hypothesis (i), we introduce two spatially distinct measurement data scenarios for calibrating a 2d hydro-morphodynamic reservoir sedimentation model of the large Banja reservoir in Albania.

Bayesian calibration typically starts with the definition of calibration parameters and the corresponding physically meaningful parameter ranges (e.g., Kim and Park 2016; Beckers et al. 2020). Based on initial model tests, we selected the four most sensitive parameters in the form of dry-bulk density of deposited sediments ρ_b, critical shear stress for erosion τ_{cr}, critical shear stress for deposition τ_d, and a diameter multiplier γ that defines the grain size distribution. The large number of four calibration parameters presents a challenge for any calibration process and results in a four-dimensional parameter space with millions of combination options, leading to problems regarding maximum floating-point precision. Hence, we implemented optimization strategies for Bayesian calibration intending to bypass precision errors (arithmetic underflow) caused by the multidimensional space of possible calibration parameter combinations. Furthermore, these parameters carry a high degree of uncertainty that must be thoroughly considered during modeling (Schmelter et al. 2015; Villaret et al. 2016). The grain size distribution, the two critical bed shear stresses for cohesive sediments, and the dry-bulk density can only be determined with great effort by field sampling. Therefore, it is important to identify and prioritize the most important parameters when planning field data collection. This insight enables the development of optimized measurement concepts, to reduce costs and workload. *Hence*, we *investigate whether our modified Bayesian calibration enables the identification of driving calibration parameters for modeling reservoir sedimentation even in a four-dimensional parameter space*. By examining the importance of four potentially important parameters driving reservoir sedimentation, we test the hypothesis (ii) that at least one of the four calibration parameters plays a dominant role in the fluvial deposition of suspended load in reservoirs. Therefore, we aim to identify the most important calibration parameter that should be addressed in sampling campaigns at reservoirs.

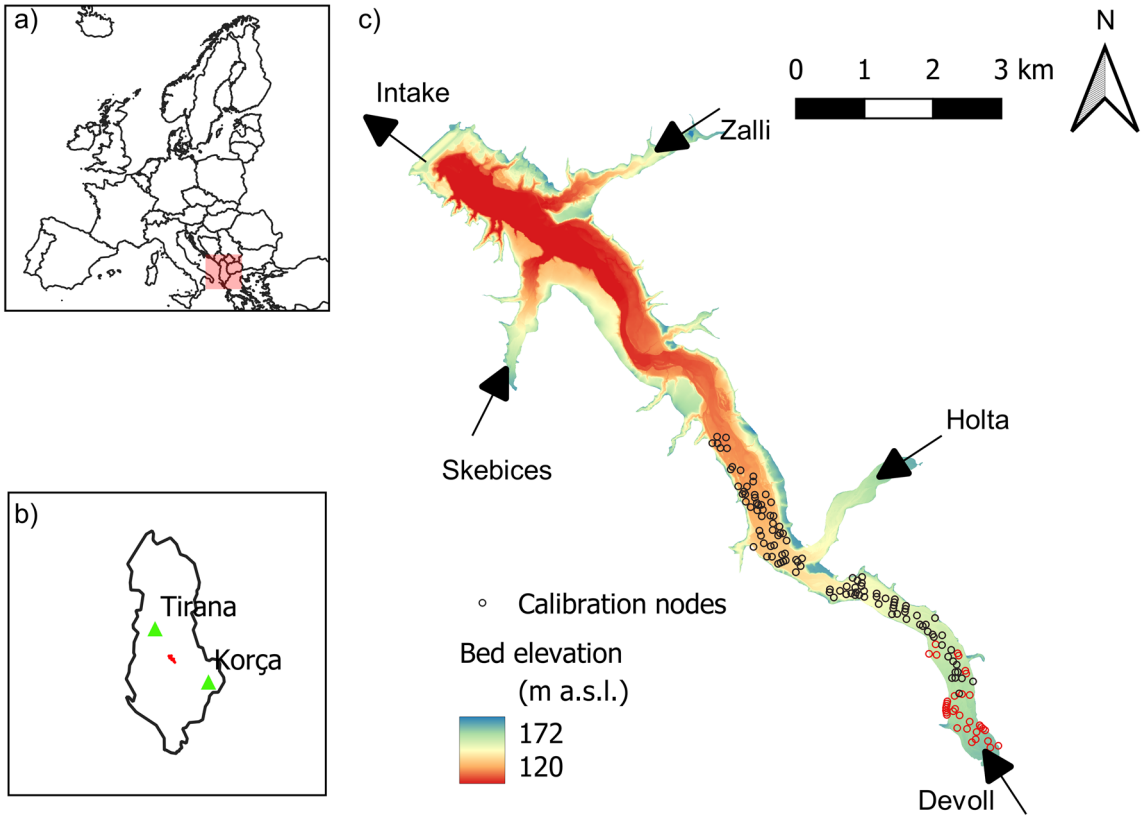

Fig. 1 Location of the study area; **a** European context, **b** national context, and **c** the bathymetry of the Banja reservoir with indication of the calibration nodes, major tributaries and turbine intake. The red calibration nodes are excluded in the VALDOME data scenario

Materials and methods

Study area

The Banja Reservoir

In this study, we numerically simulated hydro-morphodynamic processes in the Banja Reservoir at the Devoll River in central Albania. With a length of 196 km, the Devoll River is the third longest river in Albania and has its source in the Gramos Mountains near the Greek border. The river flows northwestward and is dammed after approximately 160 km, forming the Banja reservoir (see Fig. 1). The reservoir was commissioned in 2016 and has a length of 14 km, a maximum water depth of 60 m close to the dam, and a surface area of approximately 14 km², leading to a storage capacity of approximately 400 million m³. It is mainly fed by the Devoll River (89%, MQ ≈ 33 $m^3 s^{-1}$), Holta River (9%), and two smaller tributaries (Zalli and Skebices River, 1% each). The catchment of the reservoir is characterized by dry and hot summers and wet winters, resulting in low summer, high winter, and high spring flows. Since snowfall is frequent in winter at high elevations, the flow regime is driven by precipitation and snowmelt. The sediment yield of the Banja catchment is particularly high due to high rainfall erosivity on steep terrains composed of loose soils (Walling and Webb 1996; Borrelli et al. 2020; Mouris et al. 2022).

Measurement data

The initial bathymetry was interpolated onto a numerical mesh from a photogrammetry-based digital elevation model (DEM) from 2016, before filling the reservoir. In addition, the reservoir bathymetry was measured in 2019 with an acoustic Doppler current profiler (ADCP) boat providing approximately 632×10^3 bed level measurements.

The grain size distribution of the suspended sediment was determined based on suspended sediment measurements at the Devoll River upstream of the reservoir (Ardiclioglu et al. 2011) and reservoir bed samples. The per-sample median diameters of the deposited sediment ranged from 5.7 to 37.4 µm with a mean of 10.5 µm, emphasizing the cohesive nature of the deposits. Upstream of the reservoir, the extracted granulometric curve had cohesive characteristics, with 98% of the volume having grain diameters smaller than 60 µm. Neither cobble, gravel, nor coarse sand was present in the study area. Consequently, bedload was not considered

Table 1 Used input data for the Bayesian calibration of the Banja reservoir

Data set name	Survey method	Data type	Purpose in this study
Digital elevation model (2016)	Aerial survey	Georeferenced raster	Initial bathymetry
Measured bed levels (2019)	Bathymetric survey	Georeferenced shapefiles	Target (calibration) bathymetry
Water levels and outflow	Direct measurement	Text files	Liquid boundary conditions (numerical model)
Inflow discharge	Calculated based on water level and outflow	Text files	Liquid boundary conditions (numerical model)
Grain size distribution	Sediment samples (Ardiclioglu et al. 2011) and field survey in 2021	Text files	Used to define the range for the three grain size fractions
Suspended sediment concentration	Soil erosion and sediment transport model calibrated upstream of the reservoir (Mouris et al. 2022)	Text files	Boundary conditions for numerical model
Sediment samples (reservoir bed)	Measurement campaign	Text files	Verification of model assumptions

in the numerical model. The available measurement data for this study are summarized in Table 1.

Numerical full-complexity model

General setup

In this study, we used Telemac-2D (Hervouet 2007) with its sediment transport and bed evolution module GAIA (Audouin et al. 2020) to simulate reservoir sedimentation processes. Telemac-2D abstracts river landscapes with unstructured grids. The here-used unstructured, triangular numerical mesh consisted of 24,241 elements and 12,600 nodes, resulting in element sizes of approximately 40 m. We defined two roughness coefficients to differentiate between the original river course (before filling) and the newly wetted areas. Due to the low flow velocities, the influence of boundary roughness on reservoir hydrodynamics was small and we applied Manning coefficients of 0.032 s $m^{-1/3}$ (original cobble-gravel-bed river) and 0.06 s $m^{-1/3}$ elsewhere (many trees and brushes were not removed before the impoundment of the reservoir).

Telemac-2D approximates the shallow water equations with a combined explicit-implicit solver to calculate the flow field. The hydrodynamic module passes the calculated hydrodynamic variables (water depth, depth-averaged flow velocity) and bed shear stress to the GAIA module. We set the numerical model parameters with the premise of maximizing computational and numeric stability while keeping computing time short. Therefore, we applied a finite element numerical scheme and treated tidal flats (or dry-wet elements) according to software recommendations to use only positive water depths (Hervouet et al. 2011). Furthermore, the method of characteristic solves the advective part of the hydrodynamic equations and improves stability (a result of preliminary model tests). The mixing length turbulence model serves to calculate the turbulent viscosity coefficient, which is similar to the k-ε model when the transverse shear stress is the main turbulence generator, as in the case of a reservoir, but requires 20% less computing time (Dorfmann and Zenz 2016).

To calculate the depth-averaged concentration $C(x, y, t)$ of tracers (i.e., fine particles) in (g L^{-1}), the 2d advection-diffusion-equation is solved.

$$\frac{\partial(hC)}{\partial t} + \frac{\partial(huC)}{\partial x} + \frac{\partial(hvC)}{\partial y} = \frac{\partial}{\partial x}\left(h\epsilon\frac{\partial C}{\partial x}\right) + \frac{\partial}{\partial y}\left(h\epsilon\frac{\partial C}{\partial y}\right) + (E - D) \tag{1}$$

where h is the water depth (m), u (m s^{-1}) and v (m s^{-1}) are the depth-averaged components of flow velocity, ε is the turbulent diffusivity of the sediment (m^2 s^{-1}), and E and D are the erosion and deposition fluxes (kg m^{-2} s^{1}), respectively. We applied the default treatment of the diffusion term in Eq. (1) to increase numerical stability. In addition, we chose the "Edge-based N-Scheme" to solve the advective term because it provides mass conservative results and treats tidal flats. The erosion and deposition fluxes for cohesive sediment are calculated as follows:

$$D = \omega_s C\left(1 - \frac{\tau_b}{\tau_d}\right) if\, \tau_b > \tau_d \tag{2}$$

$$E = M\left(\frac{\tau_b}{\tau_{ce}} - 1\right) if\, \tau_b > \tau_{ce} \tag{3}$$

where M is the Krone-Partheniades erosion constant (kg m^{-2} s^{-1}), $\tau_b$is the bed shear stress (N m^{-2}), τ_{ce} is the critical shear stress for erosion (N m^{-2}), τ_d is the critical shear stress for deposition (N m^{-2}), and ω_s is the settling velocity (m s^{-1}). The settling velocity is a function of the mean sediment diameter, the ratio of the sediment and water densities, and the kinematic viscosity of the water. The measurement data (see above) had shown that the deposits predominantly

consisted of cohesive sediment, and therefore, only suspended transport was considered in this study.

After determining the erosion and deposition fluxes and calculating the net transport flux per element, GAIA updates the bed level using the Exner equation (Paola and Voller 2005). For a detailed description of the free surface flow and sediment modeling algorithms used, the reader is referred to Hervouet (2007, 2020) and Audouin and Tassi (2020). The steering file for the Telemac-2D simulations is available at Acuna Espinoza et al. (2022).

The focus of the numerical model was on the time-efficient simulation of suspended sediment transport in a large reservoir to ease repetitive calibration runs. Therefore, bedload was not considered and a coarse mesh resolution was used. Due to these simplifying assumptions, but also because of the general limitation of numerical models, it is not possible to accurately predict channel avulsion and erosion through previously deposited cohesive sediments (Hajek and Wolinsky 2012; Liang et al. 2015). Furthermore, channel bank failure depends on the sediment type, moisture content, and seepage processes (Luppi et al. 2009; Rinaldi and Nardi 2013; Olsen and Haun 2020). Therefore, bank failure cannot be simulated with a numerical setup for reservoir sedimentation due to fine particle deposition. Since bank failure processes only occur at the head of the reservoir, the bed level changes in this domain cannot be predicted in a physically correct and stable manner. Still, the above-introduced model setup is valid in deep-water model domains outside of the shallow deposition delta of the Devoll River.

Boundary conditions

For the simulation of reservoir sedimentation over three years, between the two surveys from August 2016 and August 2019, we defined the reservoir inflow Q_{in} ($m^3\ s^{-1}$) as a function of measured water levels and measured outflow Q_{out} ($m^3\ s^{-1}$) based on a routing equation. More detailed information can be found in SI 1.

Since the suspended sediment concentrations at the tributaries were not known for the simulation period, we implemented a previously developed indirect calculation method (Mouris et al. 2022). The indirect method builds on a calibrated soil erosion and sediment transport model with a monthly resolution (tons $month^{-1}$) to calculate the suspended sediment yield (SSY) of the catchment of the Banja reservoir. We divided the SSY from Mouris et al. (2022) at the Devoll River by the monthly inflow volume to prescribe suspended sediment concentrations (SSC) at the liquid model boundaries. Thus, SSC was constant for every month but varied from month to month. The mean SSC at the Devoll River for the calibration period was 1.36 kg m^{-3} with a maximum of 4.0 kg m^{-3} in September 2017.

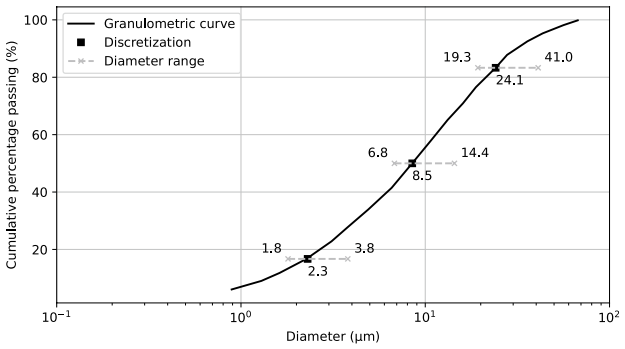

Fig. 2 Granulometric curve with the minimum and maximum grain sizes defined by the γ-multiplier

Calibration parameters

This study optimized four calibration parameters in the form of dry-bulk density of deposited sediments ρ_b, critical shear stress for erosion τ_{cr}, critical shear stress for deposition τ_d, and a diameter multiplier γ for settling velocities. The calibration parameter values were to be adapted to yield a possibly best simulation of the measured bed level changes Δz_{meas} between 2016 and 2019.

The dry-bulk density ρ_b and consolidation processes of mud-sand mixtures strongly depend on the sand content (van Rijn and Barth 2019). Because more than 98% of the deposited sediment in the Banja reservoir is cohesive, we defined ρ_b based on reported literature values for very low (< 10%) sand content. We considered the dry-bulk density a quasi-random variable with equally likely values (i.e., uniformly distributed) between 200 kg m^{-3} and 500 kg m^{-3} (van Rijn and Barth 2019; van Rijn 2020).

The critical shear stresses for erosion τ_{cr} and deposition τ_d control the exchange rate between suspended and deposited sediment. To define quasi-random, uniformly distributed value ranges for τ_{cr} and τ_d, we referred to field and laboratory tests with sediment mixtures with similar characteristics (grain size distribution, bulk density) as in the Banja reservoir. To this end, we tested value ranges for τ_{cr} between 0.05 and 0.4 Pa (Kornman and Deckere 1998; Widdows et al. 1998; Houwing 1999; Lumborg 2005; Shi et al. 2012; van Rijn 2020), and for τ_d between 0.01 and 0.1 Pa (Krone 1962; Lumborg 2005; Shi et al. 2012).

The deposition pattern in the reservoir also depends on the particle size that drives the settling velocity ω_s (see Eq. (2)). We applied the granulometric curves of suspended sediment upstream of the reservoir, which were subjected to considerable variability (i.e., uncertainty) in the model domain. Figure 2 plots the granulometric curve defined by three diameters representing the lower, middle, and upper third of the total volume. To account for uncertainty, we multiplied every diameter by a factor γ that takes uniformly distributed values between

0.8 and 1.7. Thus, the upper limit of grain sizes was 41 µm, which was larger than 95% of the sediment sample volume. The lower limit of 1.8 µm (2.3 µm • 0.8) was based on preliminary model runs, in which we tested the smallest possible sediment particles that remain in suspension and have an almost negligible influence on the deposition volume. Table 2 shows the resulting value ranges for the four calibration parameters considered in this study.

Bayesian calibration

Bayesian inference

To calibrate a numerical model using Bayesian inference, we inferred the posterior distribution $p(\omega|z_{meas})$ of the model calibration parameters (and hence the corresponding model responses) based on the measured bed levels z_{meas} and defined initial ranges for the calibration parameters. The posterior distribution $p(\omega|z_{meas})$ is the result of evaluating Bayes' theorem in the context of model updating:

$$p(\omega|z_{meas}) = \frac{p(z_{meas}|\omega) \bullet p(\omega)}{p(z_{meas})} \tag{4}$$

where $p(\omega)$ is the prior probability distribution that defines the initial probability of the calibration parameters before considering new or additional evidence (z_{meas}). $p(z_{meas}|\omega)$ is the so-called likelihood function and indicates how well the metamodel reproduces the measured data z_{meas} given a parameter combination ω. $p(\omega|z_{meas})$ is the posterior probability distribution (i.e., the updated probability of the calibration parameters ω given measured data z_{meas}), which is expected to be narrower than $p(\omega)$ (Box and Tiao 1992; Oladyshkin and Nowak 2019). $p(z_{meas})$ is a normalization factor, often referred to as Bayesian model evidence (BME), and is important when different posterior distributions are being compared with each other or several competing models are being evaluated (Mohammadi et al. 2018). Assuming that the deviations between the measured bed levels z_{meas} and the modeled bed levels z_{mod} are normally distributed and independent, the likelihood function $p(z_{meas}|\omega)$ is calculated proportionally to the sum of squared errors δ_i^2 between measured and simulated bed levels $z_{meas} - z_{mod}$ weighted by the total error e_i, where i indicates the calibration node.

$$p(z_{meas}|\omega) \propto \exp(-0.5\left[\frac{\delta_1^2}{e_1^2} + \frac{\delta_2^2}{e_2^2} + \cdots + \frac{\delta_n^2}{e_n^2}\right]) \tag{5}$$

This study provides additional novelty by improving BAL because of how we implement the measurement error e_{meas} and the metamodel error e_{meta}. In particular, we calculated the total errors e_i for each calibration node i as the sums of $e_{meas,i}$ and $e_{meta,i}$ according to the following descriptions.

The measurement errors e_{meas} resulted from the interpolation of the bed level measurements at the calibration nodes of the numerical mesh and uncertainties of field measurements. We used an interpolation radius of 3 m around the calibration nodes to average the bed level. Thus, the number of measurements per calibration node varied from 1 to 35 (8 on average). The variable amount of measurements available for averaging affected the confidence in the averaged values because, for instance, 15 measurements are more representative than two. The mean measurement error e_{meas} was approximately 0.4 m (measurement precision according to operator) where possible sources of errors were a high concentration of suspended sediment near the bottom, uncertainties in the water level of the reservoir, and the movement of the ADCP boat due to waves. Thus, to calculate the measurement errors $e_{meas,i}$ at every node, we introduce Eq. (6) where s_i is the number of observation points within the 3-m radius:

$$e_{meas,i} = \frac{adapted\ error}{1 + ln(s_i)} \tag{6}$$

where an *adaptederror* of 1.02 m was computed iteratively to ensure that the average value of e_{meas} for the total number of calibration nodes was 0.4 m. Thus, for example, $e_{meas,i}$ for a calibration node where the bed level was calculated based on 26 survey points is 0.24 m, while two survey points resulted in an $e_{meas,i}$ of 0.6 m.

In addition, we accounted for a metamodel error e_{meta} in the likelihood function because the metamodel is just an approximation of the full-complexity numerical model. We calculated e_{meta} through a leave-one-out cross-validation (LOO-CV), in which the model is repeatedly fitted on n-1 calibration nodes. Then, we calculated the LOO-CV error for each calibration node and training point. The LOO-CV error variance per calibration node was subsequently calculated and implemented as metamodel error $e_{meta,i}$. Finally,

Table 2 Calibration parameters and their value ranges for uniform distributions U(min, max) considered in this study

Calibration parameter		Investigated range		Prior assumption
Critical shear stresses for erosion	τ_{cr} (Pa)	0.05	0.4	$U(0.05, 0.4)$
Critical shear stresses for deposition	τ_d (Pa)	0.01	0.1	$U(0.01, 0.1)$
Dry-bulk density	$\rho_b\left(kgm^{-3}\right)$	200.0	500.0	$U(200, 500)$
Diameter multiplier	γ (-)	0.8 • d	1.7 • d	$U(0.8, 1.7)$

the total error e_i included in the likelihood function is composed of the calibration node-specific measurement error $e_{meas,i}$ (6) and the metamodel error $e_{meta,i}$:

$$e_i^2 = e_{meas,i}^2 + e_{meta,i}^2 \tag{7}$$

If the total errors e_i (Eq. (7)) were significant, the influence of the difference between the measured and modeled bed level on the likelihood score decreased (Eq. (5)).

Metamodel construction

Equation (4) can be approximated through Monte Carlo sampling, which requires thousands of numerical model evaluations. However, models that simulate hydrodynamic and morphodynamic processes may require a long computing time, making it computationally impractical to perform thousands of trials. To circumvent unacceptably long computing time, we employed a surrogate-assisted (referring to the metamodel being a surrogate for a full-complexity model, Oladyshkin et al. 2020) Bayesian inversion technique, which replaces the full-complexity numerical model with a metamodel. In particular, a metamodel emulates the output trends of a complex model but requires orders of magnitude less computing time (Beckers et al. 2020; An et al. 2022). Here, we used a Gaussian process emulator (GPE) as metamodel, which is discussed in more detail by Rasmussen and Williams (2006). As the GPE requires the definition of a kernel, we used a radial basis (i.e., squared exponential covariance) function (RBF) kernel in this study. The RBF needs the definition of length scales and their boundaries. The resulting GPE metamodel can then be trained with numerical model responses resulting from various combinations of possible calibration parameter values. Thus, the GPE metamodel was fitted toward a multidimensional response surface where the number of dimensions corresponds to the number of calibration parameters. Note that the metamodel cannot generally replace the numerical model and only serves the purpose of accelerating model calibration.

Bayesian active learning through metamodel training

In this study, we used the GPE metamodel to approximate the prior $p(\omega)$ through 10^6 random Monte Carlo samples. The quality of the surrogate-assisted Bayesian calibration depends on the ability of the metamodel to replicate the full-complexity model. The more training points used to train the metamodel, the better the predictions, since more information is provided to the metamodel with fewer gaps in the parameter space (i.e., fewer gaps need to be closed through stochastic interpolation). However, filling the entire parameter space with training points with a computationally expensive full-complexity model is practically not feasible because it requires several hours to compute one training point (sums up to more than 500 years of computing time in our case). To bypass long computing time, we applied BAL, which identifies optimal regions in the parameter space for calibrating parameters as a function of metamodel responses. BAL iteratively improves the metamodel in those regions of the parameter space that are most important for Bayesian inference (Oladyshkin and Nowak 2019; Oladyshkin et al. 2020).

Before starting the BAL process, a prior probability distribution $p(\omega)$ was assigned to every calibration parameter. Initially, a uniform probability distribution between two limit values was assumed. The next step is to compute an initial metamodel, using m parameter realizations and the corresponding full-complexity numerical model runs to train the metamodel. BAL starts with iteratively updating the initial metamodel with new training points so that the metamodel predictions better represent the full-complexity model. For this purpose, we sampled q parameter realizations ω_i that compete to be the next training point (exploration).

The parameter realizations constitute the *parameter space* and each combination is evaluated in the metamodel to generate an *output space*. Here, we had n outputs, associated with the location of our calibration nodes. An advantage of Gaussian processes for generating the metamodel is that each prediction of the output space consists of a mean μ_n and a standard deviation σ_n. Therefore, one can explore the *output space* using a multivariate Gaussian distribution. Figure 3 shows the BAL workflow and exemplary features two random exploration samples (black and gray circles), which in our study, are not just two but 10^5 random exploration samples forming the *output space prior*. To yield the *output space posterior* distribution, we considered two options, notably rejection sampling and Bayesian reweighting. Due to the high dimensionality of the output space (142 calibration points), the rejection rate for the first case was too high, and we chose Bayesian reweighting. For this purpose, we renormalized each value of the prior´s likelihood by their total sum to generate the posterior distribution. Consequently, all realizations (i.e., Monte Carlo samples) of the prior contributed to the posterior statistics (i.e., length scales), proportional to their likelihood. Once the prior $p(\omega)$ and posterior $p\left(\omega|z_{meas}\right)$ distributions had been generated, we used Eq. (8) to evaluate the so-called relative entropy $D_{KL}\left(p\left(\omega|z_{meas}\right),p(\omega)\right)$ (also referred to as Kullback–Leibler divergence) between both distributions (Kullback and Leibler 1951; Oladyshkin et al. 2020).

$$D_{KL}\left(p\left(\omega|z_{meas}\right),p(\omega)\right) = -ln[BME] + E_{p\left(\omega|z_{meas}\right)}\left(ln\left[p\left(z_{meas}|\omega\right)\right]\right) \tag{8}$$

where $E_{p\left(\omega|z_{meas}\right)}$ is the average of the posterior sample's likelihood (through the likelihood function, cf.

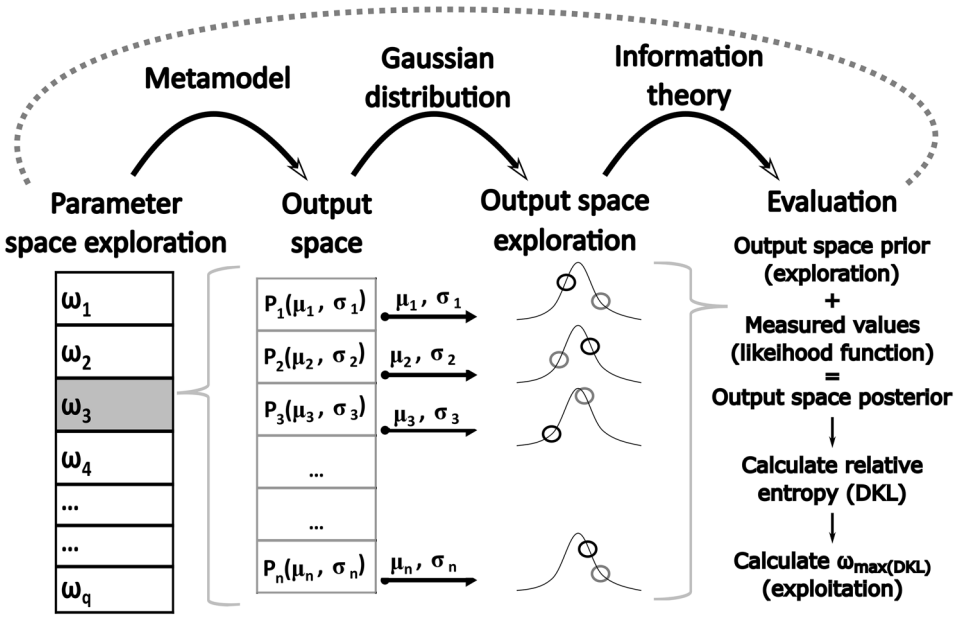

Fig. 3 Flow diagram explaining the Bayesian active learning method applied in this study

Equation (5)). In this context, the relative entropy expresses the information gain from the prior to the posterior distribution.

To this end, every BAL iteration involves the calculation of $D_{KL}\left(p\left(\omega|z_{meas}\right),p(\omega)\right)$ for q samples from the *parameter space*. After evaluating $D_{KL}\left(p\left(\omega|z_{meas}\right),p(\omega)\right)$, we calculated the parameter combination $\omega_{max(DKL)}$ that produced the maximum value of relative entropy to select the stochastically best-performing values for the calibration parameters in this iteration step (exploitation). We used the set of calibration parameters with the highest relative entropy to re-run the numerical full-complexity model and prepared the next BAL iteration step. In particular, the results of the new full-complexity model run serve as new training points for the GPE at the beginning of the next BAL iteration step. The BAL iterations continue until a stop criterion is reached, which is typically the convergence of relative entropy and BME (Oladyshkin et al. 2020). In this study, we additionally considered the evolution of the root-mean-square error (RMSE) after every BAL iteration. The BAL workflow (Fig. 3) and creation of the initial metamodel are explained in detail in the supplemental material SI 2. The complete procedure is implemented in a Python code (Acuna Espinoza et al. 2022).

Selection of calibration nodes for model calibration

The numerical model of the Banja reservoir was calibrated toward measured bed levels at the end of the three-year simulation period from 2016 to 2019. However, we could not use the totality of the available 632×10^3 bed level measurements because we needed to meet two criteria. First, the measurements needed to comply with the computational mesh and we agglomerated multiple measurements into one at the calibration nodes of the mesh. Second, the number of BAL iterations depends on the number of calibration nodes, and a large number of nodes can result in the so-called *curse of dimensionality* (Bellman 1957), which we will discuss later in light of the results. For instance, if we used 3500 measurement points, the multivariate Gaussian density for calculating the prior output space would have 3500 dimensions of spatially explicit bed level change.

Therefore, we only used nodes located at a maximum distance of 1.5 m from a measured point for calibration, and we agglomerated all measurements in a 3-m radius at the resulting calibration nodes into one bed level value. Further, we did not consider measurements in the downstream section of the reservoir, as we are only interested in the upstream area, where most sediments deposit. These selection filters resulted in 142 calibration nodes at which we evaluated modeled bed levels in the calibration process (see also Fig. 1). For testing the hypothesis (i) that Bayesian calibration only converges toward physically meaningful model parameter combinations when the model is well-conditioned, we introduced two scenarios of measurement data available for the calibration process. First, we considered all 142 calibration nodes that define the MAXME (MAximum MEasurements) data scenario (black and red calibration nodes in Fig. 1). Second, we removed points in regions where deltaic avulsion and channel erosion occurred according to the observation from 2016 to 2019 to define a VALDOME (VAlid DOmain MEasurements) data scenario, where all calibration nodes are in the domain of validity of the numerical model. In particular, we removed points adjacent to dry areas (tidal flats) and all measurements where the model uncertainty from the MAXME data scenario was high, as indicated by

LOO-CV error greater than 5.5 m based on an expert assessment. These two removal criteria essentially excluded model regions where avulsion and channel erosion occurred at the head of the reservoir, which the full-complexity model will not be able to simulate correctly. The application of these removal criteria left 109 calibration nodes that we used for the VALDOME scenario (black calibration nodes in Fig. 1).

Experimental procedure

Bayesian calibration stability

The proposed optimization of the Bayesian calibration scheme refers to the extension of the BAL framework, notably the adaptive implementation of errors in the likelihood function through LOO-CV, and its application to four calibration parameters. With these two novel aspects of BAL, we investigated the robustness of Bayesian calibration regarding the quality of the numerical model and in light of equifinality. Therefore, we applied Bayesian calibration to the two above-introduced data scenarios (MAXME and VALDOME).

To prepare the BAL iterations, we ran the full-complexity model with 15 calibration parameter combinations to train the initial metamodel. 13 of the parameter combinations stemmed from random sampling in the parameter space, and the remaining two corresponded to theoretically maximum and minimum sedimentation (i.e., high/low τ_{cr}, low/high τ_d, low/high ρ_b, high/low γ, respectively). A minimum of one training point would be sufficient for the initial metamodel, but more initial training points for BAL can reduce the total time required to achieve convergence. We tracked BME, and RMSE to evaluate if the calibration reached convergence regarding uncertainty and error (see the above section on Bayesian active learning). However, convergence may not be achieved if multiple high-probability regions cause exploitation to jump between very different calibration parameter combinations in the BAL iterations. In these cases, BAL theoretically bounces back and forth eternally between nearly equally likely combinations of calibration parameters. This phenomenon, known as equifinality, poses a great challenge for model calibration (e.g., Franks et al. 1997).

To address equifinality, we analyzed the BAL convergence in the two measurement data scenarios (see above) with 55 iterations according to literature recommendations (Mohammadi et al. 2018; Beckers et al. 2020; Scheurer et al. 2021). We verified hypothesis (i) if the VALDOME scenario led to more unique and physically meaningful maximum likelihood regions than the MAXME data scenario, and less significant, later, or no convergence in the MAXME data scenario. To this end, we investigated the evolution of BME, RMSE, and the variability of the four calibration parameters in the last five BAL iteration steps. To assess the ability of the metamodel to reproduce the results of the full-complexity model, we compared the results predicted by the metamodel with those predicted by the numerical model. We present the global model accuracy after the Bayesian calibration by comparing the calculated and measured bed level changes after running the two data scenarios.

Importance of calibration parameters

The Bayesian calibration looks for the best-fit combination of the four calibration parameters τ_{cr}, τ_d, ρ_b, and γ to investigate optimization methods for multidimensional calibration parameter spaces and find the most relevant parameters driving reservoir sedimentation in this numerical model. The four calibration parameters are known to be relevant for hydro-morphodynamic processes in reservoirs (Haun et al. 2013; Dutta and Sen 2016; Hillebrand et al. 2016). However, to our best knowledge, the four parameters have never been directly compared with each other due to the limited capacities of subjective trial-and-error calibration. The adapted Bayesian framework and the VALDOME scenario enable us to perform such a comparison of the four calibration parameters. Thus, we aim to test hypothesis (ii) that at least one of the calibration parameters τ_{cr}, τ_d, ρ_b, or γ plays a governing role in the fluvial deposition of suspended sediments in reservoirs. To this end, we made use of a multi-parameter plot of the posterior distributions (Eq. (5)) of the four calibration parameters for both data scenarios. We will accept hypothesis (ii) if at least one of the four calibration parameters has a considerably narrower posterior distribution than the other parameters. This parameter will be more important than the other calibration parameters because it has the smallest uncertainty (i.e., narrowest posterior) of the maximum likelihoods.

Results

Convergence speed

In the VALDOME scenario, the BME began converging toward a value of approximately 10^{-31} after the 46th BAL iteration, and we ran in total 55 iterations to monitor the convergence trend (see Fig. 4). The BME for the MAXME scenario fluctuated around a value of 10^{-37} during the 55 BAL iterations, and no clear convergence trend was observed. In addition, Fig. 4 also shows the evolution of the RMSE between the metamodel and full-complexity model results for every tested parameter combination used as a training point in BAL. The plots reveal that the RMSE is higher for the MAXME scenario, and more importantly, there is no decreasing trend for this scenario. In contrast, the evolution of the RMSE for the VALDOME scenario decreased.

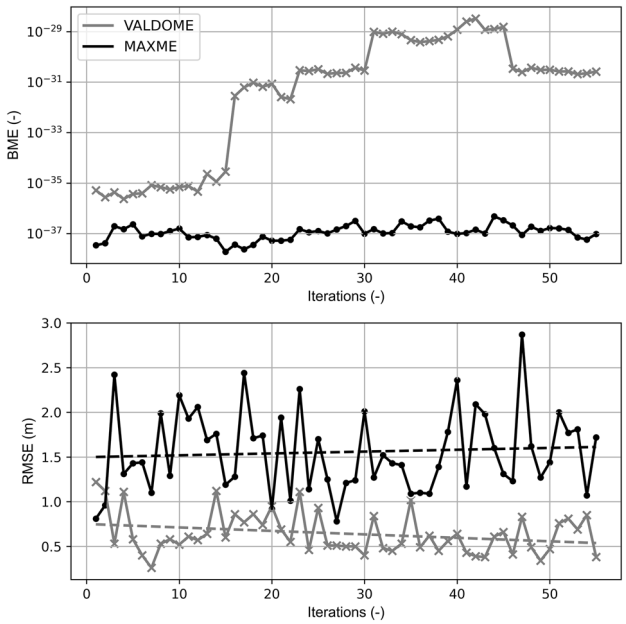

Fig. 4 BME (top) and RMSE evolution including linear trend lines (bottom) for the 55 BAL iterations and both data scenarios

Figure 5 shows the variability of the four calibration parameters in the last five BAL iterations for the VALDOME scenario in black and the MAXME scenario in gray. Comparing the two data scenarios shows that the MAXME scenario had significantly higher variability and no physical convergence for τ_{cr} and τ_d. In contrast, there was hardly any variability of ρ_b in both scenarios, whereas the variability in γ was slightly higher in the VALDOME scenario. The total computing time for the BAL iterations per scenario was approximately one month (on 12 Cores using AMD Ryzen 9 5950 × 16-(32) @ 3.4 GHz processor), which was only possible with the coarse mesh resolution.

Table 3 Calibrated parameters for the morphodynamic model of the Banja reservoir using BAL

		Maximum likelihoods	
Calibration Parameter	Prior assumption	MAXME	VALDOME
τ_{cr} (Pa)	U(0.05, 0.4)	0.39	0.25
τ_d (Pa)	U(0.01, 0.1)	0.02	0.01
$\rho_b\left(kgm^{-3}\right)$	U(200, 500)	416.2	403.6
γ (-)	U(0.8, 1.7)	0.82	0.98

Posterior distributions and importance of calibration parameters

Maximum likelihoods

Table 3 shows the maximum likelihood of posterior distributions for the calibration parameters, which is the realization of the Monte Carlo sample with the highest likelihood and comparable to a deterministic best-fit solution. The maximum likelihood of τ_{cr} was 0.39 Pa, close to the upper limit considering all calibration nodes (MAXME). In the physically relevant-only (VALDOME) scenario, τ_{cr} was 0.25 Pa. The critical shear stress for deposition τ_d was close to the lower limit at 0.02 Pa and 0.01 Pa in the MAXME and VALDOME scenarios, respectively. The maximum likelihood of

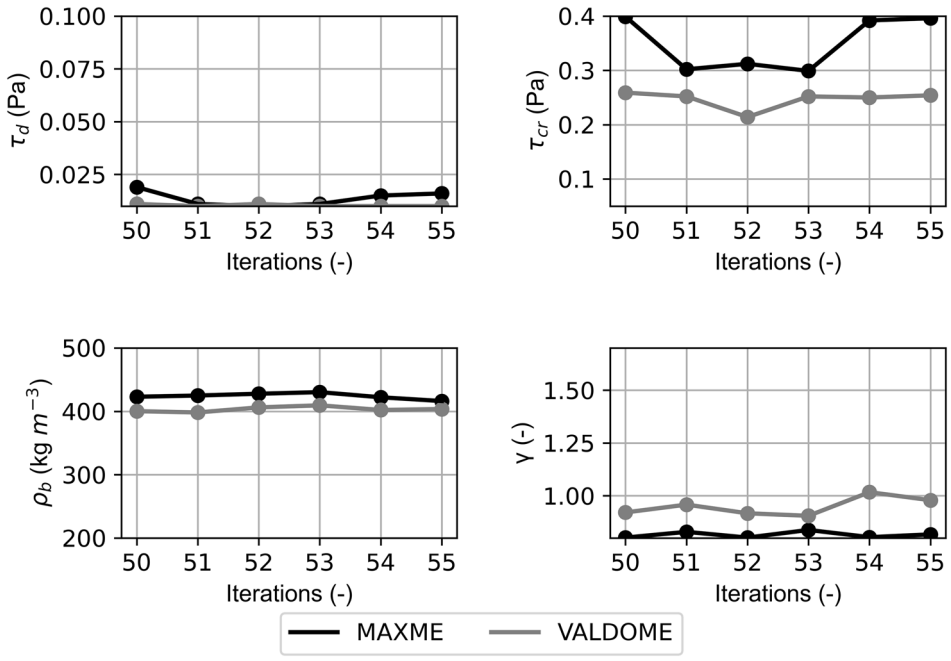

Fig. 5 Variability of the four calibration parameters for the five last BAL iterations 50–55 and both data scenarios

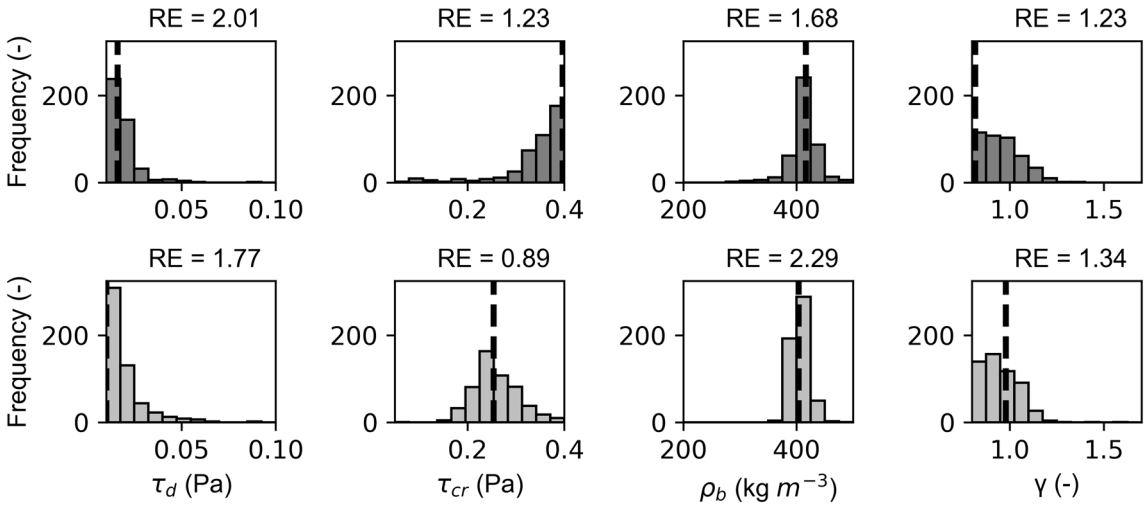

Fig. 6 Posterior distributions in the parameter space, and associated relative entropy (RE) at the end of the MAXME scenario in gray (top) and the VALDOME scenario in light gray (bottom). The dashed vertical lines indicate the maximum likelihood values of the calibration parameters

ρ_b was close to 410 kg m^{-3} in both scenarios. The diameter multiplier γ was 0.82 in the MAXME scenario and 0.98 in the VALDOME scenario. A detailed analysis of the posterior parameter space is provided below.

Posterior parameter distributions

The posterior distributions of the calibration parameters indicate the uncertainty in the maximum likelihoods listed in Table 3. Figure 6 shows the individual posterior histograms for each calibration parameter after the MAXME scenario at the top (433 posterior samples) and after the VALDOME scenario at the bottom (540 posterior samples).

As a standardized measure to identify driving calibration parameters and evaluate their uncertainty, we calculated the Kullback–Leibler divergence (Kullback and Leibler 1951), also known as relative entropy (RE), to measure the information gain between the initial (uniform) prior and the final posterior probability distribution for every calibration parameter. High RE characterizes a narrow distribution, which represents high information gain and low uncertainty in the maximum likelihoods.

Figure 6 shows that ρ_b and τ_d have the narrowest posterior distribution in both calibration scenarios, which indicates that these parameters are the most restrictive and important in the calibration process. This finding is also supported by the high RE of 1.68 and 2.29 for ρ_b and 2.01 and 1.77 for τ_d. That is, only values close to the maximum likelihood value (dashed line) led to accurate results. However, the maximum likelihood for τ_d was close to the lower limit in both data scenarios. The histogram for τ_{cr} differs significantly between the two different scenarios. For the MAXME scenario, the distribution peaks close to the upper limit, and the RE was 1.23 whereas the histogram for the VALDOME scenario peaks at 0.25 Pa and gets wider, characterized by a lower RE of 0.89. The histogram of the diameter multiplier γ peaks in both scenarios close to the lower limit of the initial range and the RE slightly increased from 1.23 to 1.34 for the VALDOME scenario.

The meaningfulness and qualitative significance of the yielded maximum likelihoods can also be interpreted by examining data patterns and regions of high and distinguishable maximum likelihoods in the parameter space. For this purpose, Fig. 7 illustrates the likelihood of all possible calibration parameter combinations of τ_d, τ_{cr}, γ, and ρ_b at the end of the VALDOME scenario. Similar plots of the results for the MAXME scenario can be found in SI Fig. 2. Since a four-dimensional parameter space cannot be plotted graphically, we created six two-dimensional plots of the possible combinations. The three plots on the right of Fig. 7 clearly show that the likelihoods for $\rho_b < 300$ kg m^{-3} are very small and quite small for $\rho_b > 450$ kg m^{-3} (in line with Fig. 6). Thus, values of ρ_b significantly lower or higher than the maximum likelihood did not lead to accurate results, and the data pattern of ρ_b confirms its high relative importance compared to the other three calibration parameters. In contrast, the boundary between high and low probabilities in the data pattern for τ_d was less distinct, with the highest likelihoods occurring for $\tau_d < 0.05$ Pa. τ_{cr} had the least pronounced data pattern, and high probabilities occurred almost throughout the entire range. In addition, the data pattern for γ showed high likelihoods over a wide range with $\gamma < 1.2$.

Furthermore, there was no significant correlation between the calibration parameters (see SI Fig. 3), which indicates that the calibration parameters were well chosen and independent. If there were high correlations between

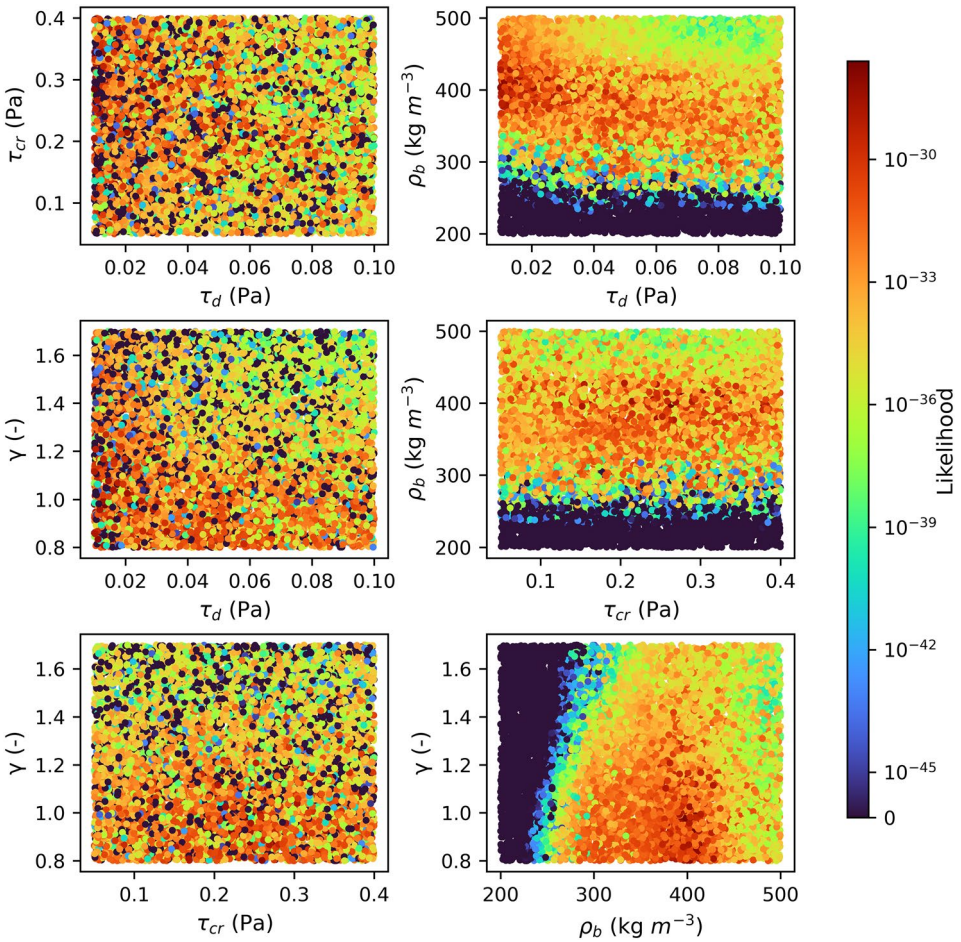

Fig. 7 Likelihood values along the six possible parameter space combinations at the end of the VALDOME scenario

the calibration parameters, they would contain redundant information and the variation in one parameter could be compensated by a change of another parameter. In such a case, calibration would be restricted to determining the ratios between the parameters.

Simulated bed level changes

Figure 8 shows the cumulative bed level changes and water depth in the Banja reservoir after the end of the three-year simulation period with the calibration parameters for the VALDOME scenario listed in Table 3. In the region near the Devoll River tributary, the water became shallow and several channels formed. The highest deposits of more than 4 m occurred in the upstream part of the reservoir. At low water levels, some of the deposited sediment in the upstream part of the reservoir was eroded, resulting in the formation of smaller channels. These channels did not occur in permanently impounded regions (shown in dark blue). The sediment deposit height decreased in flow direction because of the decreasing flow velocity and the continuous settling of sediment particles. In the reservoir, the deposition heights in flow direction were less than 4 m after 2.4 km, less than 1.5 m after 4.6 km, and less than 0.5 m after 8.0 km.

Model accuracy

Agreement between GPE metamodel and numerical model

Since the final calibration parameters stem from the metamodel, we performed two analyses to evaluate the calibration quality. First, we compared the metamodel with the 2d hydro-morphodynamic model to quantify how well the metamodel mimics the full-complexity model results. Second, we compared the calibrated numerical model with the measurement data to evaluate the final model quality.

To evaluate the quality of the metamodel results, the numerical model was run with the optimal calibration parameter combinations shown in Table 3. The inclusion of all calibration nodes (MAXME) led to a Pearson's correlation r of 0.92, an RMSE of 0.87 m, and a mean absolute error (MAE) of 0.45 m (Fig. 9). Hence, the metamodel reproduced the numerical model results with good accuracy. However, the metamodel significantly overestimated bed level changes for some calibration nodes in the upstream part near the

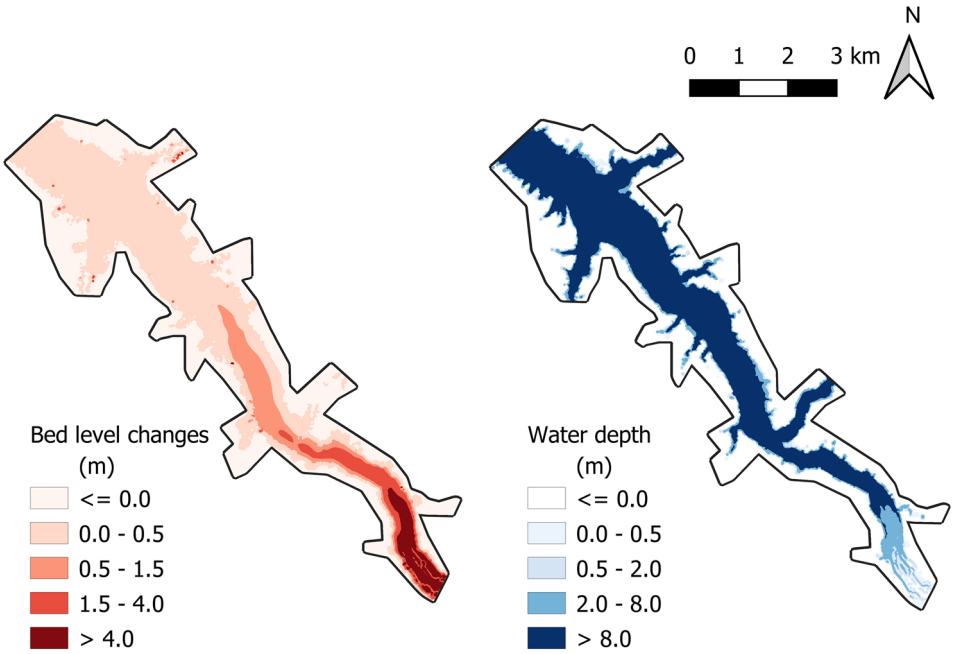

Fig. 8 Cumulative bed level changes (left) and water depth (right) after the end of the simulation period of the VALDOME scenario

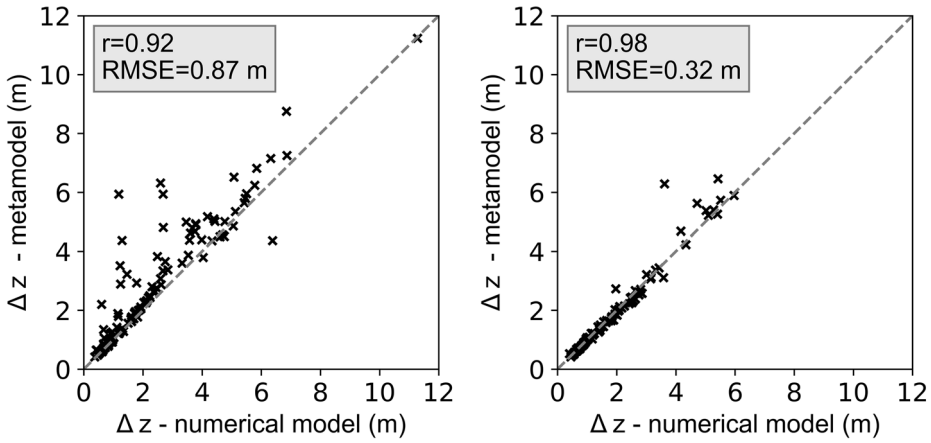

Fig. 9 Scatter plot of the computed bed level changes Δz from the metamodel and the numerical model after the MAXME scenario at the left and VALDOME scenario at the right. The dashed line represents the hypothetic perfect metamodel accuracy

Devoll River tributary. Excluding these upstream nodes (VALDOME) resulted in a significantly better r of 0.98, an RMSE of 0.32, and an MAE of only 0.13 m. Therefore, the trained metamodel accurately emulated the full-complexity numerical model results at the end of the simulation period.

To assess the regions of high uncertainty in the metamodel, we calculated the LOO-CV errors for the 142 calibration nodes and the 70 parameter combinations used as training points. We averaged the absolute values of the differences for each point to estimate the expected error between the metamodel and the full-complexity model. This analysis is important because a high model metamodel error causes decreased influence of the difference between the measured and modeled bed level on the likelihood (Eq. 5). Therefore, calibration nodes with a large LOO-CV error indicate high uncertainty in the metamodel and carry less weight in the final likelihood calculation. The LOO-CV mean errors for the MAXME scenario ranged from 0.04 to 4.04 m (0.8 m on average). The highest errors occurred near the upstream boundary, which is also shown in SI Fig. 4. In contrast, the LOO-CV errors for the VALDOME were significantly smaller and ranged from 0.03 to 1.76 m (0.35 m on average).

Modeled and measured agreement

To evaluate the quality of the calibrated hydro-morphodynamic numerical model, we calculated Pearson's r and the RMSE for both scenarios. The MAXME scenario led to an r of 0.70, RMSE of 1.62 m, and MAE of 1.17 m. The VALDOME scenario yielded a similar r of 0.66, a smaller RMSE of 1.04, and a smaller MAE of 0.91 m.

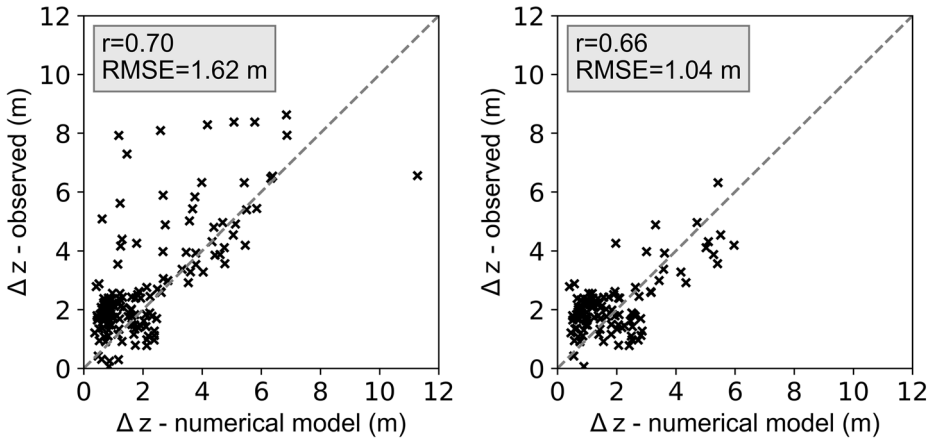

Fig. 10 Scatter plot of modeled and simulated bed level changes Δz for the MAXME scenario at the left and VALDOME scenario at the right. The dashed line represents the hypothetic perfect model accuracy

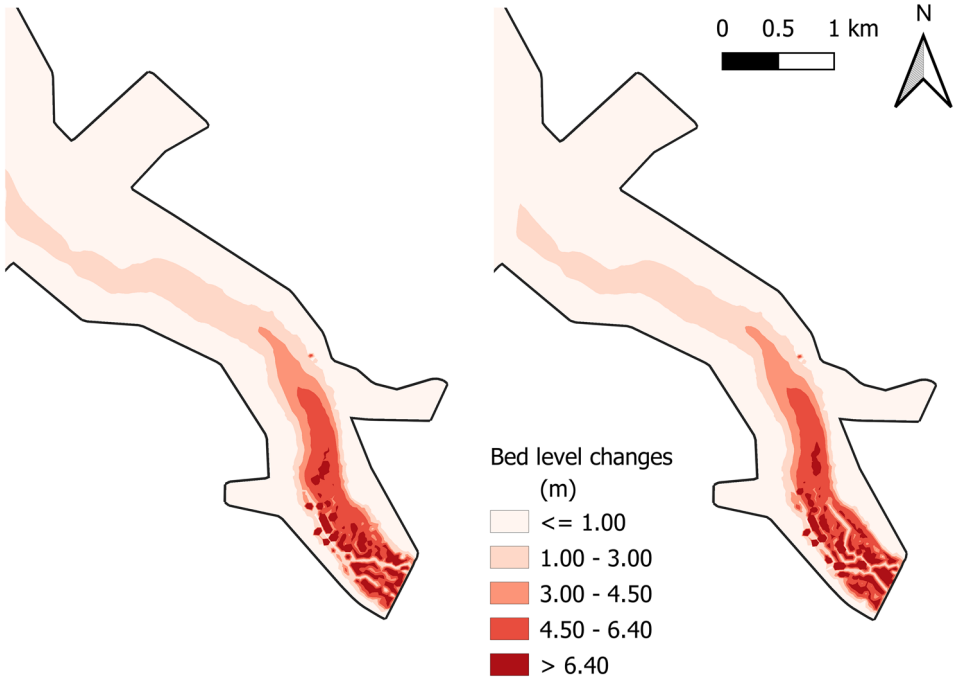

Fig. 11 Simulated bed level changes (2016–2019) in the upstream part of the reservoir for two different simulations with similar calibration parameters at the end of the simulation period

Thus, both scenarios yielded satisfactory agreement between the measured and modeled results according to global statistics indicating a good representation of the sedimentation patterns in the Banja reservoir (see Fig. 10). Still, the MAE and RSME were not negligible but significantly lower in the VALDOME scenario. In the MAXME scenario, there were 11 calibration nodes with bed level change errors greater than 2 m compared to only three such nodes in the VALDOME scenario (see SI Fig. 5). In addition, Fig. 10 indicated that the numerical model tends to underestimate small measured bed level changes by approximately 1 m in both scenarios.

Discussion

Deposition patterns and model deviations

Figure 11 shows the results of the bed level evolution in the upstream part of the reservoir after three years and for two simulations with similar parameter combinations. The figure shows several channels with high topographic gradients at different locations. Thick sediment deposits occurred next to these channels, particularly at mesh nodes that were only temporarily wet in the simulation period. These nodes can be inside a channel (small sediment deposits) in one model run and outside the channel (thick sediment deposits) in the next model run. Although the physical model environment

is similar, the patterns in Fig. 11a and b are very different, which indicates numerical instabilities that the metamodel attempted to emulate by drastically changing the calibration parameter values (see Fig. 5).

The coarse mesh used in this study (to reduce computing time) affected the accuracy of the results and numerical stability. In addition, the model only considered suspended sediment transport and was not able to reproduce shallow water regions experiencing channel erosion, deltaic avulsion, or bank failures. The simplification assumptions made the model physically not fully well defined for simulating morphological processes at the head of the reservoir. In the MAXME scenario, the BAL iterations attempted to overcome mismatches between measured and modeled erosion channels by prominent changes in the calibration parameter values, indicating equifinality. As a result, the BAL iterations were unstable and did not converge. This is reflected in the higher fluctuations of the calibration parameters (Fig. 5) and maximum likelihoods near the limit of the investigated range for three of the four calibration parameters in the MAXME scenario. In addition, the BME (Fig. 4) did not converge because every BAL iteration tried to explore numerical instability in the delta region. Yet, the adapted Bayesian calibration worked well in the model domain where suspended sediment deposition could be reproduced and the model was stable (VALDOME). The BAL converged toward a solution that is confirmed by a very low RMSE of 0.32 m and a high Pearson's r of 0.98 between the full-complexity and the metamodel. However, the RMSE of 1.04 m of the numerical model regarding measured data was significantly smaller compared to the MAXME scenario but not negligible, which is due to the limitations of the modeling approach. For instance, complex three-dimensional hydrodynamics and stratified flow cannot be represented by a 2d model, which is expected to affect the deposition pattern in the reservoir. Also, we assumed a constant ρ_b for the entire reservoir, while consolidation occurs over time and the density increases (Mehta et al. 1989; Winterwerp and Kesteren 2004; Lo et al. 2014; Hoffmann et al. 2017). Accordingly, the average bulk density in a reservoir is often heterogeneous and varies over time, which is not reflected in our model assumptions. In addition, some boundary conditions were not measured directly, and therefore, subject to additional uncertainty. For example, the inflow into the reservoir was calculated from measured outflow, reservoir water levels, and hydrological model outputs. Also, the sediment yields of the tributaries stem from a model with monthly resolution only (Mouris et al. 2022). Considering the uncertainty related to these model simplifications, as well as the mean measurement error of approximately 0.4 m, the final model quality is acceptable in the VALDOME scenario. In light of the instability of the MAXME scenario, we verify the hypothesis (i) that Bayesian calibration only converges toward physically meaningful model parameter combinations when the model is well-conditioned (i.e., measured data are in the validity domain of model assumptions).

Relevant calibration parameters

Since the Bayesian calibration only converges toward physically meaningful model parameter combinations when the calibration nodes are in the range of validity of the numerical model, we only used the VALDOME scenario to identify the calibration parameter importance for reservoir sedimentation modeling.

Figure 6 shows that the density ρ_b was the most restrictive (i.e., constraining) calibration parameter due to its narrow-shaped posterior distribution, which was not imposed by the initial value ranges (Table 2). This is also evident in the clear data pattern of ρ_b across the parameter space (Fig. 7), where high likelihoods occurred only in a very narrow range. Yet, many studies exclude ρ_b from the calibration process and use fixed literature values or empirical equations to obtain a representative value (Foster and Charlesworth 1994; Verstraeten and Poesen 2001; Banasik et al. 2021). Our findings suggest that ρ_b should be either calibrated or directly measured, rather than simply derived from the literature. This finding is important because, for instance, models for calculating the sediment yield are often calibrated against the volume change in lakes or reservoirs. Since the volume of the deposited sediments is directly related to the dry-bulk density of the sediments, an incorrect value for ρ_b results in an incorrect calculation of sediment masses. For example, if the sediment inflow is underestimated, the error can be compensated for by a lower dry-bulk density for the deposited sediment. In this study, the Bayesian calibration led to a reasonable value of 403.6 kg m^{-3} in the VALDOME scenario (van Rijn and Barth 2019; van Rijn 2020).

According to the posterior distribution (see Fig. 6), τ_d was the second most restrictive (i.e., constraining) parameter with a small maximum likelihood of 0.01 Pa. Yet, the maximum likelihood was located at the lower limit of the investigated range, which suggests that the Bayesian calibration would have tried an even smaller τ_d if possible. Hence, the posterior distribution should be interpreted carefully, as a broader range may result in a wider distribution. A possible explanation for why the Bayesian calibration preferred small values of τ_d is the maximization of suspended load trajectories. Since fine particles are kept in suspension by turbulence even at low flow velocities, the BAL attempted to compensate for the insufficient model assumptions regarding 3d turbulence (mixing length model) by decreasing τ_d. Furthermore, the actual shear stresses in a large reservoir are very small. Thus, only very small τ_d values affect the deposition process in the numerical model, especially since

we disregarded measured data in the shallow delta region in the VALDOME scenario.

The calibrated diameter multiplier γ was 0.98, which falls into the lower half of the initial range. γ was not very restrictive and yielded high likelihoods for a comparatively wide range with $\gamma < 1.2$. These small γ values indicate that the observed particle size diameters and the corresponding settling velocities were rather too large and smaller particle sizes and settling velocities lead to better results. Generally, the grain size distribution of a suspended sediment load sample represents the present hydraulic conditions. Therefore, we recommend using grain sizes in a reasonable range for calibration or varying the grain size distributions as a function of discharge. The stochastic approach led to representative grain size ranges: $d_{17} = 1.89$ to 2.25 µm, $d_{50} = 7.0$ to 8.33 µm, and $d_{83} = 19.76$ to 23.62 µm. However, flocculation processes can alter the settling velocity of cohesive particles (Dyer and Manning 1999; Winterwerp and Kesteren 2004), and therefore, the actual grain sizes of individual particles can be even smaller.

The optimum τ_{cr} was 0.25 (VALDOME) and the corresponding likelihood pattern was not very pronounced and had little impact on the calibration process, because only the very upstream calibration nodes were affected by erosion and resuspension. In contrast to a free-flowing river, sedimentation dominates in the reservoir due to the large water depths and low flow velocities. Thus, there were significant differences between the two sets of calibration nodes, underlining that particularly the upstream delta section of the reservoir was controlled by τ_{cr}. Hence, the RE further decreased with the exclusion of the calibration nodes in the upstream part (VALDOME), which emphasizes the diminishing importance and higher uncertainty of τ_{cr}.

Ultimately, we verify hypothesis (ii) since the Bayesian calibration identified ρ_b as the driving calibration parameter in the fluvial deposition of suspended sediments in reservoirs. In contrast, γ or τ_{cr} had significantly less influence on the final sedimentation pattern. Parameters with narrow posterior distributions and high relative entropy compared to a uniform distribution can be interpreted as driving and restrictive, while parameters with wide posterior distributions can be interpreted as less important and uncertain. The narrow posterior distribution for τ_d suggests a high information gain through BAL, with the maximum likelihood at the lower limit. Consequently, small τ_d lead to more accurate results, although the importance of τ_d cannot be objectively assessed.

The curse of dimensionality

The so-called curse of dimensionality (see also the methods section on Bayesian calibration) forced us to limit the number of calibration nodes. Even though we limited the number of calibration nodes, the dimensions of the response surface were still too high and both scenarios were subjected to the curse of dimensionality. This phenomenon occurred because of the exponential term of the likelihood function (Eq. (5)), which represents the (negative) weighted sum of the squared difference between the measured and modeled bed level change. The more calibration nodes we used, the larger the negative value of the sum becomes. In consequence, the exponential term became a number so close to zero that the precision of a computer is insufficient to express it. This problem, known as arithmetic underflow (e.g., Coonen 1980), caused the likelihood function to become zero, which does not allow for the calculation of convergence scores and selection of a next training point. To solve this problem, we artificially increased the total error in Eq. (7) by multiplying it by 5. The artificial error amplification was equally applied to all individual errors and represented the smallest integer amplification factor that avoided arithmetic underflow. Since the amplification factor was constant, the rank of the output realization remained unchanged.

The curse of dimensionality also affected the number of Monte Carlo (MC) samples that could be drawn to approximate the posterior distribution in Eq. (5). With increasing dimensionality, the required computing power for a representative sample increased exponentially. In consequence, the region with the highest density became more restrictive and the vast majority of the probability density function was concentrated in low-likelihood areas. To balance representativeness, the curse of dimensionality, and computing time, we limited the sample size to 10^5 MC realizations.

The curse of dimensionality also affects the generation of the posterior distribution through rejection sampling (Smith and Gelfand 1992) or the here-used Bayesian weighting strategy, as most of the samples were concentrated in low-likelihood areas. Thus, the weight of nearby all samples was close to zero or arithmetic underflow occurred. The above-introduced error multiplier helped to avoid these arithmetic underflow issues by increasing the width of the high-likelihood region and enabling a representative posterior.

Conclusion

The region where the model simplifications were not entirely valid caused stability issues in the upstream part of the reservoir, where small channels with low water depths led to high topographic gradients and large model uncertainty. Hence, the inclusion of all calibration nodes resulted in a degradation of model accuracy, fluctuating Bayesian model evidence, and higher variability of the four calibration parameters in the last five BAL iterations. In addition, the maximum likelihood values of the calibration parameters were located near the limit of the

investigated range. Consequently, Bayesian calibration only converged toward physically meaningful parameter combinations when the model was well-conditioned (i.e., when the measurement data are in physically representative regions of the model domain). The final model quality was still affected by the limitations of the 2d numerical model, leading to a considerable mean absolute error of approx. 1 m regarding the modeled deposition height.

Bayesian calibration identified the dry-bulk density as the driving and most important parameter to simulate the fluvial deposition of suspended sediments in reservoirs. Thus, the dry-bulk density should be prioritized in data collection, already before setting up a reservoir sedimentation model. In contrast, the particle diameter multiplier and the critical shear stress for erosion had less influence on the deposition pattern as can be seen from the wider posterior distribution. The importance of the critical shear stress for deposition could not be objectively assessed because the maximum likelihood is located at the lower limit of the initial range. Yet, small values led to better results because the BAL tried to maximize suspended load trajectories to compensate for insufficient model assumptions about 3d turbulence that keeps fine particles in suspension.

Ultimately, this study shows that a robust Bayesian calibration can also be achieved when global model simplification hypotheses cannot be applied to the entire model domain, requiring that the measurement data for calibration must be from model domains where the simplifying assumptions are valid. Furthermore, our modified BAL approach accounted for both measurement and metamodel errors, enabling a multi-parametric comparison and identification of driving calibration parameters even in four-dimensional parameter space.

Supplementary Information The online version contains supplementary material available at https://doi.org/10.1007/s40808-023-01712-7.

Acknowledgements This study was carried out in the framework of the DIRT-X project, which is part of AXIS, an ERA-NET initiated by JPI Climate, and funded by FFG Austria, BMBF Germany, FORMAS Sweden, NWO NL, and RCN Norway with co-funding from the European Union (Grant No. 776608). The fourth author is funded by the German Research Foundation (DFG, 327154368 – SFB 1313). The fifth author is indebted to the Baden-Württemberg Stiftung for the financial support from the Eliteprogramme for Postdocs. We also thank Nils Rüther and Slaven Conevski for providing us with input data and Maria Fernanda Morales Oreamuno and Anna Cerf for their help and fruitful discussions.

Funding Open Access funding enabled and organized by Projekt DEAL.

Data Availability All the codes and steering files of the numerical model are publicly available in an online repository. Further datasets used in this study are available from the corresponding author on reasonable request.

References

An Y, Yan X, Lu W et al (2022) An improved bayesian approach linked to a surrogate model for identifying groundwater pollution sources. Hydrogeol J 30:601–616. https://doi.org/10.1007/s10040-021-02411-2

Ardiclioglu M, Kocileri G, Kuriqi A (2011) Assessment of Sediment Transport in the Devolli River. In: 1st International Balkans Conference on Challenges of Civil Engineering

Audouin Y, Benson T, Delinares M et al (2020) Introducing GAIA, the brand new sediment transport module of the TELEMAC. https://doi.org/10.5281/ZENODO.3611600. -MASCARET system

Audouin Y, Tassi P (2020) GAIA User Manual

Acuna Espinoza E, Mouris K, Schwindt S, Mohammadi F (2022) Surrogate Assisted Bayesian Calibration. Version 0.1.0. https://github.com/eduardoAcunaEspinoza/surrogated_assisted_bayesian_calibration/tree/v0.1.0

Banasik K, Hejduk L, Krajewski A, Wasilewicz M (2021) The intensity of siltation of a small reservoir in Poland and its relationship to environmental changes. CATENA 204:105436. https://doi.org/10.1016/j.catena.2021.105436

Beckers F, Heredia A, Noack M et al (2020) Bayesian calibration and validation of a large-scale and Time-Demanding Sediment Transport Model. Water Resour Res 56. https://doi.org/10.1029/2019WR026966

Bellman R (1957) Dynamic programming. Princeton Univ. Pr, Princeton, NJ

Borrelli P, Robinson DA, Panagos P et al (2020) Land use and climate change impacts on global soil erosion by water (2015–2070). Proceedings of the National Academy of Sciences 117:21994–22001. https://doi.org/10.1073/pnas.2001403117

Box GEP, Tiao GC (1992) Bayesian Inference in Statistical Analysis, 1st edition. Wiley-Interscience, New York

Chadwick AJ, Lamb MP, Moodie AJ et al (2019) Origin of a preferential avulsion node on Lowland River Deltas. Geophys Res Lett 46:4267–4277. https://doi.org/10.1029/2019GL082491

Coonen (1980) Special feature an implementation guide to a proposed Standard for floating-point arithmetic. Computer 13:68–79. https://doi.org/10.1109/MC.1980.1653344

Dorfmann C, Zenz G (2016) The depth-averaged Mixing Length turbulence model for Telemac-2D. Proceedings of the XXIIIrd TELEMAC-MASCARET User Conference 2016, 11 to 13 October 2016, Paris, France 163–168

Dutta S, Sen D (2016) Sediment distribution and its impacts on Hirakud Reservoir (India) storage capacity. Lakes Reserv: Res Manag 21:245–263. https://doi.org/10.1111/lre.12144

Dyer KR, Manning AJ (1999) Observation of the size, settling velocity and effective density of flocs, and their fractal dimensions. J Sea Res 41:87–95. https://doi.org/10.1016/S1385-1101(98)00036-7

Foster IDL, Charlesworth SM (1994) Variability in the physical, chemical and magnetic properties of reservoir sediments; implications for sediment source tracing. IAHS Publ no 224:153–160
Franks SW, Beven KJ, Quinn PF, Wright IR (1997) On the sensitivity of soil-vegetation-atmosphere transfer (SVAT) schemes: equifinality and the problem of robust calibration. Agric For Meteorol 86:63–75. https://doi.org/10.1016/S0168-1923(96)02421-5
Hajek EA, Wolinsky MA (2012) Simplified process modeling of river avulsion and alluvial architecture: connecting models and field data. Sediment Geol 257–260:1–30. https://doi.org/10.1016/j.sedgeo.2011.09.005
Hanmaiahgari PR, Gompa NR, Pal D, Pu JH (2018) Numerical modeling of the Sakuma dam reservoir sedimentation. Nat Hazards 91:1075–1096. https://doi.org/10.1007/s11069-018-3168-4
Haun S, Kjærås H, Løvfall S, Olsen NRB (2013) Three-dimensional measurements and numerical modelling of suspended sediments in a hydropower reservoir. J Hydrol 479:180–188. https://doi.org/10.1016/j.jhydrol.2012.11.060
Hervouet J-M (2007) Hydrodynamics of Free Surface Flows: Modelling with the Finite Element Method, 1. edition. Wiley, Chichester; Hoboken, N.J
Hervouet J-M (2020) TELEMAC-2D User Manual
Hervouet J-M, Razafindrakoto E, Villaret C (2011) Dealing with dry zones in free surface flows. A New Class of Advection Schemes
Hillebrand G, Klassen I, Olsen NRB (2016) 3D CFD modelling of velocities and sediment transport in the Iffezheim hydropower reservoir. Hydrol Res 48:147–159. https://doi.org/10.2166/nh.2016.197
Hinderer M, Kastowski M, Kamelger A et al (2013) River loads and modern denudation of the Alps — a review. Earth-Sci Rev 118:11–44. https://doi.org/10.1016/j.earscirev.2013.01.001
Hoffmann T, Hillebrand G, Noack M (2017) Uncertainty analysis of settling, consolidation and resuspension of cohesive sediments in the Upper Rhine. Int J River Basin Manag 15:401–411. https://doi.org/10.1080/15715124.2017.1375509
Houwing E-J, Estuarine (1999)Coastal and Shelf Science49:545–555. https://doi.org/10.1006/ecss.1999.0518
Khorrami Z, Banihashemi MA (2021) Development of a non-coupled algorithm for simulating long-term sedimentation in the Zonouz dam reservoir, Iran. J Soils Sediments 21:545–560. https://doi.org/10.1007/s11368-020-02714-z
Kim G-E, Kim J-H, Yoo S-H (2020) Assessing the environmental benefits of multi-purpose water uses of hydropower reservoirs on the Han River in South Korea. Energy Environ 31:1167–1180. https://doi.org/10.1177/0958305X19882407
Kim Y-J, Park C-S (2016) Stepwise deterministic and stochastic calibration of an energy simulation model for an existing building. Energy Build C 455–468. https://doi.org/10.1016/j.enbuild.2016.10.009
Kondolf GM (1997) Hungry water: Effects of Dams and Gravel Mining on River channels. Environ Manag 21:533–551. https://doi.org/10.1007/s002679900048
Kornman BA, Deckere EMGTD (1998) Temporal variation in sediment erodibility and suspended sediment dynamics in the Dollard estuary. Geol Soc Spec Publ 139:231–241. https://doi.org/10.1144/GSL.SP.1998.139.01.19
Krone RB (1962) Flume studies of transport of sediment in estrarial shoaling processes. Hydraulic Engineering Laboratory and Sanitary Engineering Research Laboratory, Berkeley, CA, USA
Kullback S, Leibler RA (1951) On information and sufficiency. Ann Math Stat 22:79–86. https://doi.org/10.1214/aoms/1177729694
Langendoen EJ, Mendoza A, Abad JD et al (2016) Improved numerical modeling of morphodynamics of rivers with steep banks. Adv Water Resour 93:4–14. https://doi.org/10.1016/j.advwatres.2015.04.002
Liang M, Voller VR, Paola C (2015) A reduced-complexity model for river delta formation; part 1: modeling deltas with channel dynamics. Earth Surf Dyn 3:67–86. https://doi.org/10.5194/esurf-3-67-2015
Lo EL, Bentley SJ, Xu K (2014) Experimental study of cohesive sediment consolidation and resuspension identifies approaches for coastal restoration: Lake Lery, Louisiana. Geo-Mar Lett 34:499–509. https://doi.org/10.1007/s00367-014-0381-3
Lumborg U (2005) Modelling the deposition, erosion, and flux of cohesive sediment through Øresund. J Mar Syst 56:179–193. https://doi.org/10.1016/j.jmarsys.2004.11.003
Luppi L, Rinaldi M, Teruggi LB et al (2009) Monitoring and numerical modelling of riverbank erosion processes: a case study along the Cecina River (central Italy). Earth Surf Process Landf 34:530–546. https://doi.org/10.1002/esp.1754
Mehta AJ, Hayter EJ, Parker WR et al (1989) Cohesive sediment transport. I: process description. J Hydraul Eng 115:1076–1093. 10.1061/(ASCE)0733-9429(1989)115:8(1076)
Mohammadi F, Kopmann R, Guthke A et al (2018) Bayesian selection of hydro-morphodynamic models under computational time constraints. Adv Water Resour 117:53–64. https://doi.org/10.1016/j.advwatres.2018.05.007
Mouris K, Schwindt S, Haun S et al (2022) Introducing seasonal snow memory into the RUSLE. J Soils Sediments. https://doi.org/10.1007/s11368-022-03192-1
Muehleisen RT, Bergerson J (2016) Bayesian Calibration - What, Why And How. In: International High Performance Buildings Conference. Purdue University, West Lafayette, IN, USA
Oberkampf WL, Trucano TG, Hirsch C (2004) Verification, validation, and predictive capability in computational engineering and physics. Appl Mech Rev 57:345–384. https://doi.org/10.1115/1.1767847
Oladyshkin S, Mohammadi F, Kroeker I, Nowak W (2020) Bayesian3 active learning for the gaussian process Emulator using information theory. Entropy 22:890. https://doi.org/10.3390/e22080890
Oladyshkin S, Nowak W (2019) The connection between bayesian inference and information theory for Model Selection, Information Gain and Experimental Design. Entropy 21:1081. https://doi.org/10.3390/e21111081
Olsen NRB, Haun S (2020) A numerical geotechnical model for computing soil slides at banks of water reservoirs. Int J Geo-Eng 11:22. https://doi.org/10.1186/s40703-020-00129-w
Olsen NRB, Hillebrand G (2018) Long-time 3D CFD modeling of sedimentation with dredging in a hydropower reservoir. J Soils Sediments 18:3031–3040. https://doi.org/10.1007/s11368-018-1989-0
Paola C, Voller VR (2005) A generalized Exner equation for sediment mass balance. J Geophys Res Earth Surf 110. https://doi.org/10.1029/2004JF000274
Paul M, Negahban-Azar M (2018) Sensitivity and uncertainty analysis for streamflow prediction using multiple optimization algorithms and objective functions: San Joaquin Watershed, California. Model Earth Syst Environ 4:1509–1525. https://doi.org/10.1007/s40808-018-0483-4
Rasmussen CE, Williams CKI (2006) Gaussian processes for machine learning. MIT Press, Cambridge, Mass
van Rijn LC (2020) Erodibility of mud–sand Bed Mixtures. J Hydraul Eng 146:04019050. https://doi.org/10.1061/(ASCE)HY.1943-7900.0001677
van Rijn LC, Barth R (2019) Settling and consolidation of soft mud–sand layers. J Waterw Port Coast Ocean Eng 145:04018028. https://doi.org/10.1061/(ASCE)WW.1943-5460.0000483
Rinaldi M, Nardi L (2013) Modeling interactions between Riverbank Hydrology and Mass failures. J Hydrol Eng - ASCE 18:1231–1240. https://doi.org/10.1061/(ASCE)HE.1943-5584.0000716
Scheurer S, Schäfer Rodrigues Silva A, Mohammadi F et al (2021) Surrogate-based bayesian comparison of computationally

expensive models: application to microbially induced calcite precipitation. Comput Geosci 25:1899–1917. https://doi.org/10.1007/s10596-021-10076-9
Schleiss AJ, Franca MJ, Juez C, De Cesare G (2016) Reservoir sedimentation. J Hydraul Res 54:595–614. https://doi.org/10.1080/00221686.2016.1225320
Schmelter ML, Stevens DK (2013) Traditional and bayesian statistical models in Fluvial Sediment Transport. J Hydraul Eng 139:336–340. https://doi.org/10.1061/(ASCE)HY.1943-7900.0000672
Schmelter M, Wilcock P, Hooten M, Stevens D (2015) Multi-Fraction bayesian sediment transport model. J Mar Sci Eng 3:1066–1092. https://doi.org/10.3390/jmse3031066
Shi BW, Yang SL, Wang YP et al (2012) Relating accretion and erosion at an exposed tidal wetland to the bottom shear stress of combined current–wave action. Geomorphology 138:380–389. https://doi.org/10.1016/j.geomorph.2011.10.004
Simons RK, Canali GE, Anderson-Newton GT, Cotton GK (2000) Sediment transport modeling: Calibration, Verification, and evaluation. Soil Sediment Contam 9:261–289. https://doi.org/10.1080/10588330091134239
Smith AFM, Gelfand AE (1992) Bayesian statistics without tears: a sampling-resampling perspective. Am Stat 46:84–88. https://doi.org/10.2307/2684170
Sun J, Zhang F, Zhang X et al (2021) Severely declining suspended sediment concentration in the heavily dammed Changjiang Fluvial System. Water Resour Res 57. https://doi.org/10.1029/2021WR030370. e2021WR030370
Verstraeten G, Poesen J (2001) Variability of dry sediment bulk density between and within retention ponds and its impact on the calculation of sediment yields. Earth Surf Process Landf 26:375–394. https://doi.org/10.1002/esp.186
Villaret C, Kopmann R, Wyncoll D et al (2016) First-order uncertainty analysis using algorithmic differentiation of morphodynamic models. Comput Geosci 90:144–151. https://doi.org/10.1016/j.cageo.2015.10.012
Walling DE, Webb BW (1996) Erosion and sediment yield: a global overview. In: Proceedings of the Exeter Symposium. IAHS, Exeter, UK, pp 3–19
Widdows J, Brinsley MD, Bowley N, Barrett C (1998) A benthic annular flume forIn SituMeasurement of suspension Feeding/Biodeposition rates and Erosion potential of intertidal cohesive sediments. Estuar Coast Shelf Sci 46:27–38. https://doi.org/10.1006/ecss.1997.0259
Winterwerp JC, van Kesteren WGM (2004) Introduction to the physics of cohesive sediment in the marine environment. Elsevier, Amsterdam; Boston
Zarfl C, Lumsdon AE, Berlekamp J et al (2015) A global boom in hydropower dam construction. Aquat Sci 77:161–170. https://doi.org/10.1007/s00027-014-0377-0

Publication III.

Assessment of uncertainties in a complex modeling chain for predicting reservoir sedimentation under changing climate

Table 5.3. Metadata of publication III

Title	Assessment of uncertainties in a complex modeling chain for predicting reservoir sedimentation under changing climate
Authors	María Herminia Pesci, **Kilian Mouris**, Stefan Haun, Kristian Förster
Author Contribution	MHP and KM contributed equally to the manuscript
Journal	Modeling Earth Systems and Environment
submitted	September 21, 2022
accepted	January 18, 2023
published	February 11, 2023 (online)
DOI	https://doi.org/10.1002/esp.4889

Modeling Earth Systems and Environment (2023) 9:3777–3793
https://doi.org/10.1007/s40808-023-01705-6

ORIGINAL ARTICLE

Assessment of uncertainties in a complex modeling chain for predicting reservoir sedimentation under changing climate

María Herminia Pesci[1] · Kilian Mouris[2] · Stefan Haun[2] · Kristian Förster[1]

Received: 21 September 2022 / Accepted: 18 January 2023 / Published online: 11 February 2023

Abstract

Long-term predictions of reservoir sedimentation require an objective consideration of the preceding catchment processes. In this study, we apply a complex modeling chain to predict sedimentation processes in the Banja reservoir (Albania). The modeling chain consists of the water balance model WaSiM, the soil erosion and sediment transport model combination RUSLE-SEDD, and the 3d hydro-morphodynamic reservoir model SSIIM2 to accurately represent all relevant physical processes. Furthermore, an ensemble of climate models is used to analyze future scenarios. Although the capabilities of each model enable us to obtain satisfying results, the propagation of uncertainties in the modeling chain cannot be neglected. Hence, approximate model parameter uncertainties are quantified with the First-Order Second-Moment (FOSM) method. Another source of uncertainty for long-term predictions is the spread of climate projections. Thus, we compared both sources of uncertainties and found that the uncertainties generated by climate projections are 408% (for runoff), 539% (for sediment yield), and 272% (for bed elevation in the reservoir) larger than the model parameter uncertainties. We conclude that (i) FOSM is a suitable method for quantifying approximate parameter uncertainties in a complex modeling chain, (ii) the model parameter uncertainties are smaller than the spread of climate projections, and (iii) these uncertainties are of the same order of magnitude as the change signal for the investigated low-emission scenario. Thus, the proposed method might support modelers to communicate different sources of uncertainty in complex modeling chains, including climate impact models.

Keywords Uncertainty · Modeling chain · Model parameters · Climate projections · Runoff · Reservoir sedimentation

Introduction

Albania possesses adequate conditions for hydroelectricity production because of its location in the Balkans and its mountainous topography. Considering that the country's power supply is, with a value of 99%, almost exclusively based on hydroelectric power (IEA 2022; Lehner et al. 2005; Statkraft 2019), the Devoll River offers great potential for hydropower development due to its large streamflow. However, as a result of the active erosion processes taking place in the catchment and the consequent transport of sediments, it is also considered the most turbid river that drains into the Mediterranean Sea (Ardıçlıoğlu et al. 2011). Constructed reservoirs along the river interrupt the sediment continuum, resulting in the deposition of sediments and progressive reservoir sedimentation.

In addition, climate change may not only directly (e.g., change in temperature and precipitation) but also indirectly (e.g., change in land use) influence erosion processes in the catchment, resulting in higher sediment loads and amplified sedimentation processes in these reservoirs (e.g., Plate 1993; Walling and Fang 2003). Therefore, the lifetime of planned and constructed reservoirs and the efficiency of hydropower production may decrease (Mahmood 1987). These trends are also predicted for other areas and catchments within Europe. According to Wagner et al. (2017), the average annual electricity generation for the Alpine region will slightly decrease by the year 2050, due to the effects of climate change. Additionally, Panagos et al. (2021) stated that climate change is the main cause of the increase in mean soil erosion rates on agricultural land in Europe by the year 2050. Hence, climate change will have negative impacts on soil erosion, especially

✉ María Herminia Pesci
pesci@iww.uni-hannover.de

[1] Institute of Hydrology and Water Resources Management, Leibniz University of Hannover, Hannover, Germany

[2] Institute for Modeling Hydraulic and Environmental Systems, University of Stuttgart, Stuttgart, Germany

in regions where this process can already be considered critical, such as the Devoll River basin (Li and Fang 2016).

While several studies show an expected annual increase in sediment yield due to future climate change scenarios (Azari et al. 2016; Chen et al. 2020; Li et al. 2022), others indicate that sediment yield could even decrease in some regions (Bussi et al. 2014; Hirschberg et al. 2021). These contrasting findings suggest that the behavior of hydrological and morphological processes under the impacts of climate change depends not only on regional characteristics but also on the models involved, especially the climate models that provide the forcing data. As part of the DIRT-X project (https://dirtx-reservoirs4future.eu/), the dynamics of the different hydrological and morphological processes in the Devoll catchment are identified and their response to climate change is quantified. Hence, a special focus is given to the reservoir inflow (runoff and transported sediments) and sedimentation processes within the reservoir. Since the latter relies on the behavior of the inflow boundaries, a modeling chain is required to predict the future development of all involved variables and finally to predict the bed level changes within the reservoir (target variable).

Even though several studies were carried out for different regions worldwide to predict the erosion processes in the catchment and the resulting sediment yield, they all focused on a single model. In addition, they focused mainly on the catchment and no hydro-morphological processes in the river or reservoir were considered. For example, Shrestha et al. (2013), Azari et al. (2016), Zettam et al. (2017), Santos et al. (2021) and Li et al. (2022) employed the Soil and Water Assessment Tool (SWAT) to predict the sediment yield coming from catchments in Laos, Iran, Algeria, Brazil, and China, respectively. In the study carried out by Bronstert et al. (2014), the Water Availability in Semi-arid Areas with SEdiment Dynamics (WASA-SED) model was implemented to predict water and sediment fluxes in semi-arid environments. Other examples can be found in Nerantzaki et al. (2015) and Nunes et al. (2013), who also applied the SWAT model in Mediterranean catchments for predicting suspended sediment transport and erosion dynamics, respectively. Although the latter applied a chain of models combining SWAT with a physically based distributed erosion model, reservoir sedimentation processes were not included. Wagner et al. (2017) also focused on a modeling chain applied to an Alpine catchment. However, the modeling chain consists only of a hydrological and a hydropower model, thus the focus is not on intermediate erosion and sediment transport processes as in this study. More recently, Wild et al. (2021) developed a Python-based framework to simulate runoff, sediment, and hydropower production. Although several processes are considered in the model, the focus is on decision-making and the evaluation of possible reservoir configurations. Furthermore, the model has some limitations regarding the representation of physical processes (e.g. runoff generation), where it still relies on the output of other external models.

The novelty of our study is the development and application of a process-based modeling chain composed of three different models that aim to predict the sedimentation processes in the Banja reservoir under changing hydro-climatic conditions. With this modeling chain, we ensure a detailed representation of the physical processes leading to reservoir sedimentation, while exploiting the capabilities of state-of-the-art models tailored to particular processes. Since each model works independently and has different input and output variables (e.g., runoff or sediment yield), the subsequent models rely on accurate output variables to ensure the applicability of the modeling chain for predicting bed elevation as the final target variable.

However, when more than one model is involved in predicting a target variable, superposition effects of uncertainties from different sources may occur, resulting in a propagation and an increase in the uncertainty of the final target variable. Since the selection of model parameters and their associated values might be challenging, e.g., due to a lack of measurements, it is of interest to know not only their impact on the final simulation results but also the confidence of these results (Moges et al. 2021). Other types of uncertainties are related to the Global Climate Models (GCMs), to the downscaling techniques used for linking the large scale of GCMs to the regional models (Regional Climate Models, RCM), and finally to the model scale (Prudhomme and Davies 2009).

The significance of the aforementioned uncertainties is investigated and presented in this study. The question that arises at this point is: Are simulation results more affected by perturbations in the model parameters (parameter uncertainty) than by the spread of climate projections (climate model uncertainty)? To answer this question, approximate uncertainties related to model parameters are calculated using a simplified method and compared to the spread of climate projections by analyzing three GCM/RCMs and the Representative Concentration Pathway RCP2.6. The selection of RCP2.6 is motivated by the fact that this (mitigation) scenario is subject to the smallest change signals amongst all available emission scenarios. Consequently, results from parameterizations with only small variations are not compared to higher change signals that would result from high emission climate scenarios.

Materials and methods

Study area

The study area is located in the Devoll River catchment, upstream of the Banja reservoir in Albania, approx. 70 km

south of the capital city Tirana. The catchment covers a surface area of 3140 km^2 with varying topography and altitudes, ranging from 100 to 2000 m a.s.l. Figure 1a shows the location of the study area within Albania and the catchment area. In this figure, the catchment is subdivided into two subcatchments (Fig. 1c), which were delineated according to the topography and location of the gauging stations (Banja and Kokel). The main city located in the study area is Korça and is also shown in the figure.

Since Albania belongs to the Mediterranean climatic belt, the climate in the study area is mainly characterized by dry and hot summers and mild, rainy winters (Eftimi 2010). The mean annual temperature in Korça is 10.3 °C, with a mean value of 19.9 °C during summer (July) and 0.9 °C during winter (January) (climate-data.org 2019). The mean annual precipitation in the highland plain near Korça is around 800 mm yr^{-1} while the Western part receives up to 1600 mm yr^{-1} (Almestad 2015; climate-data.org 2019; Eftimi 2010). However, in higher altitudes, snowfall is common during the winter months. Snow cover depths and days with snow cover vary strongly, depending on the location within the catchment (Mouris et al. 2022). Although the majority of the study area is forested (30%) and covered by scrubs and herbaceous vegetation (25%), agriculture predominates in the Korça plain. Since parts of the catchment are characterized by barren and steep slopes, loose soil results in high erosion and subsequently high sediment loads entering the Devoll River from the catchment. Hence, reservoir sedimentation will be a severe challenge for existing and planned reservoirs along the Devoll River. The river is dammed approximately 160 km from its source, forming the Banja reservoir located near the town Gramsh. The embankment dam with a clay core has a maximum height of 80 m (between 95 and 175 m a.s.l.) and was impounded in 2016, with a maximum storage capacity of the reservoir of approx. 400 million m^3.

Data availability

Meteorological data

Within the study area, four meteorological stations are in operation and record daily values of precipitation, temperature, and wind speed. Measurements are available for the period from 09/2015 to 08/2020. Other variables, such as

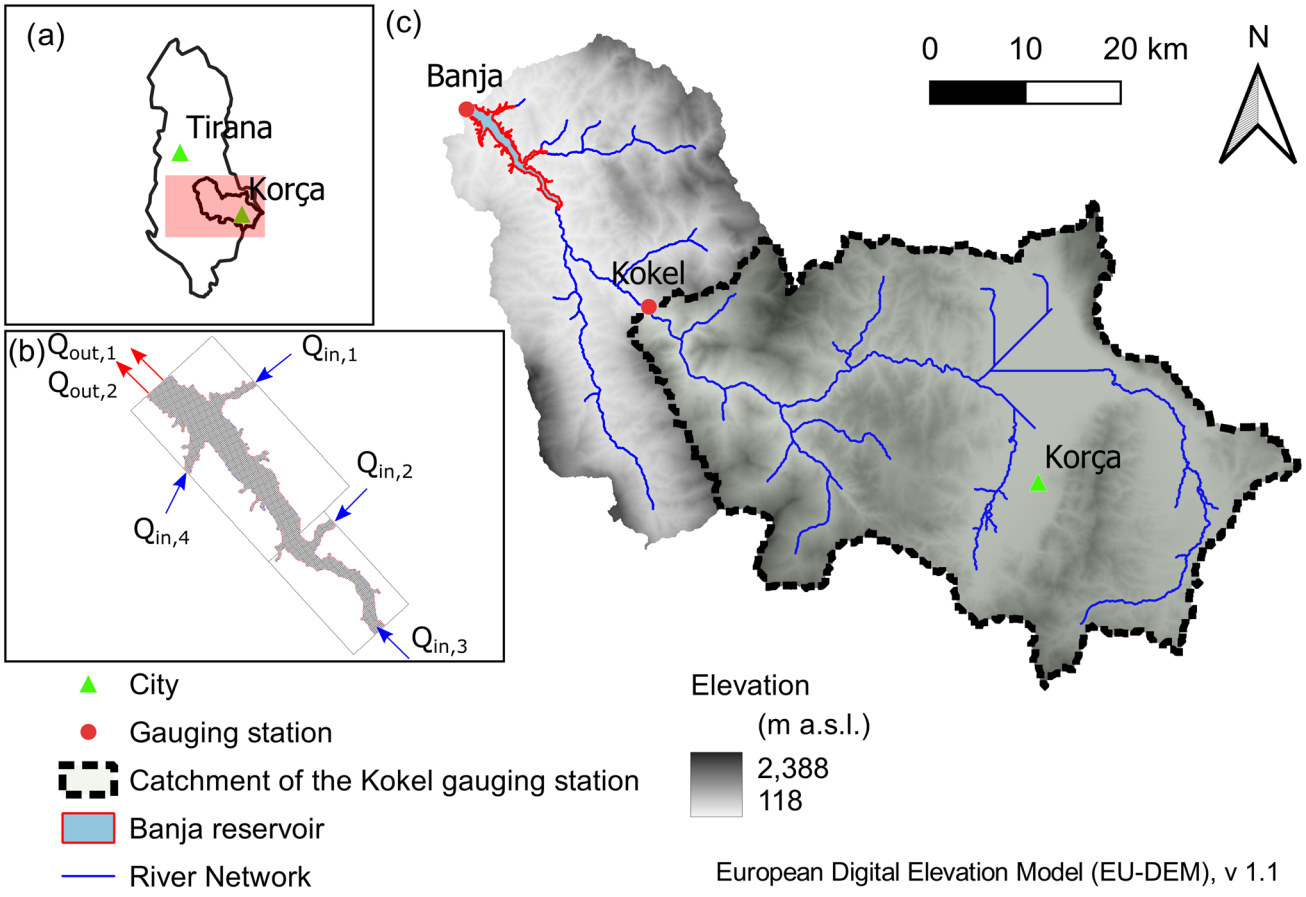

Fig. 1 **a** Location of the study area within Albania; **b** important tributaries and outflow boundaries of the Banja reservoir; **c** topography, subcatchments, gauging stations and location of the Banja reservoir. (adapted from the European Environment Agency (2016))

radiation and relative humidity, are not recorded by these stations. Thus, the prediction of the hydrological response of the catchment becomes quite challenging, since a long-term time series of all meteorological variables would be required. As a viable alternative, the ERA5 reanalysis dataset is used for the hydrological simulations. This dataset is available with an hourly resolution on a grid of approx. 31 × 31 km since 1959 onwards (Copernicus Climate Change Service 2017).

Measured data

Hourly measurements of runoff are available at the Kokel gauging station, covering the period from 03/2016 to 04/2018. Furthermore, suspended sediment concentration measurements are available at the same gauging station. The runoff and the suspended sediment concentrations are obtained by using the acoustic backscatter signal from two side-looking H-ADCPs (Horizontal-Acoustic Doppler Current Profiler; 0.6 and 1.2 MHz). The approach used to calculate suspended sediment concentrations based on acoustic backscatter data for this study site is described in Aleixo et al. (2020). Nevertheless, these measurements are only available for water depths at the gauging station exceeding 1 m. In the final step, the suspended sediment load is calculated by using the measured suspended sediment concentration and the associated runoff.

In addition, there are Digital Elevation Models (DEM) available from two bathymetric surveys of the Banja reservoir. The first survey was carried out in 2016, shortly before the impoundment of the reservoir. It was a drone survey of the terrain and a subsequent structure-from-motion post-processing. The second survey was conducted in 2019, after 3 years of operation, by moving ADCP measurements and was used to calibrate the reservoir model. A digital elevation model of differences (DoD) of the two surveys shows a general sedimentation trend, with an average deposition height of 2.7 m in the upstream part (> 5 km distance to the dam) of the reservoir.

Modeling chain

The prediction of sedimentation processes within a reservoir involves several preceding catchment processes, which need to be considered in the simulations. To tackle these processes in a reliable manner, hydrological, soil erosion, sediment transport, and hydro-morphodynamic models are necessary. In some cases, some of these processes can be simulated in a simplified way by a single model (e.g. with SWAT). However, limitations often arise regarding the representation of physical processes, and this must be considered when analyzing the results. Due to the progressive development of modeling tools and their specialization in certain processes, the use of multiple state-of-the-art models in a modeling chain seems to be a promising approach to increase the quality of simulation results. For these reasons, a modeling chain composed of different and independent models is applied in this study to benefit from several models with a specialization in particular processes.

The schematic modeling chain is depicted in Fig. 2. Besides the models used, the target variables (output variables) of each model are shown, which then serve as input for the subsequent model. For example, the target variable of the soil erosion and sediment transport model (RUSLE-SEDD) is the suspended sediment load, which serves as input for the hydro-morphodynamic reservoir model (SSIIM 2). The final target variable of the modeling chain is the bed elevation along the thalweg of the Banja reservoir. A description of each model is presented in the following section.

Model setups

This section summarizes the main processes included in the three models used in the modeling chain for the Devoll catchment and the Banja reservoir.

Water balance model

The hydrological processes are simulated by the **Wa**ter Flow and Balance **Si**mulation **M**odel (**WaSiM**, Schulla 1997, 2021). It is a physically based distributed model capable of representing the water cycle above and below the land surface. WaSiM uses physically based modeling approaches for the simulation of the different hydrological components (Schulla 2021). In this study, the Richards version 10.04.07 is used, including the most recent snow canopy interception sub-model (Förster et al. 2018). The model domain has a spatial and temporal resolution of 1 km^2 and 3 h, respectively. The calibration period spans from 05/2016 to 04/2018, for which measured runoff is available. A first year (05/2015–04/2016) is considered as a warm-up period.

Table 1 summarizes the main processes involved in WaSiM and the selected methods for obtaining the values for each of them. As the ERA5 dataset is available with a spatial resolution coarser than the model grid, the values are interpolated using the methods described in Table 1.

Soil erosion and sediment transport model

Soil loss and sediment transport are calculated at the catchment scale with the **R**evised **U**niversal **S**oil **L**oss **E**quation (**RUSLE**) model (Renard 1997) in combination with the **Se**diment **D**elivery **D**istributed (**SEDD**) model (Ferro and Porto 2000). The RUSLE calculates the gross soil erosion in the catchment, while the SEDD model estimates sediment transport and delivery. The model is

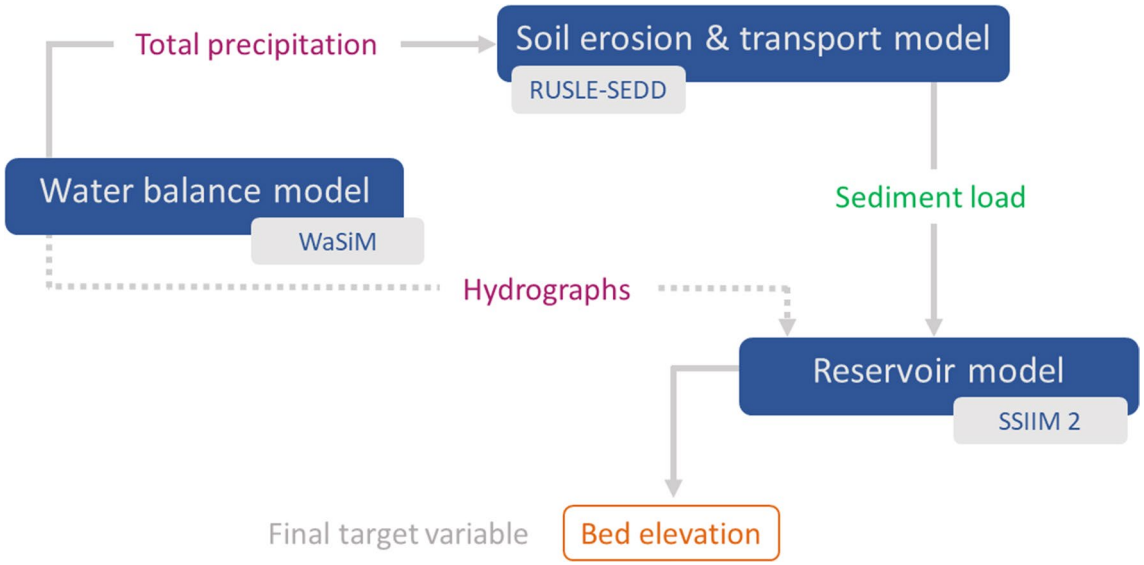

Fig. 2 Selected modeling chain and target variables for the study case of the Devoll catchment and the Banja reservoir

Table 1 Summary of the main sub-processes and approaches selected for the WaSiM simulations

Sub-processes	Selected method(s)	Comments
Temperature, precipitation and relative humidity interpolation	IDW + EDRINT[a]	Linear combination of IDW and EDRINT
Wind speed and global radiation interpolation	IDW	–
Evapotranspiration	Penman-Monteith approach for ETP[b]	ETR[c] estimated from actual soil water content and actual capillary pressure
Snow accumulation and snow melt	Energy balance approach	The fraction of snow on the total precipitation is given by a threshold temperature
Interception	Includes a bucket canopy model	Snow accumulation and melt is computed for both canopy and the surface below
Soil model	Richards approach	Model of fluxes within the unsaturated soil zone
Groundwater model	Integrated conceptual approach	Baseflow is generated as exfiltration from the groundwater system into the river surface system
Routing model	Kinematic wave approach + single linear storage	Translation is determined from Manning's formula; single reservoir to account for retention

[a]IDW = Inverse distance weight method, EDRINT = Elevation dependent regression with internal pre-processing

[b]ETP = Potential evapotranspiration

[c]ETR = Real evapotranspiration

spatially discretized into cells of 25 m x 25 m. Since this model combination enables the estimation of a monthly or annual suspended sediment load for any point in the river network, the sediment input to the reservoir is computed. Monthly suspended sediment loads from 05/2016 to 04/2018 are used for the calibration of the presented RUSLE-SEDD model.

The soil loss A [t ha^{-1} yr^{-1}] is determined as a multiplication of six erosion risk factors (Eq. (1)), which are summarized in Table 2. More detailed information on the input datasets, applied methods, and codes can be found in Mouris et al. (2022).

$$A = R \cdot K \cdot C \cdot L \cdot S \cdot P \quad (1)$$

Reservoir model

The fully 3d numerical model **S**ediment **S**imulation **I**n **I**ntakes with **M**ultiblock Option (**SSIIM 2**) is used to simulate flow characteristics, suspended sediment transport,

Table 2 Summary of the soil loss erosion risk factors

Risk factor	Unit	Description
R	MJ mm (ha h yr)$^{-1}$	Rainfall erosivity factor calculated from post-processed precipitation data from the water balance model according to Diodato and Bellocchi (2007)
K	t ha MJ^{-1} mm^{-1}	Soil erodibility factor calculated according to Wischmeier and Smith (1978)
C	–	Cover management factor calculated based on the land cover (European Environment Agency 2019)
L, S	–	Slope length and slope steepness are usually combined and represent the effect of topography on soil erosion according to Zhang et al. (2017)
P	–	Support practice factor expresses the influence of contouring on soil erosion, applied only to agricultural land

and morphodynamic processes in the Banja reservoir (Olsen 2018). SSIIM 2 solves the Reynolds-averaged Navier–Strokes equations (RANS) in three dimensions and uses a finite volume method for discretization. The adaptive grid consists of cells with a spatial resolution of 50 x 50 m, and up to 10 vertical cells in the deepest zones of the reservoir. Sediment samples demonstrate that the sediment depositions within the reservoir predominantly consist of cohesive sediments. Consequently, bedload transport is not considered in this study. Besides the initial bathymetry, the runoff hydrographs from the WaSiM model and sediment loads from the RUSLE-SEDD model are used as input data for the main tributaries. Hence, in this study, four main tributaries and two outflows (spillway and turbine) are considered (Fig. 1b). Due to the implicit time discretization, time steps up to 5400 s are used in this study and enable long-term (08-2016–12-2100) 3d sedimentation modeling in a reasonable computing time (3.5 weeks per run using 8 cores, 3.7–4.8 GHz).

Uncertainty quantification of model parameters

Several types of uncertainties are expected in modeling, arising from the complex behavior of environmental systems, simplifications in models, unknown boundaries, and missing or inaccurate input data (Shoarinezhad et al. 2020). Some of these uncertainties are related to parameters used to simulate different processes in each model. In this study, the variation in the simulation results (target variables) due to perturbations in selected model parameters is analyzed. The main objective is to achieve an approximation of the parameter's uncertainties by using a simplified method, which is more economic in terms of computing time compared to other stochastic methods (e.g., Monte-Carlo simulations). Hence, the analysis of the variations in the target variable is performed with a First-Order Second-Moment Method (FOSM) (Gelleszun et al. 2017). The FOSM method, which was successfully validated by Gelleszun et al. (2017), is based on the variance-covariance propagation and, according to Kunstmann et al. (2002), the results are comparable to the ones obtained by applying more sophisticated methods (such as Monte-Carlo methods).

The covariance matrix of the selected target variable y is expressed by the following Eq. (2):

$$C_{yy} = AC_{xx}A^T, \tag{2}$$

where C_{yy} is the covariance matrix of the calculated target variable y, with size $m \times m$; C_{xx} is the empirical covariance matrix of the selected parameters, with size $n \times n$; A is the Jacobian, sensitivity or functional matrix, with size $m \times n$ and contains the partial derivations of the model with respect to its parameters; m is the number of time steps and n is the number of parameters.

The variance of the target variable y can be obtained from the diagonal of the covariance matrix C_{yy}, according to Eq. (3):

$$var(y) = \sum_{j=1}^{n}\sum_{k=1}^{n} a_{ij}a_{ik}c_{jk}, \tag{3}$$

where a_{ij} are the elements of the Jacobian matrix A and c_{jk} are the elements of the empirical covariance matrix of the parameters C_{xx}.

The variance-covariance propagation (Eqs. (2) and (3)) gives the confidence intervals of the model with respect to the perturbations of the selected parameters. The empirical covariance matrix of the parameters, C_{xx}, can be determined with the following Eq. (4):

$$C_{xx} = {S_e}^2\left(A^TA\right)^{-1}, \tag{4}$$

where ${S_e}^2$ is the empirical residual variance (scalar value) that can be obtained for the entire simulation period according to Eq. (5):

$${S_e}^2 = \frac{\sum\left[y_{obs} - y_{sim}\right]^2}{u - n}. \tag{5}$$

y_{obs} is the observed data (of the target variable y); y_{sim} is the simulated data (of the target variable y); u is the length of the

Table 3 Target variables (output) of each model in the modeling chain

Model	Target variable	Unit	Comment
WaSiM	Runoff	mm 3 h^{-1}	Simulated runoff at Kokel
RUSLE-SEDD	Suspended sediment yield	tons $month^{-1}$	Simulated suspended sediment yield at Kokel
SSIIM 2	Bed elevation	m a.s.l.	Simulated bed elevation along the thalweg of the Devoll river within the reservoir

available observed and simulated data and n is the number of selected parameters.

The Jacobian matrix A is calculated by numerical derivation in the optimum (central differences as an approximation of the derivatives that cannot be determined analytically in the case of numerical models). Then, each parameter is changed ± 1% from its optimum value (Hill 1998), according to Eq. (6):

$$y_{\_id} = \frac{y_{\_il} - y_{\_iu}}{2 \times 0.01 \times opt\_value\_i}, \quad (6)$$

where i is the selected parameter; $y_{\_id}$ is the target variable y obtained as an approximation of the derivatives, which composes the Jacobian Matrix A; opt_value_i is the optimum value of parameter i, obtained after calibration of the model; $y_{\_il}$ is the target variable y obtained with the lower value of parameter i (opt_value_i – 1%) and $y_{\_iu}$ is the target variable y obtained with the upper value of parameter i (opt_value_i + 1%).

The empirical variance ${S_e}^2$ (Eq. (5)) gives an idea of the parameter perturbations in relation to the chosen optimization algorithm, which is used during the calibration of the model, to obtain the set of parameters that best simulate the target (output) variable y in each model. The empirical standard deviation, which has the same units as the target variable y, can be obtained as $S_e = \sqrt{{S_e}^2}$.

Finally, the approximate uncertainties of the model parameters can be represented with the standard deviation of the target variable, expressed by the root square of the variance (Eq. (7)):

$$std(y) = \sqrt{var(y)} \quad (7)$$

Target variables and selected model parameters

A target variable (output) is selected for each model. Furthermore, we choose a maximum of five parameters per model for the analysis of uncertainties to constraint computing times. Table 3 shows the target variable (output) for each of the models, whereas Table 4 summarizes the selected model parameters and their corresponding optimum values, which were obtained from the calibration processes for the single models. In addition, the lower value refers to the perturbation when the parameters have been decreased by -1%, while the upper value refers to the perturbation when the value has been increased by + 1% from the optimum value. For spatially distributed parameters, such as the C factor, or seasonal factors, such as the R factor, the respective mean values are given in Table 4. In all cases, the selected model parameters are the most sensitive ones and have the greatest impact on the simulation results in each model.

A perfect agreement between observed and simulated bed levels in the reservoir is not to be expected since the WaSiM and RUSLE-SEDD models were calibrated for the Kokel gauging station and not for the reservoir (see Fig.1). Consequently, the deviations in reservoir bed elevation may be closely related to under- or overestimation of the runoff and sediment load entering the reservoir, since they were not measured directly at the reservoir inflow.

Workflow

In total, 11 runs were carried out with WaSiM, 17 runs with RUSLE-SEDD, and finally 23 runs with SSIIM 2 to capture the changes in the parameters. Figure 3 shows the selected workflow applied to the modeling chain.

Model simulations under different climate projections

The modeling chain is used to predict the catchment's response under different future climate projections. Table 5 summarizes the GCM and RCM model combinations used under different Representative Concentration Pathways (RCP). These datasets are provided with a spatial resolution of 0.11 degrees (EUR-11 grid, WCRP 2009) and with a 3-hourly time step. As reference data, the ERA5 reanalysis dataset is used, considering a reference period from 01/1981 to 12/2010. The bias adjustment is performed according to the MultI-scale bias AdjuStment (MidAS) tool, v0.2.1, which provides cascade adjustments in time and space, using a day-of-year scaling step (Berg et al. 2022).

RCPs represent climate projections under different greenhouse gas concentrations that might lead to an increase in radiate forcing by the end of the century. For example, RCP2.6 is the lowest of all RCPs and expects a radiative forcing of 2.6 W m^{-2} by 2100. Furthermore, each RCP is related to a global mean temperature increase compared to a reference period considered from 1986 to 2005. In the

case of RCP2.6, the global mean temperature increase is 1.0 °C, for RCP4.5 1.8 °C, and for RCP8.5 3.7 °C (Collins et al. 2013).

The main objective of our study is to scrutinize whether the spread of the climate projections for future simulations is broader than the variations in simulation results as a consequence of perturbations in the model parameters. In other words, we aim to analyze whether the uncertainties inherent to model parameterization are higher than uncertainties from climate projections. The perturbations in the model parameters are represented by a ± 1% change of their optimum value, according to the method previously described. For the comparison with the spread of the climate projections, RCP2.6 is selected. In this way, a tangible comparison (1% parameter variation vs. 1.0 °C increase in temperature) is carried out. Furthermore, we would like to highlight that in this case, the smallest climate change signals are generated and thus the results of this RCP are used for comparison to the parameter perturbation approach. By doing so, we avoid overestimating climate change signals. If the spread of the climate projections exceeds the approximate parameter uncertainties in the low emission scenario, this is also to be expected for the high and medium emission scenarios.

Results

The bed level changes along the upper part of the thalweg (> 5 km distance to the dam) of the Banja reservoir are presented, considering uncertainties in selected model parameters, but also different climate projections. The results of the climate impact simulations refer not only to the final target variable of the modeling chain (bed elevation along the thalweg of the Banja reservoir) but also to intermediate results (climate variables, monthly runoff, and sediment yield). Finally, a comparison between the uncertainties of the model parameters and the climate projections is performed. Figure 4.

Uncertainty quantification of model parameters

To assess the uncertainties associated with model parameters and their impact on the simulation results, the final target variable of the modeling chain is analyzed. Figure 3 shows the measured bed elevation along the thalweg of the Banja reservoir in 2016 and 2019, together with the simulated bed elevation in 2019. In addition, the standard deviation (dark gray shaded area) is shown, which considers the spreading of the simulation results from a total of 23 model runs, and may hence be related to the approximated uncertainties of the model parameters. The figure also includes the standard deviation obtained only for the reservoir model and without considering the variations of parameters from the previous models (yellow shaded area), thus focusing only on the parameters of the reservoir model. In both cases, the values refer to the standard deviation, which was obtained after applying Eq. (7).

The average value of the standard deviation for the reservoir model only (after Eq. (7)) is 0.28 m. The average standard deviation for the entire modeling chain, considering the uncertainties of all 11 parameters, is 0.64 m. Hence, it becomes obvious, that the largest uncertainties in the modeling chain result from the reservoir model. Figure 3 indicates in addition that higher variations of the target variable are located near the head of the reservoir, where a delta formation is visible.

Model simulations under different climate projections

Since precipitation and temperature are important forcing variables for the generation of runoff, soil erosion, and the consequent transport of sediments into the reservoir, a special focus is set on future changes in these variables. Figure 5a shows the decadal changes in the mean monthly precipitation regarding the reference period (1981–2010). The values are taken as an average value of the entire catchment and refer to the ensemble mean of the three GCM/RCMs and for RCP2.6. A positive change indicates an increase in the mean monthly precipitation values (green color), whereas a negative change indicates a decrease in the values (red color). Although there is no clear trend in the changes between the decades (y-axis), a reduction in precipitation during the summer months is visible (x-axis), whereas at the same time an increase during the winter months will occur.

Figure 5b shows the mean monthly changes in temperature, where a positive change suggests that temperature will increase in the future (red color) and a negative change suggests a decrease (blue color). The figure makes it visible that the mean monthly temperature will face an increase in the future, reaching higher values, especially during the spring months (April–May).

Finally, changes in mean monthly runoff at Kokel are analyzed (Fig. 5c). In this figure, a positive change suggests that the runoff will increase in the future (purple color) and a negative change suggests a decrease (brown color). In this case, there is a clear trend in the decreasing mean monthly runoff during the spring months (April–May), becoming larger by the end of 2050 and 2090. The reduction of the mean monthly runoff during spring is related to the rise in mean monthly temperatures, which leads to an increment in the evapotranspiration values and therefore less water will be available as runoff. Furthermore, the early melting of snow (shifted to late winter months) and the decrease in snow storage

Table 4 Summary of selected model parameters for each model, including definition and units

Model	Param.	Definition	Sub-process	Unit	Optimum value	Lower value	Upper value
Water balance model	k_d	Recession constant for surface runoff	Direct runoff *	h	5.0000	4.9500	5.0500
	k_i	Recession constant for interflow	Interflow *	h	21.6375	21.4211	21.8539
	d_r	Drainage density for interflow	Interflow *	m^{-1}	6.0642	6.0036	6.1248
	k_b	Recession constant for baseflow	Baseflow *	m	1.4056	1.3915	1.4197
	Q_0	Scaling factor for baseflow	Baseflow *	mm h^{-1}	0.2186	0.2164	0.2208
Soil erosion & transport model	C	Cover and management factor	Erosion	-	0.007671	0.007594	0.007748
	β	Basin-specific parameter	Sediment delivery ratio	h^{-1}	0.5639	0.5583	0.5695
	R_{seas}	Seasonal factor for rainfall erosivity factor	Erosion	MJ mm (ha h yr)$^{-1}$	0.4860	0.4811	0.4909
Reservoir model	F_26	Fraction of compacted sediment in bed deposits	Erosion/Deposition	-	0.3500	0.3465	0.3535
	v_s	Settling velocity	Deposition	m s^{-1}	34.83×10^{-6}	34.48×10^{-6}	35.18×10^{-6}
	actlay	Active layer thickness	Erosion/Deposition	m	0.3000	0.2970	0.3030

*All sub-processes belong to the unsaturated zone model.

The optimum value refers to the value obtained from the calibration and lower and upper values refer to the ±1% variation of the optimum value

contribute to the reduction of runoff during spring. On the contrary, an increase in the mean monthly runoff is predicted mostly for the winter months. This is also due to the rise in mean temperatures, leading to early snowmelt, less snowfall and more rainfall.

Uncertainty assessment: parameter vs. climate model uncertainties

In this section, the uncertainties in model parameters and their impacts on simulation results are compared with the spread of climate projections for RCP2.6. In addition to the final target variable (i.e. bed elevation along the thalweg of the reservoir), results are also shown for the output variables of each individual model in the chain.

Mean monthly runoff at Kokel

The diagrams on the left in Fig. 6a show the mean monthly runoff at Kokel obtained from the water balance model, for three different periods as an ensemble mean of the three GCM/RCMs and RCP2.6 (rows, from bottom to top): 2011–2040, 2041–2070, and 2071–2100 and its corresponding standard deviations. In addition, the mean monthly runoff for the reference period (1981–2010, black dashed line) together with the mean monthly standard deviation due to uncertainties in model parameters (gray shaded area) are presented.

The hydrographs plotted on the bottom row for the period 2011–2040 indicate that the mean monthly runoff will not change significantly in the near future. However, a slight increase is expected during winter (an increase of 9.4 mm for January). For the rest of the year, the values will be on a similar level.

When looking at the second half of the century (middle row, period 2041–2070), there is a clear shift in the maximum value from spring (April) to late winter (March). Furthermore, the peak is below the values of the reference period (a decrease of 7.2 mm is expected for April). Similar results are obtained for the last period (upper row, period: 2071–2100), where the shift in peak flow from April to March manifests itself and a decrease of almost 9.0 mm is expected for the peak runoff.

Observing Fig. 6a, it is possible to conclude that the approximate uncertainties arising from model parameters in the water balance model are by far smaller (almost 5 times) than the ones coming from the climate impact models (spread of climate projections, measured as the standard deviation of the ensemble mean). On average, these values rise from 3.8 mm $month^{-1}$ to 15.2 mm $month^{-1}$

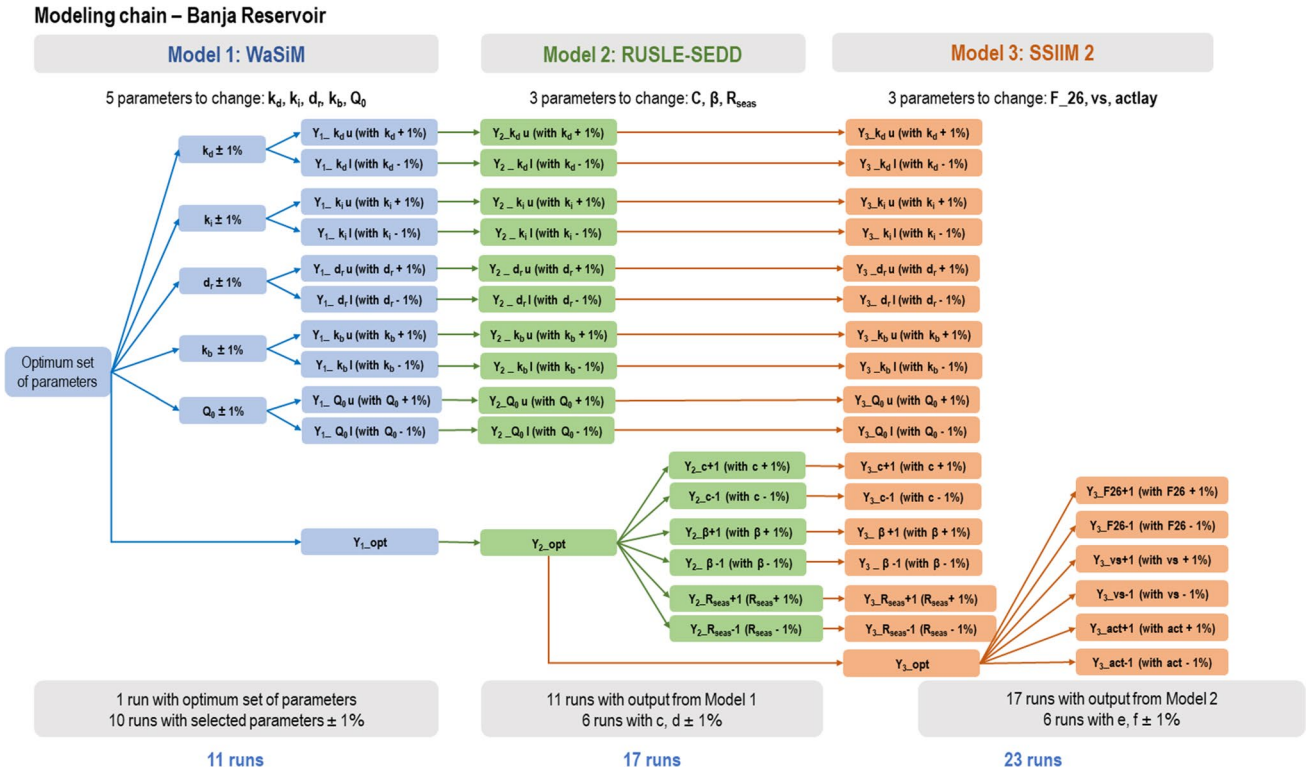

Fig. 3 Selected workflow applied for the modeling chain of the Banja reservoir located in the Devoll catchment (Albania). The three models, their parameters, perturbations and the number of model runs are shown as well

Table 5 GCMs and RCMs used in the modeling chain

GCM	RCM
ICHEC-EC-EARTH	SMHI-RCA4_v1a
MPI-M-MPI-ESM-LR	SMHI-RCA4_v1
MOHC-HadGEM2-ES	KNMI-RACMO22E_v2

(300% rise), 18.6 mm month^{-1} (389% rise), and 19.3 mm month^{-1} (407% rise) for the first, second, and third period, respectively.

Mean monthly sediment yield at Kokel

The diagrams on the right in Fig. 6b show the mean monthly sediment yield at Kokel, obtained from the soil erosion and sediment transport model, for three different periods as an ensemble mean for the three GCM/RCMs and RCP2.6 (rows, from bottom to top): 2011–2040, 2041–2070 and 2071–2100 and its corresponding standard deviation. Similarly to the mean monthly runoff, the black dashed line indicates the mean monthly sediment yield for the reference period (1981–2010). In addition, the mean monthly standard deviation regarding uncertainties from model parameters (gray shaded area) is shown in the figure.

The sediment yield behaves similarly to runoff. Consequently, the maximum values are expected from February to April (between the end of the winter season and the beginning of the spring months). In general, the mean maximum sediment yield will not experience great changes, except for the near future, where an increase of around 20,000 tons is expected for March, which corresponds to the predicted increase in runoff.

Similar to the mean monthly runoff, the values are not expected to change significantly during summer (low-flow season) because erosion is strongly correlated with precipitation and thus with runoff. Furthermore, the standard deviation of the sediment yield regarding perturbations in the model parameters (gray shaded area) is also smaller (almost 5 times) than the spread of climate projections, given by the standard deviation of the ensemble mean. In this case, the values increase on average from approx. 13,600 tons month^{-1} to 44,300 tons month^{-1} (225% rise), 55,700 tons month^{-1} (310% rise), and 86,900 tons month^{-1} (539% rise) for the first, second, and third period, respectively.

Bed elevation along the thalweg of the Banja reservoir

Figure 7 shows the bed elevation along the thalweg of the upstream part of the Banja reservoir, simulated with the

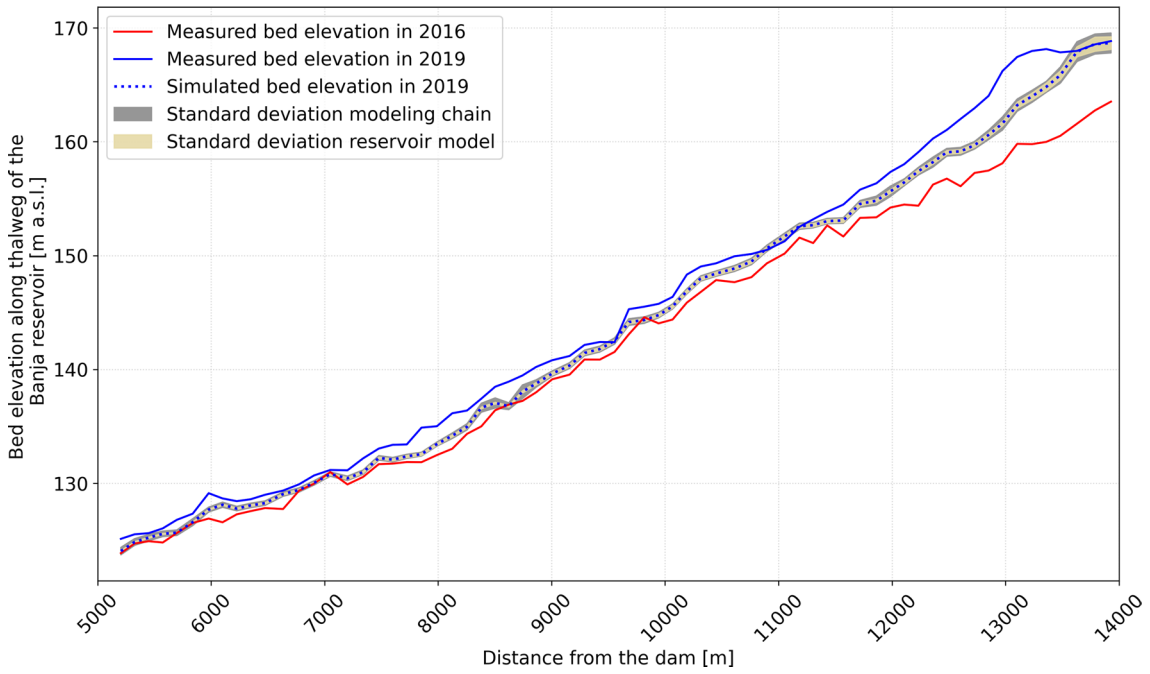

Fig. 4 Measured (solid red line for the year 2016, solid blue line for the year 2019) and simulated (dotted blue line for the year 2019) bed elevation along the thalweg of the upstream part of the Banja reservoir as a result of executing the entire modeling chain. The standard deviations for the entire model chain and the reservoir model only are indicated as dark gray shaded area and yellow shaded area, respectively

reservoir model, for three different years and for RCP2.6 as an ensemble mean of the three GCM/RCMs. The selected years are 2036, 2066, and 2100, which corresponds to 20, 50, and 84 years after the impoundment of the reservoir, respectively. The bed elevation for the reference year 2016, right before the impoundment, is also included (black dashed line) together with the mean standard deviation regarding the perturbations in the model parameters of the entire modeling chain (gray shaded area).

The simulated bed levels in the near future (2036) show an increase in bed elevation within the reservoir, especially in the upper part. Here a clear delta formation is visible (compare Morris and Fan (1998)). For the mid-term period, in the year 2066, on one hand, the bed elevation will increase, but also a delta progression becomes visible, which is in accordance with literature. The highest depositions are observed at approx. 10,500 m distance from the dam. Although in Fig. 7 it is not possible to gain insight into the impact of seasonality on the evolution of the bed elevation, in general, a higher accumulation of sediments occurs during months with high runoff and higher sediment transport (e.g., Fan and Morris (1992)).

Finally, by the year 2100, the maximum deposition height will increase from approx. 10 m in 2036 up to approx. 30 m. There is no clear difference between the maximum bed levels, but the largest increase occurs at a distance of around 9000 m upstream of the dam, which also indicates that the delta migrates further into the reservoir, when comparing the location of the delta at the end of the mid-term period (10,500 m distance to the dam). Hence, the deposition regime moves further downstream, whereas a sediment balance between erosion and deposition is established in the upstream part (9000–14,000 m distance to the dam).

In the case of the bed elevation, the spread of the climate projections is determined by the maximum difference between the ensemble members, represented finally as an average value for all the x-locations (distance from the dam). Similar to the previous simulation results (mean monthly runoff and mean monthly sediment yield at Kokel), the impact on the bed elevation along the thalweg of the Banja reservoir (target variable) is smaller than the spread of climate projections due to perturbations in the model parameters. The average change in bed elevation (along the thalweg) considering uncertainties in the model parameters is 0.64 m, whereas the average changes due to uncertainties in the climate projections are 0.96 m, 2.33 m, and 2.38 m for the years 2013, 2066, and 2100, respectively. These values represent an increase of 50%, 264%, and 272% compared to the average change of the bed elevation due to uncertainties in the model parameters.

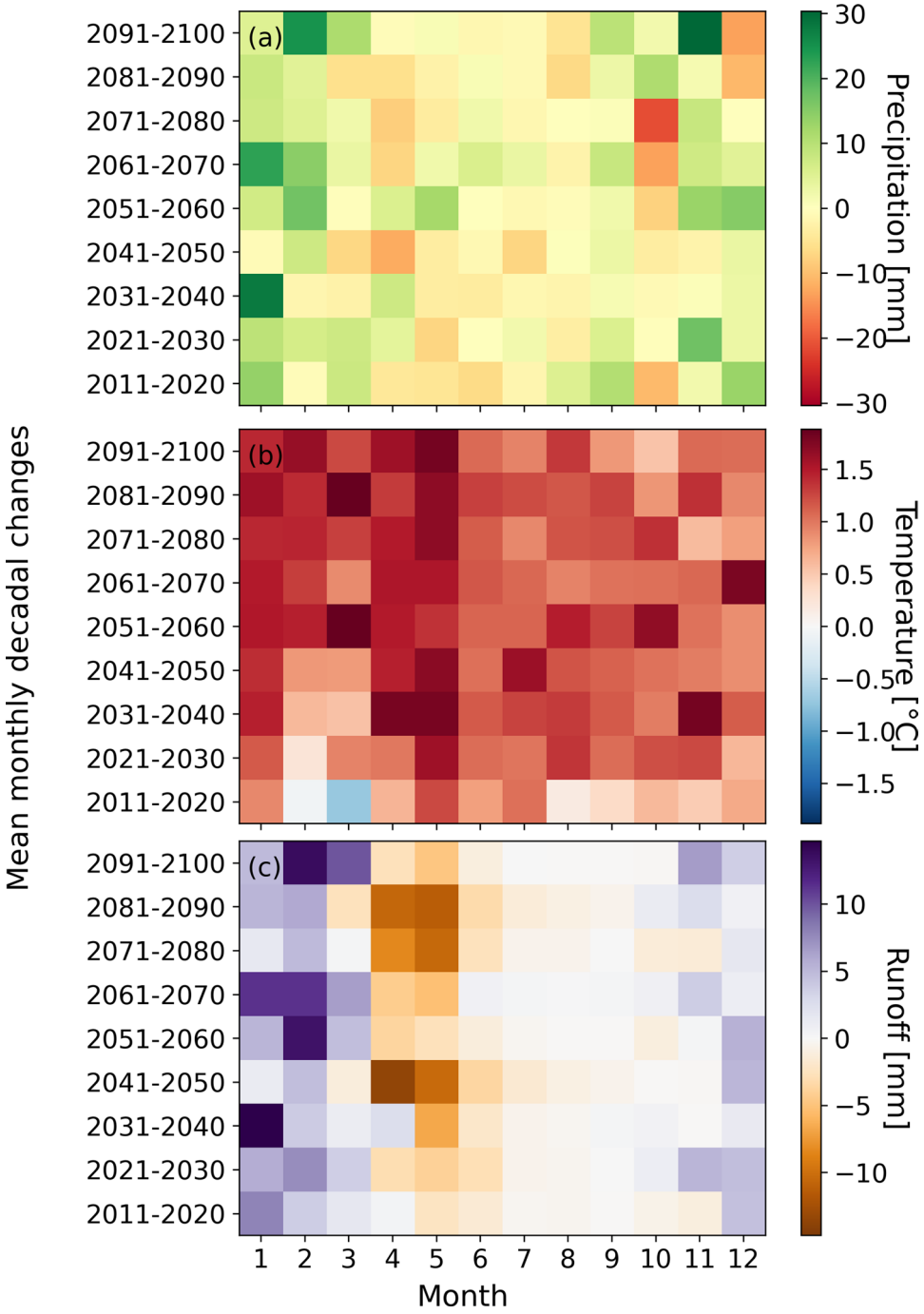

Fig. 5 Decadal changes of mean monthly values relative to the reference period (1981–2010): **a** change of the mean monthly precipitation as an average for the entire catchment [mm month^{-1}] ; **b** change of the mean monthly temperature as an average for the entire catchment [°C month^{-1}]; **c** change of the mean monthly runoff at Kokel [mm month^{-1}]. All values refer to the ensemble mean of the three GCM/RCMs and RCP2.6

Discussion

A complex modeling chain composed of different individual models is adopted to predict the sedimentation processes in the Banja reservoir in this study. The main advantage of applying such a chain lies in the detailed and process-based representation of each intermediate process. The results of the modeling chain are satisfactory and can be used for predicting the sedimentation processes under future climate conditions.

Nevertheless, uncertainties cannot be neglected. In our study, we focus mainly on parameter uncertainties and compare them to those inherent in climate models. The approximate uncertainties related to model parameters are determined by using the method developed by Gelleszun et al. (2017). The modeling chain includes three representative models that are used to study the impact of 11 sensitive parameters on the bed elevation changes of the Banja reservoir. Within this study, these 11 parameters were changed in the range of ± 1%, resulting in 23 model runs of the final

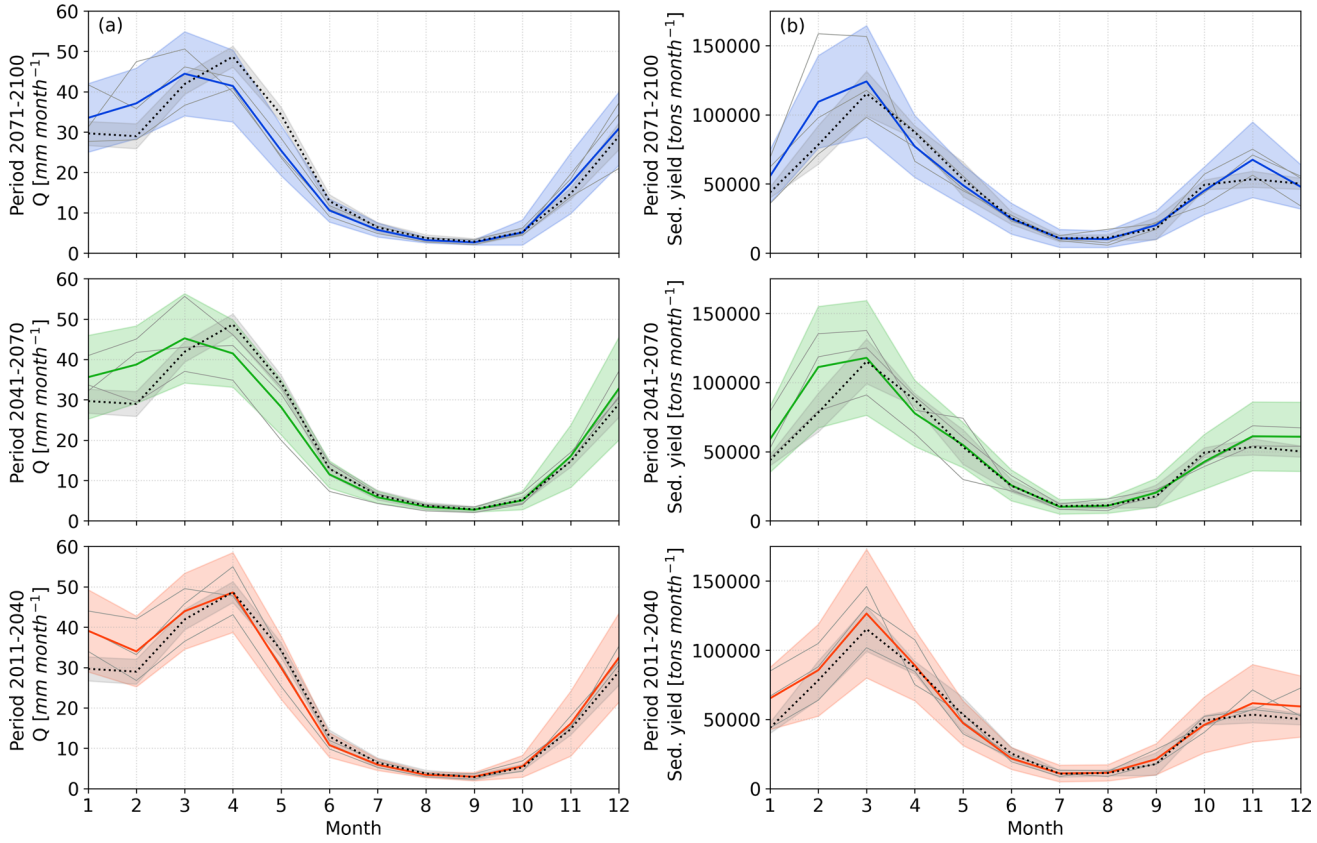

Fig. 6 Mean monthly runoff **a** and mean monthly sediment yield **b** at Kokel station for three different periods (rows, from bottom to top: 2011–2040, 2041–2070, 2071–2100). The values represent the ensemble mean of the three GCM/RCMs and RCP2.6 (dark colored solid lines ± standard deviation of the ensemble mean). The black dashed lines indicate the mean monthly runoff and mean monthly sediment yield in the past (reference period, 1981–2010, also as an ensemble mean), whereas the gray shaded areas indicate the associated standard deviations of each model regarding perturbations in the model parameters

model. According to the mentioned study, this approximate method proves to be robust and efficient, thus reducing dramatically the computing times that other sophisticated methods (such as Monte-Carlo simulations) might require.

Even though the ± 1% uncertainty of selected model parameters proved to work well, it needs to be considered that the possible change is strongly parameter-dependent, which means that for some parameters this change may be a major change, whereas for others, it might be considered as only a minor change. Hence, future studies should focus on determining how much the model parameters can deviate from their optimal value, to ensure that the approximate uncertainties are smaller than the spread of climate projections.

Additionally, uncertainties that might arise from climate model predictions are analyzed and compared to the approximate uncertainties in model parameters. In this study, the climate predictions are presented for RCP2.6, corresponding to three different GCM/RCMs realizations. The analysis of the results reveals that the approximate uncertainties in model parameters of the water balance model is significantly smaller than the uncertainties coming from the different climate projections (Fig. 6a). The same can be concluded when analyzing the simulated mean monthly sediment yield (Fig. 6b) and the final bed elevation along the thalweg of the Banja reservoir (Fig. 7). The results agree with the ones found by Kingston et al. (2011) and Wagner et al. (2017). They studied different uncertainties influencing their model results. In both studies, the authors conclude that the uncertainties arising from model parameterization are remarkably smaller than the ones generated by the climate projections for the case that the models were calibrated and validated with existing data in a first step.

Among all RCPs, RCP2.6 is seen as the lowest mitigation scenario. Although reaching RCP2.6 emission values by the end of the century may be technically feasible, urgent actions are required to achieve this. For example, reducing emissions rapidly during the first decades of the century and increasing the use of renewable energy sources, for which countries beyond the Organization for Economic and Co-operation Development (OECD) are also required to participate (van Vuuren et al. 2011). Thus, climate projections under RCP2.6 may be too optimistic and the need of contemplating other

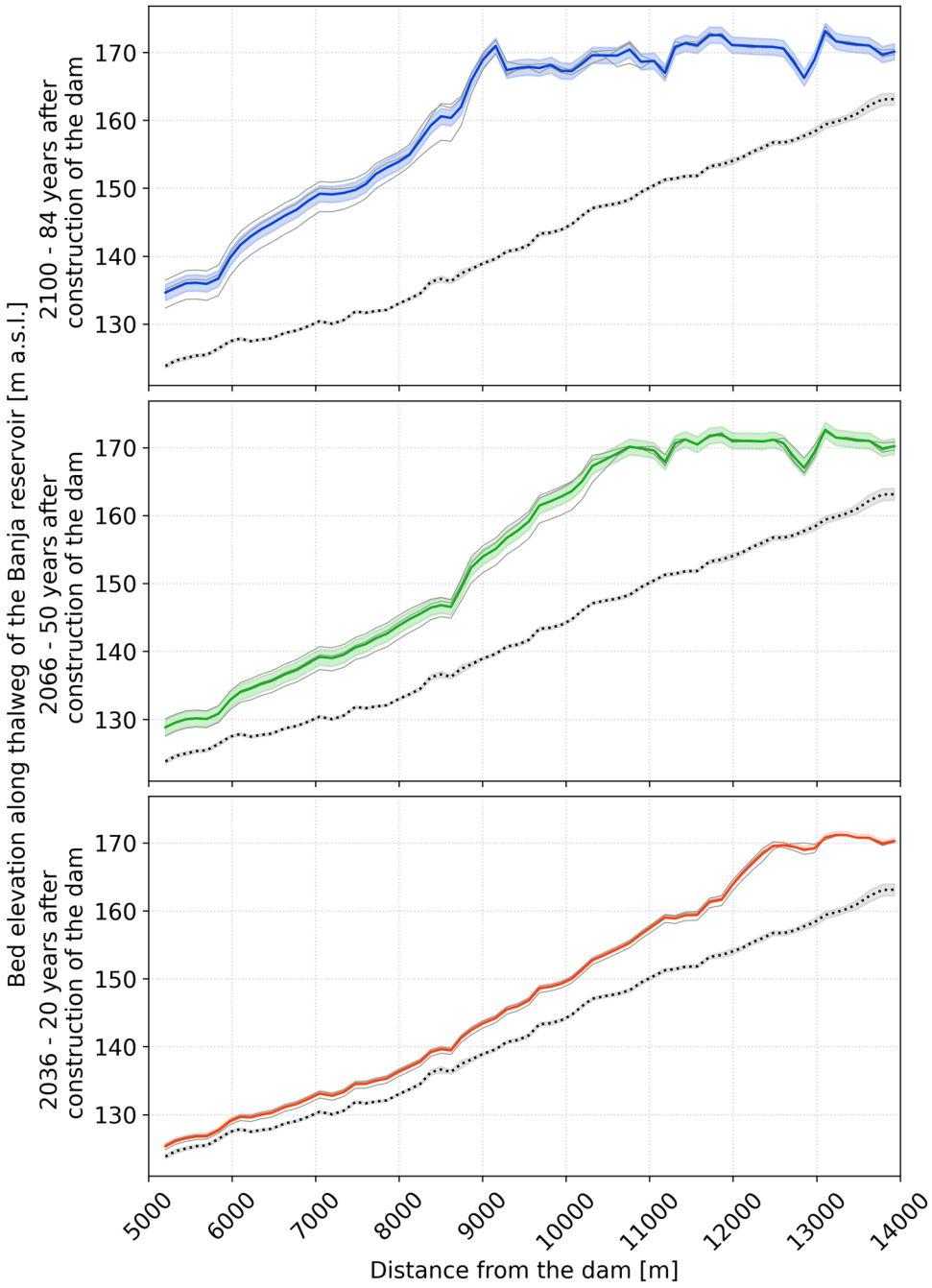

Fig. 7 Bed elevation along the thalweg of the Banja reservoir [m a.s.l.] for the years 2036, 2066, and 2100 (20, 50, and 84 years after impoundment of the dam). The ensemble means of the three GCM/RCMs for RCP2.6 are shown (dark colored solid line), together with the mean value of spread between ensemble members (colored shaded areas). The black dashed line indicates the bed elevation in the past (for the year of finalization of the dam construction, 2016), together with its standard deviation, obtained from the impacts on simulation results due to perturbations in model parameters

RCPs with higher emission scenarios comes into play, especially the RCP8.5 scenario, since the emissions for the period between 2005 and 2020 are most consistent with the historical data (Schwalm et al. 2020).

However, RCP2.6 was chosen here from a methodological perspective: we intend to scrutinize whether even the spread of results from a set of climate projections with low change signals exceeds typical variations in results achieved through perturbation in the model parameters. The climate change signal is defined as the absolute difference between the ensemble mean values obtained for the future period and the reference period (historical climate), respectively. For example, for monthly runoff in the last period of the twenty-first century (2071–2100), the climate signals are (for the ensemble mean) 3.25 mm month^{-1} for RCP2.6 (i.e., the difference between the colored and the black dashed lines), whereas a value of 6.20 mm month^{-1} is obtained when considering RCP8.5. This suggests that the climate signals in RCP2.6 are on average in the same order of magnitude as the approximate uncertainties related to model parameterization, where a mean value of 3.8 mm month^{-1} was obtained. Indeed, on a seasonal level, climate change signals can still

be higher. This is especially evident in the spring months, where the climate signal for runoff is almost 2.5 times higher. These findings show that low climate signals might be masked by model parameter uncertainties. On a minor note, the + 1 °C increase in the global mean temperature in RCP2.6 corresponds to ± 1% changes in model parameters as a mere and thus tangible comparison of numbers.

When predicting the response of a variable in the future (such as the bed elevation along the thalweg of the Banja reservoir), the use of multiple scenarios or ensembles is recommended, in order to cover further possibilities on how the climate is predicted (Collins et al. 2013). According to Teutschbein and Seibert (2010), complex Ensembled Regional Climate Models (E-RCMs) considering more than one RCM and a range of GCMs and RCPs are useful for hydrological simulations. Although our study can be classified into the mentioned group of E-RCM, considering further GCMs and RCMs might be interesting to understand how the climate spread changes and influences the prediction of the hydrological variables.

It is also worth mentioning that in our study, we focus only on the approximate uncertainties related to model parameters. However, other uncertainties might arise when applying such a modeling chain, such as the selected calibration approach (e.g., manual or automatic approach), the errors in measured data (e.g., in runoff or sediment yield), or the meteorological forcing data used as input. Additionally, changes in land use may contribute to alterations in the hydrological response of the catchment and should also be considered when predicting a catchment's response in the future (Li and Fang 2016).

Conclusion

A complex modeling chain was set up to predict the bed elevation along the thalweg of the Banja reservoir in the Devoll River (Albania), by considering hydro-climatic changes, monthly runoff, and sediment yield coming from the catchment. Despite the challenge of using three different models for predicting the final target variable, we benefit from the main features and accuracy of three process-based state-of-the-art models. As each model predicts a target variable, which serves as input for the subsequent model in the chain, the final target variable of the modeling chain depends strongly on the reliability of the antecedent results. To see how well this reliability can be ensured, model parameter uncertainties are studied for the entire modeling chain by using a simplified approach based on the FOSM Method.

These approximate parameter uncertainties (measured as a standard deviation) for predicting the bed elevation changes along the reservoir increased from 0.28 m (reservoir model parameters only) to 0.64 m when considering the uncertainties of all 11 parameters of the three models. Despite this increase, the values are still comparatively small (only 0.19% and 0.44% of the mean measured elevation bed in the year 2019, reprectively), and it can be concluded that the perturbations in the model parameters are not a significant source of uncertainty for the final simulation results.

Furthermore, three combinations of GCM/RCMs for RCP2.6 were selected to study the behavior of the involved variables in the future (until the year 2100). The spread of the climate projections is compared to the approximate uncertainties resulting from the perturbations in the model parameters. The results show that the spread of climate projections by the end of the century is on average larger than the approximate parameter uncertainties, being 408%, 539%, and 272% higher for the prediction of runoff, sediment yield, and bed elevation, respectively. However, as demonstrated in the case of runoff, they are in the same order of magnitude as the climate change signal inherent in the mitigation scenario RCP2.6. Nevertheless, and given that change signals are higher in other RCPs, the use of such a complex modeling chain is a valuable tool for predicting sedimentation processes in a reservoir for different climate change scenarios. The method described in this paper highlights how the parameter uncertainty for each model is quantified approximately, whilst demonstrating their robustness when comparing the larger spread imposed by climate projections. This is in particular helpful to guide modelers and practitioners to communicate different sources of uncertainties in complex modeling chains including climate models, and to highlight how uncertainties compare to climate change signals.

Acknowledgements This study was carried out within the framework of the DIRT-X project, which is part of AXIS, an ERA-NET initiated by JPI Climate, and funded by FFG Austria, BMBF Germany (Grants No. 01LS1902A and 01LS1902B), FOR-MAS Sweden, NWO NL, and RCN Norway with co-funding from the European Union (Grant No. 776608). Stefan Haun is indebted to the Baden-Württemberg Stiftung for the financial support by the Elite program for Postdocs. We particularly thank Thomas Bosshard from the Swedish Meteorological and Hydrological Institute for providing the bias-adjusted climate modeling results that were used as input datasets. We also thank Nils Rüther and the DIRT-X team for providing us with input data and fruitful discussions.

Author contribution María Herminia Pesci and Kilian Mouris contributed equally to the manuscript.

Funding Open Access funding enabled and organized by Projekt DEAL.

Data availability All the data used in this publication are acknowledged appropriately.

Declarations

Conflict of interest The authors declare no conflict of interest.

References

Aleixo R, Guerrero M, Nones M, Ruther N (2020) Applying ADCPs for long-term monitoring of SSC in Rivers. Water Resour Res. https://doi.org/10.1029/2019WR026087

Almestad C (2015) Modelling of water allocation and availability in Devoll River Basin, Albania. Master's degree. Norwegian University of Science and Technology

Ardıçlıoğlu M, Kocileri G, Kuriqi A (2011) Assessment of Sediment Transport in the Devolli River. https://doi.org/10.13140/2.1.2549.4085

Azari M, Moradi HR, Saghafian B, Faramarzi M (2016) Climate change impacts on streamflow and sediment yield in the North of Iran. Hydrol Sci J 61:123–133. https://doi.org/10.1080/02626667.2014.967695

Berg P, Bosshard T, Yang W, Zimmermann K (2022) MIdAS—MultI-scale bias AdjuStment. https://doi.org/10.5194/gmd-2022-6

Bronstert A, de Araújo J-C, Batalla RJ, Costa AC, Delgado JM, Francke T, Foerster S, Guentner A, López-Tarazón JA, Mamede GL, Medeiros PH, Mueller E, Vericat D (2014) Process-based modelling of erosion, sediment transport and reservoir siltation in mesoscale semi-arid catchments. J Soils Sediments 14:2001–2018. https://doi.org/10.1007/s11368-014-0994-1

Bussi G, Francés F, Horel E, López-Tarazón JA, Batalla RJ (2014) Modelling the impact of climate change on sediment yield in a highly erodible Mediterranean catchment. J Soils Sediments 14:1921–1937. https://doi.org/10.1007/s11368-014-0956-7

Chen C-N, Tfwala SS, Tsai C-H (2020) Climate Change Impacts on Soil Erosion and Sediment Yield in a Watershed. Water 12:2247. https://doi.org/10.3390/w12082247

Climate-data.org (2019) Korçë Climate. https://en.climate-data.org/europe/albania/korce/korce-5958/. Accessed 17 Dec 2019

Collins M, Knutti R, Arblaster J, Dufresne JL, Fichefet T, Friedlingstein P, Gao X, Gutowski WJ, Johns T, Krinner G, Shongwe M, Tebaldi C, Weaver AJ, Wehner M (2013) Long-term climate change: projections, Com- mitments and irreversibility. Climate Change 2013: the physical science basis. Contribution of Working Group. Cambridge University Press, Cambridge, United Kingdom and New York, NY, USA

Copernicus Climate Change Service (2017) ERA5: Fifth generation of ECMWF atmospheric reanalyses of the global climate: Copernicus Climate Change Service Climate Data Store (CDS). https://cds.climate.copernicus.eu/cdsapp#!/home. Accessed 21 Nov 2019

Diodato N, Bellocchi G (2007) Estimating monthly (R)USLE climate input in a Mediterranean region using limited data. J Hydrol 345:224–236. https://doi.org/10.1016/j.jhydrol.2007.08.008

Eftimi R (2010) Hydrogeological characteristics of Albania. Aqua-Mundi. https://doi.org/10.4409/Am-007-10-0012

European Environment Agency (2016) European Digital Elevation Model (EU-DEM), version 1.1. https://land.copernicus.eu/imagery-in-situ/eu-dem/eu-dem-v1.1?tab=metadata. Accessed 11 Nov 2019

European Environment Agency (2019) Corine Land Cover (CLC) 2018, Version 20. https://land.copernicus.eu/pan-european/corine-land-cover/clc2018. Accessed 11 Nov 2019

Fan J, Morris GL (1992) Reservoir Sedimentation. II: Reservoir Desiltation and Long-Term Storage Capacity. J Hydraul Eng 118:370–384.

Ferro V, Porto P (2000) Sediment delivery distributed (SEDD) model. J Hydrol Eng 5:411–422. https://doi.org/10.1061/(ASCE)1084-0699(2000)

Förster K, Garvelmann J, Meißl G, Strasser U (2018) Modelling forest snow processes with a new version of WaSiM. Hydrol Sci J 63:1540–1557. https://doi.org/10.1080/02626667.2018.1518626

Gelleszun M, Kreye P, Meon G (2017) Representative parameter estimation for hydrological models using a lexicographic calibration strategy. J Hydrol 553:722–734. https://doi.org/10.1016/j.jhydrol.2017.08.015

Hill MC (1998) Methods and guidelines for effective model calibration; with application to UCODE, a computer code for universal inverse modeling, and MODFLOWP, a computer code for inverse modeling with MODFLOW. Water-Resour Invest Rep 98:4005. https://doi.org/10.3133/wri984005

Hirschberg J, Fatichi S, Bennett GL, McArdell BW, Peleg N, Lane SN, Schlunegger F, Molnar P (2021) Climate change impacts on sediment yield and Debris-Flow activity in an Alpine Catchment. J Geophys Res Earth Surf. https://doi.org/10.1029/2020JF005739

IEA (2022) Energy statistics data browser, Paris. https://www.iea.org/data-and-statistics/data-tools/energystatistics-data-browser. Accessed 12 Sep 2022

Kingston DG, Thompson JR, Kite G (2011) Uncertainty in climate change projections of discharge for the Mekong River Basin. Hydrol Earth Syst Sci 15:1459–1471. https://doi.org/10.5194/hess-15-1459-2011

Kunstmann H, Kinzelbach W, Siegfried T (2002) Conditional first-order second-moment method and its application to the quantification of uncertainty in groundwater modeling. Water Resour Res. https://doi.org/10.1029/2000WR000022

Lehner B, Czisch G, Vassolo S (2005) The impact of global change on the hydropower potential of Europe: a model-based analysis. Energy Policy 33:839–855. https://doi.org/10.1016/j.enpol.2003.10.018

Li Z, Fang H (2016) Impacts of climate change on water erosion: a review. Earth Sci Rev 163:94–117. https://doi.org/10.1016/j.earscirev.2016.10.004

Li H, Yu C, Qin B, Li Y, Jin J, Luo L, Wu Z, Shi K, Zhu G (2022) Modeling the effects of climate change and land use/land cover change on sediment yield in a large reservoir basin in the east Asian Monsoonal Region. Water 14:2346. https://doi.org/10.3390/w14152346

Moges E, Demissie Y, Larsen L, Yassin F (2021) Review: sources of hydrological model uncertainties and advances in their analysis. Water 13:28. https://doi.org/10.3390/w13010028

Mahmood K (1987) Reservoir sedimentation: Impact, extent and mitigation. The World Bank, Washington, D.C

Morris GL, Fan J (1998) Reservoir Sediment Handbook. McGraw-Hill Book Co., New York

Mouris K, Schwindt S, Morales Oreamuno HAUNS, Wieprecht MF S (2022) Introducing seasonal snow memory into the RUSLE.

J Soils Sediments 22:1609–1628. https://doi.org/10.1007/s11368-022-03192-1
Nerantzaki SD, Giannakis GV, Efstathiou D, Nikolaidis NP, Sibetheros I, Karatzas GP, Zacharias I (2015) Modeling suspended sediment transport and assessing the impacts of climate change in a karstic Mediterranean watershed. Sci Total Environ 538:288–297. https://doi.org/10.1016/j.scitotenv.2015.07.092
Nunes JP, Seixas J, Keizer JJ (2013) Modeling the response of within-storm runoff and erosion dynamics to climate change in two Mediterranean watersheds: a multi-model, multi-scale approach to scenario design and analysis. CATENA 102:27–39. https://doi.org/10.1016/j.catena.2011.04.001
Olsen N (2018) A three-dimensional numerical model for simulation of sediment movements in water intakes with. User's manual, multiblock option
Panagos P, Ballabio C, Himics M, Scarpa S, Matthews F, Bogonos M, Poesen J, Borrelli P (2021) Projections of soil loss by water erosion in Europe by 2050. Environ Sci Policy 124:380–392. https://doi.org/10.1016/j.envsci.2021.07.012
Plate EJ (1993) Sustainable development of Water Resources: a challenge to Science and Engineering. Water Int 18:84–94. https://doi.org/10.1080/02508069308686154
Prudhomme C, Davies H (2009) Assessing uncertainties in climate change impact analyses on the river flow regimes in the UK. Part 1: baseline climate. Clim Change 93:177–195. https://doi.org/10.1007/s10584-008-9464-3
Renard KG, KG, Renard (1997) Agriculture handbook, no.73.United States Department of Agriculture, Washington
Santos JYGd, Montenegro SMGL, Da Silva RM, Santos CAG, Quinn NW, Dantas APX, Ribeiro Neto A (2021) Modeling the impacts of future LULC and climate change on runoff and sediment yield in a strategic basin in the Caatinga/Atlantic forest ecotone of Brazil. CATENA 203:105308. https://doi.org/10.1016/j.catena.2021.105308
Schulla J (1997) Hydrologische Modellierung von Flussgebieten zur Abschätzung der Folgen von Klimaänderungen. Dissertation, Eidgenössichen Technischen Hochschule Zürich
Schulla J (2021) Model Description WaSiM. https://www.wasim.ch/downloads/doku/wasim/wasim_2021_en.pdf. Accessed 14 Mar 2022
Schwalm CR, Glendon S, Duffy PB (2020) RCP8.5 tracks cumulative CO2 emissions. Proc Natl Acad Sci U S A 117:19656–19657. https://doi.org/10.1073/pnas.2007117117
Shoarinezhad V, Wieprecht S, HAUN S (2020) Comparison of local and global optimization methods for calibration of a 3D morphodynamic model of a Curved Channel. Water 12:1333. https://doi.org/10.3390/w12051333
Shrestha B, Babel MS, Maskey S, van Griensven A, Uhlenbrook S, Green A, Akkharath I (2013) Impact of climate change on sediment yield in the Mekong River basin: a case study of the Nam Ou basin, Lao PDR. Hydrol Earth Syst Sci 17:1–20. https://doi.org/10.5194/hess-17-1-2013
Statkraft (2019) Country series: Albania's hydropower important for the Balkans. https://www.statkraft.com/newsroom/news-and-stories/archive/2019/country-series-albanias-hydropower-important-for-the-balkans/. Accessed 16 May 2022
Teutschbein C, Seibert J (2010) Regional Climate Models for Hydrological Impact Studies at the Catchment Scale: a review of recent modeling strategies. Geogr Compass 4:834–860. https://doi.org/10.1111/j.1749-8198.2010.00357.x
van Vuuren DP, Stehfest E, den Elzen MGJ, Kram T, van Vliet J, Deetman S, Isaac M, Klein Goldewijk K, Hof A, Mendoza Beltran A, Oostenrijk R, van Ruijven B (2011) RCP2.6: exploring the possibility to keep global mean temperature increase below 2°C. Clim Change 109:95–116. https://doi.org/10.1007/s10584-011-0152-3
Wagner T, Themeßl M, Schüppel A, Gobiet A, Stigler H, Birk S (2017) Impacts of climate change on stream flow and hydro power generation in the Alpine region. Environ Earth Sci. https://doi.org/10.1007/s12665-016-6318-6
Walling DE, Fang D (2003) Recent trends in the suspended sediment loads of the world's rivers. Glob Planet Change 39:111–126. https://doi.org/10.1016/S0921-8181(03)00020-1
WCRP (2009) EURO-CORDEX: EUR-11 grid. https://www.euro-cordex.net/index.php.en. Accessed 14 Mar 2022
Wild TB, Birnbaum AN, Reed PM, Loucks DP (2021) An open source reservoir and sediment simulation framework for identifying and evaluating siting, design, and operation alternatives. Environ Model Softw 136:104947. https://doi.org/10.1016/j.envsoft.2020.104947
Wischmeier WH, Smith DD (eds) (1978) Predicting Rainfall Erosion losses:. A Guide to Conservation Planning
Zettam A, Taleb A, Sauvage S, Boithias L, Belaidi N, Sánchez-Pérez J (2017) Modelling hydrology and sediment transport in a semi-arid and Anthropized Catchment using the SWAT model: the case of the Tafna River (Northwest Algeria). Water 9:216. https://doi.org/10.3390/w9030216
Zhang H, Wei J, Yang Q, Baartman JE, Gai L, Yang X, Li S, Yu J, Ritsema CJ, Geissen V (2017) An improved method for calculating slope length (λ) and the LS parameters of the revised Universal Soil loss equation for large watersheds. Geoderma 308:36–45. https://doi.org/10.1016/j.geoderma.2017.08.006

Publication IV.

An interdisciplinary model chain quantifies the footprint of global change on reservoir sedimentation

Table 5.4. Metadata of publication IV

Title	An interdisciplinary model chain quantifies the footprint of global change on reservoir sedimentation
Authors	**Kilian Mouris**, Sebastian Schwindt, María Herminia Pesci, Silke Wieprecht, Stefan Haun
Journal	Scientific Reports
submitted	June 30, 2023
accepted	November 14, 2023
published	November 17, 2023
DOI	https://doi.org/10.1038/s41598-023-47501-1

scientific reports

Check for updates

OPEN

An interdisciplinary model chain quantifies the footprint of global change on reservoir sedimentation

Kilian Mouris[1]✉, Sebastian Schwindt[1], María Herminia Pesci[2], Silke Wieprecht[1] & Stefan Haun[1]

Global change alters hydro-climatic conditions, affects land use, and contributes to more frequent droughts and floods. Large artificial reservoirs may effectively alleviate hydro-climatic extremes, but their storage capacities are threatened by sedimentation processes, which in turn are exacerbated by land use change. Envisioning strategies for sustainable reservoir management requires interdisciplinary model chains to emulate key processes driving sedimentation under global change scenarios. Therefore, we introduce a model chain for the long-term prediction of complex three-dimensional (3d) reservoir sedimentation considering concurrent catchment, hydro-climatic, and land-use conditions. Applied to a mountainous Mediterranean catchment, the model chain predicts increased sediment production and decreased discharge for high and medium emission pathways. Increased winter precipitation, accompanied by a transition from snowfall to rainfall, is projected to aggravate reduced summer precipitation, emphasizing a growing need for reservoirs. Additionally, higher winter precipitation proliferates sediment production and reservoir sedimentation. Land use change can outweigh the increased reservoir sedimentation originating from hydro-climatic change, which highlights the significance of localized actions to reduce sediment production. Finally, a 3d hydro-morphodynamic model provides insights into interactions between global change and reservoir sedimentation with spatially explicit information on future sedimentation patterns facilitating the implementation of management strategies.

Global change driven by human legacies since the mid-twentieth century is causing a wide range of hydro-climatic and land use changes that affect the availability of water resources and water distribution[1–5]. Additionally, global warming intensifies impacts on water resources by bolstering evapotranspiration and extreme weather patterns such as more frequent and intense droughts[6]. Large artificial reservoirs for storing water are one of the most powerful tools to buffer the effects of such hydrological extremes. However, reservoir sedimentation threatens buffer capacities by reducing the storage volume and exacerbating local water availability problems[7–10]. Although the loss of storage volume depends on regional characteristics, reservoir sedimentation is a global problem, leading to an annual loss of approximately 0.5–1% in global storage volume[11–15]. This trend has led to a decline in the existing net reservoir storage volume, though more than 3500 new large dams for hydropower production have been built worldwide since 2000[16,17]. Also, the global per-capita storage capacity is shrinking even faster owing to population growth[18]. Moreover, the anticipated hydro-climatic and land use changes are expected to intensify soil erosion and the influx of suspended sediment, hastening the loss of storage volume[19–23]. Predicting reservoir sedimentation and the subsequent storage loss requires precise and holistic assessments of catchment, river, and reservoir processes. Because each system is unique, emulating relevant processes and global change impacts is challenging but necessary for designing reservoirs and implementing targeted reservoir management strategies.

A fundamental challenge is that most of the currently available modeling tools to assess global change impacts lack the necessary level of detail and capacities for simulating the principal processes driving sediment dynamics and reservoir sedimentation. For instance, some models can examine the impact of climate change on the sediment yield and loads for specific catchments[9,19,24–29] or continents[30,31], but they neglect the influence of land use change, albeit acknowledging its importance. Other models account for past land use change but do not account for future long-term climate and land use changes[22,32,33]. Only a few existing models are capable of accounting for combined land use and hydro-climatic change impacts on sediment dynamics[34–37], but they reduce reservoirs to

[1]Institute for Modelling Hydraulic and Environmental Systems, University of Stuttgart, Stuttgart, Germany. [2]Institute of Hydrology and Water Resources Management, Leibniz University of Hannover, Hannover, Germany. ✉email: kilian.mouris@iws.uni-stuttgart.de

simple lines in one-dimensional hydro-morphodynamic models[38,39] or use simple empirical estimates[40] such as the Brune or Churchill curve to assess the effect of climate change on reservoir sedimentation. Such simplistic models have limited relevance for decision-making in reservoir management, which requires explicit knowledge of sediment deposition patterns that a line-like model cannot show. Simplistic reservoir models can still approximate the storage loss of a reservoir, but they cannot account for spatially explicit morphological processes, including bed level changes such as deposition delta evolution. Furthermore, simplified models do not consider recirculation zones, lateral inflows, the influence of the outflows (e.g., turbine operation), and other complex 3d hydrodynamics. However, such information is essential for the development and implementation of appropriate and sustainable reservoir management strategies. For example, venting of rapid sediment-laden flows on the reservoir bottom, referred to as turbidity currents[41], and other sediment routing actions (e.g., sluicing) require a deep understanding of 3d hydrodynamics. Also, sediment deposits in front of the bottom outlets of a dam pose a significant risk to the safe operation of a reservoir[42], which can be alleviated through local dredging or flushing operations. Both dredging and spatio-temporally efficient flushing require 3d information on hydro-morphodynamic processes, but currently, no modeling system or chain provides such information. Thus, state-of-the-art modeling tools do not imply multidisciplinary simulations needed to predict reservoir sedimentation processes and patterns in the long term and in light of global change scenarios.

To address these challenges, we present a novel model chain that uses information on catchment physics, including the hydro-climatic state and land use to predict long-term sediment dynamics and multi-dimensional reservoir sedimentation processes. The process-based model chain accounts for changes in temperature, precipitation, discharge, sediment yield, and reservoir sedimentation, by also considering the geometry and operating scheme of the reservoir. The centerpiece of the model chain is a three-dimensional (3d) numerical model, which predicts flow dynamics and sediment transport and enables us to show how different global change scenarios impinge on reservoir sedimentation processes.

Methods

Model chain and application example

The process-based model chain assesses the effect of climatic, land use, and resulting hydrological changes on reservoir sedimentation. First, the primary impacts of climate change are predicted for three Representative Concentration Pathways (RCPs) using three different climate models, including near-surface temperature and precipitation. To predict secondary climate change impacts resulting from temperature and precipitation changes, a state-of-the-art hydrological model, a soil erosion plus sediment transport model, and a 3d hydro-morphodynamic reservoir model are set up and combined, to benefit from their specialization and the possibility to correctly account for physical processes at different scales. In addition, datasets derived from a downscaled global change analysis model[43] enable the emulation of future land use change for four Shared Socioeconomic Pathways (SSP-RCPs). The model chain served to simulate future projections of sediment trapping in a reservoir as a function of three scenarios of hydro-climatic change and four scenarios of combined climate and land use change (Fig. 1).

Although individual model input parameters are calibrated, the output is still subject to uncertainty that propagates through the entire model chain and leads to superposition effects. Additional uncertainty stems from long-term predictions of climate projections, which exceed the inherent uncertainty of the calibrated input parameters[44]. Finally, the model chain enables long-term process simulation to examine the influence of climate and land use changes on reservoir sedimentation, where quantitative outputs are still subject to uncertainty.

An application of the model chain showcases the Banja reservoir in the Devoll catchment in Southeastern Albania (Fig. 2) with a typical Mediterranean climate featuring high erosion rates and vulnerability to climate change[45–47]. The emerging region is experiencing major land use changes and large investments in hydropower[48]. The mountainous Devoll catchment spans 2900 km^2 with elevations ranging from 113 to 2390 m a.s.l. The land use is currently characterized by forest (30%), scrub and herbaceous vegetation (25%), and agriculture (25%). Over recent decades, land use has undergone substantial changes, particularly after the collapse of communism, and is increasingly influenced by global market principles[49]. Dry hot summers and wet winters characterize the Mediterranean hydro-climate with low summer and high winter and spring flows. In winter, high elevations of the catchment are frequently covered by snow leading to a precipitation and snowmelt-driven flow regime. High rainfall erosivity on steep slopes with poorly aggregated soils contributes to high sediment production and sediment yields[50,51] leading to a great potential for reservoir sedimentation of existing and planned reservoirs. Commissioned in 2016, the Banja reservoir has a length of 14 km, a maximum water depth of 60 m near the dam, a surface of 14 km2, and a maximum storage capacity of 400 million m^3. A further upstream-located reservoir, commissioned in 2020, was not included in this study because ground truth data were not available at the time of calibration.

Available ground truth data

Ground truth data on discharge and suspended sediment concentrations (SSCs) were obtained from the Kokel gauging station (Fig. 2) for a period between May 2016 and April 2018, when the water depth exceeded a minimum measurement threshold of 1 m. Discharge and SSC were monitored with two stationary-mounted horizontal acoustic Doppler current profilers (H-ADCPs)[52].

A digital elevation model (DEM) of the bathymetry was generated based on a drone survey prior to the reservoir filling in 2016. In 2019, the bathymetry of the reservoir was re-assessed using moving ADCP measurements. The 2016 and 2019 topography recordings were projected on a numerical mesh and served to calculate the height of sediment deposits in the reservoir. Calibration of the 3d numerical model was performed based on bed level changes along the thalweg. During a field survey in 2021, sediment samples were collected from the

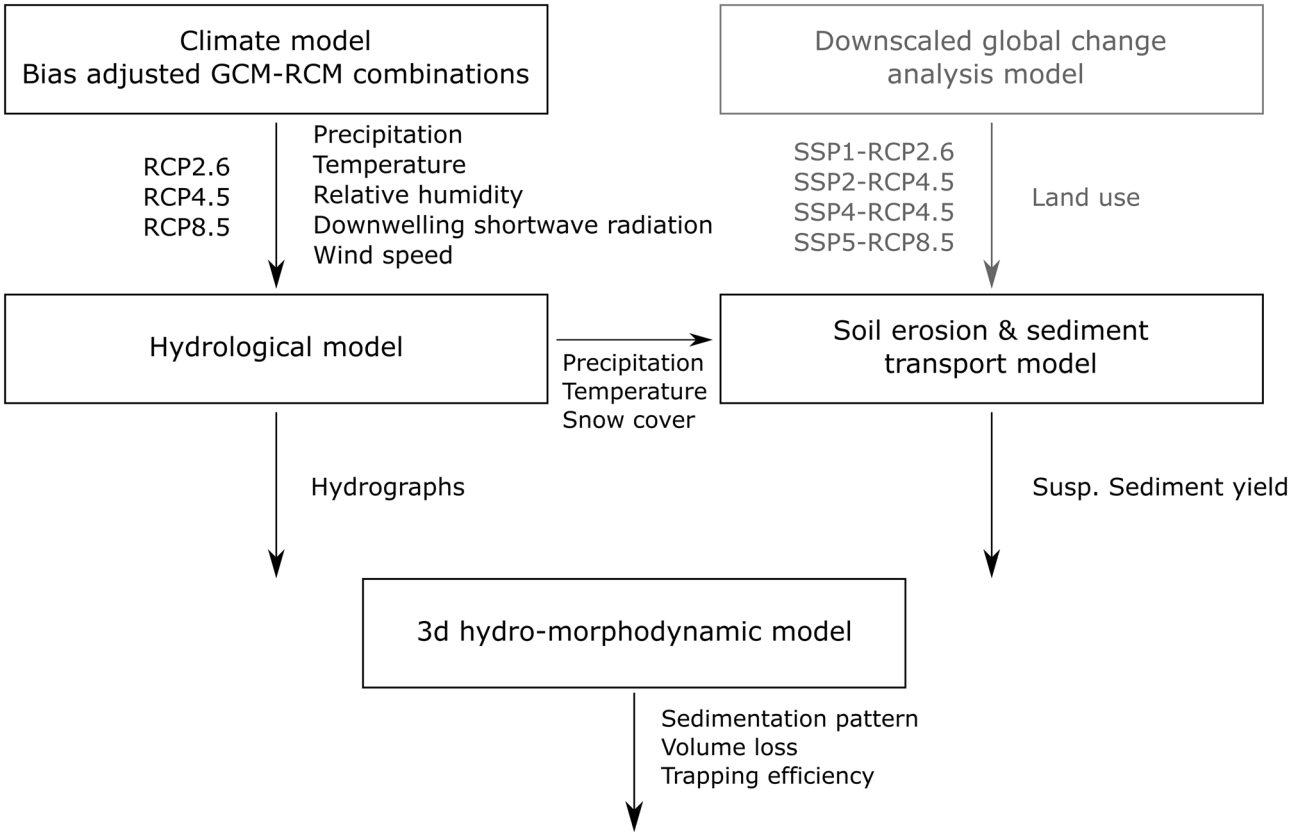

Figure 1. Model chain simulating the effects of global change on reservoir sedimentation as a function of land use (in gray and by means of Shared Socioeconomic Pathways, SSPs) and climate change based on Representative Concentration Pathways (RCPs), and three Global Climate Models (GCMs) with local refinement through two Regional Climate Models (RCMs).

reservoir bed at 27 locations in the reservoir using an Ekman grab sampler that samples the uppermost 20 cm of the deposits. Sampling was carried out in both deep (> 40 m) and shallow (near tributaries) areas of the entire reservoir. The grain size distributions of the samples were determined with a portable particle size analyzer based on laser diffraction and revealed that the sediment depositions predominantly consisted of fine sediments with cohesive characteristics (< 63 µm). A laboratory analysis of the deposited sediments showed dry bulk densities ranging from 726 to 950 kg m^{-3}.

Climate and land use projections

The impacts of climate change on reservoir sedimentation are estimated for three RCPs using ensembles of three Global Climate Models (GCMs), which are dynamically downscaled by two different Regional Climate Models (RCMs). To mitigate potential bias stemming from the selection of climate models, specific model combinations with similar climate trends for precipitation and temperature were grouped. One climate model from each group was used to represent the large variety of GCMs while using only 3 GCM-RCM combinations (Supplementary Information, Table S1). The selected combinations (Supplementary Information, Table S1) are considered representative of the large variety of GCM-RCMs. The climate models provide meteorological information on total precipitation, near-surface temperature, near-surface relative humidity, surface downwelling, shortwave radiation, and near-surface wind speed using the MultI-scale bias AdjuStment (MidAS v0.2.1) tool[53] for correcting daily mean values and the ERA5 reanalysis dataset[54] as reference data. The resulting projections have a spatial resolution of 0.11 degrees and a temporal resolution of 3 h over a period from 01/1981 to 12/2100.

The here-used three RCPs encompassed a low greenhouse gas emissions pathway (RCP2.6), a medium greenhouse gas emissions pathway (RCP4.5), and a high greenhouse gas emissions pathway (RCP8.5). In combination with hydro-climatic change scenarios, land use projections[43] were implemented in the model chain (Fig. 1) through four Shared Socioeconomic Pathways (SSPs). The SSPs embrace greenhouse gas emissions and account for climate change, population growth, economic development, and technological advancement, thereby offering more holistic global change scenarios[55] in accordance with the Coupled Model Intercomparison Project Phase 6 (CMIP6) design[56]. Thus, catchment responses to sustainable development (SSP1-RCP2.6), middle-of-the-road development (SSP2-RCP4.5), unequal development (SSP4-RCP4.5), and fossil-fueled development (SSP5-RCP8.5) were evaluated in combination with the GCMs, RCMs (Table 1; more detail in Supplementary Information, SI1). In total, the model chain was run for 21 scenarios comprising 3 RCP and 4 SSP-RCP scenarios, each

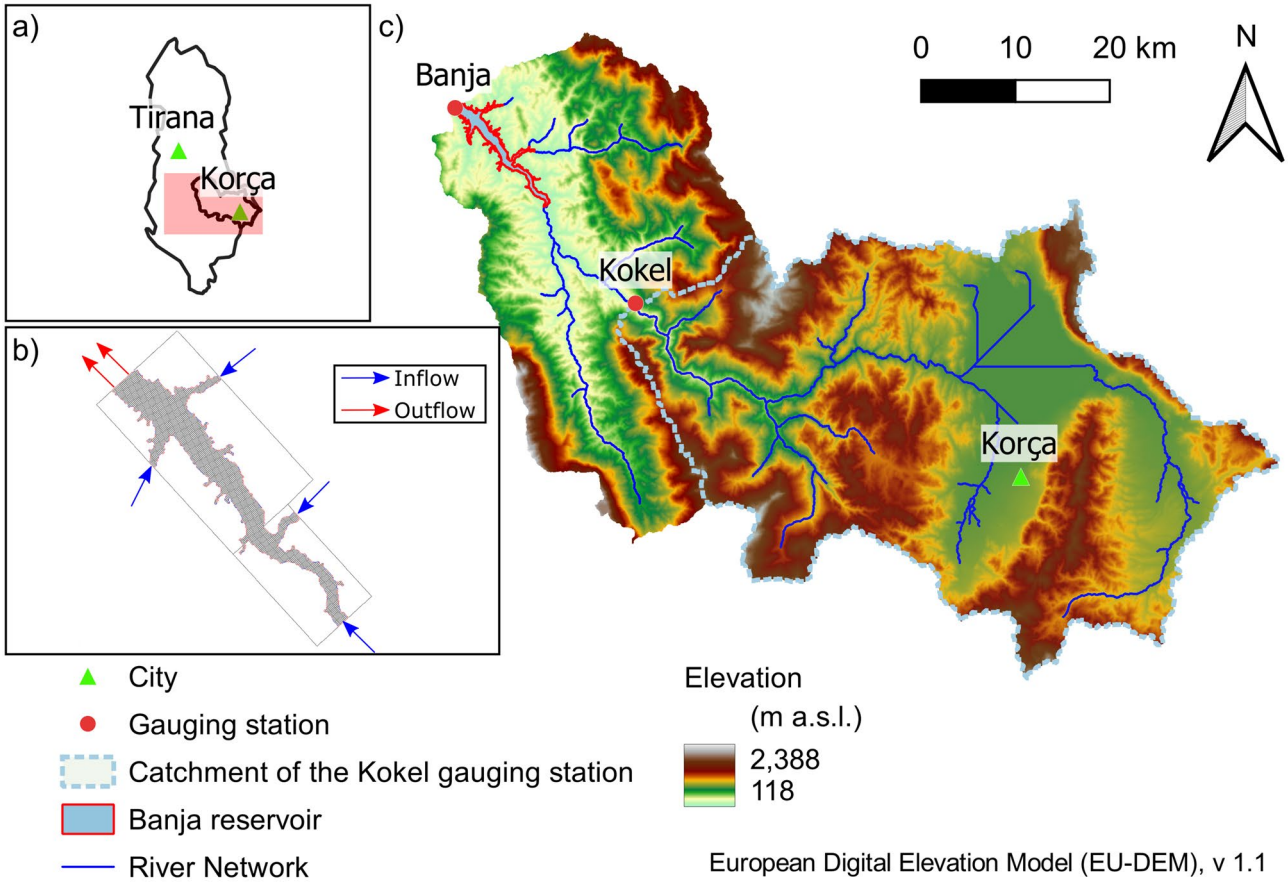

Figure 2. Location of the Mediterranean showcase catchment (**a**) in Albania, (**b**) the extent of the 3d hydro-morphodynamic numerical model including tributaries (blue arrow) and outflows (red arrows), and (**c**) the catchment topography with gauging stations, sub-catchments, and location of the Banja reservoir. The figure was created by the authors using QGIS3.18.1 (https://qgis.org/en/site/).

RCP (climate change only)	SSP-RCP (global change)
RCP2.6 (low emissions)	SSP1-RCP2.6 (sustainability)
RCP4.5 (stabilized emissions)	SSP2-RCP4.5 (middle of the road)
	SSP4-RCP4.5 (inequality)
RCP8.5 (high emissions)	SSP5-RCP8.5 (fossil-fueled development)

Table 1. Investigated scenarios to analyze climate change (RCP) and global change (SSP-RCP) impacts on reservoir sedimentation.

using 3 GCM-RCM combinations. The mean values of the climate model ensemble served to obtain robust trends and derive a range of possible outcomes due to the spread of climate projections (see details in Pesci et al.[44]).

Figure 3 illustrates the four global change scenarios for the Devoll catchment, indicating the major land use classes and their projected changes by 2100. The urban land use category shows almost no change and constitutes approximately 5% of the total area. In contrast, the distribution of crops, forests, and grasslands varies considerably across the scenarios. In the SSP1-RCP2.6, both forest and grassland areas are projected to experience a substantial increase of up to 70% by 2100. Conversely, the SSP2-RCP4.5 and SSP4-RCP4.5 scenarios predict a decline in forest and grassland cover by 40% and 55%, respectively. In both RCP4.5 scenarios, the decline in forest and grassland in the far future is primarily caused by the expansion of agricultural land, particularly for cultivating bioenergy crops. For example, the SSP2-RCP4.5 scenario shows a significant increase in energy crop production due to the requirement of reducing greenhouse gas emissions with socioeconomic trends following their original course. Bioenergy crops are commonly used grain-based crops, such as rapeseed, corn, and sunflower. In the SSP5-RCP8.5 scenario, the land use changes marginally, as technological progress is achieved through fossil-fueled development. Popp et al.[57] provide more details on land use projections for various SSPs.

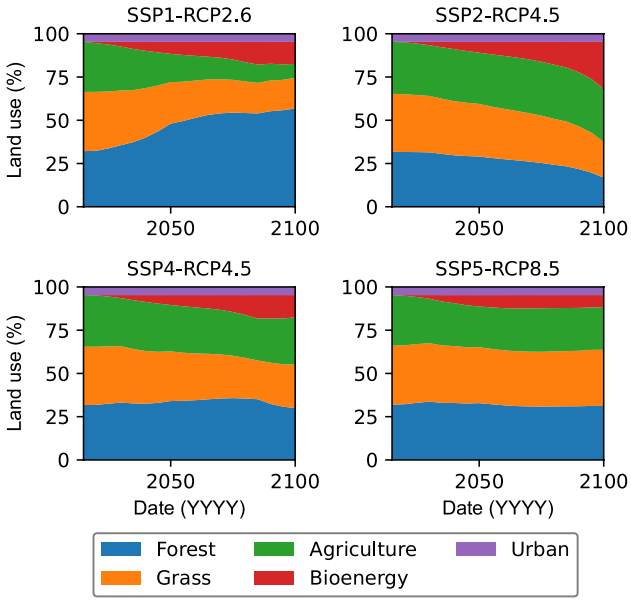

Figure 3. Projected land use changes in the Devoll catchment for the four investigated global change scenarios (combinations of RCPs and SSPs).

Hydrological model

The hydrological processes in the catchment are implemented in the model chain in the form of the Water Flow and Balance Simulation Model (WaSiM[58,59]) using the process-oriented Richards approach, with an additional sub-model for snow interception under forest canopies[60]. The model domain is defined at a spatial resolution of 1 km^2 and a temporal resolution of 3 h. In the case of the Devoll catchment, the calibration period spanned from May 2016 to April 2018 for which discharge measurements were available. WaSiM was initiated with a warm-up period of one year (May 2015 to April 2016). WaSiM produces hydrographs that constitute the liquid upstream boundary for the 3d hydro-morphodynamic model. Snow cover was estimated by WaSiM based on an energy balance approach and served as input for the soil erosion and sediment transport model. Missing information on the climate variables of relative humidity, wind speed, and global radiation was interpolated through inverse distance weighting. In addition, missing precipitation and temperature data were derived with a combination of elevation-dependent regression and inverse distance weighting in the model. More detailed information on the hydrological model, its calibration and validation, and the selected modeling approaches is provided in Supplementary Information SI2.

Soil erosion and sediment transport model

In the model chain, the Revised Universal Soil Loss Equation (RUSLE)[61] serves to predict gross soil erosion, and the SEdiment Delivery Distributed (SEDD)[62] model estimates the sediment delivery and transport at the catchment scale. The predicted monthly suspended sediment yields constitute the solid-materials upstream boundary of the 3d hydro-morphodynamic reservoir model. A semi-automated (Python) workflow evaluates the combination of the RUSLE and SEDD model to account for the non-erosivity of snowfall and the erosivity of snowmelt by introducing a seasonal memory into the RUSLE. In the case of the Devoll catchment, the combined soil erosion and sediment transport model was calibrated using suspended sediment load measurements from 05/2016 to 04/2018[50]. Alternative methods for estimating sediment concentrations, such as constant concentration-discharge relationships, are not suitable because they are likely to vary with climate change. The key advantage of choosing the RUSLE-SEDD combination is the efficient consideration of future changes in land use, precipitation, and temperature (Fig. 1). To implement the calculated Suspended Sediment Yield (SSY) into boundary conditions for the next model element, it must be converted into a time-discrete Suspended Sediment Concentration (SSC). SSY is the total suspended sediment transported by the river (or through the outlet of a catchment) over a specific period, and SSC refers to the concentration of sediment particles suspended in the water column. Hence, the SSC is calculated back from the monthly SSY and is therefore constant for each month. Detailed information on the RUSLE-SEDD, the validation, and the conversion of SSY to SEDD are provided with the Supplementary Information SI3.

3d hydro-morphodynamic model

The centerpiece of the interdisciplinary model chain for the coupled simulation of hydro-morphodynamic processes driving reservoir sedimentation is a 3d numerical model (SSIIM 2-Sediment Simulation In Intakes with Multiblock Option)[63]. 3d modeling is particularly important to represent variations in vertical suspended sediment concentrations, velocities, and the complex three-dimensional flow field with helical flows. For modeling reservoir sedimentation resulting from fine sediment deposition, multiple grain sizes are considered in the model. For the Banja reservoir, the model accounted for four inflow and two outflow boundaries (spillway and

turbine inlet), with inflow discharges and inflowing sediment derived from the hydrological model and the soil erosion and sediment transport model, respectively. The outflow was calculated as a function of the reservoir water level, the inflow, the storage curve, and site-specific operating rules that target a seasonal water level. The model calibration was performed based on the observed bed changes between the bathymetric surveys conducted in 2016 and 2019.

Since the computing time of a hydro-morphodynamic numerical 3d model tends to take several weeks to months (Supplementary Information, SI4), several simplifications were made to obtain acceptable runtimes for predicting global change impacts by 2100. For example, the resolution of the computational mesh may be as coarse as 50-m edge lengths, which then require specific turbulence models, such as the Reynolds-averaged Navier–Stokes (RANS) equations. Furthermore, SSIIM2 uses an implicit solver for the Navier–Stokes equations, which allows the use of large time steps (5400 s) and consequently reasonable computing times[64,65]. Also, additional algorithms, such as flow limiters, were implemented for computational stability in flat or triangular cells near the reservoir banks that may result from the wetting and drying algorithm. The advantage is that only wetted cells are considered in SSIIM2, which reduces the number of cells during calculation, especially when the water level changes, but also when reservoir sedimentation occurs.

The physical simplifications and numerical workarounds are expressed in the numerical model by calibration parameters that must be adjusted individually for each reservoir[66]. In the context of calibration, the evaluation of uncertainties is of paramount importance and can only be estimated by data-driven approaches, such as Bayesian calibration[67,68]. Still, 3d-modeling is physically more precise than often-used 1d or 2d hypotheses that reduce the complex flow patterns in a reservoir to a geometric line or plan. As a result of detailed spatial modeling of hydro-morphodynamic processes, the related uncertainties are lower[69], leading to less risk of equifinality[70]. Further details on the 3d hydro-morphodynamic model and the developed codes used to generate the upstream and downstream boundary conditions can be found in Supplementary Information SI4.

Results

The process-based model chain was used to assess the impact of hydro-climatic and land use changes on reservoir sedimentation and its preceding processes in the Devoll catchment and Banja reservoir from January 1981 to December 2100. The first 30 years (1981–2010) served as a reference period for comparison with three future periods: the 2011–2040 period represents the near future, the 2041–2070 period the mid future, and the 2071–2100 period the far future. The subsequent reservoir sedimentation of the Banja reservoir was simulated from impoundment in 2016 to December 2100 (84 years).

Climate change impacts

Temperature and precipitation

Climate change primarily affects temperature and precipitation (primary climate change impacts) which drive hydrological and sediment-related processes, such as discharge, soil erosion, and the transport of sediments into the reservoir (secondary climate change impacts). The mean annual temperature in the catchment increases the most for RCP8.5, notably by 2.5 °C for the mid future and by 4.3 °C for the far future compared to the reference period (Fig. 4a and Supplementary Information, Fig. S4). The temperature increase is smaller for medium (RCP4.5) and low (RCP2.6) emissions for the mid (1.8 °C and 1.3 °C, respectively) and (2.2 °C and 1.3 °C, respectively) far future. Also, the seasonal temperature trends are expected to remain nearly unchanged for all RCPs, with slightly higher temperature increases in summer compared to winter, particularly for RCP8.5 (Fig. 4a).

Predicted changes in precipitation patterns are less clear (Fig. 4b), with trends toward more winter (January to March) and less summer precipitation. Thus, typical Mediterranean precipitation patterns of wet winters and dry summers can be expected to slightly intensify (Supplementary Information, Fig. S5). This trend is evident across all emission RCPs but is most pronounced for RCP8.5. In the far future, total annual precipitation is expected to increase by 2–4% for RCP2.6, while total annual precipitation is expected to decrease by up to − 9% for RCP8.5 (Supplementary Information, Table S7). No considerable total precipitation changes are expected for RCP4.5

Discharge and suspended sediment yield

As a result of higher temperatures (Fig. 4a), mean annual snow storage is projected to decrease substantially in all RCPs, with the largest decrease of 83% anticipated for RCP8.5 and the smallest decrease of 36% for RCP2.6 in the far future (2071–2100) (Supplementary Information, Table S7, and Fig. S6).

Similar to precipitation, RCP2.6 results in a higher mean annual discharge than the other scenarios, most prominently in the near to mid future with an increase of up to 6%. However, the mean annual discharges show a declining trend in both the RCP4.5 and RCP8.5, with an accelerated decrease over time. Particularly for RCP8.5, the mean annual discharge is expected to decrease by more than 20% in the far future (Supplementary Information, Table S8). The seasonal variations are similar for the three RCPs and intensify with increasing emissions, with spring and summer discharge decreasing (e.g., by more than 40% in May) and January and February discharge increasing (Fig. 5a). Due to the changes in the precipitation regime, the decrease in snow storage, and the earlier snowmelt, the discharge peak is predicted to shift from April to March (Supplementary Information, Fig. S7). While annual and monthly discharge averages exhibit decreasing trends, the occurrence of extreme events such as floods with a 50-year return period increase by 7% (RCP2.6), 11% (RCP4.5), and 19% (RCP8.5) in the far future, also effecting on soil erosion.

The annual suspended sediment yield (SSY) of the Mediterranean Devoll catchment is expected to increase from 1.2 million tons year^{-1} by up to 9% for RCP2.6 and by up to 4% for RCP4.5 (Supplementary Information, Table S8). Despite a decrease in precipitation and discharge for RCP8.5, the simulations show an increase in SSY by 5% in the near to mid future. Only in the far future will the SSY also decrease by approximately 3%. The

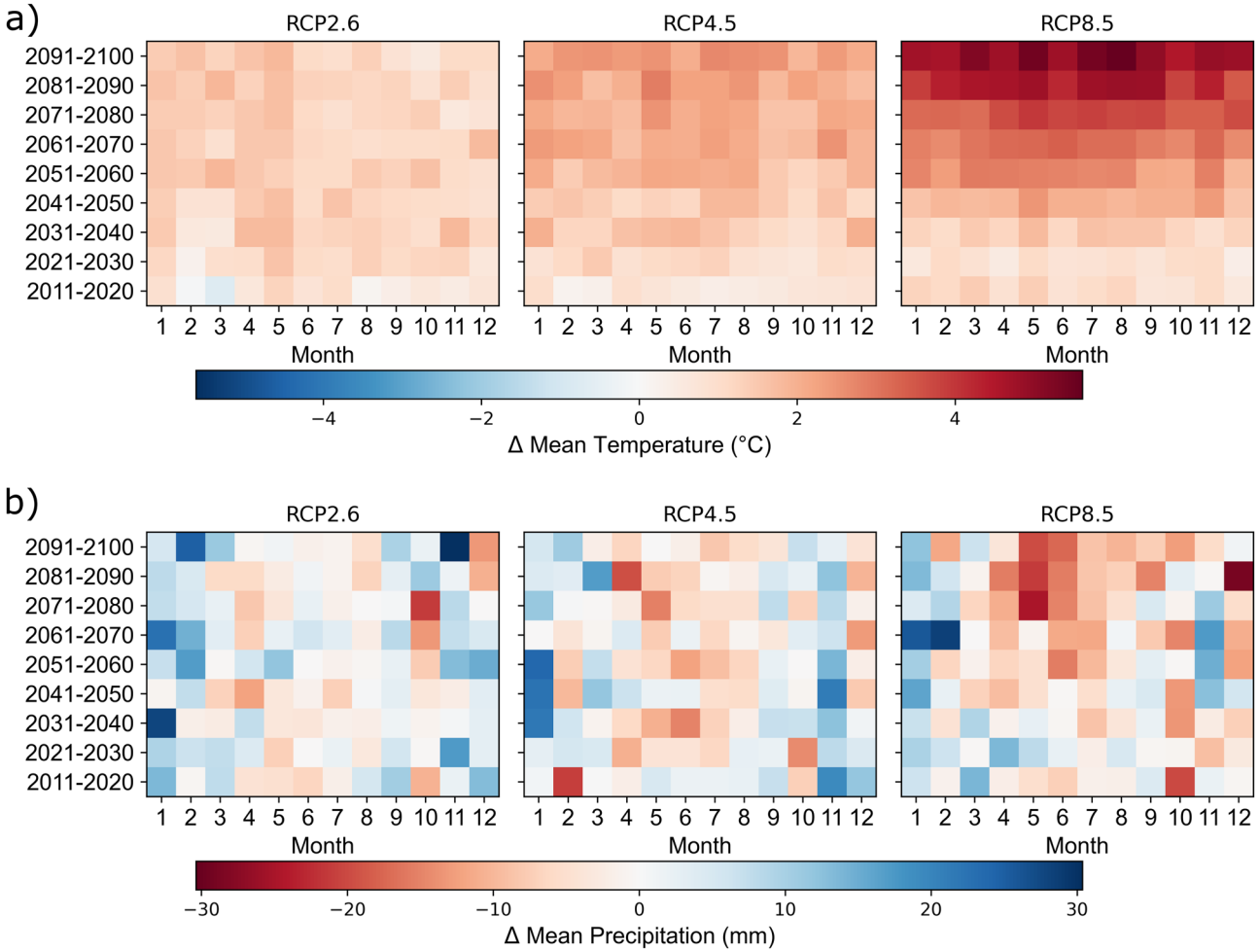

Figure 4. Decadal changes in monthly and spatial averages for the Mediterranean Devoll catchment relative to the reference period (1981–2010). (**a**) Average monthly temperature change (°C) and (**b**) average monthly precipitation change (mm). The figure was created by the authors using Matplotlib 3.5.1 (https://matplotlib.org/).

predicted seasonal changes are similar to the predictions for precipitation and discharge and show a considerable increase in the winter months and a decrease in spring and summer (Fig. 5b). In contrast to the annual SSY, the mean annual SSC increases for all emission scenarios but most substantially for RCP8.5 (27%) in the far future (Supplementary Information, Table S8). The increase in SSC for RCP2.6 is the lowest and ranges from 3 to 8%. The resulting predictions of discharge and sediment yield control the amounts of water and sediment arriving at the upstream boundary of the 3d reservoir sedimentation model.

Reservoir sedimentation

The predicted loss in storage volume of the Banja reservoir was most prominent for RCP2.6 (Fig. 6a). Specifically, the loss is estimated to be 23% after 85 years since the impoundment and is caused by the highest sediment flow along with the highest discharges for RCP2.6. However, the uncertainty in the climate projections is highest for RCP2.6 which is indicated by the high standard deviation (Fig. 6a). The storage volume loss for RCP4.5 and RCP8.5 is similar with approximately 21%. Interestingly, in the far future, the storage volume loss for RCP4.5 slightly surpasses that of RCP8.5, which can be explained by the declining SSY associated with RCP8.5 in the far future. In addition, the spread of climate projections is smallest for RCP4.5, where all climate projections within the ensemble resulted in similar volume losses.

The sedimentation rate and subsequent decrease in reservoir storage volume are not only determined by the sediment inflow but also by the trapping efficiency (TE, Fig. 6b), which depends on geometric reservoir characteristics and its operation. TE represents the ratio of the deposited sediments to the time-integrated sediment inflow over a certain period. During the first simulation decade, nearly all inflowing sediment is trapped, resulting in a TE exceeding 99%. TE decreases for all RCPs to 95.8 to 97.2% after 80 years of impoundment as a result of changed hydrodynamics because of bathymetric change (i.e., fine sediment deposition). Yet, the trend is not generally continuous. For instance, in the case of RCP2.6, TE exhibits an initial increase to more than 98% after 50–60 years but decreases abruptly afterward. This fluctuation is caused by a predicted wet season with exceptionally high inflows over several weeks in one of the climate projections within the RCP2.6 ensemble, leading

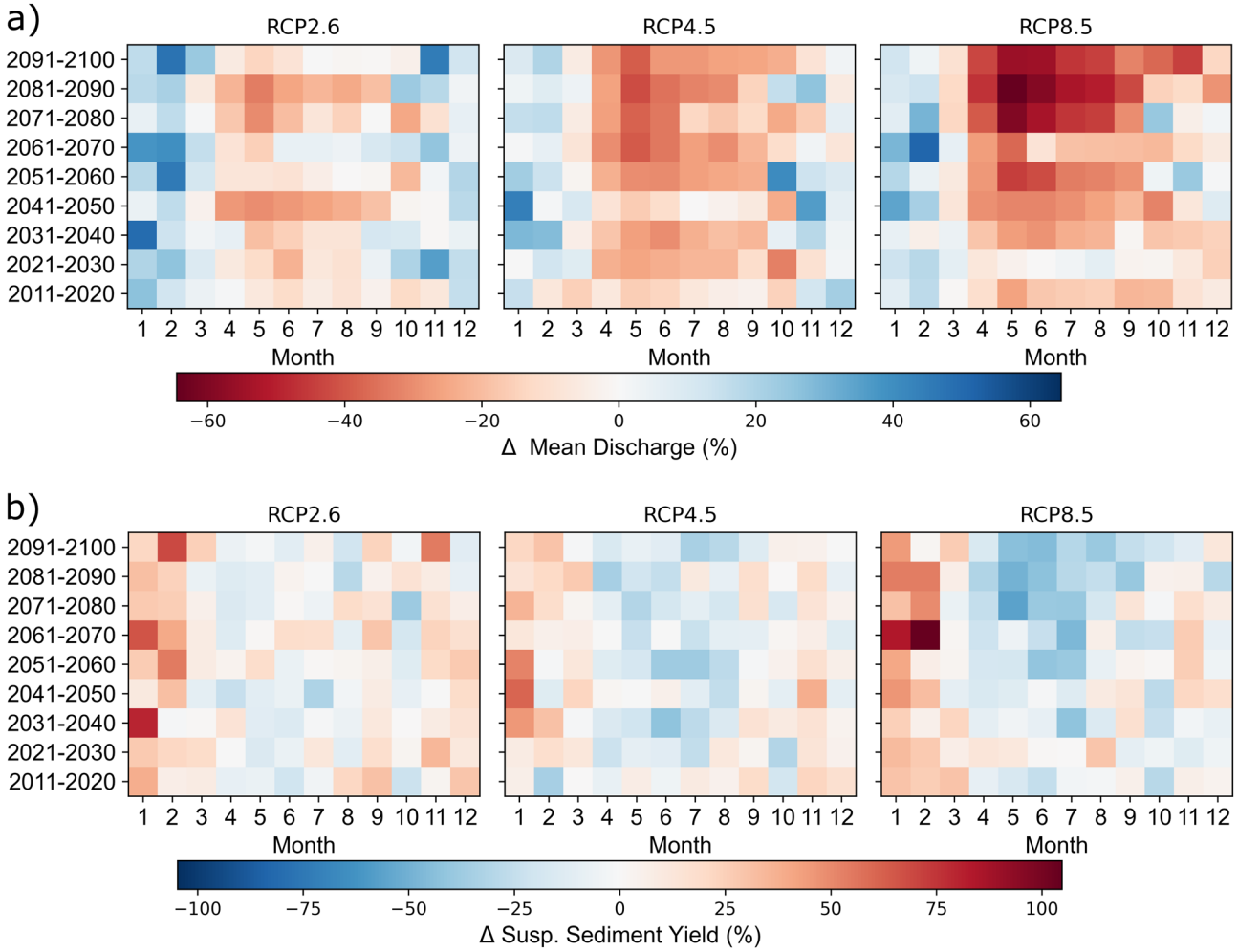

Figure 5. Decadal percent changes relative to the reference period (1981–2010) for the three climate change scenarios investigated. (**a**) Changes in mean monthly discharge (%) and (**b**) changes in mean monthly suspended sediment yield (%) of the Mediterranean Devoll River. The figure was created by the authors using Matplotlib 3.5.1 (https://matplotlib.org/).

to a decrease in TE and also contributing to increased uncertainty. The TE trends are subjected to significant uncertainty due to the variability in climate projections and the resulting timing of flood events, which means that a statistically significant difference between the RCPs cannot be identified.

The reservoir bed levels after 84 years of operation show similar sedimentation patterns across the RCPs and climate models (Fig. 7). Following the commissioning of the dam, the reservoir is in a deposition regime, characterized by ongoing sedimentation primarily concentrated at the head of the reservoir. As sedimentation progresses, the deposition delta gradually moves in the downstream direction. Consequently, a river channel develops in the upstream section of the reservoir, which reaches a state of sediment balance (see bed level evolution in Supplementary Information, SI9). The channel and delta progression extends slightly further downstream in RCP2.6 because the sediment yield is higher compared to RCP4.5 and RCP8.5 (Fig. 7). In addition, the substantial sediment deposition at the confluence of the two main tributaries causes the eastern tributary in RCP2.6 to be temporally disconnected for MOHC-HadGem2 at low water levels.

Global change impacts through combined and isolated climate and land use change

The application of projected land use change in addition to climate change projections amplifies the differences in future predictions for the SSY (Fig. 8). The only global change scenario with a decreasing SSY trend for the Mediterranean Devoll catchment is SSP1-RCP2.6 with − 3% for the mid and − 8% for the far future (Supplementary Information, Table S9). The SSY increases the most for SSP2-RCP4.5 in the mid (21%) and the far (41%) future. SSP4-RCP4.5 leads to a slightly lower increase in SSY in the mid (12%) and far (19%) future. SSP5-RCP8.5 causes a peak increase in SSY of 13% in the mid future, while SSY increases by 8% in the far future. The SSY seasonality is not affected by land use change and is solely driven by hydro-climatic variables, which is why all four scenarios show a decrease in spring and summer and an increase in winter.

The isolated effects of hydro-climatic and land use change on the SSY of the Devoll catchment reveal that land use exerts a continuous influence resulting in either a steady decrease (e.g., SSP1-RCP2.6, see Fig. 9) or increase (e.g., SSP2-RCP4.5, see Fig. 9). Hydro-climatic change does not exhibit such a continuous change pattern. For

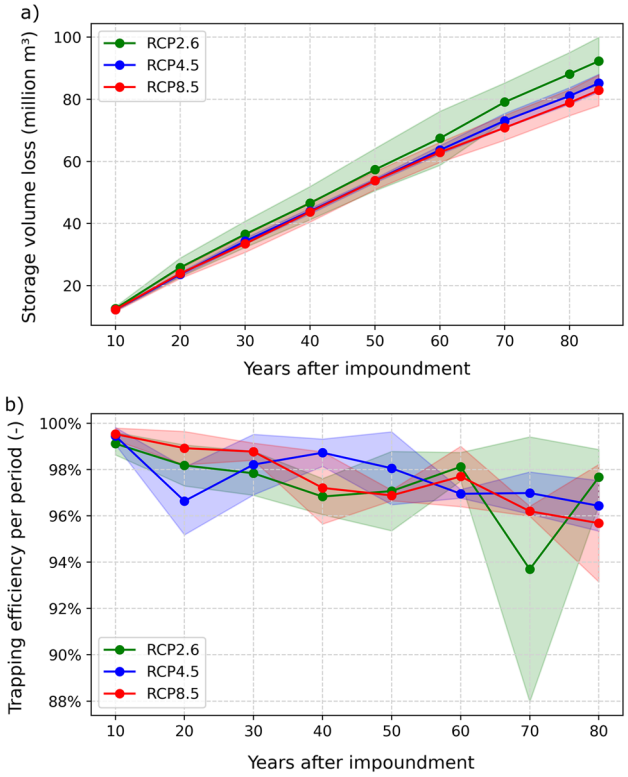

Figure 6. Evolution of (**a**) the loss in storage volume after impoundment and (**b**) the trapping efficiency at 10-year periods for the Banja reservoir and the three investigated RCPs. The shadowed areas represent the spread of ensemble climate projections, calculated as the mean value ± standard deviation.

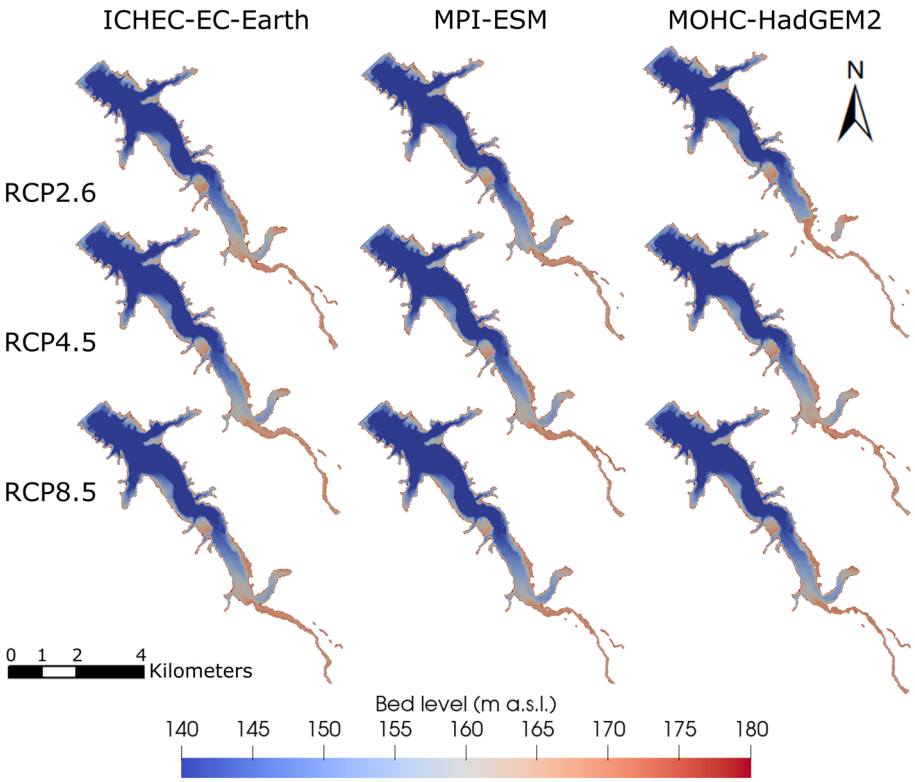

Figure 7. Comparison of reservoir bed levels across three RCPs and three climate models after 84 years of operation (2100).

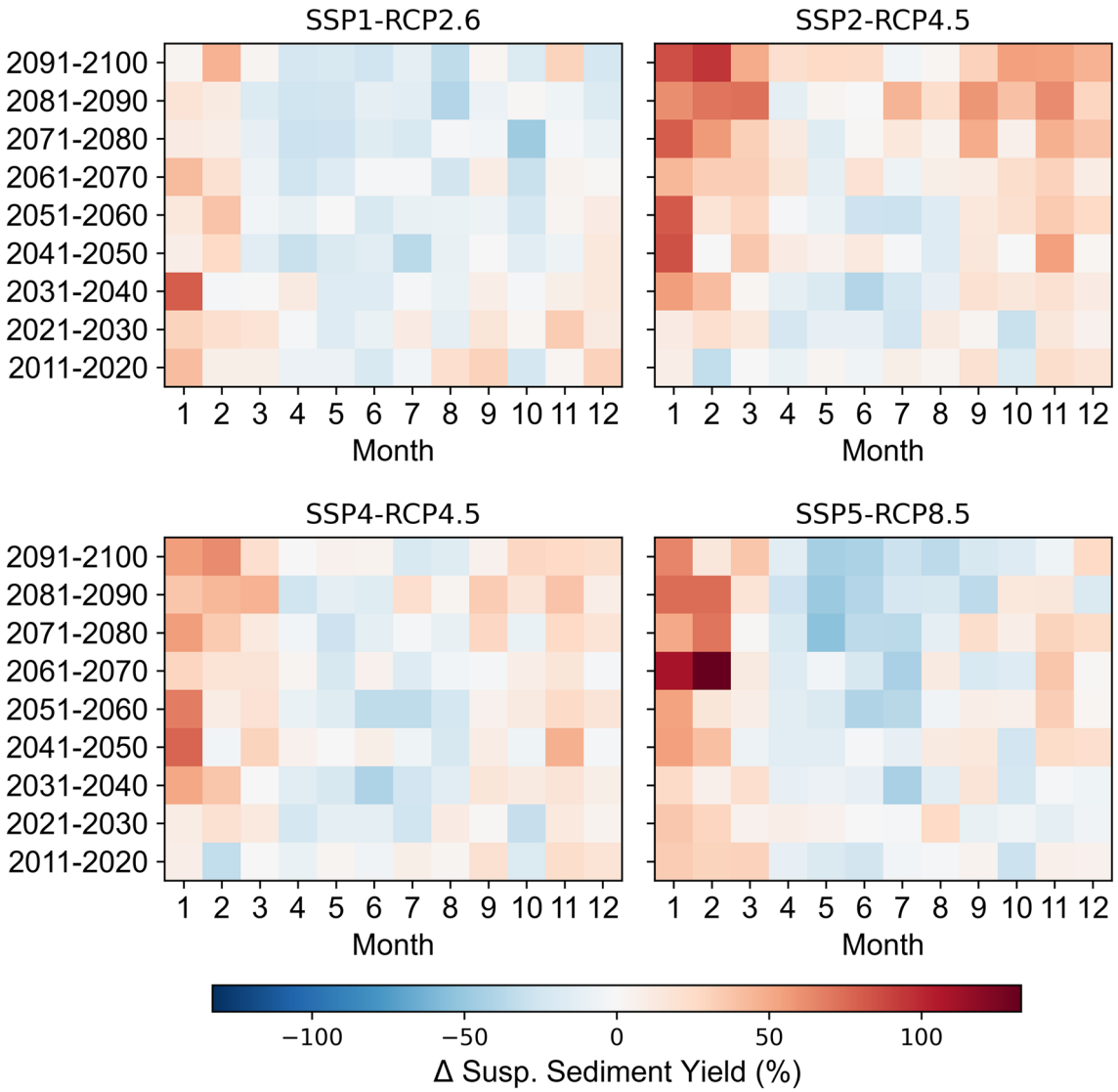

Figure 8. Decadal percent changes relative to the reference period (1981–2010) of the mean monthly change in the suspended sediment yield, SSY (%), of the Mediterranean Devoll catchment for the four global change scenarios investigated. The figure was created by the authors using Matplotlib 3.5.1 (https://matplotlib.org/).

example, the influence of hydro-climatic change on the SSY for SSP1- RCP2.6, SSP2-RCP4.5, and SSP4-RCP4.5 peaks in the mid future and decreases in the far future. For SSP5- RCP8.5, the trend changes completely in the far future, and hydro-climatic changes only result in a lower annual SSY compared to the reference period due to a decrease in precipitation.

The considerable changes in the SSY effect on sedimentation processes in the reservoir. Among the global change scenarios, the greatest volume loss is observed for SSP2-RCP4.5, while SSP1-RCP2.6 leads to the lowest loss (Supplementary Information, Fig. S8a). The differences between the global change scenarios are much more significant than those observed among isolated climate change scenarios. Similar to the climate change scenarios, the TE decreases across all SSPs over 84 years of impoundment, declining from initial values exceeding 99% to values ranging between 96.3 and 98.6% (Supplementary Information, Fig. S8b). Notably, no statistically significant differences in TE were identified among the SSPs, while the deposition patterns point to considerable delta formation and progression for SSP2, and less pronounced, SSP4. Specifically, these two scenarios with high SSY cause the delta to advance up to 4.5 km into the reservoir after 84 years of operation (Fig. 10). In contrast, for SSP1, the scenario with the lowest SSY, the delta does not reach the eastern tributary. Furthermore, scenarios with higher storage losses and consequently lower storage volumes tend to exhibit lower TEs.

Discussion

The model chain was applied to the Mediterranean Devoll catchment, serving as a representative example of regions characterized by high erosion rates and a Mediterranean hydro-climatic pattern. Temperature and precipitation trends aligned with studies conducted in other Mediterranean areas and impact both discharge and sediment production within the catchment[1,28,45,71]. While the average precipitation patterns vary marginally for

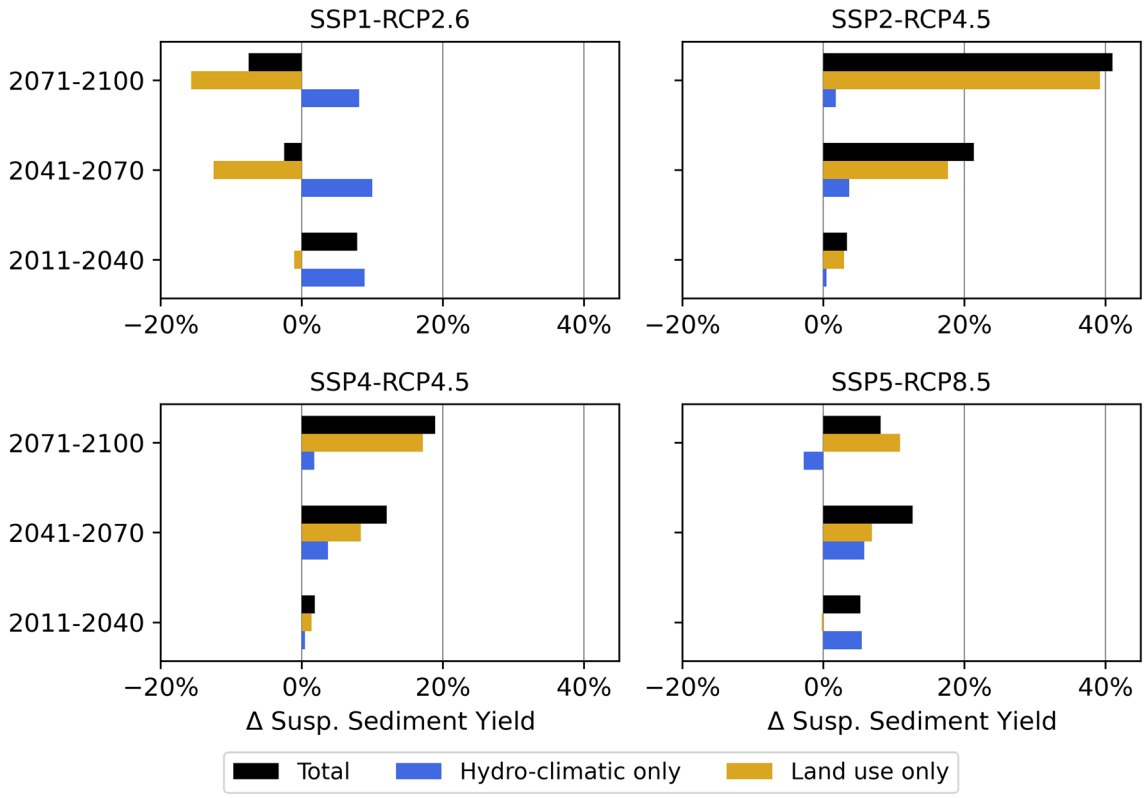

Figure 9. Influence of global (land use and hydro-climatic) change on the SSY (%) of the highly erosive Mediterranean catchment of the Devoll River for future 30-year periods.

RCP4.5 and the average decreases for RCP8.5, the seasonal variations for these pathways without emission reduction are projected to intensify with less precipitation and discharge in spring and summer. Projected increases in winter precipitation are unlikely to be stored as snow due to significant temperature rises across all RCPs. As a result, the elevated winter precipitation will be less available during the even drier spring and summer months, which are crucial for plant growth and agriculture[72]. Consequently, Mediterranean regions are expected to require increased artificial water storage, irrespective of the ultimately adopted RCP. Furthermore, more sediment will be mobilized due to less snow and higher peak flows in winter appearing nearly one month earlier in the year[1,73], which will increase reservoir sedimentation in Mediterranean regions.

Reservoir sedimentation is controlled by the sediment yield and discharge coming from the catchment. Seasonal changes in the sediment yield show an increase in the winter months and a decrease in spring and summer. However, the changes in the sediment yield may not necessarily be proportional to changes in precipitation and discharge[30,74]. Despite considerable reductions in discharge for RCP4.5 and 8.5, the sediment yield either increases or remains within the margin of error of the model chain, providing evidence of rising sediment concentrations, particularly in high emissions scenarios. The higher sediment yields occur despite reduced discharge, which can be attributed to more frequent extreme precipitation events and winter rainfall (instead of snow) on less vegetated soils, which are more susceptible to erosion. Consequently, more erosive rainfall affects erodible soils, especially in the most likely and less sustainable climate change scenarios of RCP4.5 and RCP8.5. The consideration of the decreasing share of grassland and forest in SSP2-RCP4.5 and SSP4-RCP4.5 leads to an even more pronounced increase in soil erosion and sediment yield. Thus, unsustainable development in Mediterranean catchments leads to higher soil erosion and consequently soil loss, which threatens the livelihood of large portions of the population[75]. Particularly for SSP4-RCP4.5, a vicious circle risks opening up, since global inequality might lead to further environmental degradation and thus even more soil loss[76]. Land use change in the SSP1-RCP2.6 sustainability scenario results in a trend reversal and the sediment yield decreases due to the expansion of grasslands and forests despite increasing precipitation.

In the Mediterranean Devoll catchment, the impact of land use change on annual sediment yield outweighs the effect of hydro-climatic changes, particularly in the far future (Fig. 9). The crucial importance of land use on erosion and sediment yield is consistent with previous findings[22,25,33,77]. For example, alterations in land use resulting from climate change were shown to have a more pronounced effect on soil erosion than changes in precipitation or temperature alone[78]. Therefore, effective management of local land use represents an opportunity to alleviate the effects of climate change[79]. Actions such as afforestation[78], contour farming, or riparian buffers can effectively reduce sediment yields and subsequent reservoir sedimentation. In cases where bioenergy production requires acreage (e.g., SSP2), the considerate selection of bioenergy crops can help regulate sediment production in a catchment[80]. Preferably, the cultivation of perennial grasses with extensive vegetation cover should be favored over grain-based energy crops, such as soybean, corn, and rapeseed[81]. However, not all sediment production

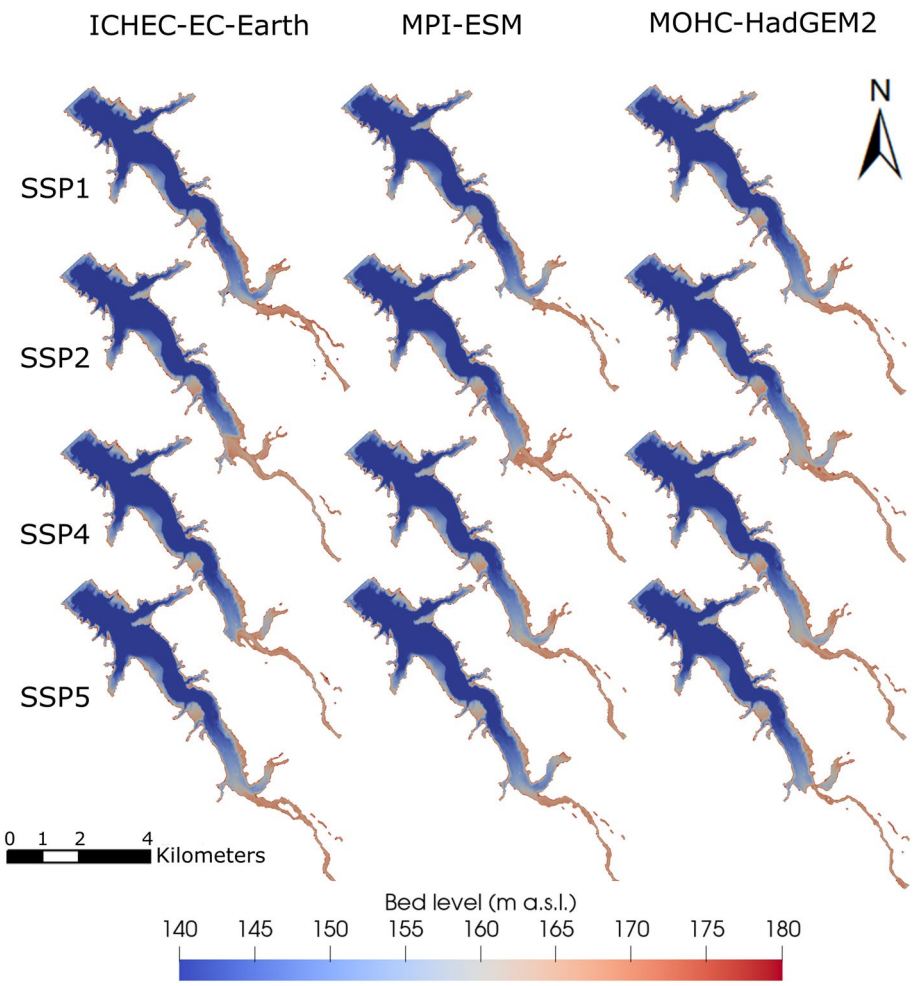

Figure 10. Comparison of reservoir bed levels across four SSPs and three climate models after 84 years of operation (2100).

processes are directly driven by land use. For instance, fluvial erosion is affected by bank stability and the basal shear stress of a river.

While projections for the Devoll catchment indicate that land use change will dominate over the effects of climate change on soil erosion and suspended sediment yield in Mediterranean areas, contrasting results are expected in regions with substantial increases in rainfall erosivity[47]. For instance, in central Europe or along the North American East coast, hydro-climatic change is likely to exert a greater influence on soil erosion than changes in land use.

Reservoirs can mitigate seasonal hydrological fluctuations caused by global change, provided that sediment inflow does not substantially diminish their storage capacity. However, storage capacity is expected to decrease as sedimentation rates increase, which in turn will affect, for example, the availability of water for irrigation. To this end, sustainable reservoir operation should aim for a small trapping efficiency, which naturally declines over time due to narrower cross-sections with higher sediment conveyance capacity through increased mean flow velocities[42]. In the Banja reservoir, a typical decrease in TE is observed (Fig. 6), especially in scenarios characterized by high sediment yield. However, the high uncertainty in the climate projections hampers a clear differentiation between TE trends among RCPs and SSPs. Due to higher flow velocities and transport capacities in the reservoir, TE decreases primarily when high discharges occur over a period of several weeks, while sediment originating from stochastically occurring singular extreme events tends to be largely trapped. Beyond TE, the predicted reservoir bed levels (Fig. 10) indicate considerable sedimentation at the reservoir head (delta deposition), leading also to the formation of a channel. This process of channel formation is a common characteristic observed in large reservoirs[42,82]. The most significant difference among the global and climate change scenarios is that the channel and the delta progression extend further downstream in scenarios with high sediment yield (e.g., RCP2.6, SSP2-RCP4-5, and SSP4-RCP4.5).

These findings provide valuable insights for implementing targeted reservoir management strategies. For example, one option to reduce significant upstream sediment deposition is to lower the water level before the anticipated high sediment inflow during the wet season. This approach allows sediments to be re-suspended and transported closer to the dam, with the option of routing them through the reservoir or storing them in the dead

storage. However, these sediment deposits near the dam can pose safety concerns, such as blockage of bottom outlets, while offering opportunities for easier flushing that facilitates reservoir management[7]. Thus, the precise 3d modeling also aids in delineating dam safety concerns, but the model chain cannot yet process feedback of decreasing reservoir storage on water availability and thus on land use.

Although this study did not consider specific management strategies and the monitoring period was limited, it emphasizes the capacities of a novel interdisciplinary model chain to predict long-term reservoir sedimentation in Mediterranean areas. Still, absolute sediment-related quantities are subject to considerable uncertainty, primarily stemming from variations in climate projections and their propagation through the model chain. On the contrary, the lower uncertainty because of the physically greater precision of the 3d numerical model played a subordinate role. Thus, to address the uncertainty in long-term predictions of reservoir sedimentation, a primary concern will be to improve the accuracy of climate predictions. Ultimately, the climate projections only determine the framework conditions of this inherently precise and efficient model chain, which produces predictions of reservoir sedimentation with unprecedented precision and time horizons to test and implement effective land-use management actions, even in remote regions.

Conclusions

A complex interdisciplinary and physics-informed model chain demonstrates considerable impacts of hydro-climatic and land use changes on water availability, sediment production, and reservoir sedimentation in a Mediterranean region Applied to the Devoll catchment, a typical Mediterranean mountainous region with high sediment production, the model chain shows that global change leads to increased sediment yields and decreased river discharge, with seasonal shifts for most of the climate and land use change projections considered. A low-emission scenario (SSP1-RCP2.6) sustains higher discharges by 2100, while mid to high greenhouse gas emission and unequal development (SSP4-RCP4.5) or fossil-fueled development (SSP5-RCP8.5) scenarios amplify water scarcity. Specifically, increased winter rainfall, reduced snowfall, and decreased summer precipitation contribute to limited water availability during hot and dry Mediterranean summers, emphasizing the need for artificial water storage in reservoirs.

In the low-emissions scenarios, higher discharges lead to elevated sediment yields but lower sediment concentrations compared to less sustainable emissions scenarios. In particular, the sediment concentration decreases with the implementation of sustainable land use (SSP1-RCP2.6). In contrast, less sustainable land use leads to higher sediment concentrations and sediment yields (SSP2-RCP4.5 and SSP4-RCP4.5) due to decreased forest and grassland areas. The scenarios with higher sediment yields experience the most substantial loss of storage volume and the delta moves further downstream, resulting also in a decrease in trapping efficiency (TE).

The three-dimensional (3d) hydro-morphodynamic model at the end of the model chain goes beyond simplistic parameters, such as TE, and provides valuable insights into sedimentation patterns and processes controlled by global change. Although simplistic models may yield similar TE results as multidimensional numerical models, a spatially explicit 3d model pinpoints hotspots of sedimentation, providing crucial information for sustainable reservoir management practices like dredging or reservoir flushing.

Ultimately, the interdisciplinary model chain highlights that land use change outweighs climate change effects in Mediterranean regions. Therefore, localized management actions for land use change in the catchment, such as policy-enforced crop adaptations and afforestation, can reduce soil loss and sediment production. In addition, the long-term prediction strength of the model and the spatially explicit deposition patterns enable the implementation of targeted reservoir management strategies.

Data availability

The complete datasets generated during and/or analyzed during the current study are available from the corresponding author on reasonable request.

Received: 30 June 2023; Accepted: 14 November 2023
Published online: 17 November 2023

References

1. García-Ruiz, J. M., López-Moreno, J. I., Vicente-Serrano, S. M., Lasanta-Martínez, T. & Beguería, S. Mediterranean water resources in a global change scenario. *Earth Sci. Rev.* **105**, 121–139 (2011).
2. Alcamo, J. & Henrichs, T. Critical regions: A model-based estimation of world water resources sensitive to global changes. *Aquat. Sci.* **64**, 352–362 (2002).
3. Nilawar, A. P. & Waikar, M. L. Impacts of climate change on streamflow and sediment concentration under RCP 4.5 and 8.5: A case study in Purna river basin, India. *Sci. Total Environ.* **650**, 2685–2696 (2019).
4. Hamududu, B. H. & Ngoma, H. Impacts of climate change on water resources availability in Zambia: Implications for irrigation development. *Environ. Dev. Sustain.* **22**, 2817–2838 (2020).
5. Dallison, R. J. H., Patil, S. D. & Williams, A. P. Impacts of climate change on future water availability for hydropower and public water supply in Wales, UK. *J. Hydrol. Reg. Stud.* **36**, 100866 (2021).
6. Trenberth, K. E. *et al.* Global warming and changes in drought. *Nat. Clim. Change* **4**, 17–22 (2014).
7. Kondolf, G. M. *et al.* Sustainable sediment management in reservoirs and regulated rivers: Experiences from five continents. *Earth's Future* **2**, 256–280 (2014).
8. Schleiss, A. J., Franca, M. J., Juez, C. & De Cesare, G. Reservoir sedimentation. *J. Hydraul. Res.* **54**, 595–614 (2016).
9. Ahmad, M.-D. *et al.* Climate change and reservoir sedimentation implications for irrigated agriculture in the Indus Basin Irrigation System in Pakistan. *J. Hydrol.* **603**, 126967 (2021).
10. Yasarer, L. M. W. & Sturm, B. S. M. Potential impacts of climate change on reservoir services and management approaches. *Lake Reserv. Manag.* **32**, 13–26 (2016).
11. Mahmood, K. Reservoir sedimentation-impact, extent and mitigation. *World Bank Tech. Pap.* **71**, 1–10 (1987).

12. Yoon, Y. N. The state and the perspective of the direct sediment removal methods from reservoirs. *Int. J. Sediment Res.* **7**, 99–115 (1992).
13. Bruk, S. Reservoir sedimentation and sustainable management of water resources: The international perspective. in *Proceedings of the International Conference on Reservoir Sedimentation*, 9–13 (1996).
14. Sumi, T. Reservoir sedimentation management with bypass tunnels in Japan. in *Proceedings of the Ninth International Symposium on River Sedimentation* (2004).
15. Basson, G. R. Management of siltation in existing and new reservoirs. in *Proceedings of the 23rd Congress of the International Commission on Large Dams CIGB-ICOLD*, vol. 2 (2009).
16. Annandale, G. *Quenching the Thirst: Sustainable Water Supply and Climate Change* (CreateSpace Independent Publishing Platform, 2013).
17. Zarfl, C. *et al.* Future large hydropower dams impact global freshwater megafauna. *Sci. Rep.* **9**, 18531 (2019).
18. UNESCO. *The United Nations World Water Development Report 2021: Valuing Water* (United Nations, 2021).
19. Shrestha, B. *et al.* Impact of climate change on sediment yield in the Mekong River basin: A case study of the Nam Ou basin, Lao PDR. *Hydrol. Earth Syst. Sci.* **17**, 1–20 (2013).
20. Panagos, P. *et al.* Projections of soil loss by water erosion in Europe by 2050. *Environ. Sci. Policy* **124**, 380–392 (2021).
21. Patro, E. R., De Michele, C., Granata, G. & Biagini, C. Assessment of current reservoir sedimentation rate and storage capacity loss: An Italian overview. *J. Environ. Manage.* **320**, 115826 (2022).
22. Shi, X. *et al.* The response of the suspended sediment load of the headwaters of the Brahmaputra River to climate change: Quantitative attribution to the effects of hydrological, cryospheric and vegetation controls. *Glob. Planet* **210**, 103753 (2022).
23. Eekhout, J. P. C., Hunink, J. E., Terink, W. & de Vente, J. Why increased extreme precipitation under climate change negatively affects water security. *Hydrol. Earth Syst. Sci.* **22**, 5935–5946 (2018).
24. Rajbanshi, J. & Bhattacharya, S. Modelling the impact of climate change on soil erosion and sediment yield: A case study in a subtropical catchment, India. *Model. Earth Syst. Environ.* **1**, 1–23. https://doi.org/10.1007/s40808-021-01117-4 (2021).
25. Lu, X. X. *et al.* Sediment loads response to climate change: A preliminary study of eight large Chinese rivers. *Int. J. Sediment Res.* **28**, 1–14 (2013).
26. Azari, M., Moradi, H. R., Saghafian, B. & Faramarzi, M. Climate change impacts on streamflow and sediment yield in the North of Iran. *Hydrol. Sci.* **61**, 123–133 (2016).
27. Hirschberg, J. *et al.* Climate change impacts on sediment yield and debris-flow activity in an alpine catchment. *J. Geophys. Res. Earth Surf.* **126**, e005739 (2021).
28. Nerantzaki, S. D. *et al.* Modeling suspended sediment transport and assessing the impacts of climate change in a karstic Mediterranean watershed. *Sci. Total Environ.* **538**, 288–297 (2015).
29. Uber, M. *et al.* Climate change impacts on soil erosion and sediment delivery to German federal waterways: A case study of the Elbe Basin. *Atmosphere* **13**, 1752 (2022).
30. de Oliveira Fagundes, H. *et al.* An assessment of South American sediment fluxes under climate changes. *Sci. Total Environ.* **879**, 163056 (2023).
31. Moragoda, N. & Cohen, S. Climate-induced trends in global riverine water discharge and suspended sediment dynamics in the 21st century. *Glob. Planet* **191**, 103199 (2020).
32. Khoi, D. N. & Suetsugi, T. Impact of climate and land-use changes on hydrological processes and sediment yield: A case study of the Be River catchment, Vietnam. *Hydrol. Sci* **59**, 1095–1108 (2014).
33. Zhao, G. *et al.* Assessing response of sediment load variation to climate change and human activities with six different approaches. *Sci. Total Environ.* **639**, 773–784 (2018).
34. Sinha, R. K., Eldho, T. I. & Subimal, G. Assessing the impacts of land cover and climate on runoff and sediment yield of a river basin. *Hydrol. Sci* **65**, 2097–2115 (2020).
35. Nunes, J. P., Seixas, J. & Keizer, J. J. Modeling the response of within-storm runoff and erosion dynamics to climate change in two Mediterranean watersheds: A multi-model, multi-scale approach to scenario design and analysis. *Catena* **102**, 27–39 (2013).
36. Mullan, D., Favis-Mortlock, D. & Fealy, R. Addressing key limitations associated with modelling soil erosion under the impacts of future climate change. *Agric. For. Meteorol.* **156**, 18–30 (2012).
37. Routschek, A., Schmidt, J. & Kreienkamp, F. Impact of climate change on soil erosion: A high-resolution projection on catchment scale until 2100 in Saxony/Germany. *Catena* **121**, 99–109 (2014).
38. Khan, M. A., Stamm, J. & Haider, S. Simulating the impact of climate change with different reservoir operating strategies on sedimentation of the Mangla reservoir, Northern Pakistan. *Water* **12**, 2736 (2020).
39. Ehrbar, D. *et al.* Continuous seasonal and large-scale periglacial reservoir sedimentation. *Sustainability* **10**, 3265 (2018).
40. Bussi, G. *et al.* Impact of dams and climate change on suspended sediment flux to the Mekong delta. *Sci. Total Environ.* **755**, 142468 (2021).
41. Chamoun, S., De Cesare, G. & Schleiss, A. J. Managing reservoir sedimentation by venting turbidity currents: A review. *Int. J. Sediment Res.* **31**, 195–204 (2016).
42. Morris, G. L. & Fan, J. *Reservoir Sedimentation Handbook: Design and Management of Dams, Reservoirs, and Watersheds for Sustainable Use* (McGraw-Hill, 1998).
43. Chen, M. *et al.* Global land use for 2015–2100 at 0.05° resolution under diverse socioeconomic and climate scenarios. *Sci. Data* **7**, 320 (2020).
44. Pesci, M. H., Mouris, K., Haun, S. & Förster, K. Assessment of uncertainties in a complex modeling chain for predicting reservoir sedimentation under changing climate. *Model. Earth Syst. Environ.* https://doi.org/10.1007/s40808-023-01705-6 (2023).
45. Bangash, R. F. *et al.* Ecosystem services in Mediterranean river basin: Climate change impact on water provisioning and erosion control. *Sci. Total Environ.* **458–460**, 246–255 (2013).
46. Walling, D. E. & Webb, B. W. Erosion and sediment yield: A global overview. in *Proceedings of the Exeter Symposium*, vol. 236, 3–19 (IAHS, 1996).
47. Borrelli, P. *et al.* Land use and climate change impacts on global soil erosion by water (2015–2070). *Proc. Natl. Acad. Sci.* **117**, 21994–22001 (2020).
48. Carolli, M. *et al.* Impacts of existing and planned hydropower dams on river fragmentation in the Balkan region. *Sci. Total Environ.* **871**, 161940 (2023).
49. Müller, D. & Sikor, T. Effects of postsocialist reforms on land cover and land use in South-Eastern Albania. *Appl. Geogr.* **26**, 175–191 (2006).
50. Mouris, K., Schwindt, S., Haun, S., Morales Oreamuno, M. F. & Wieprecht, S. Introducing seasonal snow memory into the RUSLE. *J. Soils Sediments* https://doi.org/10.1007/s11368-022-03192-1 (2022).
51. Matta, E. *et al.* Data integration for investigating drivers of water quality variability in the Banja reservoir watershed. *Water* **15**, 607 (2023).
52. Aleixo, R., Guerrero, M., Nones, M. & Ruther, N. Applying ADCPs for long-term monitoring of SSC in rivers. *Water Resour. Res.* **56**, 6087 (2020).
53. Berg, P., Bosshard, T., Yang, W. & Zimmermann, K. MIdASv0.2.1 – MultI-scale bias AdjuStment. *Geosci. Model. Dev.* **15**, 6165–6180 (2022).
54. Hersbach, H. *et al.* The ERA5 global reanalysis. *Q. J. R. Meteorol. Soc.* **146**, 1999–2049 (2020).

55. Riahi, K. *et al.* The shared socioeconomic pathways and their energy, land use, and greenhouse gas emissions implications: An overview. *Glob. Environ. Change* **42**, 153–168 (2017).
56. Eyring, V. *et al.* Overview of the coupled model intercomparison project phase 6 (CMIP6) experimental design and organization. *Geosci. Model. Dev.* **9**, 1937–1958 (2016).
57. Popp, A. *et al.* Land-use futures in the shared socio-economic pathways. *Glob. Environ. Change* **42**, 331–345 (2017).
58. Schulla, J. *Hydrologische Modellierung von Flussgebieten zur Abschätzung der Folgen von Klimaänderungen* (ETH Zurich, 1997). https://doi.org/10.3929/ethz-a-001763261.
59. Schulla, J. *Model Description WaSiM*. http://www.wasim.ch/downloads/doku/wasim/wasim_2021_en.pdf (2021).
60. Förster, K., Garvelmann, J., Meißl, G. & Strasser, U. Modelling forest snow processes with a new version of WaSiM. *Hydrol. Sci.* **63**, 1540–1557 (2018).
61. Renard, K. G., Foster, G. R., Weesies, G. A. & Porter, J. P. RUSLE: Revised universal soil loss equation. *J. Soil Water Conserv.* **46**(1), 30–33 (1991).
62. Ferro, V. & Porto, P. Sediment delivery distributed (SEDD) model. *J. Hydrol. Eng.* **5**, 411–422 (2000).
63. Olsen, N. R. B. *A Three-Dimensional Numerical Model for Simulation of Sediment Movements in Water Intakes with Multiblock Option. User's Manual* (Springer, 2018).
64. Olsen, N. R. B. & Hillebrand, G. Long-time 3D CFD modeling of sedimentation with dredging in a hydropower reservoir. *J. Soils Sediments* **18**, 3031–3040 (2018).
65. Haun, S., Kjærås, H., Løvfall, S. & Olsen, N. R. B. Three-dimensional measurements and numerical modelling of suspended sediments in a hydropower reservoir. *J. Hydrol.* **479**, 180–188 (2013).
66. Shoarinezhad, V., Wieprecht, S. & Haun, S. Comparison of local and global optimization methods for calibration of a 3D morphodynamic model of a curved channel. *Water* **12**, 1333 (2020).
67. Schwindt, S. *et al.* Bayesian calibration points to misconceptions in three-dimensional hydrodynamic reservoir modeling. *Water Resour. Res.* **59**, e033660 (2023).
68. Kennedy, M. C. & O'Hagan, A. Bayesian calibration of computer models. *J. R. Stat. Soc. B* **63**, 425–464 (2001).
69. Mosselman, E. & Le, T. B. Five common mistakes in fluvial morphodynamic modeling. *Adv. Water Resour.* **93**, 15–20 (2016).
70. Mouris, K. *et al.* Stability criteria for Bayesian calibration of reservoir sedimentation models. *Model. Earth Syst. Environ.* https://doi.org/10.1007/s40808-023-01712-7 (2023).
71. Wasti, A. *et al.* Climate change and the hydropower sector: A global review. *Wiley Interdiscip. Rev. Clim. Change* **13**, e757 (2022).
72. Saadi, S. *et al.* Climate change and Mediterranean agriculture: Impacts on winter wheat and tomato crop evapotranspiration, irrigation requirements and yield. *Agric. Water Manag.* **147**, 103–115 (2015).
73. Adam, J. C., Hamlet, A. F. & Lettenmaier, D. P. Implications of global climate change for snowmelt hydrology in the twenty-first century. *Hydrol. Process.* **23**, 962–972 (2009).
74. Tian, P., Lu, H., Feng, W., Guan, Y. & Xue, Y. Large decrease in streamflow and sediment load of Qinghai-Tibetan Plateau driven by future climate change: A case study in Lhasa River Basin. *Catena* **187**, 104340 (2020).
75. Barbier, E. B. & Hochard, J. P. Does land degradation increase poverty in developing countries?. *PLOS ONE* **11**, e0152973 (2016).
76. Boyce, J. K. Inequality as a cause of environmental degradation. *Ecol. Econ.* **11**, 169–178 (1994).
77. Romano, G., Abdelwahab, O. M. M. & Gentile, F. Modeling land use changes and their impact on sediment load in a Mediterranean watershed. *Catena* **163**, 342–353 (2018).
78. Li, Z. & Fang, H. Impacts of climate change on water erosion: A review. *Earth Sci. Rev.* **163**, 94–117 (2016).
79. Eekhout, J. P. C. & de Vente, J. Global impact of climate change on soil erosion and potential for adaptation through soil conservation. *Earth Sci. Rev.* **226**, 103921 (2022).
80. Wu, Y. *et al.* Bioenergy production and environmental impacts. *Geosci. Lett.* **5**, 14 (2018).
81. Wang, E. *et al.* Strategic switchgrass (*Panicum virgatum*) production within row cropping systems: Regional-scale assessment of soil erosion loss and water runoff impacts. *Glob. Change Biol. Bioenergy* **12**, 955–967 (2020).
82. Rulot, F., Dewals, B. J., Erpicum, S., Archambeau, P. & Pirotton, M. Long-term sediment management for sustainable hydropower. In *Comprehensive Renewable Energy* (ed. Sayigh, A.) 355–376 (Elsevier, 2012). https://doi.org/10.1016/B978-0-08-087872-0.00620-X.

Acknowledgements

This study was conducted within the DIRT-X project, which is part of AXIS, an ERA-NET initiated by JPI Climate and funded by FFG Austria, BMBF Germany, FORMAS Sweden, NWO NL, and RCN Norway with co-funding from the European Union (Grant No. 776608). The last author is indebted to the Baden-Württemberg Stiftung for financial support through the Elite Program for Postdocs. We also thank Nils Rüther, Kordula Schwarzwälder, Slaven Conevski, Behnam Balouchi, and Thomas Bosshard for providing input data, and Kristian Förster, Maria Fernanda Morales Oreamuno, Jadran Surac, André Maffert, and Anna Cerf for their help and productive discussions.

Author contributions

K.M.: Methodology, conceptualization, writing-original draft and editing, visualization, investigation, software, and formal analysis. S.S.: Review and editing, conceptualization, supervision and project administration. M.H.P. Methodology, investigation, review and editing. S.W. Review and editing, supervision, funding acquisition and resources. S.H. Review and editing, conceptualization, supervision, funding acquisition and project administration.

Funding

Open Access funding enabled and organized by Projekt DEAL.

Competing interests

The authors declare no competing interests.

Additional information

Supplementary Information The online version contains supplementary material available at https://doi.org/10.1038/s41598-023-47501-1.

Correspondence and requests for materials should be addressed to K.M.

Institut für Wasser- und Umweltsystemmodellierung
Universität Stuttgart

Pfaffenwaldring 61
70569 Stuttgart (Vaihingen)
Telefon (0711) 685 - 60156
Telefax (0711) 685 - 51073
E-Mail: iws@iws.uni-stuttgart.de
http://www.iws.uni-stuttgart.de

Direktoren
Prof. Dr.-Ing. Rainer Helmig
Prof. Dr.-Ing. Wolfgang Nowak
Prof. Dr.-Ing. Silke Wieprecht

Emeriti
Prof. Dr.-Ing. habil. Dr.-Ing. E.h. Jürgen Giesecke
Prof. Dr.h.c. Dr.-Ing. E.h. Helmut Kobus, PhD

Lehrstuhl für Wasserbau und Wassermengenwirtschaft
Leiterin: Prof. Dr.-Ing. Silke Wieprecht
Stellv.: Dr.-Ing. Kristina Terheiden
Versuchsanstalt für Wasserbau
Leiter: Stefan Haun, PhD

Lehrstuhl für Hydromechanik und Hydrosystemmodellierung
Leiter: Prof. Dr.-Ing. Rainer Helmig
Stellv.: apl. Prof. Dr.-Ing. Holger Class

Lehrstuhl für Stochastische Simulation und Sicherheitsforschung für Hydrosysteme
Leiter: Prof. Dr.-Ing. Wolfgang Nowak
Stellv.: apl. Prof. Dr.-Ing. Sergey Oladyshkin
Hydrogeophysik der Vadosen Zone
(mit Forschungszentrum Jülich)
Leiter: Prof. Dr. J.A. Sander Huisman

***VEGAS,* Versuchseinrichtung zur Grundwasser- und Altlastensanierung**
Leiter: Dr.-Ing. Simon Kleinknecht
PD Dr.-Ing. Claus Haslauer

Verzeichnis der Mitteilungshefte

7 *Sonderheft anläßlich des 65. Geburtstages von Prof. Arthur Röhnisch mit Beiträgen von* Benk, Dieter; Breitling, J.; Gurr, Siegfried; Haberhauer, Robert; Honekamp, Hermann; Kuz, Klaus Dieter; Marotz, Günter; Mayer-Vorfelder, Hans-Jörg; Miller, Rudolf; Plate, Erich J.; Radomski, Helge; Schwarz, Helmut; Vollmer, Ernst; Wildenhahn, Eberhard; 1967

8 Jumikis, Alfred: *Beitrag zur experimentellen Untersuchung des Wassernachschubs in einem gefrierenden Boden und die Beurteilung der Ergebnisse*, 1968

9 Marotz, Günter: *Technische Grundlagen einer Wasserspeicherung im natürlichen Untergrund*, 1968

10 Radomski, Helge: *Untersuchungen über den Einfluß der Querschnittsform wellenförmiger Spundwände auf die statischen und rammtechnischen Eigenschaften*, 1968

11 Schwarz, Helmut: *Die Grenztragfähigkeit des Baugrundes bei Einwirkung vertikal gezogener Ankerplatten als zweidimensionales Bruchproblem*, 1969

12 Erbel, Klaus: *Ein Beitrag zur Untersuchung der Metamorphose von Mittelgebirgsschneedecken unter besonderer Berücksichtigung eines Verfahrens zur Bestimmung der thermischen Schneequalität*, 1969

13 Westhaus, Karl-Heinz: *Der Strukturwandel in der Binnenschiffahrt und sein Einfluß auf den Ausbau der Binnenschiffskanäle*, 1969

14 Mayer-Vorfelder, Hans-Jörg: *Ein Beitrag zur Berechnung des Erdwiderstandes unter Ansatz der logarithmischen Spirale als Gleitflächenfunktion*, 1970

15 Schulz, Manfred: *Berechnung des räumlichen Erddruckes auf die Wandung kreiszylindrischer Körper*, 1970

16 Mobasseri, Manoutschehr: *Die Rippenstützmauer. Konstruktion und Grenzen ihrer Standsicherheit*, 1970

17 Benk, Dieter: *Ein Beitrag zum Betrieb und zur Bemessung von Hochwasserrückhaltebecken*, 1970

18 Gàl, Attila: *Bestimmung der mitschwingenden Wassermasse bei überströmten Fischbauchklappen mit kreiszylindrischem Staublech*, 1971, *vergriffen*

19 Kuz, Klaus Dieter: *Ein Beitrag zur Frage des Einsetzens von Kavitationserscheinungen in einer Düsenströmung bei Berücksichtigung der im Wasser gelösten Gase*, 1971, *vergriffen*

20 Schaak, Hartmut: *Verteilleitungen von Wasserkraftanlagen*, 1971

21 *Sonderheft zur Eröffnung der neuen Versuchsanstalt des Instituts für Wasserbau der Universität Stuttgart mit Beiträgen von* Brombach, Hansjörg; Dirksen, Wolfram; Gàl, Attila; Gerlach, Reinhard; Giesecke, Jürgen; Holthoff, Franz-Josef; Kuz, Klaus Dieter; Marotz, Günter; Minor, Hans-Erwin; Petrikat, Kurt; Röhnisch, Arthur; Rueff, Helge; Schwarz, Helmut; Vollmer, Ernst; Wildenhahn, Eberhard; 1972

22 Wang, Chung-su: *Ein Beitrag zur Berechnung der Schwingungen an Kegelstrahlschiebern*, 1972

23 Mayer-Vorfelder, Hans-Jörg: *Erdwiderstandsbeiwerte nach dem Ohde-Variationsverfahren*, 1972

24 Minor, Hans-Erwin: *Beitrag zur Bestimmung der Schwingungsanfachungsfunktionen überströmter Stauklappen*, 1972, *vergriffen*

25 Brombach, Hansjörg: *Untersuchung strömungsmechanischer Elemente (Fluidik) und die Möglichkeit der Anwendung von Wirbelkammerelementen im Wasserbau*, 1972, *vergriffen*

26 Wildenhahn, Eberhard: *Beitrag zur Berechnung von Horizontalfilterbrunnen*, 1972

27 Steinlein, Helmut: *Die Eliminierung der Schwebstoffe aus Flußwasser zum Zweck der unterirdischen Wasserspeicherung, gezeigt am Beispiel der Iller*, 1972

28 Holthoff, Franz Josef: *Die Überwindung großer Hubhöhen in der Binnenschiffahrt durch Schwimmerhebewerke*, 1973

29 Röder, Karl: *Einwirkungen aus Baugrundbewegungen auf trog- und kastenförmige Konstruktionen des Wasser- und Tunnelbaues*, 1973

30 Kretschmer, Heinz: *Die Bemessung von Bogenstaumauern in Abhängigkeit von der Talform*, 1973

31 Honekamp, Hermann: *Beitrag zur Berechnung der Montage von Unterwasserpipelines*, 1973

32 Giesecke, Jürgen: *Die Wirbelkammertriode als neuartiges Steuerorgan im Wasserbau*, und Brombach, Hansjörg: *Entwicklung, Bauformen, Wirkungsweise und Steuereigenschaften von Wirbelkammerverstärkern*, 1974

33 Rueff, Helge: *Untersuchung der schwingungserregenden Kräfte an zwei hintereinander angeordneten Tiefschützen unter besonderer Berücksichtigung von Kavitation*, 1974

34 Röhnisch, Arthur: *Einpreßversuche mit Zementmörtel für Spannbeton - Vergleich der Ergebnisse von Modellversuchen mit Ausführungen in Hüllwellrohren*, 1975

35 *Sonderheft anläßlich des 65. Geburtstages von Prof. Dr.-Ing. Kurt Petrikat mit Beiträgen von*: Brombach, Hansjörg; Erbel, Klaus; Flinspach, Dieter; Fischer jr., Richard; Gàl, Attila; Gerlach, Reinhard; Giesecke, Jürgen; Haberhauer, Robert; Hafner Edzard; Hausenblas, Bernhard; Horlacher, Hans-Burkhard; Hutarew, Andreas; Knoll, Manfred; Krummet, Ralph; Marotz, Günter; Merkle, Theodor; Miller, Christoph; Minor, Hans-Erwin; Neumayer, Hans; Rao, Syamala; Rath, Paul; Rueff, Helge; Ruppert, Jürgen; Schwarz, Wolfgang; Topal-Gökceli, Mehmet; Vollmer, Ernst; Wang, Chung-su; Weber, Hans-Georg; 1975

36 Berger, Jochum: *Beitrag zur Berechnung des Spannungszustandes in rotationssymmetrisch belasteten Kugelschalen veränderlicher Wandstärke unter Gas- und Flüssigkeitsdruck durch Integration schwach singulärer Differentialgleichungen*, 1975

37 Dirksen, Wolfram: *Berechnung instationärer Abflußvorgänge in gestauten Gerinnen mittels Differenzenverfahren und die Anwendung auf Hochwasserrückhaltebecken*, 1976

38 Horlacher, Hans-Burkhard: *Berechnung instationärer Temperatur- und Wärmespannungsfelder in langen mehrschichtigen Hohlzylindern*, 1976

39 Hafner, Edzard: *Untersuchung der hydrodynamischen Kräfte auf Baukörper im Tiefwasserbereich des Meeres*, 1977, ISBN 3-921694-39-6

40 Ruppert, Jürgen: *Über den Axialwirbelkammerverstärker für den Einsatz im Wasserbau*, 1977, ISBN 3-921694-40-X

41 Hutarew, Andreas: *Beitrag zur Beeinflußbarkeit des Sauerstoffgehalts in Fließgewässern an Abstürzen und Wehren*, 1977, ISBN 3-921694-41-8, *vergriffen*

42 Miller, Christoph: *Ein Beitrag zur Bestimmung der schwingungserregenden Kräfte an unterströmten Wehren*, 1977, ISBN 3-921694-42-6

43 Schwarz, Wolfgang: *Druckstoßberechnung unter Berücksichtigung der Radial- und Längsverschiebungen der Rohrwandung*, 1978, ISBN 3-921694-43-4

44 Kinzelbach, Wolfgang: *Numerische Untersuchungen über den optimalen Einsatz variabler Kühlsysteme einer Kraftwerkskette am Beispiel Oberrhein*, 1978, ISBN 3-921694-44-2

45 Barczewski, Baldur: *Neue Meßmethoden für Wasser-Luftgemische und deren Anwendung auf zweiphasige Auftriebsstrahlen*, 1979, ISBN 3-921694-45-0

46 Neumayer, Hans: *Untersuchung der Strömungsvorgänge in radialen Wirbelkammerverstärkern*, 1979, ISBN 3-921694-46-9

47 Elalfy, Youssef-Elhassan: *Untersuchung der Strömungsvorgänge in Wirbelkammerdioden und -drosseln*, 1979, ISBN 3-921694-47-7

48 Brombach, Hansjörg: *Automatisierung der Bewirtschaftung von Wasserspeichern*, 1981, ISBN 3-921694-48-5

49 Geldner, Peter: *Deterministische und stochastische Methoden zur Bestimmung der Selbstdichtung von Gewässern*, 1981, ISBN 3-921694-49-3, *vergriffen*

50 Mehlhorn, Hans: *Temperaturveränderungen im Grundwasser durch Brauchwassereinleitungen*, 1982, ISBN 3-921694-50-7, *vergriffen*

51 Hafner, Edzard: *Rohrleitungen und Behälter im Meer*, 1983, ISBN 3-921694-51-5

52 Rinnert, Bernd: *Hydrodynamische Dispersion in porösen Medien: Einfluß von Dichteunterschieden auf die Vertikalvermischung in horizontaler Strömung*, 1983, ISBN 3-921694-52-3, *vergriffen*

53 Lindner, Wulf: *Steuerung von Grundwasserentnahmen unter Einhaltung ökologischer Kriterien*, 1983, ISBN 3-921694-53-1, *vergriffen*

54 Herr, Michael; Herzer, Jörg; Kinzelbach, Wolfgang; Kobus, Helmut; Rinnert, Bernd: *Methoden zur rechnerischen Erfassung und hydraulischen Sanierung von Grundwasserkontaminationen*, 1983, ISBN 3-921694-54-X

55 Schmitt, Paul: *Wege zur Automatisierung der Niederschlagsermittlung*, 1984, ISBN 3-921694-55-8, *vergriffen*

56 Müller, Peter: *Transport und selektive Sedimentation von Schwebstoffen bei gestautem Abfluß*, 1985, ISBN 3-921694-56-6

57 El-Qawasmeh, Fuad: *Möglichkeiten und Grenzen der Tropfbewässerung unter besonderer Berücksichtigung der Verstopfungsanfälligkeit der Tropfelemente*, 1985, ISBN 3-921694-57-4, *vergriffen*

58 Kirchenbaur, Klaus: *Mikroprozessorgesteuerte Erfassung instationärer Druckfelder am Beispiel seegangsbelasteter Baukörper*, 1985, ISBN 3-921694-58-2

59 Kobus, Helmut (Hrsg.): *Modellierung des großräumigen Wärme- und Schadstofftransports im Grundwasser*, Tätigkeitsbericht 1984/85 (DFG-Forschergruppe an den Universitäten Hohenheim, Karlsruhe und Stuttgart), 1985, ISBN 3-921694-59-0, *vergriffen*

60 Spitz, Karlheinz: *Dispersion in porösen Medien: Einfluß von Inhomogenitäten und Dichteunterschieden*, 1985, ISBN 3-921694-60-4, *vergriffen*

61 Kobus, Helmut: *An Introduction to Air-Water Flows in Hydraulics*, 1985, ISBN 3-921694-61-2

62 Kaleris, Vassilios: *Erfassung des Austausches von Oberflächen- und Grundwasser in horizontalebenen Grundwassermodellen*, 1986, ISBN 3-921694-62-0

63 Herr, Michael: *Grundlagen der hydraulischen Sanierung verunreinigter Porengrundwasserleiter*, 1987, ISBN 3-921694-63-9

64 Marx, Walter: *Berechnung von Temperatur und Spannung in Massenbeton infolge Hydratation*, 1987, ISBN 3-921694-64-7

65 Koschitzky, Hans-Peter: *Dimensionierungskonzept für Sohlbelüfter in Schußrinnen zur Vermeidung von Kavitationsschäden*, 1987, ISBN 3-921694-65-5

66 Kobus, Helmut (Hrsg.): *Modellierung des großräumigen Wärme- und Schadstofftransports im Grundwasser*, Tätigkeitsbericht 1986/87 (DFG-Forschergruppe an den Universitäten Hohenheim, Karlsruhe und Stuttgart) 1987, ISBN 3-921694-66-3

67 Söll, Thomas: *Berechnungsverfahren zur Abschätzung anthropogener Temperaturanomalien im Grundwasser*, 1988, ISBN 3-921694-67-1

68 Dittrich, Andreas; Westrich, Bernd: *Bodenseeufererosion, Bestandsaufnahme und Bewertung*, 1988, ISBN 3-921694-68-X, *vergriffen*

69 Huwe, Bernd; van der Ploeg, Rienk R.: *Modelle zur Simulation des Stickstoffhaushaltes von Standorten mit unterschiedlicher landwirtschaftlicher Nutzung*, 1988, ISBN 3-921694-69-8, *vergriffen*

70 Stephan, Karl: *Integration elliptischer Funktionen*, 1988, ISBN 3-921694-70-1

71 Kobus, Helmut; Zilliox, Lothaire (Hrsg.): *Nitratbelastung des Grundwassers, Auswirkungen der Landwirtschaft auf die Grundwasser- und Rohwasserbeschaffenheit und Maßnahmen zum Schutz des Grundwassers*. Vorträge des deutsch-französischen Kolloquiums am 6. Oktober 1988, Universitäten Stuttgart und Louis Pasteur Strasbourg (Vorträge in deutsch oder französisch, Kurzfassungen zweisprachig), 1988, ISBN 3-921694-71-X

72 Soyeaux, Renald: *Unterströmung von Stauanlagen auf klüftigem Untergrund unter Berücksichtigung laminarer und turbulenter Fließzustände*,1991, ISBN 3-921694-72-8

73 Kohane, Roberto: *Berechnungsmethoden für Hochwasserabfluß in Fließgewässern mit überströmten Vorländern*, 1991, ISBN 3-921694-73-6

74 Hassinger, Reinhard: *Beitrag zur Hydraulik und Bemessung von Blocksteinrampen in flexibler Bauweise*, 1991, ISBN 3-921694-74-4, *vergriffen*

75 Schäfer, Gerhard: *Einfluß von Schichtenstrukturen und lokalen Einlagerungen auf die Längsdispersion in Porengrundwasserleitern*, 1991, ISBN 3-921694-75-2

76 Giesecke, Jürgen: *Vorträge, Wasserwirtschaft in stark besiedelten Regionen; Umweltforschung mit Schwerpunkt Wasserwirtschaft*, 1991, ISBN 3-921694-76-0

77 Huwe, Bernd: *Deterministische und stochastische Ansätze zur Modellierung des Stickstoffhaushalts landwirtschaftlich genutzter Flächen auf unterschiedlichem Skalenniveau*, 1992, ISBN 3-921694-77-9, *vergriffen*

78 Rommel, Michael: *Verwendung von Kluftdaten zur realitätsnahen Generierung von Kluftnetzen mit anschließender laminar-turbulenter Strömungsberechnung*, 1993, ISBN 3-92 1694-78-7

79 Marschall, Paul: *Die Ermittlung lokaler Stofffrachten im Grundwasser mit Hilfe von Einbohrloch-Meßverfahren*, 1993, ISBN 3-921694-79-5, *vergriffen*

80 Ptak, Thomas: *Stofftransport in heterogenen Porenaquiferen: Felduntersuchungen und stochastische Modellierung*, 1993, ISBN 3-921694-80-9, *vergriffen*

81 Haakh, Frieder: *Transientes Strömungsverhalten in Wirbelkammern,* 1993, ISBN 3-921694-81-7

82 Kobus, Helmut; Cirpka, Olaf; Barczewski, Baldur; Koschitzky, Hans-Peter: *Versuchseinrichtung zur Grundwasser- und Altlastensanierung VEGAS, Konzeption und Programmrahmen*, 1993, ISBN 3-921694-82-5

83 Zang, Weidong: *Optimaler Echtzeit-Betrieb eines Speichers mit aktueller Abflußregenerierung*, 1994, ISBN 3-921694-83-3, *vergriffen*

84 Franke, Hans-Jörg: *Stochastische Modellierung eines flächenhaften Stoffeintrages und Transports in Grundwasser am Beispiel der Pflanzenschutzmittelproblematik*, 1995, ISBN 3-921694-84-1

85 Lang, Ulrich: *Simulation regionaler Strömungs- und Transportvorgänge in Karstaquiferen mit Hilfe des Doppelkontinuum-Ansatzes: Methodenentwicklung und Parameteridenti-fikation*, 1995, ISBN 3-921694-85-X, *vergriffen*

86 Helmig, Rainer: *Einführung in die Numerischen Methoden der Hydromechanik*, 1996, ISBN 3-921694-86-8, *vergriffen*

87 Cirpka, Olaf: *CONTRACT: A Numerical Tool for Contaminant Transport and Chemical Transformations - Theory and Program Documentation -*, 1996, ISBN 3-921694-87-6

88 Haberlandt, Uwe: *Stochastische Synthese und Regionalisierung des Niederschlages für Schmutzfrachtberechnungen*, 1996, ISBN 3-921694-88-4

89 Croisé, Jean: *Extraktion von flüchtigen Chemikalien aus natürlichen Lockergesteinen mittels erzwungener Luftströmung*, 1996, ISBN 3-921694-89-2, *vergriffen*

90 Jorde, Klaus: *Ökologisch begründete, dynamische Mindestwasserregelungen bei Ausleitungskraftwerken*, 1997, ISBN 3-921694-90-6, *vergriffen*

91 Helmig, Rainer: *Gekoppelte Strömungs- und Transportprozesse im Untergrund - Ein Beitrag zur Hydrosystemmodellierung-*, 1998, ISBN 3-921694-91-4, *vergriffen*

92 Emmert, Martin: *Numerische Modellierung nichtisothermer Gas-Wasser Systeme in porösen Medien,* 1997, ISBN 3-921694-92-2

93 Kern, Ulrich: *Transport von Schweb- und Schadstoffen in staugeregelten Fließgewässern am Beispiel des Neckars*, 1997, ISBN 3-921694-93-0, *vergriffen*

94 Förster, Georg: *Druckstoßdämpfung durch große Luftblasen in Hochpunkten von Rohrleitungen 1997*, ISBN 3-921694-94-9

95 Cirpka, Olaf: *Numerische Methoden zur Simulation des reaktiven Mehrkomponententransports im Grundwasser*, 1997, ISBN 3-921694-95-7, *vergriffen*

96 Färber, Arne: *Wärmetransport in der ungesättigten Bodenzone: Entwicklung einer thermischen In-situ-Sanierungstechnologie*, 1997, ISBN 3-921694-96-5

97 Betz, Christoph: *Wasserdampfdestillation von Schadstoffen im porösen Medium: Entwicklung einer thermischen In-situ-Sanierungstechnologie*, 1998, SBN 3-921694-97-3

98 Xu, Yichun: *Numerical Modeling of Suspended Sediment Transport in Rivers*, 1998, ISBN 3-921694-98-1, *vergriffen*

99 Wüst, Wolfgang: *Geochemische Untersuchungen zur Sanierung CKW-kontaminierter Aquifere mit Fe(0)-Reaktionswänden,* 2000, ISBN 3-933761-02-2

100 Sheta, Hussam: *Simulation von Mehrphasenvorgängen in porösen Medien unter Einbeziehung von Hysterese-Effekten*, 2000, ISBN 3-933761-03-4

101 Ayros, Edwin: *Regionalisierung extremer Abflüsse auf der Grundlage statistischer Verfahren*, 2000, ISBN 3-933761-04-2, *vergriffen*

102 Huber, Ralf: *Compositional Multiphase Flow and Transport in Heterogeneous Porous Media*, 2000, ISBN 3-933761-05-0

103 Braun, Christopherus: *Ein Upscaling-Verfahren für Mehrphasenströmungen in porösen Medien*, 2000, ISBN 3-933761-06-9

104 Hofmann, Bernd: *Entwicklung eines rechnergestützten Managementsystems zur Beurteilung von Grundwasserschadensfällen*, 2000, ISBN 3-933761-07-7

105 Class, Holger: *Theorie und numerische Modellierung nichtisothermer Mehrphasenprozesse in NAPL-kontaminierten porösen Medien,* 2001, ISBN 3-933761-08-5

106 Schmidt, Reinhard: *Wasserdampf- und Heißluftinjektion zur thermischen Sanierung kontaminierter Standorte*, 2001, ISBN 3-933761-09-3

107 Josef, Reinhold: *Schadstoffextraktion mit hydraulischen Sanierungsverfahren unter Anwendung von grenzflächenaktiven Stoffen*, 2001, ISBN 3-933761-10-7

108 Schneider, Matthias: *Habitat- und Abflussmodellierung für Fließgewässer mit unscharfen Berechnungsansätzen*, 2001, ISBN 3-933761-11-5

109 Rathgeb, Andreas: *Hydrodynamische Bemessungsgrundlagen für Lockerdeckwerke an überströmbaren Erddämmen*, 2001, ISBN 3-933761-12-3

110 Lang, Stefan: *Parallele numerische Simulation instätionärer Probleme mit adaptiven Methoden auf unstrukturierten Gittern*, 2001, ISBN 3-933761-13-1

111 Appt, Jochen; Stumpp Simone: *Die Bodensee-Messkampagne 2001, IWS/CWR Lake Constance Measurement Program 2001*, 2002, ISBN 3-933761-14-X

112 Heimerl, Stephan: *Systematische Beurteilung von Wasserkraftprojekten,* 2002, ISBN 3-933761-15-8, *vergriffen*

113 Iqbal, Amin: *On the Management and Salinity Control of Drip Irrigation,* 2002, ISBN 3-933761-16-6

114 Silberhorn-Hemminger, Annette: *Modellierung von Kluftaquifersystemen: Geostatistische Analyse und deterministisch-stochastische Kluftgenerierung,* 2002, ISBN 3-933761-17-4

115 Winkler, Angela: *Prozesse des Wärme- und Stofftransports bei der In-situ-Sanierung mit festen Wärmequellen,* 2003, ISBN 3-933761-18-2

116 Marx, Walter: *Wasserkraft, Bewässerung, Umwelt - Planungs- und Bewertungsschwerpunkte der Wasserbewirtschaftung,* 2003, ISBN 3-933761-19-0

117 Hinkelmann, Reinhard: *Efficient Numerical Methods and Information-Processing Techniques in Environment Water,* 2003, ISBN 3-933761-20-4

118 Samaniego-Eguiguren, Luis Eduardo: *Hydrological Consequences of Land Use / Land Cover and Climatic Changes in Mesoscale Catchments*, 2003, ISBN 3-933761-21-2

119 Neunhäuserer, Lina: *Diskretisierungsansätze zur Modellierung von Strömungs- und Transportprozessen in geklüftet-porösen Medien*, 2003, ISBN 3-933761-22-0

120 Paul, Maren: *Simulation of Two-Phase Flow in Heterogeneous Poros Media with Adaptive Methods*, 2003, ISBN 3-933761-23-9

121 Ehret, Uwe: *Rainfall and Flood Nowcasting in Small Catchments using Weather Radar*, 2003, ISBN 3-933761-24-7

122 Haag, Ingo: *Der Sauerstoffhaushalt staugeregelter Flüsse am Beispiel des Neckars - Analysen, Experimente, Simulationen -,* 2003, ISBN 3-933761-25-5

123 Appt, Jochen: *Analysis of Basin-Scale Internal Waves in Upper Lake Constance,* 2003, ISBN 3-933761-26-3

124 Hrsg.: Schrenk, Volker; Batereau, Katrin; Barczewski, Baldur; Weber, Karolin und Koschitzky, Hans-Peter: *Symposium Ressource Fläche und VEGAS - Statuskolloquium 2003, 30. September und 1. Oktober 2003,* 2003, ISBN 3-933761-27-1

125 Omar Khalil Ouda: *Optimisation of Agricultural Water Use: A Decision Support System for the Gaza Strip,* 2003, ISBN 3-933761-28-0

126 Batereau, Katrin: *Sensorbasierte Bodenluftmessung zur Vor-Ort-Erkundung von Schadensherden im Untergrund*, 2004, ISBN 3-933761-29-8

127 Witt, Oliver: *Erosionsstabilität von Gewässersedimenten mit Auswirkung auf den Stofftransport bei Hochwasser am Beispiel ausgewählter Stauhaltungen des Oberrheins*, 2004, ISBN 3-933761-30-1

128 Jakobs, Hartmut: *Simulation nicht-isothermer Gas-Wasser-Prozesse in komplexen Kluft-Matrix-Systemen*, 2004, ISBN 3-933761-31-X

129 Li, Chen-Chien: *Deterministisch-stochastisches Berechnungskonzept zur Beurteilung der Auswirkungen erosiver Hochwasserereignisse in Flussstauhaltungen,* 2004, ISBN 3-933761-32-8

130 Reichenberger, Volker; Helmig, Rainer; Jakobs, Hartmut; Bastian, Peter; Niessner, Jennifer: *Complex Gas-Water Processes in Discrete Fracture-Matrix Systems: Up-scaling, Mass-Conservative Discretization and Efficient Multilevel Solution,* 2004, ISBN 3-933761-33-6

131 Hrsg.: Barczewski, Baldur; Koschitzky, Hans-Peter; Weber, Karolin; Wege, Ralf: *VEGAS - Statuskolloquium 2004,* Tagungsband zur Veranstaltung am 05. Oktober 2004 an der Universität Stuttgart, Campus Stuttgart-Vaihingen, 2004, ISBN 3-933761-34-4

132 Asie, Kemal Jabir: *Finite Volume Models for Multiphase Multicomponent Flow through Porous Media*. 2005, ISBN 3-933761-35-2

133 Jacoub, George: *Development of a 2-D Numerical Module for Particulate Contaminant Transport in Flood Retention Reservoirs and Impounded Rivers,* 2004, ISBN 3-933761-36-0

134 Nowak, Wolfgang: *Geostatistical Methods for the Identification of Flow and Transport Parameters in the Subsurface,* 2005, ISBN 3-933761-37-9

135 Süß, Mia: *Analysis of the influence of structures and boundaries on flow and transport processes in fractured porous media*, 2005, ISBN 3-933761-38-7

136 Jose, Surabhin Chackiath: *Experimental Investigations on Longitudinal Dispersive Mixing in Heterogeneous Aquifers,* 2005, ISBN: 3-933761-39-5

137 Filiz, Fulya: *Linking Large-Scale Meteorological Conditions to Floods in Mesoscale Catchments,* 2005, ISBN 3-933761-40-9

138 Qin, Minghao: *Wirklichkeitsnahe und recheneffiziente Ermittlung von Temperatur und Spannungen bei großen RCC-Staumauern*, 2005, ISBN 3-933761-41-7

139 Kobayashi, Kenichiro: *Optimization Methods for Multiphase Systems in the Subsurface - Application to Methane Migration in Coal Mining Areas*, 2005, ISBN 3-933761-42-5

140 Rahman, Md. Arifur: *Experimental Investigations on Transverse Dispersive Mixing in Heterogeneous Porous Media,* 2005, ISBN 3-933761-43-3

141 Schrenk, Volker: *Ökobilanzen zur Bewertung von Altlastensanierungsmaßnahmen,* 2005, ISBN 3-933761-44-1

142 Hundecha, Hirpa Yeshewatesfa: *Regionalization of Parameters of a Conceptual Rainfall-Runoff Model*, 2005, ISBN: 3-933761-45-X

143 Wege, Ralf: *Untersuchungs- und Überwachungsmethoden für die Beurteilung natürlicher Selbstreinigungsprozesse im Grundwasser,* 2005, ISBN 3-933761-46-8

144 Breiting, Thomas: *Techniken und Methoden der Hydroinformatik - Modellierung von komplexen Hydrosystemen im Untergrund*, 2006, ISBN 3-933761-47-6

145 Hrsg.: Braun, Jürgen; Koschitzky, Hans-Peter; Müller, Martin: *Ressource Untergrund: 10 Jahre VEGAS: Forschung und Technologieentwicklung zum Schutz von Grundwasser und Boden,* Tagungsband zur Veranstaltung am 28. und 29. September 2005 an der Universität Stuttgart, Campus Stuttgart-Vaihingen, 2005, ISBN 3-933761-48-4

146 Rojanschi, Vlad: *Abflusskonzentration in mesoskaligen Einzugsgebieten unter Berücksichtigung des Sickerraumes,* 2006, ISBN 3-933761-49-2

147 Winkler, Nina Simone: *Optimierung der Steuerung von Hochwasserrückhaltebeckensystemen,* 2006, ISBN 3-933761-50-6

148 Wolf, Jens: *Räumlich differenzierte Modellierung der Grundwasserströmung alluvialer Aquifere für mesoskalige Einzugsgebiete*, 2006, ISBN: 3-933761-51-4

149 Kohler, Beate: *Externe Effekte der Laufwasserkraftnutzung*, 2006, ISBN 3-933761-52-2

150 Hrsg.: Braun, Jürgen; Koschitzky, Hans-Peter; Stuhrmann, Matthias: *VEGAS-Statuskolloquium 2006,* Tagungsband zur Veranstaltung am 28. September 2006 an der Universität Stuttgart, Campus Stuttgart-Vaihingen, 2006, ISBN 3-933761-53-0

151 Niessner, Jennifer: *Multi-Scale Modeling of Multi-Phase - Multi-Component Processes in Heterogeneous Porous Media*, 2006, ISBN 3-933761-54-9

152 Fischer, Markus: *Beanspruchung eingeerdeter Rohrleitungen infolge Austrocknung bindiger Böden,* 2006, ISBN 3-933761-55-7

153 Schneck, Alexander: *Optimierung der Grundwasserbewirtschaftung unter Berücksichtigung der Belange der Wasserversorgung, der Landwirtschaft und des Naturschutzes*, 2006, ISBN 3-933761-56-5

154 Das, Tapash: *The Impact of Spatial Variability of Precipitation on the Predictive Uncertainty of Hydrological Models,* 2006, ISBN 3-33761-57-3

155 Bielinski, Andreas: *Numerical Simulation of CO_2 sequestration in geological formations*, 2007, ISBN 3-933761-58-1

156 Mödinger, Jens: *Entwicklung eines Bewertungs- und Entscheidungsunterstützungssystems für eine nachhaltige regionale Grundwasserbewirtschaftung*, 2006, ISBN 3-933761-60-3

157 Manthey, Sabine: *Two-phase flow processes with dynamic effects in porous media - parameter estimation and simulation,* 2007, ISBN 3-933761-61-1

158 Pozos Estrada, Oscar: *Investigation on the Effects of Entrained Air in Pipelines,* 2007, ISBN 3-933761-62-X

159 Ochs, Steffen Oliver: *Steam injection into saturated porous media – process analysis including experimental and numerical investigations*, 2007, ISBN 3-933761-63-8

160 Marx, Andreas: *Einsatz gekoppelter Modelle und Wetterradar zur Abschätzung von Niederschlagsintensitäten und zur Abflussvorhersage, 2007,* ISBN 3-933761-64-6

161 Hartmann, Gabriele Maria: *Investigation of Evapotranspiration Concepts in Hydrological Modelling for Climate Change Impact Assessment*, 2007, ISBN 3-933761-65-4

162 Kebede Gurmessa, Tesfaye: *Numerical Investigation on Flow and Transport Characteristics to Improve Long-Term Simulation of Reservoir Sedimentation*, 2007, ISBN 3-933761-66-2

163 Trifković, Aleksandar: *Multi-objective and Risk-based Modelling Methodology for Planning, Design and Operation of Water Supply Systems*, 2007, ISBN 3-933761-67-0

164 Götzinger, Jens: *Distributed Conceptual Hydrological Modelling - Simulation of Climate, Land Use Change Impact and Uncertainty Analysis*, 2007, ISBN 3-933761-68-9

165 Hrsg.: Braun, Jürgen; Koschitzky, Hans-Peter; Stuhrmann, Matthias: *VEGAS – Kolloquium 2007,* Tagungsband zur Veranstaltung am 26. September 2007 an der Universität Stuttgart, Campus Stuttgart-Vaihingen, 2007, ISBN 3-933761-69-7

166 Freeman, Beau: *Modernization Criteria Assessment for Water Resources Planning; Klamath Irrigation Project, U.S.*, 2008, ISBN 3-933761-70-0

167 Dreher, Thomas: *Selektive Sedimentation von Feinstschwebstoffen in Wechselwirkung mit wandnahen turbulenten Strömungsbedingungen*, 2008, ISBN 3-933761-71-9

168 Yang, Wei: *Discrete-Continuous Downscaling Model for Generating Daily Precipitation Time Series*, 2008, ISBN 3-933761-72-7

169 Kopecki, Ianina: *Calculational Approach to FST-Hemispheres for Multiparametrical Benthos Habitat Modelling,* 2008*,* ISBN 3-933761-73-5

170 Brommundt, Jürgen: *Stochastische Generierung räumlich zusammenhängender Niederschlagszeitreihen*, 2008, ISBN 3-933761-74-3

171 Papafotiou, *Alexandros: Numerical Investigations of the Role of Hysteresis in Heterogeneous Two-Phase Flow Systems*, 2008, ISBN 3-933761-75-1

172 He, Yi: *Application of a Non-Parametric Classification Scheme to Catchment Hydrology*, 2008, ISBN 978-3-933761-76-7

173 Wagner, Sven: *Water Balance in a Poorly Gauged Basin in West Africa Using Atmospheric Modelling and Remote Sensing Information*, 2008, ISBN 978-3-933761-77-4

174 Hrsg.: Braun, Jürgen; Koschitzky, Hans-Peter; Stuhrmann, Matthias; Schrenk, Volker: *VEGAS-Kolloquium 2008 Ressource Fläche III*, Tagungsband zur Veranstaltung am 01. Oktober 2008 an der Universität Stuttgart, Campus Stuttgart-Vaihingen, 2008, ISBN 978-3-933761-78-1

175 Patil, Sachin: *Regionalization of an Event Based Nash Cascade Model for Flood Predictions in Ungauged Basins*, 2008, ISBN 978-3-933761-79-8

176 Assteerawatt, Anongnart: *Flow and Transport Modelling of Fractured Aquifers based on a Geostatistical Approach,* 2008, ISBN 978-3-933761-80-4

177 Karnahl, Joachim Alexander: *2D numerische Modellierung von multifraktionalem Schwebstoff- und Schadstofftransport in Flüssen*, 2008, ISBN 978-3-933761-81-1

178 Hiester, Uwe: *Technologieentwicklung zur In-situ-Sanierung der ungesättigten Bodenzone mit festen Wärmequellen,* 2009, ISBN 978-3-933761-82-8

179 Laux, Patrick: *Statistical Modeling of Precipitation for Agricultural Planning in the Volta Basin of West Africa,* 2009, ISBN 978-3-933761-83-5

180 Ehsan, Saqib: *Evaluation of Life Safety Risks Related to Severe Flooding,* 2009, ISBN 978-3-933761-84-2

181 Prohaska, Sandra: *Development and Application of a 1D Multi-Strip Fine Sediment Transport Model for Regulated Rivers,* 2009, ISBN 978-3-933761-85-9

182 Kopp, Andreas: *Evaluation of CO_2 Injection Processes in Geological Formations for Site Screening,* 2009, ISBN 978-3-933761-86-6

183 Ebigbo, Anozie: *Modelling of biofilm growth and its influence on CO_2 and water (two-phase) flow in porous media,* 2009, ISBN 978-3-933761-87-3

184 Freiboth, Sandra: *A phenomenological model for the numerical simulation of multiphase multicomponent processes considering structural alterations of porous media*, 2009, ISBN 978-3-933761-88-0

185 Zöllner, Frank: *Implementierung und Anwendung netzfreier Methoden im Konstruktiven Wasserbau und in der Hydromechanik*, 2009, ISBN 978-3-933761-89-7

186 Vasin, Milos: *Influence of the soil structure and property contrast on flow and transport in the unsaturated zone*, 2010, ISBN 978-3-933761-90-3

187 Li, Jing: *Application of Copulas as a New Geostatistical Tool*, 2010, ISBN 978-3-933761-91-0

188 AghaKouchak, Amir: *Simulation of Remotely Sensed Rainfall Fields Using Copulas*, 2010, ISBN 978-3-933761-92-7

189 Thapa, Pawan Kumar: *Physically-based spatially distributed rainfall runoff modelling for soil erosion estimation*, 2010, ISBN 978-3-933761-93-4

190 Wurms, Sven: *Numerische Modellierung der Sedimentationsprozesse in Retentionsanlagen zur Steuerung von Stoffströmen bei extremen Hochwasserabflussereignissen*, 2011, ISBN 978-3-933761-94-1

191 Merkel, Uwe: *Unsicherheitsanalyse hydraulischer Einwirkungen auf Hochwasserschutzdeiche und Steigerung der Leistungsfähigkeit durch adaptive Strömungsmodellierung*, 2011, ISBN 978-3-933761-95-8

192 Fritz, Jochen: *A Decoupled Model for Compositional Non-Isothermal Multiphase Flow in Porous Media and Multiphysics Approaches for Two-Phase Flow*, 2010, ISBN 978-3-933761-96-5

193 Weber, Karolin (Hrsg.): *12. Treffen junger WissenschaftlerInnen an Wasserbauinstituten*, 2010, ISBN 978-3-933761-97-2

194 Bliefernicht, Jan-Geert: *Probability Forecasts of Daily Areal Precipitation for Small River Basins,* 2011, ISBN 978-3-933761-98-9

195 Hrsg.: Koschitzky, Hans-Peter; Braun, Jürgen: *VEGAS-Kolloquium 2010 In-situ-Sanierung - Stand und Entwicklung Nano und ISCO -,* Tagungsband zur Veranstaltung am 07. Oktober 2010 an der Universität Stuttgart, Campus Stuttgart-Vaihingen*,* 2010*,* ISBN 978-3-933761-99-6

196 Gafurov, Abror: *Water Balance Modeling Using Remote Sensing Information - Focus on Central Asia,* 2010, ISBN 978-3-942036-00-9

197 Mackenberg, Sylvia: *Die Quellstärke in der Sickerwasserprognose: Möglichkeiten und Grenzen von Labor- und Freilanduntersuchungen,* 2010, ISBN 978-3-942036-01-6

198 Singh, Shailesh Kumar: *Robust Parameter Estimation in Gauged and Ungauged Basins,* 2010, ISBN 978-3-942036-02-3

199 Doğan, Mehmet Onur: *Coupling of porous media flow with pipe flow,* 2011, ISBN 978-3-942036-03-0

200 Liu, Min: *Study of Topographic Effects on Hydrological Patterns and the Implication on Hydrological Modeling and Data Interpolation,* 2011, ISBN 978-3-942036-04-7

201 Geleta, Habtamu Itefa: *Watershed Sediment Yield Modeling for Data Scarce Areas,* 2011, ISBN 978-3-942036-05-4

202 Franke, Jörg: *Einfluss der Überwachung auf die Versagenswahrscheinlichkeit von Staustufen,* 2011, ISBN 978-3-942036-06-1

203 Bakimchandra, Oinam: *Integrated Fuzzy-GIS approach for assessing regional soil erosion risks,* 2011, ISBN 978-3-942036-07-8

204 Alam, Muhammad Mahboob: *Statistical Downscaling of Extremes of Precipitation in Mesoscale Catchments from Different RCMs and Their Effects on Local Hydrology,* 2011, ISBN 978-3-942036-08-5

205 Hrsg.: Koschitzky, Hans-Peter; Braun, Jürgen: *VEGAS-Kolloquium 2011 Flache Geothermie - Perspektiven und Risiken,* Tagungsband zur Veranstaltung am 06. Oktober 2011 an der Universität Stuttgart, Campus Stuttgart-Vaihingen*,* 2011*,* ISBN 978-3-933761-09-2

206 Haslauer, Claus: *Analysis of Real-World Spatial Dependence of Subsurface Hydraulic Properties Using Copulas with a Focus on Solute Transport Behaviour,* 2011, ISBN 978-3-942036-10-8

207 Dung, Nguyen Viet: *Multi-objective automatic calibration of hydrodynamic models – development of the concept and an application in the Mekong Delta,* 2011, ISBN 978-3-942036-11-5

208 Hung, Nguyen Nghia: *Sediment dynamics in the floodplain of the Mekong Delta, Vietnam,* 2011, ISBN 978-3-942036-12-2

209 Kuhlmann, Anna: *Influence of soil structure and root water uptake on flow in the unsaturated zone,* 2012, ISBN 978-3-942036-13-9

210 Tuhtan, Jeffrey Andrew: *Including the Second Law Inequality in Aquatic Ecodynamics: A Modeling Approach for Alpine Rivers Impacted by Hydropeaking,* 2012, ISBN 978-3-942036-14-6

211 Tolossa, Habtamu: *Sediment Transport Computation Using a Data-Driven Adaptive Neuro-Fuzzy Modelling Approach,* 2012, ISBN 978-3-942036-15-3

212 Tatomir, Alexandru-Bodgan: *From Discrete to Continuum Concepts of Flow in Fractured Porous Media,* 2012, ISBN 978-3-942036-16-0

213 Erbertseder, Karin: *A Multi-Scale Model for Describing Cancer-Therapeutic Transport in the Human Lung,* 2012, ISBN 978-3-942036-17-7

214 Noack, Markus: *Modelling Approach for Interstitial Sediment Dynamics and Reproduction of Gravel Spawning Fish,* 2012, ISBN 978-3-942036-18-4

215 De Boer, Cjestmir Volkert: *Transport of Nano Sized Zero Valent Iron Colloids during Injection into the Subsurface*, 2012, ISBN 978-3-942036-19-1

216 Pfaff, Thomas: *Processing and Analysis of Weather Radar Data for Use in Hydrology*, 2013, ISBN 978-3-942036-20-7

217 Lebrenz, Hans-Henning: *Addressing the Input Uncertainty for Hydrological Modeling by a New Geostatistical Method*, 2013, ISBN 978-3-942036-21-4

218 Darcis, Melanie Yvonne: *Coupling Models of Different Complexity for the Simulation of CO_2 Storage in Deep Saline Aquifers*, 2013, ISBN 978-3-942036-22-1

219 Beck, Ferdinand: *Generation of Spatially Correlated Synthetic Rainfall Time Series in High Temporal Resolution - A Data Driven Approach*, 2013, ISBN 978-3-942036-23-8

220 Guthke, Philipp: *Non-multi-Gaussian spatial structures: Process-driven natural genesis, manifestation, modeling approaches, and influences on dependent processes*, 2013, ISBN 978-3-942036-24-5

221 Walter, Lena: *Uncertainty studies and risk assessment for CO_2 storage in geological formations*, 2013, ISBN 978-3-942036-25-2

222 Wolff, Markus: *Multi-scale modeling of two-phase flow in porous media including capillary pressure effects,* 2013, ISBN 978-3-942036-26-9

223 Mosthaf, Klaus Roland: *Modeling and analysis of coupled porous-medium and free flow with application to evaporation processes,* 2014, ISBN 978-3-942036-27-6

224 Leube, Philipp Christoph: *Methods for Physically-Based Model Reduction in Time: Analysis, Comparison of Methods and Application*, 2013, ISBN 978-3-942036-28-3

225 Rodríguez Fernández, Jhan Ignacio: *High Order Interactions among environmental variables: Diagnostics and initial steps towards modeling*, 2013, ISBN 978-3-942036-29-0

226 Eder, Maria Magdalena: *Climate Sensitivity of a Large Lake*, 2013, ISBN 978-3-942036-30-6

227 Greiner, Philipp: *Alkoholinjektion zur In-situ-Sanierung von CKW Schadensherden in Grundwasserleitern: Charakterisierung der relevanten Prozesse auf unterschiedlichen Skalen*, 2014, ISBN 978-3-942036-31-3

228 Lauser, Andreas: *Theory and Numerical Applications of Compositional Multi-Phase Flow in Porous Media*, 2014, ISBN 978-3-942036-32-0

229 Enzenhöfer, Rainer: *Risk Quantification and Management in Water Production and Supply Systems*, 2014, ISBN 978-3-942036-33-7

230 Faigle, Benjamin: *Adaptive modelling of compositional multi-phase flow with capillary pressure*, 2014, ISBN 978-3-942036-34-4

231 Oladyshkin, Sergey: *Efficient modeling of environmental systems in the face of complexity and uncertainty*, 2014, ISBN 978-3-942036-35-1

232 Sugimoto, Takayuki: *Copula based Stochastic Analysis of Discharge Time Series*, 2014, ISBN 978-3-942036-36-8

233 Koch, Jonas: *Simulation, Identification and Characterization of Contaminant Source Architectures in the Subsurface*, 2014, ISBN 978-3-942036-37-5

234 Zhang, Jin: *Investigations on Urban River Regulation and Ecological Rehabilitation Measures, Case of Shenzhen in China*, 2014, ISBN 978-3-942036-38-2

235 Siebel, Rüdiger: *Experimentelle Untersuchungen zur hydrodynamischen Belastung und Standsicherheit von Deckwerken an überströmbaren Erddämmen,* 2014, ISBN 978-3-942036-39-9

236 Baber, Katherina: *Coupling free flow and flow in porous media in biological and technical applications: From a simple to a complex interface description,* 2014, ISBN 978-3-942036-40-5

237 Nuske, Klaus Philipp: *Beyond Local Equilibrium — Relaxing local equilibrium assumptions in multiphase flow in porous media,* 2014, ISBN 978-3-942036-41-2

238 Geiges, Andreas: *Efficient concepts for optimal experimental design in nonlinear environmental systems*, 2014, ISBN 978-3-942036-42-9

239 Schwenck, Nicolas: *An XFEM-Based Model for Fluid Flow in Fractured Porous Media*, 2014, ISBN 978-3-942036-43-6

240 Chamorro Chávez, Alejandro: *Stochastic and hydrological modelling for climate change prediction in the Lima region, Peru*, 2015, ISBN 978-3-942036-44-3

241 Yulizar: *Investigation of Changes in Hydro-Meteorological Time Series Using a Depth-Based Approach*, 2015, ISBN 978-3-942036-45-0

242 Kretschmer, Nicole: *Impacts of the existing water allocation scheme on the Limarí watershed – Chile, an integrative approach*, 2015, ISBN 978-3-942036-46-7

243 Kramer, Matthias: *Luftbedarf von Freistrahlturbinen im Gegendruckbetrieb*, 2015, ISBN 978-3-942036-47-4

244 Hommel, Johannes: *Modeling biogeochemical and mass transport processes in the subsurface: Investigation of microbially induced calcite precipitation*, 2016, ISBN 978-3-942036-48-1

245 Germer, Kai: *Wasserinfiltration in die ungesättigte Zone eines makroporösen Hanges und deren Einfluss auf die Hangstabilität*, 2016, ISBN 978-3-942036-49-8

246 Hörning, Sebastian: *Process-oriented modeling of spatial random fields using copulas*, 2016, ISBN 978-3-942036-50-4

247 Jambhekar, Vishal: *Numerical modeling and analysis of evaporative salinization in a coupled free-flow porous-media system,* 2016, ISBN 978-3-942036-51-1

248 Huang, Yingchun: *Study on the spatial and temporal transferability of conceptual hydrological models*, 2016, ISBN 978-3-942036-52-8

249 Kleinknecht, Simon Matthias: *Migration and retention of a heavy NAPL vapor and remediation of the unsaturated zone*, 2016, ISBN 978-3-942036-53-5

250 Kwakye, Stephen Oppong: *Study on the effects of climate change on the hydrology of the West African sub-region*, 2016, ISBN 978-3-942036-54-2

251 Kissinger, Alexander: *Basin-Scale Site Screening and Investigation of Possible Impacts of CO_2 Storage on Subsurface Hydrosystems*, 2016, ISBN 978-3-942036-55-9

252 Müller, Thomas: *Generation of a Realistic Temporal Structure of Synthetic Precipitation Time Series for Sewer Applications*, 2017, ISBN 978-3-942036-56-6

253 Grüninger, Christoph: *Numerical Coupling of Navier-Stokes and Darcy Flow for Soil-Water Evaporation*, 2017, ISBN 978-3-942036-57-3

254 Suroso: *Asymmetric Dependence Based Spatial Copula Models: Empirical Investigations and Consequences on Precipitation Fields*, 2017, ISBN 978-3-942036-58-0

255 Müller, Thomas; Mosthaf, Tobias; Gunzenhauser, Sarah; Seidel, Jochen; Bárdossy, András: *Grundlagenbericht Niederschlags-Simulator (NiedSim3)*, 2017, ISBN 978-3-942036-59-7

256 Mosthaf, Tobias: *New Concepts for Regionalizing Temporal Distributions of Precipitation and for its Application in Spatial Rainfall Simulation,* 2017, ISBN 978-3-942036-60-3

257 Fenrich, Eva Katrin: *Entwicklung eines ökologisch-ökonomischen Vernetzungsmodells für Wasserkraftanlagen und Mehrzweckspeicher,* 2018, ISBN 978-3-942036-61-0

258 Schmidt, Holger: *Microbial stabilization of lotic fine sediments*, 2018, ISBN 978-3-942036-62-7

259 Fetzer, Thomas: *Coupled Free and Porous-Medium Flow Processes Affected by Turbulence and Roughness–Models, Concepts and Analysis*, 2018, ISBN 978-3-942036-63-4

260 Schröder, Hans Christoph: *Large-scale High Head Pico Hydropower Potential Assessment*, 2018, ISBN 978-3-942036-64-1

261 Bode, Felix: *Early-Warning Monitoring Systems for Improved Drinking Water Resource Protection*, 2018, ISBN 978-3-942036-65-8

262 Gebler, Tobias: *Statistische Auswertung von simulierten Talsperrenüberwachungsdaten zur Identifikation von Schadensprozessen an Gewichtsstaumauern*, 2018, ISBN 978-3-942036-66-5

263 Harten, Matthias von: *Analyse des Zuppinger-Wasserrades – Hydraulische Optimierungen unter Berücksichtigung ökologischer Aspekte*, 2018, ISBN 978-3-942036-67-2

264 Yan, Jieru: *Nonlinear estimation of short time precipitation using weather radar and surface observations*, 2018, ISBN 978-3-942036-68-9

265 Beck, Martin: *Conceptual approaches for the analysis of coupled hydraulic and geomechanical processes*, 2019, ISBN 978-3-942036-69-6

266 Haas, Jannik: *Optimal planning of hydropower and energy storage technologies for fully renewable power systems*, 2019, ISBN 978-3-942036-70-2

267 Schneider, Martin: *Nonlinear Finite Volume Schemes for Complex Flow Processes and Challenging Grids*, 2019, ISBN 978-3-942036-71-9

268 Most, Sebastian Christopher: *Analysis and Simulation of Anomalous Transport in Porous Media*, 2019, ISBN 978-3-942036-72-6

269 Buchta, Rocco: *Entwicklung eines Ziel- und Bewertungssystems zur Schaffung nachhaltiger naturnaher Strukturen in großen sandgeprägten Flüssen des norddeutschen Tieflandes*, 2019, ISBN 978-3-942036-73-3

270 Thom, Moritz: *Towards a Better Understanding of the Biostabilization Mechanisms of Sediment Beds*, 2019, ISBN 978-3-942036-74-0

271 Stolz, Daniel: *Die Nullspannungstemperatur in Gewichtsstaumauern unter Berücksichtigung der Festigkeitsentwicklung des Betons*, 2019, ISBN 978-3-942036-75-7

272 Rodriguez Pretelin, Abelardo: *Integrating transient flow conditions into groundwater well protection*, 2020, ISBN: 978-3-942036-76-4

273 Weishaupt, Kilian: *Model Concepts for Coupling Free Flow with Porous Medium Flow at the Pore-Network Scale: From Single-Phase Flow to Compositional Non-Isothermal Two-Phase Flow*, 2020, ISBN: 978-3-942036-77-1

274 Koch, Timo: *Mixed-dimension models for flow and transport processes in porous media with embedded tubular network systems*, 2020, ISBN: 978-3-942036-78-8

275 Gläser, Dennis: *Discrete fracture modeling of multi-phase flow and deformation in fractured poroelastic media*, 2020, ISBN: 978-3-942036-79-5

276 Seitz, Lydia: *Development of new methods to apply a multi-parameter approach – A first step towards the determination of colmation*, 2020, ISBN: 978-3-942036-80-1

277 Ebrahim Bakhshipour, Amin: *Optimizing hybrid decentralized systems for sustainable urban drainage infrastructures planning*, 2021, ISBN: 978-3-942036-81-8

278 Seitz, Gabriele: *Modeling Fixed-Bed Reactors for Thermochemical Heat Storage with the Reaction System CaO/Ca(OH)$_2$*, 2021, ISBN: 978-3-942036-82-5

279 Emmert, Simon: *Developing and Calibrating a Numerical Model for Microbially Enhanced Coal-Bed Methane Production*, 2021, ISBN: 978-3-942036-83-2

280 Heck, Katharina Klara: Modelling and analysis of multicomponent transport at the interface between free- and porous-medium flow - influenced by radiation and roughness, 2021, ISBN: 978-3-942036-84-9

281 Ackermann, Sina: *A multi-scale approach for drop/porous-medium interaction*, 2021, ISBN: 978-3-942036-85-6

282 Beckers, Felix: *Investigations on Functional Relationships between Cohesive Sediment Erosion and Sediment Characteristics*, 2021, ISBN: 978-3-942036-86-3

283 Schlabing, Dirk: *Generating Weather for Climate Impact Assessment on Lakes*, 2021, ISBN: 978-3-942036-87-0

284 Becker, Beatrix: *Efficient multiscale multiphysics models accounting for reversible flow at various subsurface energy storage sites*, 2021, ISBN: 978-3-942036-88-7

285 Reuschen, Sebastian: *Bayesian Inversion and Model Selection of Heterogeneities in Geo-statistical Subsurface Modeling*, 2021, ISBN: 978-3-942036-89-4

286 Michalkowski, Cynthia: *Modeling water transport at the interface between porous GDL and gas distributor of a PEM fuel cell cathode*, 2022, ISBN: 978-3-942036-90-0

287 Koca, Kaan: *Advanced experimental methods for investigating flow-biofilm-sediment interactions*, 2022, ISBN: 978-3-942036-91-7

288 Modiri, Ehsan: *Clustering simultaneous occurrences of extreme floods in the Neckar catchment*, 2022, ISBN: 978-3-942036-92-4

289 Mayar, Mohammad Assem: *High-resolution spatio-temporal measurements of the colmation phenomenon under laboratory conditions*, 2022, ISBN: 978-3-942036-93-1

290 Schäfer Rodrigues Silva, Aline: *Quantifying and Visualizing Model Similarities for Multi-Model Methods*, 2022, ISBN: 978-3-942036-94-8

291 Moreno Leiva, Simón: *Optimal planning of water and renewable energy systems for copper production processes with sector coupling and demand flexibility*, 2022, ISBN 978-3-942036-95-5

292 Schönau, Steffen: *Modellierung von Bodenerosion und Sedimentaustrag bei Hochwasserereignissen am Beispiel des Einzugsgebiets der Rems*, 2022, ISBN 978-3-942036-96-2

293 Glatz, Kumiko: *Upscaling of Nanoparticle Transport in Porous Media,* 2022, ISBN 978-3-942036-97-9

294 Pavía Santolamazza, Daniela: *Event-based flood estimation using a random forest algorithm for the regionalization in small catchments*, 2022, ISBN 978-3-942036-98-6

295 Haun, Stefan: *Advanced Methods for a Sustainable Sediment Management of Reservoirs*, 2022, ISBN 978-3-942036-99-3

296 Herma, Felix: *Data Processing and Model Choice for Flood Prediction*, 2022, ISBN 978-3-910293-00-7

297 Weinhardt, Felix: *Porosity and permeability alterations in processes of biomineralization in porous media - microfluidic investigations and their interpretation*, 2022, ISBN 978-3-910293-01-4

298 Sadid, Najibullah: *Bedload Transport Estimation in Mountainous Intermittent Rivers and Streams*, 2023, ISBN 978-3-910293-02-1

299 Mohammadi, Farid: *A Surrogate-Assisted Bayesian Framework for Uncertainty-Aware Validation Benchmarks*, 2023, ISBN 978-3-910293-03-8

300 Praditia, Timothy: *Physics-informed Neural Networks for Learning Dynamic, Distributed and Uncertain Systems*, 2023, ISBN 978-3-910293-04-5

301 Gyawali, Dhiraj Raj: *Development and parameter estimation of conceptual snow-melt models using MODIS snow-cover distribution*, 2023, ISBN 978-3-910293-05-2

302 Görtz, Jan: *Coupled modeling approach for physico-chemical processes during the deterioration of cement-based structures*, 2023, ISBN 978-3-910293-06-9

303 Veyskarami, Maziar: *Coupled free-flow–porous media flow processes including drop formation*, 2023, ISBN 978-3-910293-07-6

304 El Hachem, Abbas: *Spatial Extent of Precipitation Extremes in Hydrology*, 2023, ISBN 978-3-910293-08-3

305 Banerjee, Ishani: *Stochastic Model Comparison and Refinement Strategies for Gas Migration in the Subsurface*, 2023, ISBN 978-3-910293-09-0

306 Anwar, Faizan: *Spatial aspects of hydrological extremes: Description and simulation*, 2024, ISBN 978-3-910293-10-6

307 Mouris, Kilian: *A holistic approach to assess the impact of global change on reservoir sedimentation*, 2024, ISBN 978-3-910293-11-3

Die Mitteilungshefte ab der Nr. 134 (Jg. 2005) stehen als pdf-Datei über die Homepage des Instituts: www.iws.uni-stuttgart.de zur Verfügung.